Heralding Photonic Qubits for Quantum Communication

by

Evan Meyer-Scott

A thesis
presented to the University of Waterloo
in fulfillment of the
thesis requirement for the degree of
Doctor of Philosophy
in
Physics (Quantum Information)

Waterloo, Ontario, Canada, 2016

Author's Declaration

This thesis consists of material all of which I authored or co-authored: see Statement of Contributions included in the thesis. This is a true copy of the thesis, including any required final revisions, as accepted by my examiners.

I understand that my thesis may be made electronically available to the public.

Statement of Contributions

This thesis contains work done in collaboration with others but to which I made the major contribution. In this thesis I use "I" when reporting work I did on my own, and "we" when reporting collaborative work. Please see the beginning of each chapter 2-7 for complete statements of contribution, including the contribution of each co-author.

Chapter 1:	I wrote the introductory chapter.
Chapter 2:	I wrote this chapter about work I did with others towards a loophole-free Bell test. I include only work to which I directly contributed, the most significant of which was solving the fibre-to-fibre coupling problem.
Chapter 3:	I conceived the amplifier idea based on previous work by the other authors. I co-authored the introduction, and did all the analysis and writing of the DI-QKD section.
Chapter 4:	I conceived the precertification idea (independently of another author), performed the experiment, analyzed the data, and wrote the paper with input from all authors.
Chapter 5:	I conceived the idea for single-photon four-wave mixing with other authors and co-authored the paper.
Chapter 6:	I performed the entangled photon generation experiment, analyzed the data, and wrote the paper with input from all authors.
Chapter 7:	I conceived and performed the photon pair generation experiments with other authors. I analyzed the data and wrote the paper with input from all authors.
Chapter 8:	I wrote the concluding chapter.

Abstract

Quantum communication attempts to harness the unique rules of quantum mechanics to perform communication tasks that are difficult or impossible using classical rules. To realize these benefits, information must be carried on quantum systems. Photons make excellent carriers because they interact very little with the environment, move quickly, and can naturally store quantum information in their polarization. However, it is notoriously difficult to detect a single photon without destroying it. Standard detectors simply absorb the photon, losing the quantum information. This is a critical outstanding problem in quantum communication, as advanced protocols need to know exactly when a photon has arrived at a receiver after transmission through the atmosphere or an optical fibre before performing further quantum-information-processing tasks. Certifying a photon's presence is of particular interest in tests of Bell's inequalities, which have only recently been performed without loopholes arising from photon loss, and in device-independent quantum cryptography, which relies on such Bell tests for security.

In this thesis, I first present work on directly reducing losses in a successful loophole-free Bell test. This is an extremely difficult task that cannot be extended for long-distance communication. Therefore I then focus on ways to circumvent loss by detecting photons without destroying them while preserving their quantum information. First I analyze theoretically a way to herald photons using only linear-optical elements (beam splitters and phase shifters) and extra ancilla photons. Similar but older methods have been demonstrated experimentally by other groups, and my improvements will help future advanced quantum communication protocols.

The main experiment in this thesis certifies the presence of a photon in a rather simple way: split the photon into two using a nonlinear optical crystal, then detect one of the pair to herald the other. I show in this first proof-of-principle experiment that photonic qubit precertification indeed preserves qubit states, with up to $(92.3 \pm 0.6)\,\%$ fidelity and rates of 1100 events per hour. With reductions in detector dark counts, precertification could outperform direct transmission, even with extremely lossy fibre links.

Finally, I present two sources of photons based on nonlinearities in optical fibres. One of the limitations of the photon splitting scheme for heralding is the low success probability due to the very low likelihood of splitting a photon in two. In these fibre photon sources I investigate increasing the splitting likelihood in four-wave mixing through advanced materials and fibre designs. I use polarization-maintaining fibres to generate entangled photon pairs as a prerequisite to precertification, with $(92.2 \pm 0.2)\,\%$ fidelity to a maximally-entangled state. Then I show that one type of highly nonlinear chalcogenide glass, never before used for photon pair generation, could outperform standard nonlinear crystals by two orders of magnitude, with calculated conversion efficiency up to 10^{-3}. To approach the single photon regime, I generate photon pairs in chalcogenide microwires with pump powers as low as $480\,\mathrm{nW}$ and verify their timing correlations.

These advances demonstrate the capability of nondestructive precertification of photons to allow advanced quantum communications protocols even over long distance, and could lead to the first implementations of fully device-independent quantum cryptography.

Acknowledgements

A thousand thank-yous to my supervisor Thomas Jennewein, for his guidance, support, enthusiasm and counsel. I also thank the members of my committee, Kevin Resch, Norbert Lütkenhaus, and Joseph Emerson, for answering my many questions and providing constructive feedback. Finally I thank Hugo Zbinden for examining this thesis.

Many thanks to Krister Shalm, Sae Woo Nam, Richard Mirin, Bradley Christensen, and everyone at NIST who made my stays enjoyable and productive. I thank my collaborators Marek Bula, Karol Bartkiewicz, Antonín Černoch, Jan Soubusta, and Karel Lemr who made the work on the linear-optical photon amplifier possible. Thanks to Daniel McCloskey, Klaudia Gołos, Jeff Salvail, Kent Fisher, Deny Hamel, and Adán Cabello for their work on the qubit precertification experiment, and to Aaron Miller for selling us nice detectors. I thank Vincent Roy, Pascal Deladurantaye, Jean-Philippe Bourgoin, Brendon Higgins, and Krister Shalm for making the sausage source possible. Thanks to Audrey Dot, Raja Ahmad, Lizhu Li, and Martin Rochette for their excellent theory and experimental contributions on four-wave mixing with chalcogenide microwires, to Piotr Kolenderski for helpful discussions, and to Coractive High-Tech for providing the chalcogenide glass used in the experiments.

I cherish the time I spent in the Quantum Photonics Lab. Thanks to Sascha Agne, Elena Anisimova, Jean-Philippe Bourgoin, Eric Choi, Audrey Dot, Aimee Gunther, Brendon Higgins, Catherine Holloway, Rolf Horn, Jeongwan Jin, Sarah Kaiser, Piotr Kolenderski, Christopher Pugh, Nigar Sultana, and Yanbao Zhang for the countless discussions and joke-scussions. Thanks also to our next-door neighbours Kent Fisher, John Donohue, Mike Mazurek, Jeff Salvail, Jean-Philippe Maclean, Matt Brown, Megan Agnew, Jonathan Lavoie, and Lydia Vermeyden of the Quantum Optics and Quantum Information lab for all the stuff I borrowed, and for knowing everything I didn't.

I would like to give special thanks to Deny Hamel. His guidance and friendship enabled and improved much of the work in this thesis, and contributed very strongly to my scientific and personal well-being.

Finally, thank you, Kirstyn Meyer-Scott, for supporting me in this long period of schooling, and for raising Elliot and Jenny *so well*.

I gratefully acknowledge the funding agencies that have contributed to this work, NSERC, Ontario Ministry of Research and Innovation, CIFAR, FedDev Ontario, Industry Canada, and CFI. I was personally funded by NSERC, the Government of Alberta, and the University of Waterloo, for which I am very thankful.

Dedication

To Kirstyn, Elliot, and Jenny.

Table of Contents

List of Tables

List of Figures

Chapter 1

Background: quantum communication and heralding qubits

I this thesis I present theory and experiments in advanced practical quantum communication. An overview of the work is given in fig. 1.1.

1.1 Quantum communication

The field of quantum communication seeks to harness the power of quantum mechanics to perform communication tasks that are difficult or impossible in classical physics. Protocols such as dense coding [1, 2], quantum key distribution [3, 4, 5, 6], quantum teleportation [7, 8, 9, 10, 11], and tests of local realism based on Bell's inequality [12, 13, 14] outperform their classical counterparts. Additionally the secure generation of random numbers [15, 16] uses similar principles. Many of these protocols have been implemented in realistic communications settings: quantum teleportation [17] over long-distance free-space [18, 19] and fibre channels [11, 20]; quantum key distribution over long distance [21, 22, 23, 24, 25] and at high rate [23, 26, 27, 28]; and tests of Bell's inequalities in many scenarios [13, 14, 29, 30, 31, 32, 33, 34].

However, the most significant advantage quantum communication can provide, device

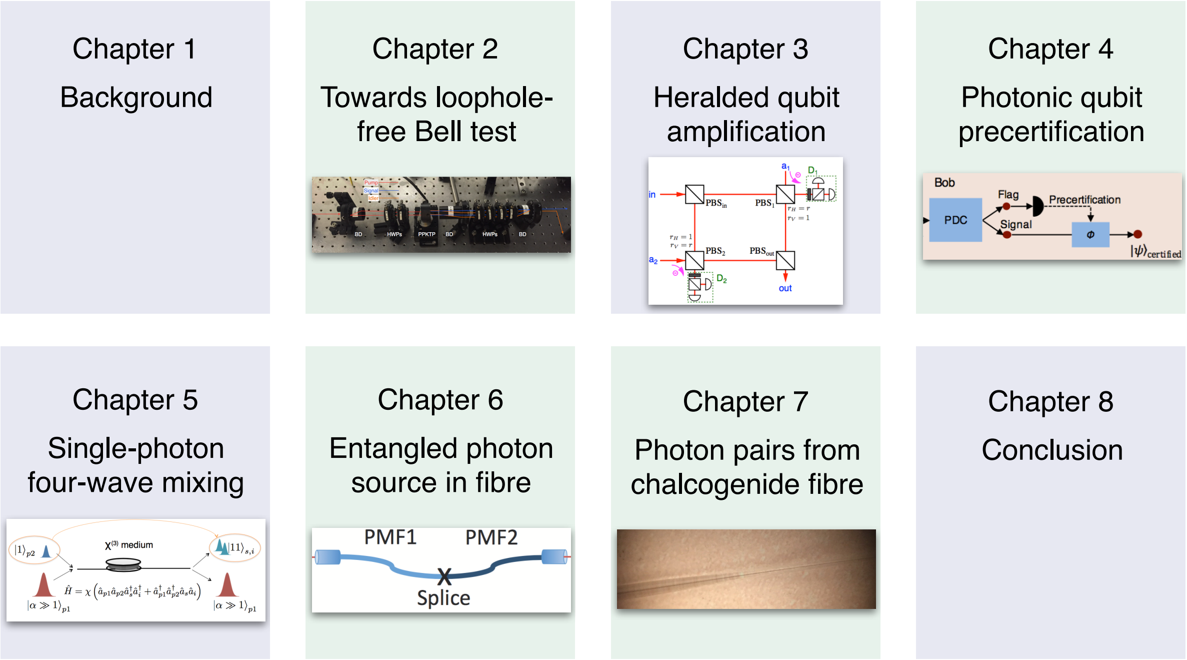

$\hat{H} = \chi\left(\hat{a}_{p1}\hat{a}_{p2}\hat{a}_s^\dagger\hat{a}_i^\dagger + \hat{a}_{p1}^\dagger\hat{a}_{p2}^\dagger\hat{a}_s\hat{a}_i\right)$

Figure 1.1: Overview of the work presented in this thesis. The images are hyperlinks to their respective chapters in the electronic version. Green backgrounds indicate experiments.

independence [35, 36], has yet to be realized. By violating a Bell inequality, the legitimate parties in device-independent communication can exclude eavesdroppers even without detailed knowledge or characterization of their devices. The difficulty in implementing device-independent quantum communication is that it requires a Bell inequality violation without loopholes, something that has only recently become possible experimentally [37, 38, 39].

1.1.1 Bell's inequalities

Bell's theorem of 1964 [12] shows that the predictions of quantum mechanics, specifically those involving separated measurements on entangled states, cannot be replicated by local realistic theories. Local realism, which seems like a natural physical assumption, has two parts: locality requires that spacelike-separated events cannot influence one another (i.e. influences cannot travel faster than the speed of light), and realism requires that physical systems have pre-existing properties independent of measurements. That local realism is incompatible with quantum mechanics (and that quantum mechanics is correct) requires abandoning local realism as a fundamental principle of the universe. Some people do not like this [40]. Nonetheless, recent loophole-free violations of Bell's inequalities leave us with little choice [37, 38, 39].

Bell's 1964 inequality was transformed to more easily tested forms by Clauser, Horne, Shimony, and Holt [41], and by Clauser and Horne (CH) [42]. A general experimental setup for a test of Bell's inequality (or a Bell test, for short) is shown in fig. 1.2. A source of entangled photon pairs sends one photon to each of two parties commonly named Alice and Bob, who make measurements on each photon. Alice and Bob compare their measurement results to infer the underlying joint probabilities of measurement outcomes, which are plugged into an inequality to look for a violation. Though Bell's inequalities have been violated with other quantum systems [31, 43, 44, 45], I restrict myself here to photons, as these are the most suitable carriers of quantum information for communication. The CH form of Bell's inequality is

$$p_{AB}(a,b) + p_{AB}(a,b') + p_{AB}(a',b) - p_{AB}(a',b') - p_A(a) - p_B(b) \leq 0, \tag{1.1}$$

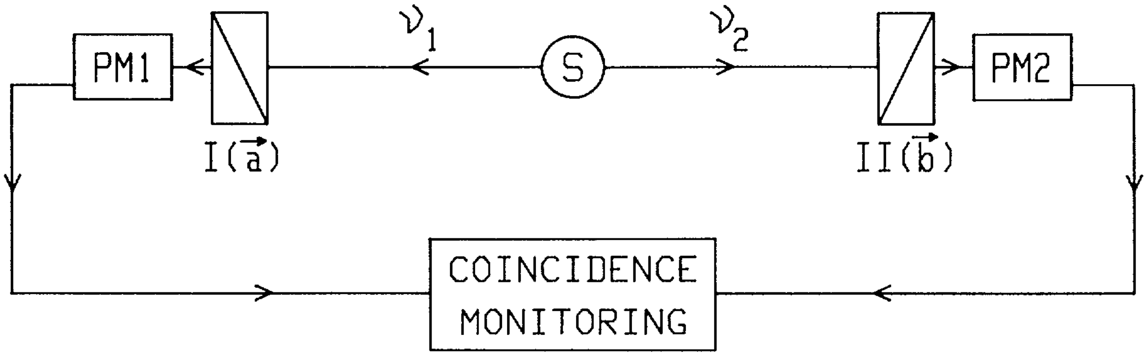

Figure 1.2: The general form of a Bell test. A source of S entangled photon pairs (ν_1, ν_2) sends them to distant receivers. The receivers make measurements with settings I($\vec{a}$) and II($\vec{b}$) and detectors PM1 and PM2 to find the terms of the Bell inequality (1.1). Figure reprinted with permission from [13]. © 1982 by the American Physical Society.

where $p_{AB}(a^{(\prime)}, b^{(\prime)})$ is the probability of a coincident detection by Alice and Bob for measurement settings $a^{(\prime)}$ and $b^{(\prime)}$ respectively, and $p_A(a)/p_B(b)$ is the probability of a single detection at Alice/Bob for measurement setting a/b independent of the other party. Probability distributions governed by local realism can saturate the inequality but not violate it. Quantum mechanics predicts a maximum value for the left-hand side of inequality (1.1) of $\frac{\sqrt{2}-1}{2} \approx 0.207$ [46]. This maximum violation is obtained for the maximally-entangled two-qubit states

$$\begin{aligned} |\Phi^{\pm}\rangle &= \frac{1}{\sqrt{2}} \left(|0\rangle_A |0\rangle_B \pm |1\rangle_A |1\rangle_B \right) \\ |\Psi^{\pm}\rangle &= \frac{1}{\sqrt{2}} \left(|0\rangle_A |1\rangle_B \pm |1\rangle_A |0\rangle_B \right), \end{aligned} \tag{1.2}$$

known as the Bell states. Here A and B refer to the modes sent to Alice and Bob respectively. In this thesis the qubit states $|0\rangle$ and $|1\rangle$ are often written as horizontal and vertical photon polarizations $|H\rangle$ and $|V\rangle$.

Inequality (1.1) can only be violated with maximally-entangled states if each photon is detected with total efficiency >82.8 %, since the singles terms scale with efficiency and the coincidence terms scale with the square of efficiency. An important step towards photonic tests of Bell's inequalities came with the calculation by Eberhard that for imperfect photon detectors, the maximum violation comes from nonmaximally-entangled states [47], for example

$$|\Phi(\theta)\rangle = \cos\theta\,|H\rangle_A\,|H\rangle_B + \sin\theta\,|V\rangle_A\,|V\rangle_B\,. \tag{1.3}$$

Similar forms exist for the other three Bell states. With perfect detection efficiency the CH inequality is maximally violated using $|\Phi(45°)\rangle = |\Phi^+\rangle$ with measurement polarizer angles $a = 11.25°$, $a' = -33.75°$, $b = -11.25°$, and $b' = 33.75°$, for 0° horizontal. With 70 % detection efficiency and 0.02 % background noise, for example, the angles for maximal violation shift to $a = 1.7°$, $a' = -19.7°$, $b = -1.7°$, and $b' = 19.7°$, and the optimal entangled state is $|\Phi(82.3°)\rangle = 0.135\,|H\rangle_A\,|H\rangle_B + 0.991\,|V\rangle_A\,|V\rangle_B$.

The reason nonmaximally-entangled states help violate the CH inequality (1.1) is that they increase the ratio of the positive to negative terms, partially compensating the effect of loss at the cost of decreasing all the terms. This happens because the state is biased toward $|V\rangle_A\,|V\rangle_B$ while Alice and Bob's measurement angles move toward $|H\rangle_A\,|H\rangle_B$ (see Supplementary Information of [48]). Moving the state away from the polarizer settings decreases the the singles probabilities faster than the coincidences probabilities because the singles terms depend only on a and b, which are closest to $|H\rangle_A\,|H\rangle_B$, while the coincidence terms depend on all four measurement angles. This can be seen by writing down the detection probability for the state (1.3) with measurement $|H_\alpha\rangle = \cos\alpha\,|H\rangle + \sin\alpha\,|V\rangle$, where α is the angle of the polarizer [49]. Assuming efficiency η and no noise, the probability of a single count with polarizer angle a is, summing over the other mode,

$$P(a) = \eta\,|\langle H_a|\Phi(\theta)\rangle|^2 = \eta\left(\cos^2 a\cos^2\theta + \sin^2 a\sin^2\theta\right), \tag{1.4}$$

and the probability of a coincidence count with angles a and b is

$$\begin{aligned} P(a,b) &= \eta^2\,|\langle H_a H_b|\Phi(\theta)\rangle|^2 \\ &= \eta^2\left(\cos^2 a\cos^2 b\cos^2\theta + \sin^2 a\sin^2 b\sin^2\theta + \frac{1}{4}\sin 2a\sin 2b\sin 2\theta\right). \end{aligned} \tag{1.5}$$

In fig. 1.3 I plot these probabilities as the sum of the positive and negative terms in the CH inequality (1.1), and the mean of singles and coincidence terms for fixed measurement

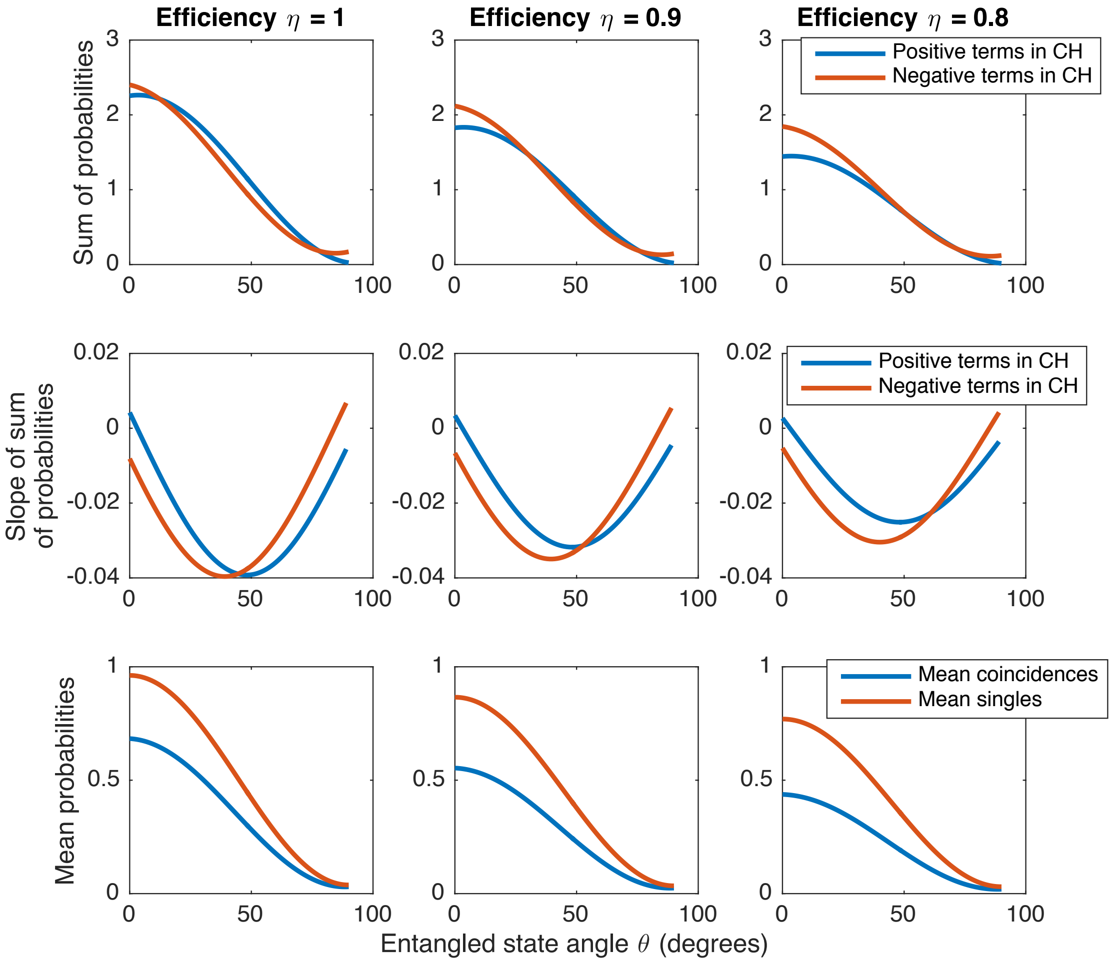

Figure 1.3: Calculated detection probabilities for CH inequality violation versus angle of non-maximally entangled state $|\Phi(\theta)\rangle$, with measurement angles fixed. In the top row I plot the sums of the positive and negative terms in the CH inequality (1.1); a violation occurs where the blue line is above the orange. For total detection efficiency $\eta = 0.8$ the violation is tiny, and only occurs in a small region around $\theta = 62°$. In the middle row I plot the slopes of the above curves. The maximal violation occurs for the θ where the slopes cross. In the bottom row I plot the mean of the coincidence and singles terms in the CH inequality, showing that singles decrease faster than coincidences for increasing θ.

angles. For the lossless case, there is a wide range of θ where the inequality is violated, but as efficiency decreases, the range of θ shrinks and is pushed to larger values, and the amount of violation drops. By plotting also the slope of the sums of positive and negative terms, it is clear that the optimal violation occurs at the θ where the positive terms start decreasing faster than the negative terms, i.e. where the slopes cross.

In order to put the Eberhard technique into practice, in section 2.5 I numerically optimize the state and measurement angles based on detection efficiency and background noise. See fig. 1.4 for the variation of the optimized state and measurement angles and the value of the left-hand side of inequality (1.1) versus total detection efficiency and dark counts. Eberhard's improvement allows a violation of the CH inequality with a minimum efficiency of 66.7 %, crucial for the photonic Bell experiments that have closed the detection loophole [37, 38, 48, 50]

1.1.2 Device independence

If Alice and Bob can violate a Bell inequality by a sufficient amount, they can generate a secret key with information-theoretic security against eavesdroppers [5, 51, 52]. If they violate the inequality in a way that is loophole free [53] (see below), they can prove the security of their secret key without making reference to the actual workings of their measurement devices [35, 36, 54], though they are required to ensure their labs do not leak information. This is called device-independent security. The intuition is that violation of a Bell inequality implies nonlocal correlation between Alice and Bob that cannot be reproduced by an eavesdropper. Quoting Acín *et al.* [35], "Considered in the perspective of QKD, the fact that Alice's and Bob's symbols are correlated in a nonlocal way, whatever be the underlying physical details of the apparatuses that produced those symbols, implies that Eve cannot have full information about them, otherwise her own symbol would be a local variable able to reproduce the correlations."

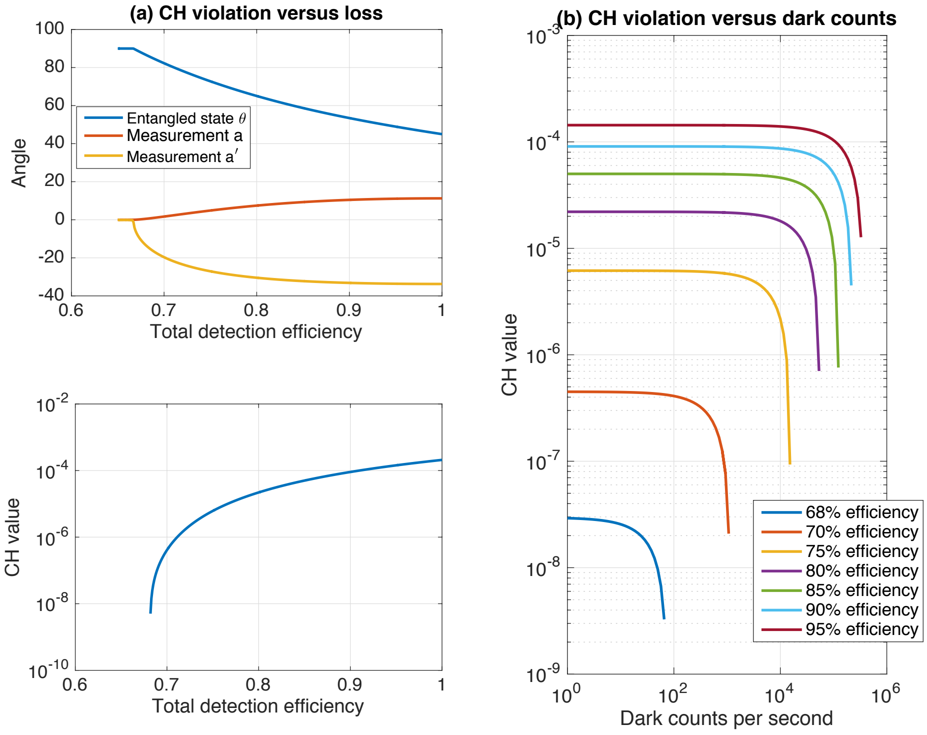

Figure 1.4: Numerically-optimized entangled state and measurement polarizer angles for a CH-inequality violation in the presence of loss and noise. Loss is characterized by the total detection efficiency for each photon, assumed to be the same for Alice and Bob. Noise is characterized by dark counts per second in each detector, and translated to a probability by multiplying by a 200 ps coincidence window. Here I consider probabilistic entangled-pair creation at a rate of 40 000 pairs/s from a pump at 80 MHz rate, but no higher-order emissions. The plots versus loss (a) have 100 darks/s while the plot versus dark counts (b) has 68 % to 95 % efficiency. The angles collapse toward the horizontal and the state toward the vertical for low efficiency, but because the noise here is unpolarized, the optimal angles are nearly independent of the number of dark counts (not shown). CH values greater than zero indicate a violation of inequality (1.1); in (a) at least 68 % efficiency is required, and in (b) the number of tolerable dark counts depends strongly on the detection efficiency. The CH values are very small compared to the maximum value of $\frac{\sqrt{2}-1}{2}$ because the probabilities are per experimental run (i.e. per laser pulse) and most pulses produce no photons at all.

The need for device independence

Why is device independence important? Beyond the desire to saturate the quantum advantage over classical communications, practical attacks on quantum communications systems could be excluded all at once. These side-channel attacks exploit imperfections in the devices used for quantum cryptography, partially or totally compromising the security of secret key generation. Many attacks focus on photon detectors, exploiting mismatches in efficiency [55, 56] or timing [57], directly controlling detectors with bright light [58, 59, 60, 61, 62], or analyzing back-reflections from detection setups [63, 64, 65]. Additional side channels can be introduced if the source produces photons with correlations between their spectral, temporal, or spatial mode and their bit value [66], leading to further attacks [67, 68, 69]. Using these techniques Bell's inequality has been violated with classical light [70], underscoring the need for true device-independent quantum communication.

Loophole-free Bell tests

The reason Bell's inequality was able to be violated by classical light in [70] is that the Bell test therein made assumptions beyond the minimum necessary set, opening loopholes. References [53] and [71] give a thorough description of assumptions and loopholes in Bell tests. The two most common loopholes are the two most difficult to avoid: the locality loophole, and the fair-sampling (or detector) loophole.

Bell's theorem requires Alice and Bob to be sufficiently isolated that one's measurement choice cannot influence the other's measurement outcome. If Alice and Bob are close together or make measurements slowly, a local signal could propagate from one to the other, opening the locality loophole. This loophole can be closed (or the assumption of locality justified) by spacelike separating Alice and Bob's events, and carefully characterizing the relevant distances and times.

The fair-sampling loophole arises when not all the photons emitted by the source are detected and one assumes that the detected sample is a fair sample of the entire ensemble [72]. This is commonly done in experiments in order to show a Bell inequality violation even with low detection efficiency. Since each particle gets to learn the measurement setting before deciding whether or not to be detected, the detected sample may violate a Bell inequality while the entire ensemble, which could then be described by local realism, could not. The fair-sampling assumption can be removed by detecting a large enough fraction of the particles, or justified by heralding the preparation of the desired quantum state as discussed in section 1.2.

Thus following [53] I take "loophole-free" to mean that the Bell test is performed under only two assumptions: that local realism is true, where locality is justified by space and time measurements, and that superdeterminism does not hold, since, from reference [73], "Unless we proceed under the assumption that hidden conspiracies of this sort [superdeterminism] do not occur, we have abandoned in advance the whole enterprise of discovering the laws of nature by experimentation." Violating a Bell inequality in a loophole-free scenario rejects one or both of those assumptions.[1]

Early implementations

Closing the fair-sampling and locality loopholes simultaneously is difficult due to their conflicting demands: the former requires photons to be detected with high efficiency, while the latter requires photons to be sent over long distances. Photons propagating in optical fibre are transmitted with probability exponentially small in distance due to absorption and scattering (sec. 9.3 of [74]), and those in free space suffer at least quadratic losses with distance due to diffraction (sec. 4.3 of [74]). Though the first loophole-free Bell tests with photons have succeeded by minimizing losses as much as possible, this strategy cannot hold for distances longer than a few kilometres. Thus quantum cryptographic protocols that provide some device independence without a loophole-free Bell-inequality violation have emerged.

Measurement-device independence [75, 76] seeks to remove detector-side-channel attacks at the cost of stringent requirements on the photon source [77]. Measurement-device-independent quantum key distribution uses a central untrusted party to interfere photons sent from Alice and Bob and project them onto Bell states. Alice and Bob can use the

---

[1] I suspect most people would rather reject local realism than accept superdeterminism.

knowledge of the states they sent and the announced outcomes of the Bell-state projections to generate a secret key. Since the security proof does not assume the detectors are held by Alice and Bob, they can be interrogated or controlled by malicious parties without compromising the secret key. This has led to many proof-of-principle implementations [78, 79, 80, 81, 82, 83], including the interference of weak laser pulses from sources very far apart.

Related to measurement-device independence is an even weaker version called detector-device independence [84, 85, 86]. This brings the Bell-state projection into Bob's lab, and performs it between two degrees of freedom on Alice's photon, rather than on interference between two photons. This is much easier to implement, but could be subject to some detector attacks [87].

Demonstrating a loophole-free Bell test is a key step towards device-independent quantum cryptography. The detection loophole has been closed using ions [31, 43], superconducting quantum circuits [88], and photons [50, 48]. The locality loophole has been closed using pairs [14, 89] and triplets of photons [90], the latter of which I made a major contribution to. Finally, the detector and locality loopholes have been closed simultaneously using nitrogen-vacancy spins [39], and using photons [37, 38]. My contributions to the experiment in [37] are shown in chapter 2, which took the strategy of minimizing losses directly to avoid the fair-sampling assumption, and bringing Alice and Bob just far enough apart to close the locality loophole.

1.2 Qubit heralding

Device-independent communication is limited by the challenges of the loophole-free Bell test, namely closing the detector and locality loopholes. The detector loophole is particularly difficult, since every source of loss between the production of photon pairs and final detection counts against the efficiency. For example, the lowest-loss commercial optical fibres have attenuation of around $0.164\,\mathrm{dB\,km^{-1}}$ [21]. This allows only $10.7\,\mathrm{km}$ of fibre between the source and receiver before falling below the Eberhard bound of $66.7\,\%$ efficiency, even before accounting for component losses and detector efficiency. To achieve full device-independent quantum communication and perform loophole-free Bell tests over distances of more than a few kilometres requires strategies for dealing with inevitable photon loss due to scattering, absorption, and diffraction.

1.2.1 Dealing with loss

The general strategy for dealing with loss is to make measurements only when some external signal has certified the readiness of the quantum systems. This signal must be generated outside the light cone of Alice and Bob's measurement choices, justifying the fair-sampling assumption while preserving locality. In other words, if the quantum systems in the Bell test must declare their readiness before they learn the measurement settings, the detector loophole is not opened by throwing away data that came without the readiness signal (see p. 105 of ref. [91]).

Event-ready Bell tests

After Bell's initial suggestion [91], the next practical idea along this line was "event-readiness," where entanglement swapping is used to certify that entangled photon pairs have been successfully generated [92]. Here two separate sources of entangled photon pairs each send one photon to Alice or Bob and one photon towards a central station. This central station projects the two incoming photons onto a Bell state, entangling the distant photons headed toward Alice and Bob. Since the Bell-state projection comes with a certain pattern of detector clicks, one can say when the distant photons have been prepared in the correct state. However, using spontaneous parametric down-conversion to produce photon pairs limits the usefulness of event readiness for photons because the probability to produce one pair from each source is commensurate with the probability to produce two pairs from one source. In the latter case, the readiness signal might fire even though there is no photon sent to one party. This can be partially mitigated by pumping the two sources with very different strengths or adding loss before the central station [10].

Additionally, event readiness has been successfully adapted to atomic and spin systems [31, 39, 43]. Instead of using down-conversion, entanglement between single photons and quantum emitters is swapped, leaving the emitters in a ready entangled state [93]. Each emitter is entangled to a photon that it sends towards a central station. The central station projects the photons onto a Bell state, swapping the entanglement to the two distant emitters. Since single quantum emitters can produce at most one photon, the multiphoton problem is avoided, allowing successful Bell tests.

Quantum nondemolition measurements

Quantum nondemolition measurements [94] seek to measure a property of a quantum state without disturbing its other properties; in our case, to measure the presence of a photon without disturbing its qubit state [95]. Proposals and implementations using the optical Kerr effect [95, 96, 97, 98, 99], linear optics [95, 100], cavity quantum electrodynamics [101, 102], and doped waveguides [103] have not seen uptake towards dealing with loss in quantum communication, due to the difficulty and strict requirements of such schemes.

1.2.2 Heralded qubit amplification

Heralded qubit amplification [104], rather than detecting photons, increases the relative one-photon component $|1\rangle$ over the vacuum component $|0\rangle$ in a heralded way. Since deterministic noiseless amplification is impossible in quantum mechanics [105, 106, 107], these amplifiers operate nondeterministically, emitting a ready signal when amplification was successful. Heralded qubit amplification is based on the noiseless amplifier of Ralph and Lund [108], which itself comes from the quantum scissors of Pegg, et al. [109]. The noiseless amplifier was implemented for single photons [110, 111] and continuous-variable states [112, 113], and adapted and implemented [114, 115] for qubit states as in fig. 1.5. A number of improvements to heralded qubit amplification have been proposed [116, 117, 118], one of which appears in chapter 3.

The idea of heralded qubit amplification (fig. 1.5) is to teleport the input state in the vacuum/one-photon basis using linear optics, with an ancilla photon detection heralding successful teleportation to the output. The teleportation is biased with a tuneable beam splitter towards the one-photon state, amplifying this over the vacuum. Two of these

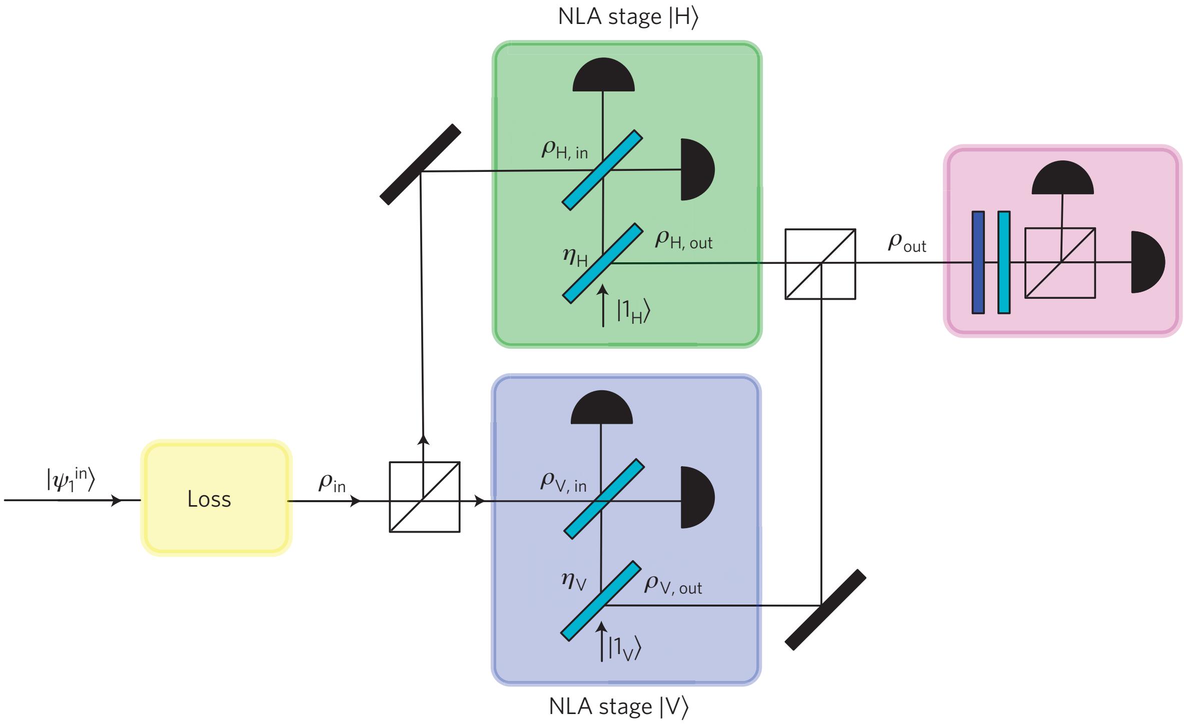

Figure 1.5: Heralded qubit amplification. A photonic qubit undergoes loss, then has both its polarization components teleported to the output in the one-photon/vacuum basis, with a bias towards one photon. Two detections in the noiseless linear amplifier (NLA) stages herald successful amplification, indicating the increased probability of a single photon at the output. Reprinted by permission from Macmillan Publishers Ltd: Nature Physics [114], © 2013.

amplifiers operated coherently in parallel, one for each polarization, allow qubits to be amplified. In implementations, the nominal gain, defined as the probability of a photon at the output after heralded amplification divided by the probability of a photon at the input $G_{\mathrm{nom}} = \frac{P_{\mathrm{out}}}{P_{\mathrm{in}}}$ has reached $G_{\mathrm{nom}} = 9$, but the output probability ($P_{\mathrm{out}} \approx 20\,\%$) has not reached the levels needed for a Bell test or device-independent communication [115]. This is limited by the coupling efficiency of the two ancilla photons needed for teleportation.

1.2.3 Photonic qubit precertification

In contrast to the linear optics of heralded qubit amplification, photonic qubit precertification employs nonlinear optics to certify the presence of a photonic qubit. I proposed a version of precertification using four-wave mixing in 2011, combining the ideas of heralded qubit amplification [104] and coherent photon conversion [119]. Precertification was proposed independently by Cabello and Sciarrino using parametric down-conversion (PDC) in 2012 [120]. In both cases, a lossy photon arrives at a receiver, and is split in two as in fig. 1.6. One photon, the flag, is detected to precertify the presence of the other, labeled signal, which carries the initial (possibly entangled) qubit state.[2] For polarization qubits, this requires that the splitting process preserve the polarization of the input photon. Since the flag photon can only be produced with a corresponding signal photon, detecting the flag acts as the readiness indicator for the signal photon for a Bell test or device-independent quantum communication. A first demonstration of photonic qubit precertification is shown in chapter 4. Currently, precertification is limited by the efficiency of converting one photon into two. In chapter 5 I show ways to improve this efficiency in fibre media, with experiments towards this goal in chapters 6 and 7.

Qubit precertification is similar in effect to heralded qubit amplification, in that it removes the vacuum component of a photonic qubit state at the cost of small success probability. However, precertification has a number of key advantages over amplification. The most important is there is no need for mode-matched ancilla photons generated at remote locations (which has not been accomplished in previous amplifier experiments): the

---

[2] Here I use “flag” rather than “idler” to make clear the function of this photon.

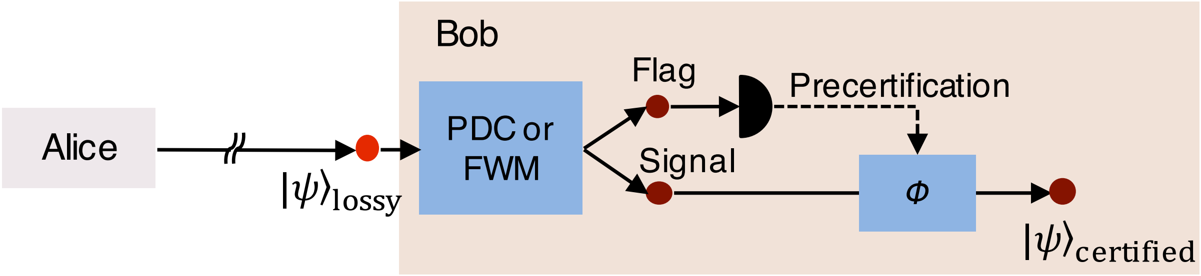

Figure 1.6: Photonic qubit precertification. A photonic qubit experiences channel loss, then undergoes polarization-preserving parametric down-conversion (PDC) or four-wave mixing (FWM), probabilistically producing a photon pair. The flag photon is detected to precertify the signal, which carries the initial qubit state. For half the flag detections, a feedforward phase correction (ϕ) is needed on the signal.

only shared resource needed is for the wavelength of Alice's photons to match Bob's down-conversion acceptance bandwidth. Furthermore, heralded qubit amplification experiments have so far been limited to operation triggered by Alice's detection, which makes these implementations unsuitable for Bell tests. We condition only on the flag detector, allowing precertification independent of any signals from Alice. Additionally, there is in principle a tradeoff in some versions of heralded qubit amplification between success probability and the remaining vacuum in the heralded state, whereas precertification in principle removes all vacuum components. There is the similar drawback in both schemes in practice that the vacuum component remains significant at the output: for the amplifiers this is due to limited coupling efficiencies of the ancilla photons; and for precertification it is due to dark counts in the flag detector, which can both be overcome by technical improvements. Coincidentally, despite different architectures, current implementations of heralded qubit amplification and photonic qubit precertification have about the same final count rates, on the order of 1000 per hour [115].

1.3 Quantum photon sources

Most of the protocols discussed above rely on the production of pairs of entangled photons, and in the case of precertification, also producing pairs *from* single photons. Therefore I now describe photon pair production in nonlinear media, and how pair sources can be transformed to entangled pair sources. Following chapter 1 of [121] with slight differences in notation, I define the Hamiltonian of the electromagnetic field as

$$\hat{H} = \sum_{\sigma} \int \frac{\hbar\omega_k}{2} \left[\hat{b}^{\dagger}_{\sigma}(k)\hat{b}_{\sigma}(k) + \hat{b}_{\sigma}(k)\hat{b}^{\dagger}_{\sigma}(k)\right] dk, \tag{1.6}$$

where σ is the polarization and k is the wavevector of the mode associated with annihilation operator $\hat{b}_{\sigma}(k)$. The mode has frequency ω_k and is a plane wave with mode function $u(k,r,t) = \frac{e^{ik\cdot r - i\omega_k t}}{\sqrt{(2\pi)^3 2\omega_k}}$. The position r and wavevector k are indeed vectors (though I drop the vector notation as it is unneeded here), and t is time. To construct operators for the realistic modes we have in the lab $f(r,t)$ we can superpose plane waves as

$$f(r,t) = \int \left[\alpha^*(k)u(k,r,t) + \beta^*(k)u^*(k,r,t)\right] dk, \tag{1.7}$$

with coefficients $\alpha(k)$ and $\beta(k)$. These coefficients can be calculated from scalar products with plane waves as $\alpha(k) = u(k,r,t) \cdot f(r,t)$ and $\beta(k) = -u^*(k,r,t) \cdot f(r,t)$ (see section 1.2.2 of [121]). Then the annihilation operators become

$$\hat{a}_{f\sigma} = \int \left[\alpha(k)\hat{a}_{\sigma}(k) + \beta(k)\hat{a}^{\dagger}_{\sigma}(k)\right] dk \tag{1.8}$$

with commutation relations $\left[\hat{a}_{f_j\sigma}, \hat{a}_{f_k,\sigma'}\right] = 0$ and $\left[\hat{a}_{f_j\sigma}, \hat{a}^{\dagger}_{f_k,\sigma'}\right] = \delta_{\sigma\sigma'}\delta_{jk}$ for orthonormal $\{f_j\}$. These $\{\hat{a}_{f_j\sigma}\}$ are now nicely behaved annihilation operators of the quantum harmonic oscillator and we can neglect the mode functions, labelling the appropriate modes as needed.

1.3.1 Three- and four-wave mixing

Nonlinear optics is the study of interactions of light and matter where the material response P (for polarization of the electric dipoles in the material) is nonlinear in the input electric field E (often called the pump). This response can generate new frequencies of light. The material polarization (not to be confused with the polarization of the electric field) is often expanded in a power series in electric field as

$$P = \epsilon_0 \left(\chi^{(1)} E + \chi^{(2)} E^2 + \chi^{(3)} E^3 + ... \right), \tag{1.9}$$

where ϵ_0 is the permittivity of free space, the $\chi^{(n)}$ are tensors of nonlinear susceptibility of rank n, and E and P are vectors such that E^n is also a rank-n tensor (see chapter 1 of [122]). Often we can work with just one element of the nonlinearity tensor and scalar electric fields and polarization. The nonlinear processes governed by eq. (1.9) are called parametric processes, where a nonlinear material mediates a mixing interaction between modes of light without changing its own state. The number of modes involved in a mixing process is one more than the order of the nonlinearity n, since n waves enter through E^n and one more from the induced polarization.

Here I focus on the three-wave mixing process called spontaneous parametric down-conversion (PDC), wherein one pump photon is annihilated, creating two daughter photons while preserving energy and momentum, following chapter 4 of [121]. The twin photons are normally labeled *signal* and *idler* such that the signal photon has the higher frequency and the idler the lower. Thus the interaction Hamiltonian

$$\hat{H}_{\mathrm{PDC}} = \Gamma \hat{a}_p \hat{a}_s^\dagger \hat{a}_i^\dagger + \Gamma^* \hat{a}_p^\dagger \hat{a}_s \hat{a}_i \tag{1.10}$$

has three modes, labeled p, s, and i. Here Γ contains the strength of PDC, given by the strength of the nonlinearity $\chi^{(2)}$, the interaction length L, the cross-sectional geometry, and the phasematching. Phasematching amounts to energy and momentum conservation, given by $\omega_p = \omega_s + \omega_i$ and $k_p = k_s + k_i$. Often an extra term is added to momentum conservation by periodic poling [123] for quasi-phasematching [124], allowing momentum conservation where material dispersion and birefringence would normally not permit it [122]. For strong pump beams, the approximation $\hat{a}_p \approx \hat{a}_p^\dagger \approx |\alpha|$ is often made, with $|\alpha|$ then absorbed into Γ. For photonic qubit precertification, the pump is a single photon so this approximation cannot hold. In either case, the signal and idler photons are always created in pairs, enabling entanglement production and precertification. PDC is broadly categorized into three types: type-0, where all modes have the same polarization, type-I, where the signal and idler have the same polarization, perpendicular to the pump, and type-II, where the signal and idler have perpendicular polarizations, one of which is parallel to the pump.

Three-wave mixing for PDC requires anisotropic media, as $\chi^{(2)} = 0$ in isotropic crystals and glasses. By contrast, four-wave mixing occurs in anisotropic and isotropic media, including glass optical fibres. Using fibres gives four-wave mixing long interaction lengths and tight mode confinement, allowing strong effective nonlinearities despite $\chi^{(3)}$ generally being smaller than $\chi^{(2)}$. Spontaneous four-wave mixing (FWM) generates photon pairs with the Hamiltonian

$$\hat{H}_{\mathrm{FWM}} = \Gamma \hat{a}_{p1} \hat{a}_{p2} \hat{a}_s^\dagger \hat{a}_i^\dagger + \Gamma^* \hat{a}_{p2}^\dagger \hat{a}_{p2}^\dagger \hat{a}_s \hat{a}_i, \tag{1.11}$$

where now two pump modes $p1$ and $p2$ contribute a photon each, and Γ contains $\chi^{(3)}$ and similar geometric considerations as above. For precertification, the strong pump $p1$ can be treated classically such that $\hat{a}_{p1} \approx \hat{a}_{p1}^\dagger \approx |\alpha|$, leading to an effective PDC Hamiltonian as in eq. (1.10).

1.3.2 Entangled photon sources

Photon pair sources can be transformed into entanglement sources by interfering two nonlinear pair production processes that are indistinguishable in all degrees of freedom except the one in which entanglement is generated. Entangled photon sources are characterized by coincidence rate, heralding efficiency, fidelity to a maximally-entangled state, and entanglement visibility. For all these parameters, higher is generally better.

The coincidence rate C is the number of coincident pair counts per second, while the singles rates S_A and S_B are the single counts per second at Alice and Bob respectively. The heralding efficiency [125] is a measure of the likelihood for Alice/Bob to detect a photon, given a detection by Bob/Alice. The coincidence rate can be approximated as $C = \eta_A \eta_B P$ and the singles as $S_A = \eta_A P$ and $S_B = \eta_B P$, where $\eta_{A/B}$ is Alice/Bob's heralding efficiency, and P is the pair production rate in the nonlinear medium before losses. Thus the heralding efficiencies are approximately

$$\eta_A = \frac{C}{S_B}, \quad \eta_B = \frac{C}{S_A}. \tag{1.12}$$

Fidelity is defined as

$$F = \left[\mathrm{Tr}\left(\sigma^{1/2}\rho\sigma^{1/2}\right)\right]^2 \tag{1.13}$$

for density matrices ρ and σ, or

$$F = |\langle\psi|\phi\rangle|^2 \tag{1.14}$$

for pure states $|\psi\rangle$ and $|\phi\rangle$ [121]. Entanglement visibility, in a particular basis where the polarizations of the two photons are expected to be parallel, is given by

$$V = \frac{N_\parallel - N_\perp}{N_\parallel + N_\perp}, \tag{1.15}$$

where $N_{\parallel/\perp}$ is the number of coincident counts with parallel/perpendicular polarizers between the Alice and Bob analyzers. For a realistic loophole-free Bell test with photons, the required visibilities are >99 % and the required heralding efficiencies are >72 %.

Entanglement from three-wave mixing

A nice overview of entanglement-generation architectures using PDC is given in [126], and the schemes I discuss are depicted in fig. 1.7. I define one photon in the horizontal/vertical polarization mode of the signal/idler beam as $|H/V\rangle_{s/i}$.

The first high-brightness source of entangled pairs used a type-II $\chi^{(2)}$ crystal to produce pairs of photons, one beam of $|H\rangle$ and one beam of $|V\rangle$. By interfering these two beams on a 50:50 beam splitter and post-selecting on the cases where the photons exit at different ports, the $|\Psi^+\rangle$ state is produced as in fig. 1.7(a) [127, 128].

The next evolution was to remove post-selection, using a crystal that produced two intersecting cones of PDC light, one $|H\rangle$ and the other $|V\rangle$ [129]. By collecting light at the left and right intersections of the cones, the two processes are $|H\rangle_p \rightarrow |H\rangle_{\text{left}}\,|V\rangle_{\text{right}}$ and $|H\rangle_p \rightarrow |V\rangle_{\text{left}}\,|H\rangle_{\text{right}}$, leading to polarization entanglement as in fig. 1.7(b). A similar version selects the “left” and “right” modes in frequency rather than space [130, 131].

An improved source uses two crystals back-to-back, one producing $\left|V\right\rangle_p \rightarrow \left|H\right\rangle_s \left|H\right\rangle_i$ and the other $\left|H\right\rangle_p \rightarrow \left|V\right\rangle_s \left|V\right\rangle_i$.[3] Pumping at 45° polarization leads to a coherent superposition of these processes, giving entanglement as in fig. 1.7(c) [132].

A recent workhorse for entangled pairs has been the Sagnac interferometer, where pairs can be produced in either direction around a Sagnac loop as in fig. 1.7(d) [133, 134]. In one direction, pairs are produced as $\left|H\right\rangle_p \rightarrow \left|H\right\rangle_s \left|V\right\rangle_i$, while in the other direction they are flipped to $\left|V\right\rangle_p \rightarrow \left|V\right\rangle_s \left|H\right\rangle_i$, interfering to give entanglement. The benefit of this source is its intrinsic phase stability, as both pumping directions traverse the same path.

The interferometer can also be unfolded to a Mach-Zehnder configuration as in fig. 1.7(e), avoiding the need for optics that work at three distant wavelengths (pump, signal, and idler). One path produces $\left|H\right\rangle_p \rightarrow \left|H\right\rangle_s \left|H\right\rangle_i$ and the other $\left|V\right\rangle_p \rightarrow \left|V\right\rangle_s \left|V\right\rangle_i$, generally requiring active stabilization to ensure a constant phase [135, 136]. By building a compact Mach-Zehnder interferometer using beam displacers and sending both paths through the same PDC crystal, active stabilization can be avoided [137]. We used a compact source of this type for a loophole-free Bell test [37], as described in chapter 2.

Polarization-entangled pairs can also be generated from cascaded emissions in quantum dots [138, 139]. Beyond polarization, coherence between early and late pump pulses can generate time-bin-entangled photon pairs [140, 141].

Entanglement from four-wave mixing

Similar to crystal $\chi^{(2)}$ sources, fibre $\chi^{(3)}$ sources employ a number of different architectures. I developed a two-fibre scheme for polarization entanglement similar to the two-crystal scheme, shown in chapter 6 [142]. Sagnac loops have been used for generating polarization entanglement in isotropic fibre [143, 144, 145], and also using birefringent single-mode fibre [146] and birefringent microstructured fibre [147, 148, 149]. Sagnac loops [150] and Faraday mirrors [151] have been used for polarization entanglement based on time delays between orthogonal pump pulses in isotropic fibre.

---

[3] Called a “sandwich source,” inspiring the “sausage source” of chapter 6.

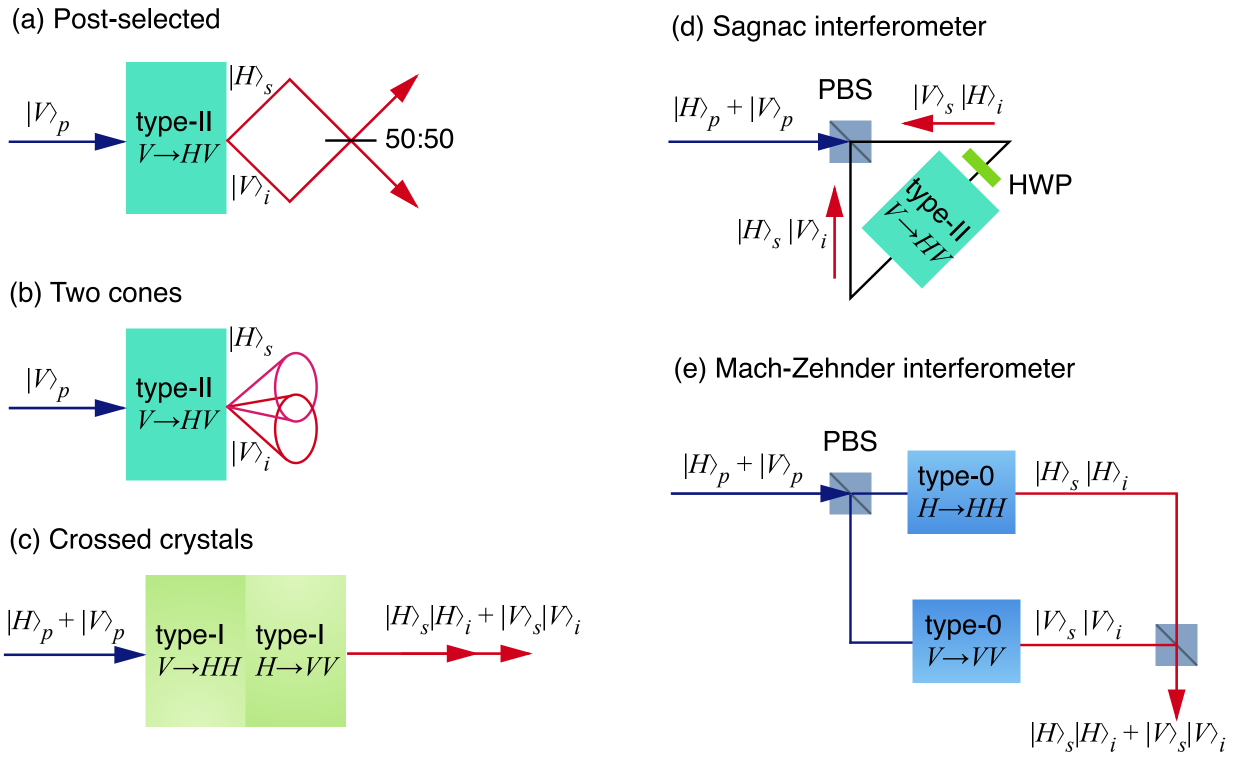

Figure 1.7: The most common polarization-entangled photon generation architectures. The pump beam is blue and the PDC beams are red. The PDC crystals are labeled with the type of phasematching. The schemes (c), (d), and (e) and their analogues using four-wave mixing in fibre can support photonic-qubit precertification since the polarization of the pump is mapped to the entangled state.

1.3.3 Connection between entanglement sources and precertification

Because photonic qubit precertification requires splitting a photon into two through PDC or FWM in a way that preserves polarization,[4] there is a close connection between entangled-photon pair sources and precertification. In general, the entanglement sources where the coherence between processes depends on the coherence between two pump states are useful for precertification, while others are not. A handy shorthand is that entanglement sources where the pump is at 45° polarization are usually suitable for precertification.

Sources based on post-selection and on selecting portions of the output light in space or frequency are not useful for precertification (fig. 1.7(a) and (b)), since only one pump polarization gives rise to both processes. The two-crystal sandwich sources (fig. 1.7(c)) and two-fibre sausage sources (as employed in chapter 6) are suitable, since one crystal/fibre down-converts each input polarization. Fibre and crystal sources based on Sagnac loops and Mach-Zehnder interferometers (fig. 1.7(d) and (e)) are suitable also, and the latter is used in the precertification experiment in chapter 4. Beyond polarization, it is possible to map orbital angular momentum states from pump to down-converted photons [152], which could be useful in future high-dimensional precertification schemes.

---

[4] Here I focus on polarization, but other degrees of freedom can be used too.

Chapter 2

Towards an experimental loophole-free violation of Bell's inequality

This chapter is based on the work I did during a study period abroad in 2014-2015 at the National Institute of Standards and Technology, Boulder, Colorado. At the time NIST was working towards a loophole-free Bell test with photons, since completed. Here I provide technical details about the source and measurement setup and leave the experimental results and full story to [37].

Statement of contributions: As reference [37] has 34 authors, I will restrict this statement to the work presented here. I assisted LKS in building the entangled photon source, troubleshooting nonlinear crystals, and with initial measurements. TG built the fibre spectrometer. I designed and built the high-efficiency fast measurement setup. I wrote code to optimize the entangled state and measurement settings.

2.1 Introduction

NIST is pursuing a long-term project to build a server for certified random numbers based on quantum mechanics [16]. The first step is a loophole-free violation of Bell's inequality. To close the locality and detector loopholes simultaneously, Alice and Bob are separated by a few hundred metres, and all losses minimized. The latter requires careful design of the entanglement source and measurement apparatus, as well as optimization of each component and painstaking alignment. Here I show our troubleshooting of a PDC crystal, the entanglement source built with an improved crystal, the high-efficiency measurement setup Alice and Bob used for high-speed polarization measurements, and the code to optimize the entangled state and measurement settings for maximum violation of the CH inequality [42].

2.2 Troubleshooting a PDC crystal

Using a fibre time-of-flight spectrometer [153, 154], we measured the joint spectral density of NIST's photon pair source based on a 10 mm, type-II periodically-poled potassium titanyl phosphate (PPKTP) crystal with 46.48 µm poling period from AdvR Inc.[1] This crystal produces degenerate photon pairs at wavelength 1554 nm from a pump of 776 nm. The pump is a mode-locked free-space Ti:sapphire laser, which is sent through a single-mode optical fibre to produce a clean spatial mode. The fibre spectrometer uses dispersion in 10 km optical fibres to translate photon wavelength into arrival time. By recording coincident arrival times between two photons and using the known fibre dispersion, a joint spectrum can be obtained in a few seconds. One initial problem we solved using the fibre spectrometer was self-phase modulation of the pump in its mode-cleaning fibre, which broadened the pump bandwidth by a factor of two. Shortening this fibre from 2 m to 20 cm reduced this effect to negligible levels.

---

[1] The use of trade names is intended to allow the measurements to be appropriately interpreted, and does not imply endorsement by the US government or by me, nor does it imply these are necessarily the best available for the purpose used here.

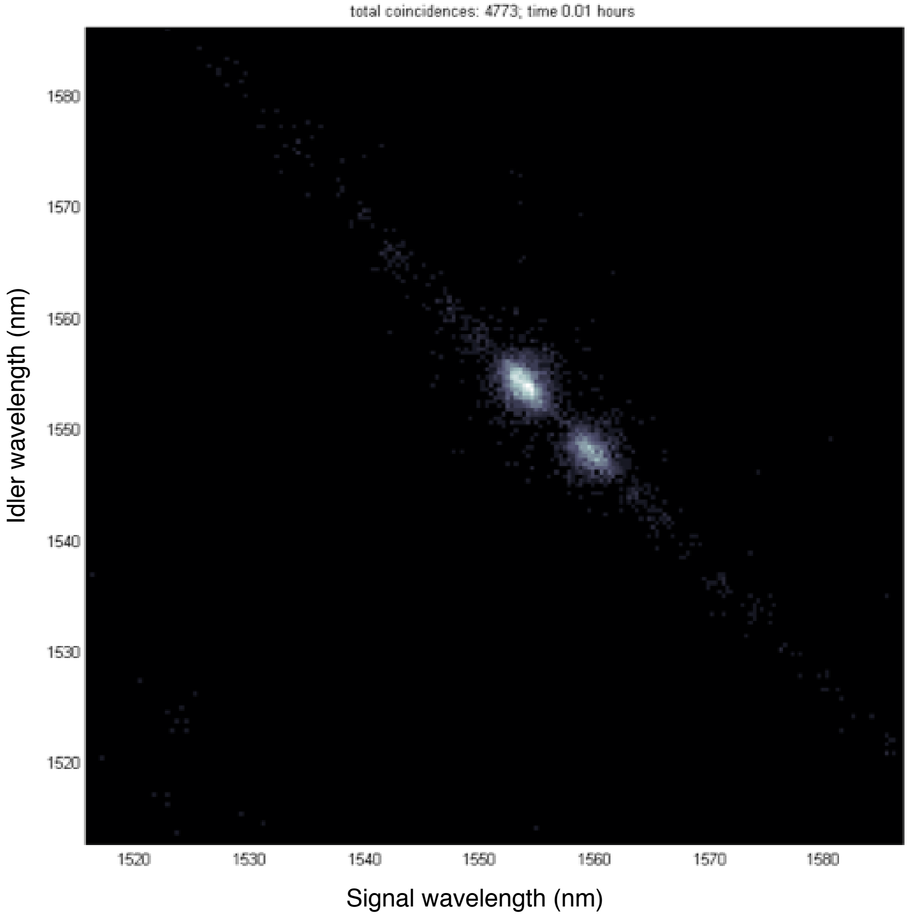

Figure 2.1: Joint spectrum from PPKTP crystal from AdvR Inc. measured by a time-of-flight spectrometer. The joint spectrum characterizes the spectral correlations between photons produced from PDC, with the signal photon's wavelength plotted on the x-axis and the idler photon's on the y-axis. The intensity indicates the number of coincidences with specific signal and idler wavelengths, giving information on the pump bandwidth, crystal phasematching, and signal-idler frequency correlations. We expect a single peak from degenerate photon pairs, but also see another along the anti-diagonal, indicating this second peak is due to a phasematching problem rather than a pump laser problem.

As shown in fig. 2.1, two distinct photon wavelengths were emitted by this crystal. This is a unique and disturbing result; unique because this effect would be washed out for a shorter crystal due to broader phasematching and very difficult to detect using sum-frequency generation, and disturbing because this second peak is unexpected and lowers our effective heralding efficiency due to the difficulty in coupling both peaks simultaneously. We can preferentially couple either of the peaks by tipping a coupling mirror in front of the collection fibre, indicating the two modes are emitted at slightly different angles (fig. 2.2). However, the small inferred angle is not enough to explain the difference in wavelength.

Two (somehow) interleaved poling periods could explain the second peak, as shown by calculations from SPDCalc (fig. 2.3) [156]. However, viewing the crystal under a microscope shows no poling defects and the Fourier transform of the poling image shows a single period, as seen in fig. 2.4. It may be that the resolution of the microscope is not sufficient to resolve the very similar poling periods of 46.1 µm and 46.5 µm.

The problem was finally resolved by purchasing a similar crystal from Raicol Crystals Ltd., which exhibits only the desired phasematching under the same experimental conditions (fig. 2.5).

2.3 Entangled photon pair source

We then transformed this pair source into a source of entangled photons using the design of ref. [137]. We constructed the Mach-Zehnder interferometer of fig. 2.6 with two α-BBO beam displacers, chosen for their similar dispersion at the pump and photon wavelengths. The pump is focused with a 1 m lens and split into horizontal and vertical polarization components in the first beam displacer. The two beams, separated horizontally by about 2 mm, then pass through separate half-wave plates, one at 45° to flip the vertical polarization to horizontal, and the other at 0° to balance the phase accrued by the other beam. Both beams then enter the same PPKTP crystal, and undergo degenerate type-II PDC to 1550 nm. The down-converted photons pass through a second beam displacer, this time oriented to send the vertically-polarized idler photons down towards the table, keeping the horizontally-polarized signal photons on top. Now, each of the four beams passes through

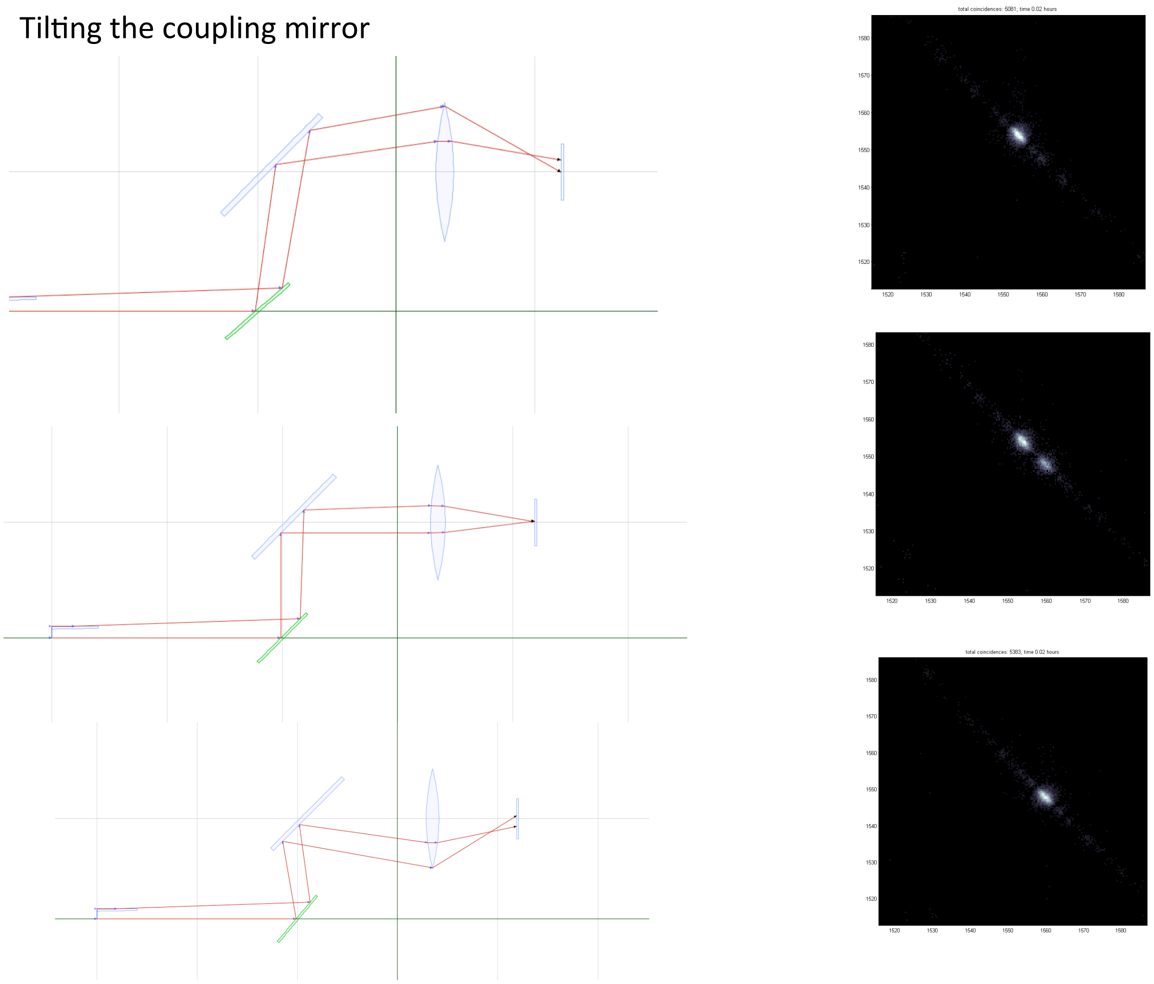

Figure 2.2: Ray tracing diagram from OpticalRayTracer [155] of tilting the coupling mirror and corresponding measured joint spectrum. On the left of the diagram, two rays corresponding to the two joint-spectrum peaks are emitted from the AdvR PPKTP crystal at slightly different angles. Tilting the coupling mirror clockwise moves the bottom ray away from the centre of the output plane (which represents the fibre tip) and vice versa. Thus tipping the coupling mirror can preferentially couple one of the emitted wavelengths into fibre. Note that the ray tracing is only an illustration of what could be happening, as the parameters are not exactly matched to the experiment.

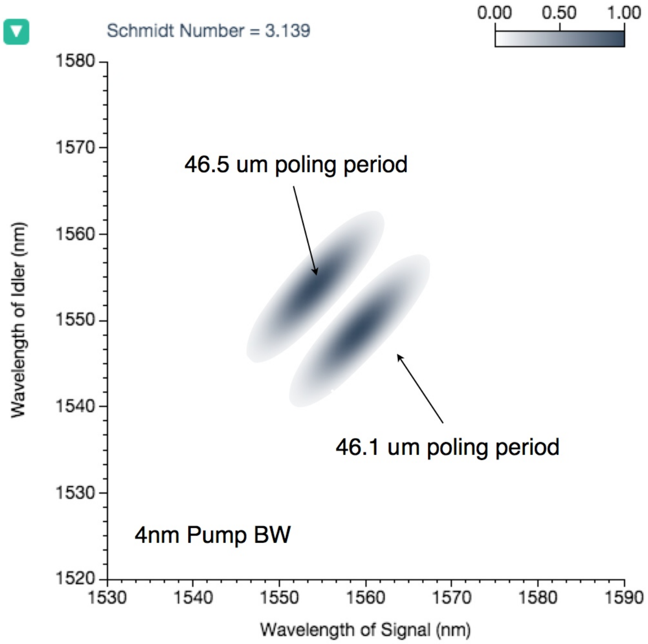

Figure 2.3: The calculation of phasematching for two interleaved poling periods reproduces the behaviour we observed from the AdvR crystal. Here a broader pump bandwidth was used, leading to larger peaks along the diagonal.

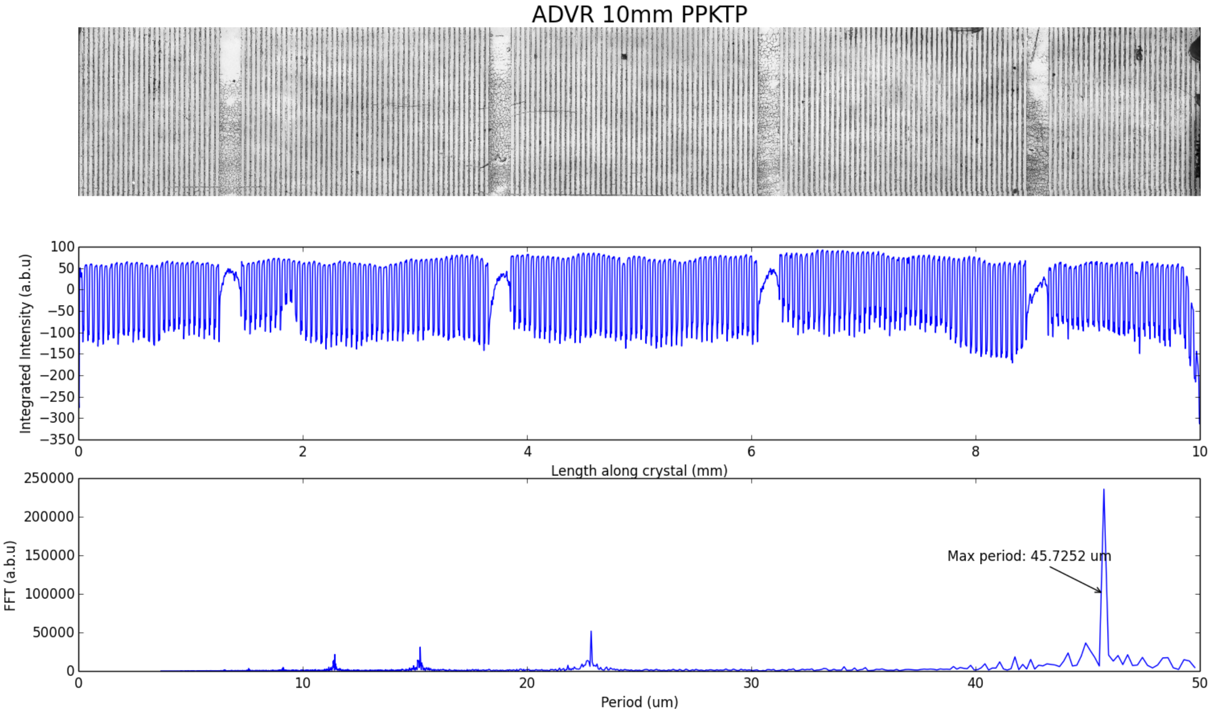

Figure 2.4: A micrograph of the AdvR crystal (top), where poled regions have been preferentially etched, allows calculation of the poling period by fast fourier transform (bottom), which shows only a single poling period. AdvR says the four large blank areas allow them to align the electrode mask better, and are an integer number of poling periods long.

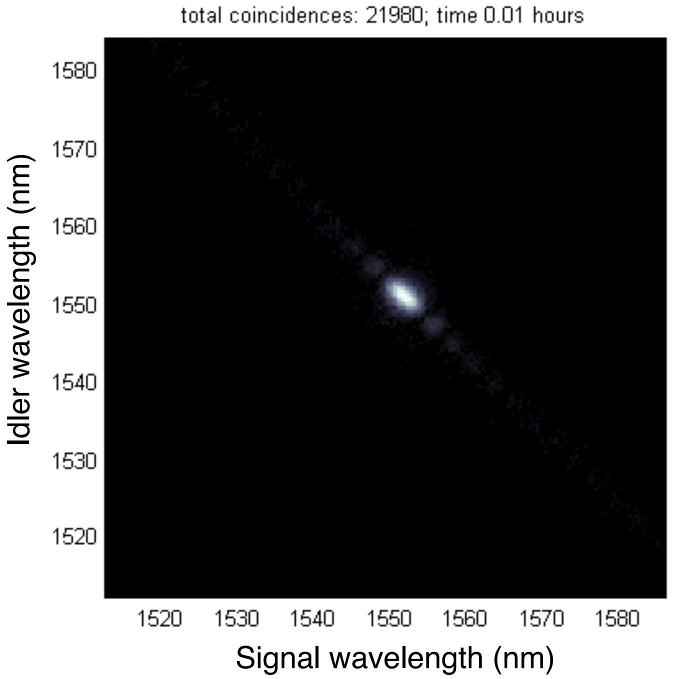

Figure 2.5: Joint spectrum from the 11 mm Raicol PPKTP crystal. We see only a single peak and its sinc lobes, indicating this crystal should work well for generating entangled pairs with high heralding efficiency.

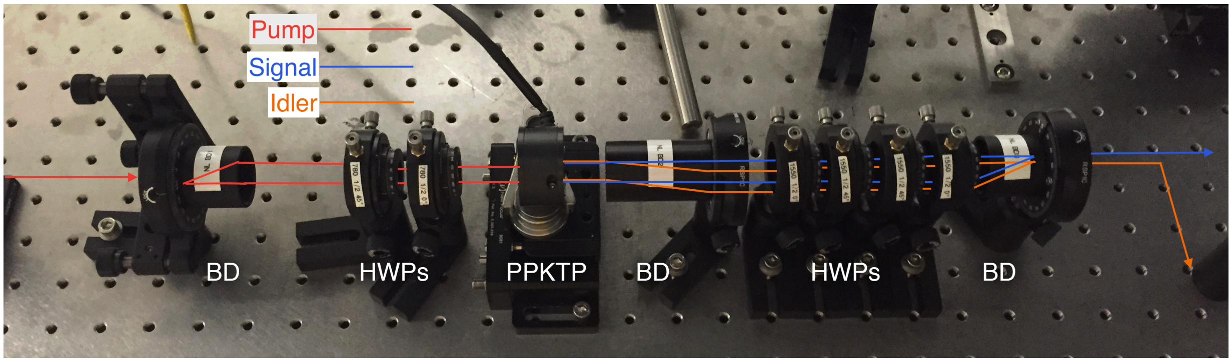

Figure 2.6: Interferometer for polarization-entangled photon source, based on α-BBO beam displacers (BD), and half-wave plates (HWP) that have been diced into quarters. The PPKTP down-conversion crystal is in the centre.

its own half-wave plate, two at 45° to flip polarizations, and two at 0° to maintain the interferometer's balance. The final beam displacer recombines the two horizontally-separated paths to complete the interferometer. The idler beam is picked off with a half-mirror and sent to Alice, while the signal beam passes over the half-mirror to Bob, both being recollimated by 25 cm lenses. The beams are coupled into single-mode telecommunications fibre with 11 mm aspheric lenses. All components are antireflection-coated to reduce losses, and the only filtering after SPDC is a silicon wafer to remove the pump. Slightly tipping the first beam displacer sets the phase of the entangled state.

We found this is a stable source (only a few degrees' phase change over 24 h) with polarization visibilities up to $(99.81 \pm 0.07)\,\%$, average of H/V = $(99.91 \pm 0.03)\,\%$ and D/A = $(99.70 \pm 0.06)\,\%$ bases. We also measured a CHSH parameter [41] of $S = 2.813 \pm 0.002$, just below the maximum value allowed by quantum mechanics of $2\sqrt{2} \approx 2.828$ [157]. These numbers were measured without background subtraction and without narrowband filters. We employed only the silicon wafer to remove the pump and a 1 ns coincidence window to remove background counts. Here we used a HydraHarp in T3 mode synchronized to the laser repetition rate, detecting the signal and idler with NIST's superconducting nanowire single photon detectors.

The alignment of the source was a bit tedious, but it was sufficient to align the three beam displacers' and six half-wave plates' rotation first with a reference polarizer, then drop them in. All optics were aligned by back-reflecting the beam, and it was helpful to use a camera to ensure the half-wave plates intersected only one of the four beams. In this way, the H/V visibility was immediately >99 %, while the D/A visibility required tweaking the pump polarization balance and first beam displacer tip and tilt to ensure indistinguishability of the two arms of the interferometer. We found the best way to set the phase of the entangled state was to tip very slightly in the x-direction the input beam displacer. The y-direction tilt can be used also for a less sensitive phase change. With these tweaks the D/A visibility was also >99 % within one day. The visibilities shown in fig. 2.7 are more than sufficient for a loophole-free Bell violation, and are limited in that experiment by double-pair emissions, as the source is pumped harder to increase the pair rate.

For the highest visibilities reported above, we pumped with 12.8 mW average power

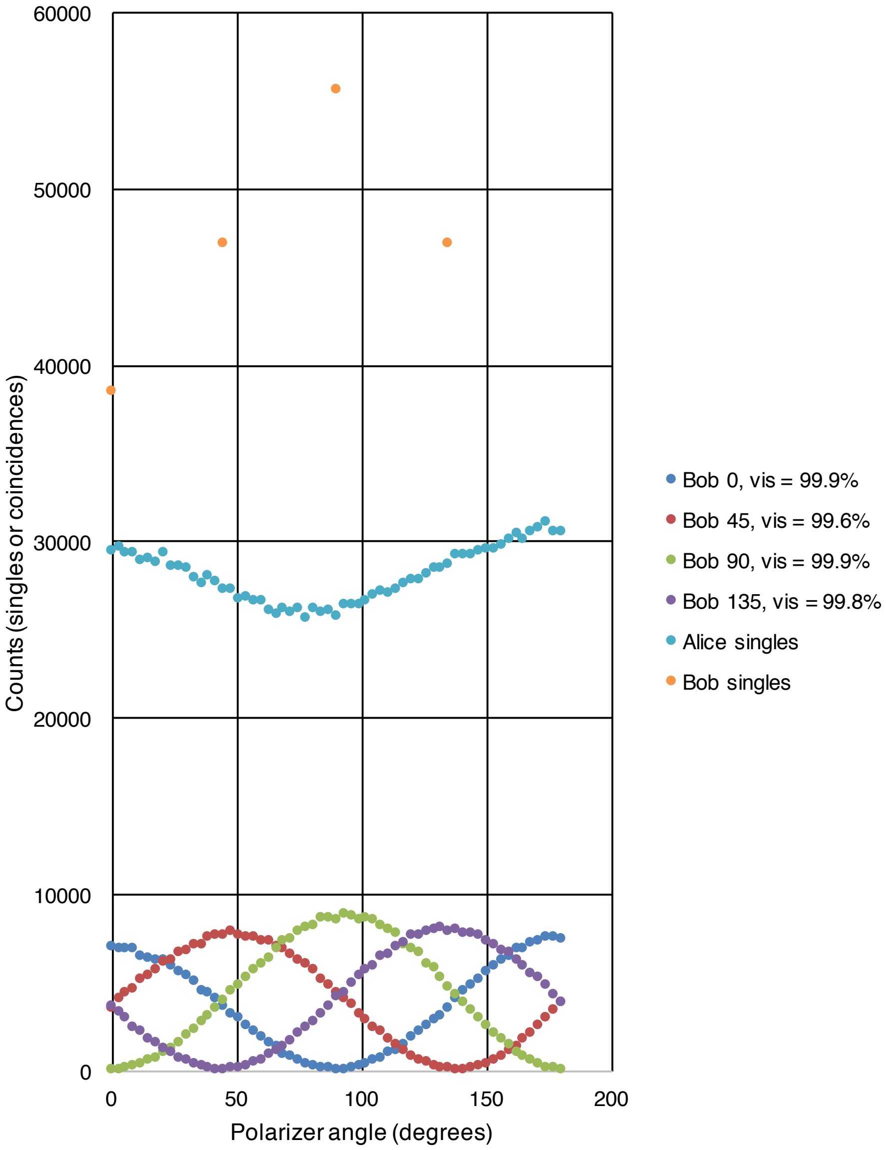

Figure 2.7: Measured coincidences and singles counts for rotating Alice's polarizer while keeping Bob's fixed at one of four angles, giving visibility $(99.91 \pm 0.03)\,\%$ in the H/V basis and $(99.70 \pm 0.06)\,\%$ in the D/A basis. The singles counts for Alice and for Bob's four settings are to the top of the graph. Later source optimization symmetrized the four coincidence curves, removed the angular dependence of the singles curves, and symmetrized and drastically increased the coincidences-to-singles ratios.

from an 80 MHz, picosecond Ti:sapphire laser. This gave a measured pair rate around 2000 coincidences/s, with raw heralding efficiencies of ∼20 % and ∼30 % for the idler and signal respectively. After optimizing the lenses and coupling and increasing the pump power, we measured a pair rate of 38 000 coincidences/s and 44 200 singles/s, giving up to to $\eta_A = \eta_b = 86\,\%$ raw heralding efficiency. This includes all losses and detector efficiency of about 90 %, meaning the total efficiency of coupling from the crystal into single-mode fibre was about 95 %. This heralding efficiency is sufficient for a loophole-free Bell test [47], giving about 10 % efficiency overhead to be consumed by transmission losses and losses in the measurement setup [37].

2.4 Coupling efficiency from fibre to fibre through a Pockels cell

Many experiments in quantum optics require fast switching, whether for routing, measurement, or feedforward. The critical point in many cases, and especially in Bell tests and precertification, is to switch polarization using a fast Pockels cell with minimum loss. Pockels cells operate by applying a high voltage across an anisotropic crystal (called a cell). This voltage modifies the refractive indices of the crystal, producing a wave plate whose retardance depends on the applied voltage (see ch. 20 of [74]). Varying the voltage allows switching polarization states or measurements.

In our experiment [37], photon transmission and detection both occur in optical fibre while the Pockels cell is in free space, necessitating high-efficiency optical coupling in and out of fibre. I achieved 96.1 % coupling from free space into single-mode fibre at 1550 nm and 91.9 % fibre – free space – fibre coupling through the Pockels cell, including antireflection-(AR)-coated fibres. I directly measured up to 92.3 % and 88.2 % respectively, and factored out the measured 96 % transmission from the uncoated fibre to free-space power meter to get the numbers above. In further iterations of the setup, the fibre – free space – fibre coupling including all AR-coatings was measured using laser light and photon pairs to be 90 % to 92 %, including also all wave plates and polarizers. Estimated uncertainties due to non-uniformity of the power meter are ±1 percentage point.

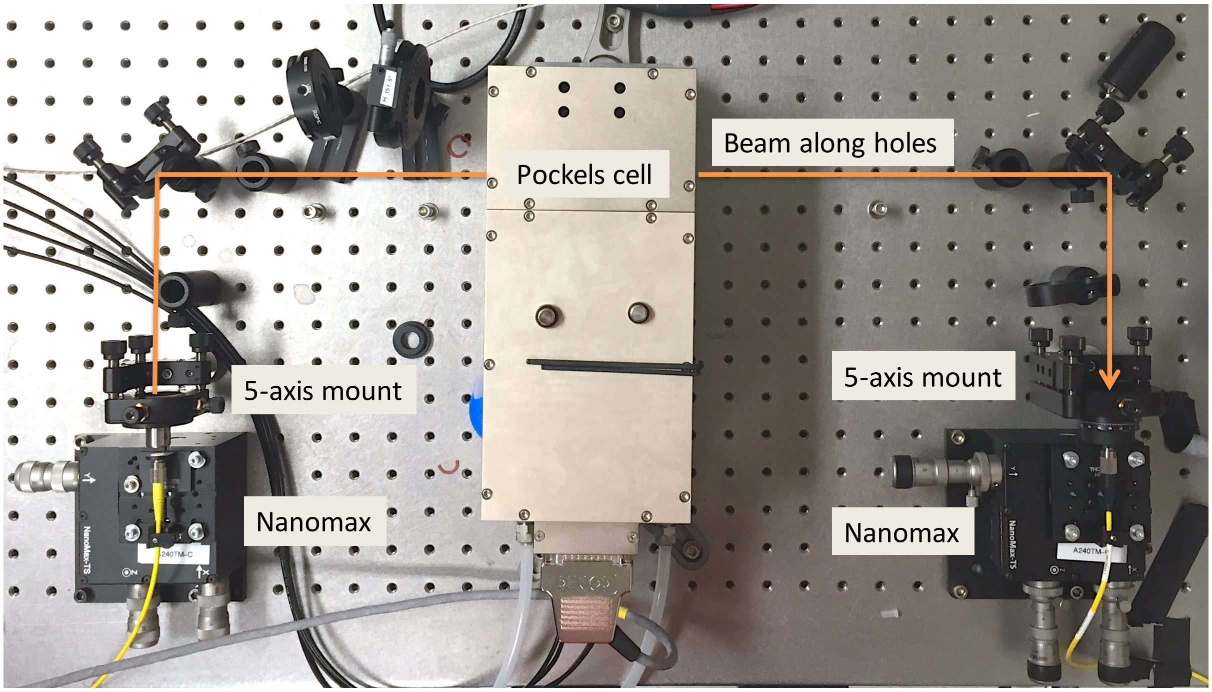

Figure 2.8: Fibre – free space – fibre coupling through Pockels cell, as used for Alice and Bob's measurements. See the text for component description and alignment procedure.

The basis choice setup is depicted in fig. 2.8. Key components include: Thorlabs P1-SMF28-EAR AR-coated patch cables, matched A240TM-C aspheric lenses with 8 mm focal length and ∼99 % transmission, two MAX313D Nanomax stages for fibre positioning, two K5X1 5-axis mounts to position the lenses, silver mirrors to use a red alignment beam (which were later upgraded for lower loss at 1550 nm to Newport SuperMirrors), and a BBO LightGate 2.6R Pockels cell from Gooch and Housego, with 98 % transmission on a tip/tilt/translation mount (e.g. Newport 9071). Later designs added two thin-film plate polarizers (e.g. Thorlabs PBSW-1550) that provide a combined 7000:1 polarization contrast and 99.3 % reflection. For the best polarization contrast and reflection it is important to align the plate polarizers before optimizing coupling as the optimal angle of incidence may not be 45°. Here 8 mm focal length lenses are used instead of 11 mm because their smaller beam size gives better transmission through the 2.6 mm aperture of the Pockels cell. Also, 5724-H-C 8 mm lenses from New Focus were found to have only 95 % transmission, likely due to the choice of glass, making them unsuitable for this application. I found that despite also giving control of the fibre's tip and tilt, the 9091 fibre aligner from Newport had too much instability and hysteresis to achieve the really high coupling efficiencies.

The first method I attempted for aligning the fibre couplers was, with the lens fixed to the Nanomax, to ensure the beam flies straight and level down the optical table, meaning the fibre tip is aligned to the lens. Then I walked the tip/tilt of the coupling mirrors and fibre foci to optimize coupling. Using this method I was limited to around 80 % coupling from free space into fibre.

Based on a suggestion from David Schmid from Paul Kwiat's group at the University of Illinois at Urbana-Champaign, I detached the lens from the Nanomax and put it in a separate 5-axis mount. This allowed aligning the lens to the incoming beam first, and then positioning the fibre tip to capture the focused light. This allowed the high efficiencies reported above, with the majority of the increase coming from having the 5-axis mount where the light was coupled back into fibre, and a small gain on the input side.

The recipe I developed for achieving high coupling efficiency is as follows, with "input" referring to the coupler where light exits the fibre, and "output" where light re-enters the fibre after the Pockels cell:

1. Using an alignment beam, roughly collimate the input light and ensure it runs level and along the table holes, for now with the input lens fixed to the input fibre translation stage.
2. Mount the steering mirrors in centring mounts in the table holes.
3. Using two irises mounted in the table holes between the mirrors, align the beam along the holes between the mirrors using the input coupler's fibre translation and the first mirror.
4. Add a third iris in a table hole after the second mirror and use the second mirror to align the beam through it.
5. Put the output coupling lens in a 5-axis mount (tip/tilt and x/y translation) with the curved surface toward the collimated beam.

6. Back-align and centre the output coupling lens using an alignment beam you can see easily (e.g. 630 nm) and for which the lens is improperly coated, giving a large back-reflection. Look for it using the iris or a white card with a hole about 5 cm from the lens. When nearly aligned there should be a large double-blob reflection and also much smaller Airy rings. How visible they are also depends on the focus of the incoming beam. The two-blob reflection will move mostly with lens translation (each blob in opposite directions) as it is from the convex first surface, and the Airy rings mostly with tip/tilt, as they are from the flat second surface.
7. Using the third iris or card just before the lens, align the Airy rings and blobs to be centred on the incoming beam by adjusting the tip/tilt and x/y translation of the lens, ensuring the lens is centred and flat.
8. Add the output fibre and translate it until some alignment light comes out. If none ever comes, send an alignment beam back through this fibre and through the iris.
9. Now consider the output lens and mirrors locked and don't move them.
10. Switch to your true wavelength and optimize both couplers' x-y fibre translation on power out the output fibre.
11. Adjust the input coupler's focus in small steps, optimizing x-y each time. Every two steps or so, optimize the output coupler's focus, x, and y. This and similar steps below are the main time investments, taking up to an hour each.
12. Try small tweaks to the output lens translation and tip/tilt, optimizing the output coupler focus, x, and y each time. Probably little gain here.
13. Send the alignment beam back through the output coupler and replace the fixed input lens with a lens on a 5-axis mount, as in steps 5-7.
14. Repeat steps 10-12 with the true wavelength from input to output. Some people prefer to keep the fibre positioners fixed now, and tip and tilt the mirrors instead. Both ways achieve similar coupling efficiency.

15. Place the Pockels cell in the beam and tweak it by hand to optimize the power in the output fibre.

16. Repeat step 11, with also tweaking the Pockels cell tip and tilt between tweaking the fibre couplers.

17. Shoot for 95 % coupling efficiency from free-space into fibre! Be careful to put the free-space beam in the same place on the power meter that the fibre does, as I often found a 10 % variation in the reported powers based on the position of the beam on the detector.

18. When adding more optics to be beam, iterate moving the fibres' foci and optimizing x/y, and tipping/tilting the Pockels cell.

2.5 Optimizing the entangled state and measurement settings

As seen in section 1.1.1, Bell's inequalities are maximally violated for nonmaximally-entangled states when the detector efficiency is less than perfect [47]. Thus a method to determine the optimal state and corresponding measurement settings is needed. I wrote MATLAB code that takes measured values for heralding efficiency and dark counts, and computes the state and measurement settings to get the largest violation of the CH inequality (1.1). This code is based on the Quantum Optics Toolbox by Sze M. Tan [158] available as of this date at http://qo.phy.auckland.ac.nz/toolbox/, and quantum photonics functions by Thomas Jennewein [159], available by contacting me or Dr. Jennewein. My code and comments are provided in appendix A. The simulation reproduced the experimental count statistics with high accuracy and was used to set the state and measurement angles for the loophole-free Bell test [37].

Chapter 3

Theory of a linear-optical device for heralding qubits

This chapter is based on a theory collaboration in 2013. Heralded qubit amplification is emerging as a method to circumvent channel losses in quantum communication as an alternative to the extreme difficulty of removing them. We show here an improvement to the initial design that would allow faster device-independent key distribution over longer distance.

Statement of contributions: I conceived the idea based on previous work by KL and others, co-authored the introduction, and performed the analysis for and wrote the DI-QKD section with input from TJ. MB, KB, AČ, JS, and KL wrote the balance of the paper with my input (one section of which is not reproduced here). The content of this chapter was published in expanded form as [118]:

E. Meyer-Scott, M. Bula, K. Bartkiewicz, A. Černoch, J. Soubusta, T. Jennewein, and K. Lemr. Entanglement-based linear-optical qubit amplifier. *Phys. Rev. A*, **88**:012327, 2013.

I am allowed by the policies of Phys. Rev. A and by permission from my co-authors to republish this work here.

3.1 Introduction

Quantum communication suffers from various technological limits, especially channel losses, background noise, and the need to trust imperfect detectors and single-photon sources. Loss and noise limit the maximum distance for unconditionally secure communications [160]. Long-distance quantum key distribution (QKD) has been realized over 144 km in free space [161] and over 260 km in an optical fibre [23]. Trust in imperfect devices used for cryptography allows eavesdroppers to attack unintended leakages of information or control detectors. These are known as side-channel attacks. [59].

Side-channel attacks can be solved in principle by using Bell-state projection measurements or using entanglement-based protocols. The simpler approach is measurement-device-independent QKD [75, 76]. In this case a projection on a Bell state in the middle of the communication line removes all detector side channels. The more complete approach is device-independent QKD (DI-QKD) [36, 114, 117, 104] and its security is based on the loophole-free violation of a Bell inequality. DI-QKD removes all source and detector side channels but requires closing the detector (high-efficiency detection) and locality (distant detectors) loopholes, which has only recently been achieved simultaneously [37, 38, 39].

For DI-QKD and other protocols requiring high-efficiency detection, a method is required to circumvent the channel losses inherent in photon transmission. In classical optical communication networks the problem of losses is solved using amplifiers of the classical signal. For quantum communication, losses are more fundamental. The quantum signals are stored in polarization, temporal, angular momentum, or other modes of individual photons and any quantum amplifier is bound by the limits of the no-cloning theorem [106]. Several proposals of quantum amplifiers were recently introduced, wherein the quantum limit can be respected while still providing single-photon amplification by making the amplifier non-deterministic. This type of amplification is called heralded noiseless amplification [112] and is already seeing implementation [110, 111, 114].

Here we propose a new design of a linear-optical heralded qubit amplifier that can restore an attenuated qubit and is also capable of distilling deteriorated entanglement. Our amplifier is ready to be used in DI-QKD schemes, and it outperforms some previously published proposals. In contrast to the Gisin *et al.* scheme [104], the success probability of our device does not asymptotically approach zero when increasing the amplification gain. Furthermore in comparison to the Pitkanen *et al.* scheme [117], our device provides tuneable gain and for the case of infinite gain allows better success probability due to its intrinsic elimination of the two-photon component after heralding. However, the Pitkanen *et al.* device may perform better when using a probabilistic source for the ancilla photons due to its extra stage of heralding. The scheme by Curty and Moroder makes use of entanglement as in our device, but it is limited to infinite gain [116], and in fact is comparable to our amplifier set to infinite gain. We present an investigation of the gain versus success probability tradeoff, which is a crucial figure of merit for probabilistic amplifiers, and analyze the performance of these amplifiers for DI-QKD.

3.2 Principle of operation

The amplifier (depicted in fig. 3.1) consists of four polarizing beam splitters. Two of them ($\mathrm{PBS_{in}}$ and $\mathrm{PBS_{out}}$) form a Mach-Zehnder interferometer between signal input port "in" and output port "out". These polarizing beam splitters transmit horizontally-polarized light and reflect light with vertical polarization. The other two are partially-polarizing beam splitters, denoted as $\mathrm{PPBS_1}$ and $\mathrm{PPBS_2}$, and placed in their respective arms of the interferometer. A PPBS can be built using a multilayer thin-film dielectric coating on a glass plate to provide the desired splitting ratios. $\mathrm{PPBS_1}$ totally reflects vertically-polarized light, while having reflectivity r for horizontal polarization ($r = 0$ for a standard PBS). In terms of creation operators this transformation reads

$$\begin{aligned} \hat{a}^\dagger_{\mathrm{in,H}} &\rightarrow r\hat{a}^\dagger_{\mathrm{out,H}} + \sqrt{1-r^2}\hat{a}^\dagger_{\mathrm{D1,H}} \\ \hat{a}^\dagger_{\mathrm{a1,H}} &\rightarrow -r\hat{a}^\dagger_{\mathrm{D1,H}} + \sqrt{1-r^2}\hat{a}^\dagger_{\mathrm{out,H}} \\ \hat{a}^\dagger_{\mathrm{a1,V}} &\rightarrow -\hat{a}^\dagger_{\mathrm{D1,V}}, \end{aligned} \tag{3.1}$$

where the labelling of spatial modes has been adopted from fig. 3.1 and H, V denote horizontal and vertical polarizations. Similarly $\mathrm{PPBS_2}$ completely reflects the horizontal

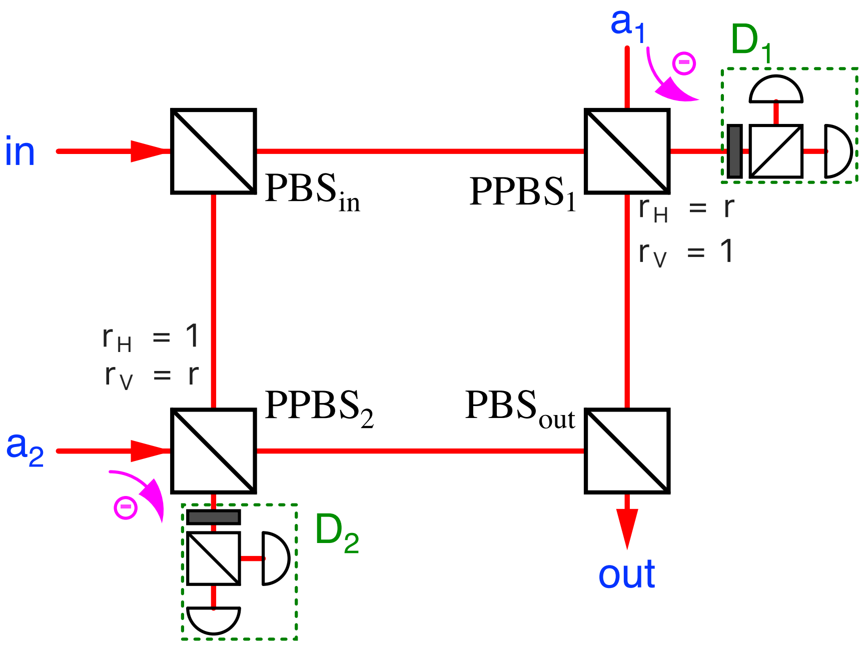

Figure 3.1: Scheme for entanglement-based linear-optical qubit amplifier. A deteriorated qubit state enters through port *in*, and undergoes amplification heralded by detections in D_1 and D_2 in the diagonal basis. The modes a_1 and a_2 each input half of a maximally-entangled pair. The pink minus signs indicate the reflection in the PPBS that picks up a π phase shift.

polarization and reflects the vertical polarization with reflectivity r, giving transformations

$$\begin{aligned}
\hat{a}^{\dagger}_{\mathrm{in,V}} &\rightarrow r\hat{a}^{\dagger}_{\mathrm{out,V}} + \sqrt{1-r^2}\hat{a}^{\dagger}_{\mathrm{D2,V}} \\
\hat{a}^{\dagger}_{\mathrm{a2,V}} &\rightarrow -r\hat{a}^{\dagger}_{\mathrm{D2,V}} + \sqrt{1-r^2}\hat{a}^{\dagger}_{\mathrm{out,V}} \\
\hat{a}^{\dagger}_{\mathrm{a2,H}} &\rightarrow -\hat{a}^{\dagger}_{\mathrm{D2,H}}.
\end{aligned} \tag{3.2}$$

This can be implemented with the same device as PPBS$_1$ plus half-wave plates. The parameter r is to be tuned as explained below. Successful operation of the amplifier is heralded by a two-photon coincidence detection between detection blocks D$_1$ and D$_2$.

To demonstrate the principle of operation, let us assume the input signal to be a coherent superposition of vacuum and a polarization-encoded single photon qubit

$$|\psi_{\mathrm{in}}\rangle = \alpha|0\rangle + \beta_H|H\rangle + \beta_V|V\rangle, \tag{3.3}$$

where $|0\rangle$ denotes vacuum, $|H\rangle$ and $|V\rangle$ denote horizontal and vertical polarization states respectively and the coefficients meet the normalization condition $|\alpha|^2 + |\beta_H|^2 + |\beta_V|^2 = 1$. The amplifier makes use of a pair of ancillary photons impinging on ports a_1 and a_2 of PPBS$_1$ and PPBS$_2$ respectively. These ancilla photons are initially in a maximally-entangled Bell state of the form

$$|\Phi^+_{a_1a_2}\rangle = \frac{1}{\sqrt{2}}(|H_{a_1}H_{a_2}\rangle + |V_{a_1}V_{a_2}\rangle), \tag{3.4}$$

where the indices denote the ancillary photons' spatial modes. The total state entering the amplifier composed of the signal and ancillary photons reads

$$\begin{aligned}
|\psi_T\rangle &= |\psi_{\mathrm{in}}\rangle \otimes |\Phi^+_{a_1a_2}\rangle \\
&= \frac{1}{\sqrt{2}}\left[\alpha|0_{\mathrm{in}}H_{a1}H_{a2}\rangle + \alpha|0_{\mathrm{in}}V_{a1}V_{a2}\rangle\right. \\
&+ \beta_H|H_{\mathrm{in}}H_{a1}H_{a2}\rangle + \beta_H|H_{\mathrm{in}}V_{a1}V_{a2}\rangle \\
&+ \left.\beta_V|V_{\mathrm{in}}H_{a1}H_{a2}\rangle + \beta_V|V_{\mathrm{in}}V_{a1}V_{a2}\rangle\right].
\end{aligned} \tag{3.5}$$

Now we inspect the evolution of all the individual terms in the input state. Since the successful operation of the amplifier is conditioned by a coincidence detection of exactly two photons between D$_1$ and D$_2$, we post-select on such cases. This gives transformations

$$\begin{aligned} |0_{\text{in}} H_{a1} H_{a2}\rangle &\rightarrow r|0_{\text{out}} H_{D1} H_{D2}\rangle \\ |0_{\text{in}} V_{a1} V_{a2}\rangle &\rightarrow r|0_{\text{out}} V_{D1} V_{D2}\rangle \\ |H_{\text{in}} H_{a1} H_{a2}\rangle &\rightarrow (2r^2-1)|H_{\text{out}} H_{D1} H_{D2}\rangle \\ |H_{\text{in}} V_{a1} V_{a2}\rangle &\rightarrow r^2|H_{\text{out}} V_{D1} V_{D2}\rangle \\ |V_{\text{in}} H_{a1} H_{a2}\rangle &\rightarrow r^2|V_{\text{out}} H_{D1} H_{D2}\rangle \\ |V_{\text{in}} V_{a1} V_{a2}\rangle &\rightarrow (2r^2-1)|V_{\text{out}} V_{D1} V_{D2}\rangle. \end{aligned} \tag{3.6}$$

Note that for $r = 0$ it is impossible to have more than one photon in the output mode, even for multiple photons in the input mode, as there is no path between the input and output modes. Subsequently we perform polarization-sensitive detection on D$_1$ and D$_2$ in the basis of diagonal $|D\rangle \propto (|H\rangle + |V\rangle)$ and anti-diagonal $|A\rangle \propto (|H\rangle - |V\rangle)$ linear polarization. In this way we erase the information about the ancillary state and project the signal at the output port to

$$|\psi_{\text{out}}\rangle \propto \alpha r|0\rangle + \frac{3r^2-1}{2}\left(\beta_H|H\rangle + \beta_V|V\rangle\right), \tag{3.7}$$

where we have incorporated the fact that only if both the detected polarizations on D$_1$ and D$_2$ are identical (DD or AA coincidences) the device heralds a successful amplification and thus only half of the measurement outcomes contribute to the success probability.

At this point, we define the amplification gain G as a fraction between signal and vacuum probabilities

$$G = \frac{(3r^2-1)^2}{4r^2} \tag{3.8}$$

and calculate the corresponding success probability

$$P = r^2\left[|\alpha|^2 + G\left(|\beta_H|^2 + |\beta_V|^2\right)\right]. \tag{3.9}$$

Note that while the gain itself is independent of the input state, the success probability depends on both the gain and the input state parameters. This reflects the intuitive fact that it is impossible to amplify a qubit that is not present in the input state ($\beta_H = \beta_V = 0$).

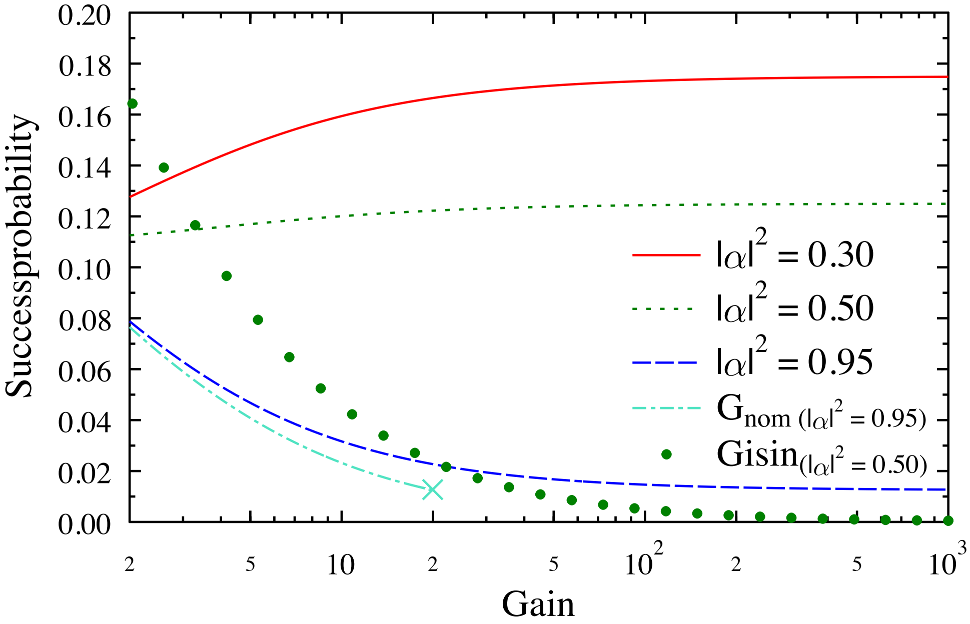

Figure 3.2: Calculated success probability as a function of gain for three different input states parametrized by $|\alpha|^2$, the fraction of the input state in the vacuum. For comparison, the success probability of the Gisin *et al.* scheme [104] is presented for $|\alpha|^2 = 0.5$. The success probability of our amplifier converges asymptotically to a non-zero value for any state with $|\alpha|^2 < 1$. Success probability is also plotted as a function of nominal gain G_{nom} for $|\alpha|^2 = 0.95$. According to the definition eq. (3.10), the nominal gain is upper bounded by the value of 20 in this case (marked with an X).

Let us analyze the results further. The gain $G = 1$ is obtained for $r = 1$ with success probability $P = 1$ independent on the input state. On the other hand, an infinite gain is obtained for $r = 0$ with success probability of $P = (|\beta_H|^2 + |\beta_V|^2)/4$. In this case it is possible to increase the success probability by a factor two by including detection coincidences DA and AD accompanied by a feed-forward operation $V \to -V$ on the output state. Figure 3.2 depicts the tradeoff between success probability and gain for three different input states containing different amounts of vacuum.

Another measure of amplifier performance proposed in [114] is the nominal gain G_{nom}, defined as the single-photon probability at the output over the single-photon probability at the input,

$$G_{\mathrm{nom}} \equiv \frac{P_{\mathrm{out}}}{P_{\mathrm{in}}} = \frac{G}{|\alpha|^2 + G(|\beta_H|^2 + |\beta_V|^2)} = \frac{r^2 G}{P}. \tag{3.10}$$

While the ordinary gain G describes how much the qubit to vacuum probability ratio has been increased under the amplification procedure, the nominal gain shows how much the overall probability of finding a qubit in the output has increased. For this reason, the nominal gain is bounded by the inverse value of the initial qubit probability P_{in} (e.g. for $|\beta_H|^2 + |\beta_V|^2 = 0.2$, the maximum value of nominal gain is 5 and in this case the vacuum state is completely eliminated). Figure 3.2 depicts the success probability as a function of nominal gain for one particular initial state ($|\alpha|^2 = 0.95$).

In contrast to the Gisin *et al.* scheme [104], the success probability does not decrease asymptotically to 0 with increasing gain (also illustrated in fig. 3.2 for comparison). However in the case of infinite gain, the scheme performs exactly as well as standard teleportation [116]. However, standard teleportation does not allow tuning the amplification gain and therefore the superposition of vacuum and qubit state collapses either onto vacuum or qubit state. Our scheme allows for the coherent superposition of these two terms to be maintained. Keeping coherence between vacuum and qubit terms is crucial in applications involving dual-rail encoding.

3.3 Device-independent quantum key distribution

Photon amplifiers can find application in device-independent quantum key distribution [35, 104]. As mentioned above, DI-QKD does not require any knowledge of Alice and Bob's measurement devices, but does require closing the detection loophole [72]. A number of ways of closing this loophole have been demonstrated, including using trapped ions [31, 43] and efficient photon detection [50], but none has done so over the many-kilometre distances needed for cryptography due to the intrinsic loss associated with photon transmission in fibre or free space. Gisin *et al.* recently proposed using a photon amplifier to herald incoming photons, closing the detection loophole and allowing DI-QKD [104]. In their scheme, as in the recently proposed improvements [116, 117], a source of photons near Alice emits entangled photon pairs. One photon is sent to Alice, which she detects directly with high efficiency, and the other photon is sent over a long channel to Bob. Bob routes the incoming photon through a heralded amplifier (e.g. the one proposed by Gisin *et al.* or by us) before detection, closing the detection loophole by performing a measurement only upon successful amplification.

In order to compare the performance of the previous amplifiers with ours, we performed numerical quantum-optical simulations of the amplifiers. The initial source of entanglement was spontaneous parametric down-conversion, with photon pair probability set to 2×10^{-3}, and all amplifiers used on-demand photon sources (two single photons for the Gisin *et al.* and Pitkanen *et al.* schemes and a maximally-entangled Bell state for ours) as ancillae. To mirror a likely experimental scenario, we used bucket detectors with 95 % detection efficiency and 91 % coupling efficiency as heralding detectors, and untrusted noiseless photon-number resolving detectors with the same efficiencies for the detection of the photons after heralding. The former are modelled on fast superconducting nanowire detectors [162] and the latter transition edge sensors [163]. We optimized all amplifiers over their tunable beam splitter reflectivity at each point. Finally we calculated the secure key rate per laser pulse from eq. (11) of the Supplementary Information of ref. [104] as

$$R = \mu_{cc} \left[1 - h(Q) - I_E(S, \mu)\right], \tag{3.11}$$

where μ_{cc} is the probability of a conclusive event for both Alice and Bob (including source emission probabilities), $h(Q)$ is the binary entropy function of the measured quantum bit error rate, and $I_E(S, \mu)$ is Eve's information based on the Bell inequality violation S and the ratio of inconclusive to conclusive results μ. The full expression is

$$R = \mu_{cc}\left[1 - h(Q) - \left((1-\mu)\chi\left(\frac{S-4\mu}{1-\mu}\right) + \mu\right)\right], \tag{3.12}$$

adapted from eq. (23) of the Supplementary Information of ref. [104], where

$$\chi(x) = h\left(\frac{1+\sqrt{(x/2)^2-2}}{2}\right). \tag{3.13}$$

As discussed by Pitkanen *et al.* this key rate assumes a restricted class of eavesdropping strategies, which allows discarding the inconclusive results during data postprocessing [117]. Future work could compare the amplifiers' performance using the more general key rate of ref. [117].

As shown in fig. 3.3, our amplifier outperforms the Gisin *et al.* scheme and can also tolerate more dark counts in the heralding detectors. As with the other proposed improvements, this is because we eliminate the possibility for both ancilla photons to be detected at the same time, heralding the vacuum at the output. Our proposal additionally outperforms the Pitkanen *et al.* scheme by a nearly constant factor, where this factor comes from improvements in success probability and the ratio of conclusive to inconclusive events after heralding. This is possible because in the Pitkanen *et al.* scheme, the elimination of the unwanted two-photon component at the output after heralding even for ideal ancilla photons comes at the cost of vanishing success probability, a tradeoff our amplifier does not suffer from. The optimal key rate in this DI-QKD scenario for our amplifier occurs with $r = 0$ for all values of channel loss, such that it performs identically to the Curty and Moroder proposal [116]. However, there could be a regime (e.g. with noise in the final Bell test detectors) where higher success probability is needed to maximize key rate, at the cost of a larger vacuum component after the amplifier.

3.4 Conclusion

We have presented a linear-optical qubit amplifier. With the help of a maximally-entangled photon pair, this device is able to change the ratio between vacuum and single-qubit com-

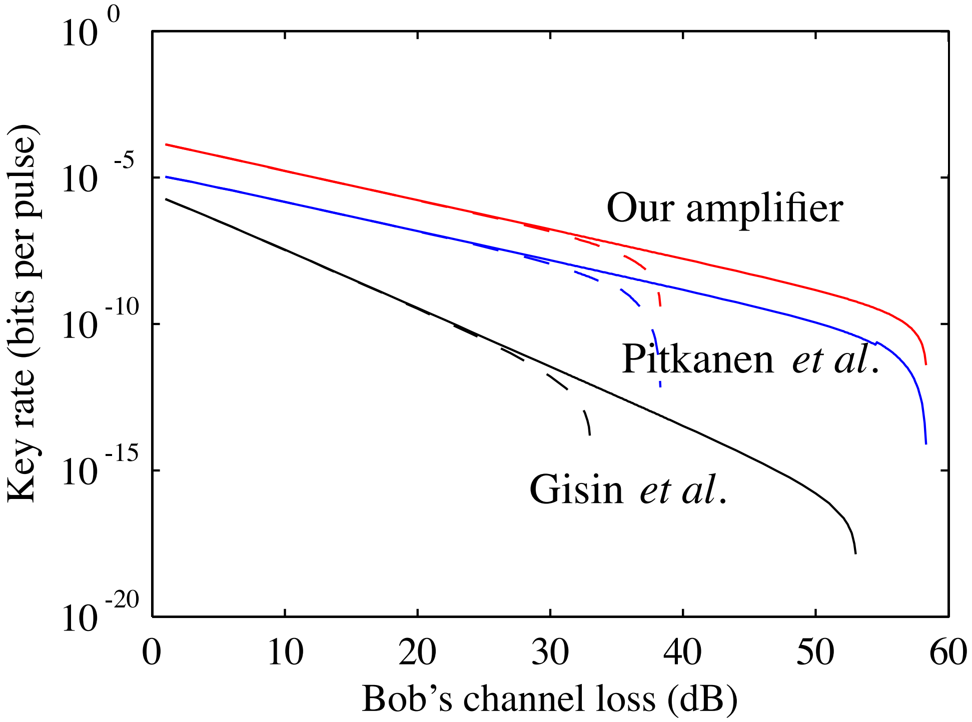

Figure 3.3: Simulated key rate per laser pulse for device-independent quantum key distribution versus Bob’s channel loss. The solid lines have 1 dark count/s and the dashed lines 100 dark counts/s in the heralding detectors. Assuming 100 ps timing resolution in the heralding detectors leads to 10^{-10} and 10^{-8} dark count probability per pulse respectively. Our entangled photon amplifier allows more key to be extracted than the Gisin *et al.* scheme, and even shows better scaling with loss. It additionally delivers approximately 12 times the key rate of the Pitkanen *et al.* scheme.

ponents, thus introducing qubit gain. In contrast to other proposals, our scheme achieves infinite gain with non-zero probability of success. Moreover, we have shown that the success probability of implementing infinite gain equals the success probability of standard teleportation. To demonstrate the capabilities of our amplifier, we have presented its potential application to device-independent quantum key distribution, and the improvements this amplifier makes over previously proposed devices, including a key rate more than three orders of magnitude better for 100 km transmission distance (20 dB channel loss). Practical implementation of the proposed scheme will be limited as in the other proposals by detection efficiency and coupling efficiency of ancillae.

Chapter 4

Experimental precertification of qubits through three-wave mixing

This chapter is based on an experiment performed in 2015. Photonic qubit precertification, similarly to heralded qubit amplification, seeks to circumvent channel losses for quantum communication but is based on nonlinear optics. Here we show the first implementation of precertification and characterize its performance in terms of process fidelity and heralding efficiency.

Statement of contributions: I conceived the idea (in parallel with AC), rebuilt DH's triplets setup to do precertification, analyzed the data, and wrote the paper with input from all authors. DM, KG, JZS, and KAGF built Alice's photon source, and DM and JZS helped conduct the experiment. DH built the original photon triplets setup and wrote data-analysis code. KAGF provided process tomography code. KJR and TJ supervised the experiment. The content of this chapter was accepted by Physical Review Letters on January 4, 2016 in condensed form as [164]:

E. Meyer-Scott, D. McCloskey, K. Gołos, J. Z. Salvail, K. A. G. Fisher, D. Hamel, A. Cabello, K. J. Resch, and T. Jennewein. Certifying the presence of a photonic qubit by splitting it in two. *Phys. Rev. Lett.*, 2016. © 2016 American Physical Society.

I am allowed by the policies of Phys. Rev. Lett. and by permission from my co-authors to republish this work here.

4.1 Introduction

Learning if and when a photon has arrived at a receiver without destroying it is fundamentally difficult [97]. Yet over reasonable transmission distances, this is required by advanced quantum communication protocols such as device-independent secure communication [165, 166], private secure randomness amplification [167], and fundamental tests of nonlocality [12]. These proposals fail in the presence of even moderate channel losses, but can be made practical with techniques that circumvent the effects of loss by certifying that the quantum system is ready after transmission. This certification is an attractive alternative to the nearly impossible task of eliminating fundamental transmission-loss mechanisms.

One approach using traditional destructive photodetection is entanglement swapping [92], which certifies that stationary quantum systems such as atoms or crystal defect centres are ready in the desired quantum states [44]. This method has recently been applied to nitrogen-vacancy centres for a violation of Bell's inequality free of the detector and locality loopholes [39]. However, the synchronization and indistinguishability of photons from disparate sources required for entanglement swapping is difficult to achieve, and low photon collection efficiencies from the stored quantum systems lead to low experimental rates.

Thus we look to nondestructive optical methods of certifying a photon's arrival to indicate that the photon itself is ready. One technique is heralded qubit amplification [104, 116, 117, 118], which uses ancilla photons interfering with the signal photon and specific detection patterns to herald the signal's arrival. This technique requires synchronization between distant and indistinguishable photon sources and as such implementations to date have not employed a separated source and receiver [111, 114, 115]. Similarly, quantum nondemolition measurements based on cavity quantum electrodynamics and cross-phase modulation have stringent requirements on incoming photons and low repetition rates [99, 102, 103, 168].

A promising solution for heralding the arrival of a photon after loss is photonic qubit

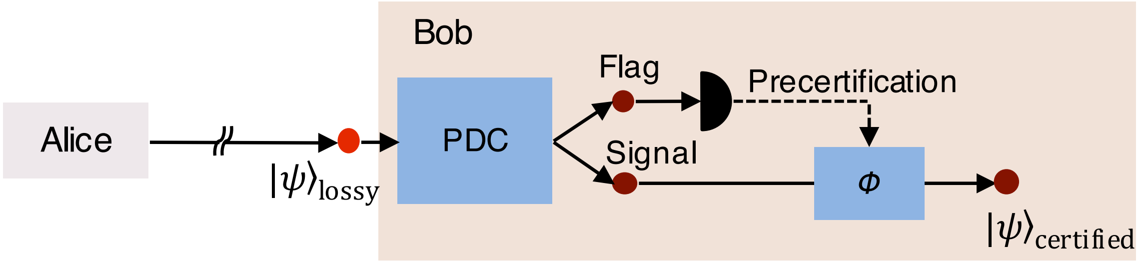

Figure 4.1: Photonic qubit precertification. Alice sends a photonic qubit through a lossy channel to Bob, where it undergoes polarization-preserving parametric down-conversion (PDC), producing a photon pair with some probability. The flag photon is detected to precertify the signal, which carries the initial qubit state. For half the flag detections, a feedforward phase correction (ϕ) is performed on the signal.

precertification, proposed by Cabello and Sciarrino [120]. Precertification does not require synchronization or indistinguishability, and acts directly on flying photonic qubits. This approach therefore offers greater utility than entanglement swapping and qubit amplification and could be employed in a wide array of quantum communication implementations. Precertification is applicable to both photonic and spin-photon entanglement, where it can overcome low coupling efficiencies out of quantum emitters.

In precertification, the sender, Alice, transmits a photonic qubit encoded in polarization to the receiver, Bob, over a lossy channel. Bob splits the incoming photon into two photons, labeled flag and signal, through polarization-preserving single-photon parametric down-conversion (PDC) as shown in fig. 4.1. Since the flag photon is never produced without the corresponding signal photon, the detection of the flag precertifies the presence of the signal. The configuration is such that the signal photon bears the same quantum information initially encoded by Alice. No timing synchronization is required between Alice and Bob, but the wavelength of Alice's photon must match the acceptance band of Bob?s down-conversion crystal, within about 0.5 nm in our implementation. The key component of precertification, single-photon PDC, has been performed with photons from both spontaneous parametric down-conversion [169] and from an atomic ensemble [170].

Here we report a proof-of-principle implementation of photonic qubit precertification based on single-photon PDC with separated source and receiver. We demonstrate that qubit states are preserved during precertification by performing process tomography, and measurements of heralding efficiency show how our device could become useful in device-independent quantum communication.

4.2 Precertification experiment

The polarization-preserving down-conversion process has the Hamiltonian

$$H_{\mathrm{PDC}} = \Gamma \left(a_{H_i} a^{\dagger}_{H_f} a^{\dagger}_{H_s} + a_{V_i} a^{\dagger}_{V_f} a^{\dagger}_{V_s} + H.c. \right), \tag{4.1}$$

where Γ determines the probability of down-conversion, the subscripts i, f, and s refer to the input, flag, and signal modes respectively, H and V label two orthogonal polarization modes, and $H.c.$ means Hermitian conjugate. Unlike typical PDC the pump is a single photon and cannot be treated classically. This Hamiltonian preserves the qubit state by mapping $|H\rangle_i \to |H\rangle_f |H\rangle_s$ and $|V\rangle_i \to |V\rangle_f |V\rangle_s$. Thus an arbitrary polarization input state $|\psi\rangle_i = \alpha |H\rangle_i + \beta |V\rangle_i$ down-converts as

$$\alpha |H\rangle_i + \beta |V\rangle_i \to \alpha |H\rangle_f |H\rangle_s + \beta |V\rangle_f |V\rangle_s . \tag{4.2}$$

Writing the flag mode in the diagonal basis, with $|D\rangle = \frac{1}{\sqrt{2}} (|H\rangle + |V\rangle)$ and $|A\rangle = \frac{1}{\sqrt{2}} (|H\rangle - |V\rangle)$, gives

$$\begin{aligned} &\alpha |H\rangle_i + \beta |V\rangle_i \to \\ &\frac{1}{\sqrt{2}} \left[\alpha(|D\rangle_f + |A\rangle_f) |H\rangle_s + \beta(|D\rangle_f - |A\rangle_f) |V\rangle_s \right] \\ =&\frac{1}{\sqrt{2}} \left[|D\rangle_f (\alpha |H\rangle_s + \beta |V\rangle_s) + |A\rangle_f (\alpha |H\rangle_s - \beta |V\rangle_s) \right] . \end{aligned} \tag{4.3}$$

Detecting the flag qubit in $|D\rangle_f$ or $|A\rangle_f$ thus precertifies the signal qubit in the desired state, with an extra phase flip in the case of an $|A\rangle_f$ detection, which we correct by feedforward. The scheme works equally well if the input qubit is part of an entangled state, mapping its entanglement to the signal qubit after precertification [120]. This scheme does not violate the no-cloning theorem [106], as measuring the flag photon in the diagonal basis provides no information on the coefficients α and β [120]. In fact, the input qubit state is shared across the flag and signal photons, such that neither photon in isolation can reproduce an unknown input qubit state.

Our experimental setup (fig. 4.2) comprises a source (Alice) and receiver (Bob) in separate labs with no communication except the quantum channel. Alice prepares photonic qubits through type-II down-conversion to 776 nm wavelength in periodically-poled potassium titanyl phosphate. Alice's photons are produced in pairs with orthogonally-polarized photons, which are split off at the PBS and detected at $D5$ to enable measurement of the heralding efficiency after precertification. Alice's prepared photons are sent through a 30 m fibre to Bob, where he performs precertification by down-converting the incoming photon in a polarization-based Mach-Zehnder interferometer. In the interferometer, one path down-converts $|H\rangle_i$ and the other $|V\rangle_i$ in periodically-poled lithium niobate (PPLN) waveguides [169, 171, 172]. The waveguides are from HC Photonics Corp. and are made of congruent lithium niobate doped with magnesium oxide [173]. We observe around 50 % coupling at the fibre-waveguide input and output interfaces. Since these type-0 waveguides down-convert only one polarization, in the $|V\rangle$ path the polarization-maintaining fibre is rotated 90° before and −90° after the waveguide. The conversion efficiency in the PPLN waveguides strongly depends on the input photon wavelength (see fig. 5.2 of ref. [174]), so we operate near the degeneracy point of fig. 4.3, where the conversion efficiency reaches its maximum value of $(3.4 \pm 3.0) \times 10^{-6}$. This is not as high as the value reported previously for these waveguides ($\approx 7 \times 10^{-6}$ from sec. 4.8.2 of [175]), but as we did not perform multiple independent characterizations of the efficiency, the values in [175] are likely more trustworthy.

The interferometer is phase-stabilized by injecting a laser at 780 nm (not shown), then using proportional-integral-derivative feedback on the output intensity after a polarizer to control fibre stretchers from Evanescent Optics, Inc. in the interferometer. We used a free-space noise eater from Brockton Electro-Optics Corp before sending the stabilization light into the interferometer, ensuring stable polarization and power. It is also critical to use a stabilization laser with relatively short coherence length, to avoid fluctuations due to cavity effects between fibre connectors. Using a long-coherence strong pump at the input

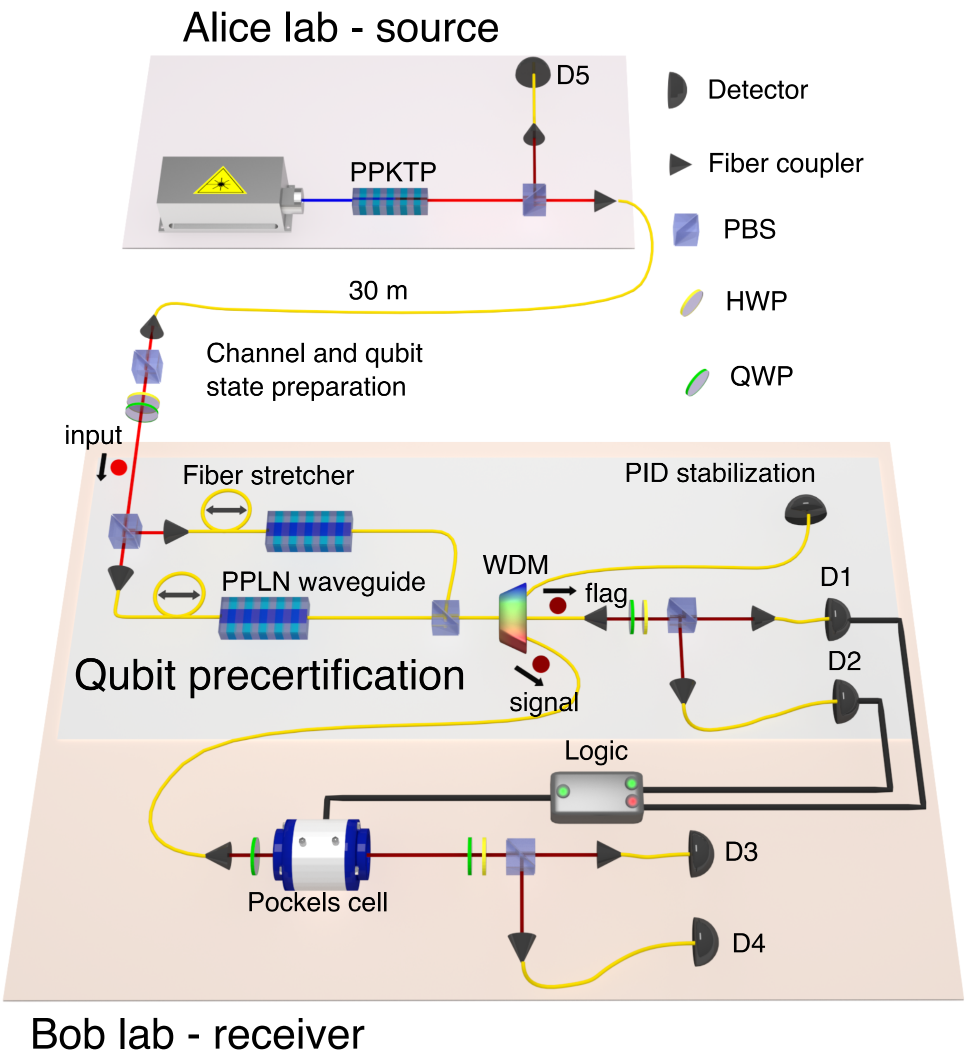

Figure 4.2: Qubit precertification experiment. Alice sends a photonic qubit at a random time to Bob in a separate lab, who precertifies the photon's arrival by splitting it into flag and signal photons before detecting the flag. The splitting is accomplished by using the photon to pump polarization-preserving PDC, built with two crystals in a Mach-Zehnder polarization interferometer. PPKTP - periodically-poled potassium titanyl phosphate crystal, PBS - polarization beam splitter, HWP - half-wave plate, QWP - quarter-wave plate, PPLN - periodically-poled lithium niobate, WDM - wavelength-division demultiplexer, PID - proportional-integral-derivative.

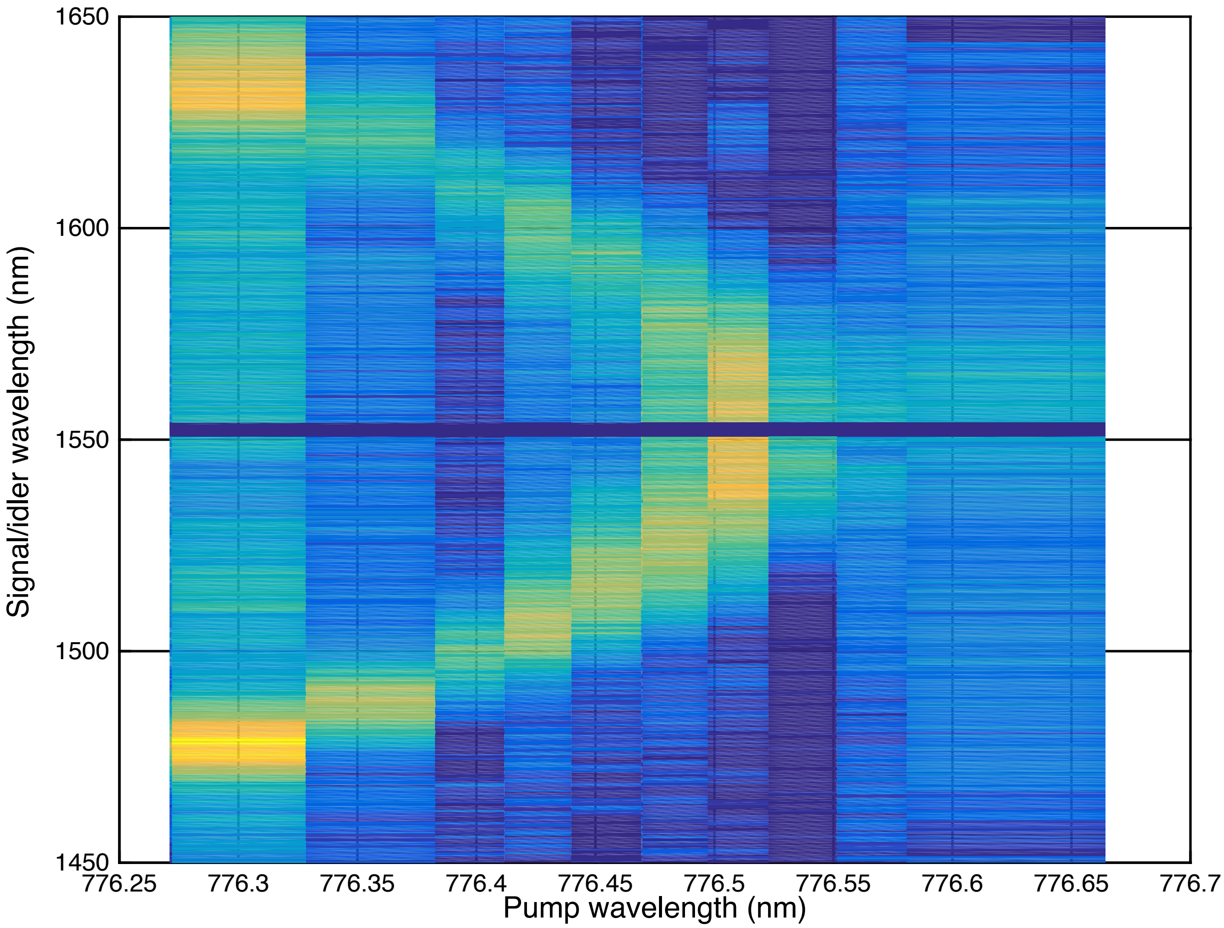

Figure 4.3: Measured phasematching for PPLN waveguides. A strong laser pump was set to a few wavelengths, as measured by a wavemeter from Bristol Instruments, Inc. At each pump setting a down-conversion spectrum was recorded in an optical spectrum analyzer. Because the pump power to measure these spectra is significantly stronger than the single input photons of precertification, the wavelength labels may not correspond to the correct wavelengths during precertification due to heating of the crystals.

wavelength, we carefully matched the lengths of fibre after the PPLN waveguides by maximizing entanglement visibility in the diagonal basis for the flag and signal photons. This is important because the broadband flag and signal photons give path distinguishability due to dispersive broadening if these lengths are not identical (see fig. 4.6 of [174]). Then we used a picosecond pulsed laser to match the total lengths of each arm of the interferometer.

The flag and signal photons centred at 1540 nm and 1564 nm respectively are split in a wavelength-division multiplexer; see appendix B for details on transmission efficiency. The flag photon is projected onto $\left|D\right\rangle_f$ or $\left|A\right\rangle_f$ with a half-wave plate, quarter-wave plate, and polarization beam splitter, then detected with superconducting nanowire single photon detectors from Quantum Opus, LLC. Please see appendix B for characterization of these detectors. The $\left|D\right\rangle_f$ or $\left|A\right\rangle_f$ outcome is fedforward to a Pockels cell, which performs the phase correction for $\left|A\right\rangle_f$ flags necessary to restore the signal photon to the input polarization state ($\left|H\right\rangle_s \to \left|H\right\rangle_s$, $\left|V\right\rangle_s \to -\left|V\right\rangle_s$). Please see section 2.4 for a description of the Pockels cell setup, and specifically, instructions to achieve >90 % coupling efficiency from input fibre to output fibre. The qubit state of the signal photon is analyzed, and it is also detected by nanowire detectors.

To record data, detections D1-D4 are registered as timetags in a coincidence logic unit from UQDevices, Inc. Alice's detection D5 (silicon avalanche photodiode) is excluded from timetagging to permit untriggered precertification, but counting rates from D1-D5 are recorded on a separate logic unit to measure heralding efficiencies. To find the optical and electronic delays between Alice and Bob (needed for characterization, but not for precertification), we sent the 776 nm input photons through the interferometer, bypassing the WDM, and through Bob's flag measurement setup to detectors $D1$ and $D2$. There were just enough detection events to see a timing histogram between $D5$ and the flag detectors, giving an estimate for the time delay, which, when the length of fibre removed for the WDM was estimated and included, let us see triple coincidences.

The loss in count rate induced by precertification is 76 dB. We determine the loss by comparing Bob's certified pair rate $(D1 \vee D2) \wedge (D3 \vee D4)$ (1100 events per hour), with the single detection rate when the qubit is measured directly by Alice (1.2×10^7 counts per second). Here we define coincident detections using logical notation: $D_i \wedge D_j$ means logical AND between detectors i and j, i.e. a coincident detection, and $\vee$ means logical OR.

The raw detection efficiencies (as measured by the Klyshko efficiency, coincidence counts divided by single counts in the other arm as in eq. (4.4) [125]) when Bob's precertification stage is pumped by a strong laser are 10 %, 14 %, 19 %, and 19 %, for D1-D4 respectively, with respective dark count rates per second of 550, 160, 1500, and 1000.

As an aside, the precertification stage is perhaps the weakest-pumped entangled photon pair source ever demonstrated. Because the pump is a single photon, accidental coincidences are nearly eliminated, as seen in the signal-to-noise ratio of 229:1 (defined as number of counts inside the central coincidence bin divided by the average number of counts in other bins) in fig. 4.4. The triple coincidence timing histogram in fig. 4.5 shows also the tight timing correlations of the signal and flag photons with Alice's $D5$ detections. Figure 4.6 shows the reconstructed density matrices for the entangled pair states produced by pumping the precertification stage with $|D\rangle_i$ and $|A\rangle_i$. The former has $(93.5 \pm 0.5)\,\%$ fidelity to $|\Phi^+\rangle$ and the latter has $(91.2 \pm 0.6)\,\%$ fidelity to $|\Phi^-\rangle$. This run produced 21 545 entangled pairs in 13.7 h.

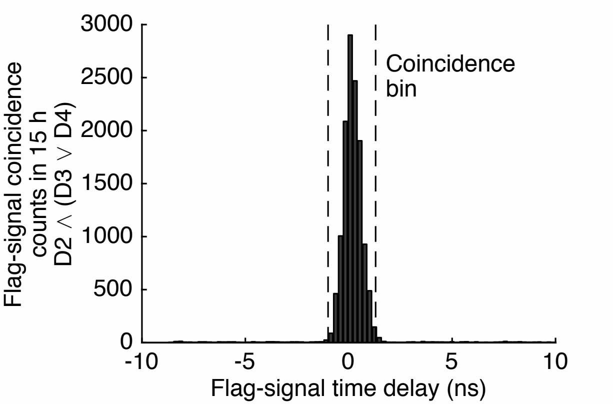

Figure 4.4: Measured timing histogram for two-fold coincidences between Bob's flag and signal detectors $D2 \wedge (D3 \vee D4)$, for the precertification stage pumped by single photons (equivalent to 1 pW average power). The histogram has a bin width of 234 ps to see detector jitter, with the 2.3 ns (diameter) coincidence bin as in the experiment marked with dashed lines. The time delay has been shifted to 0 ns.

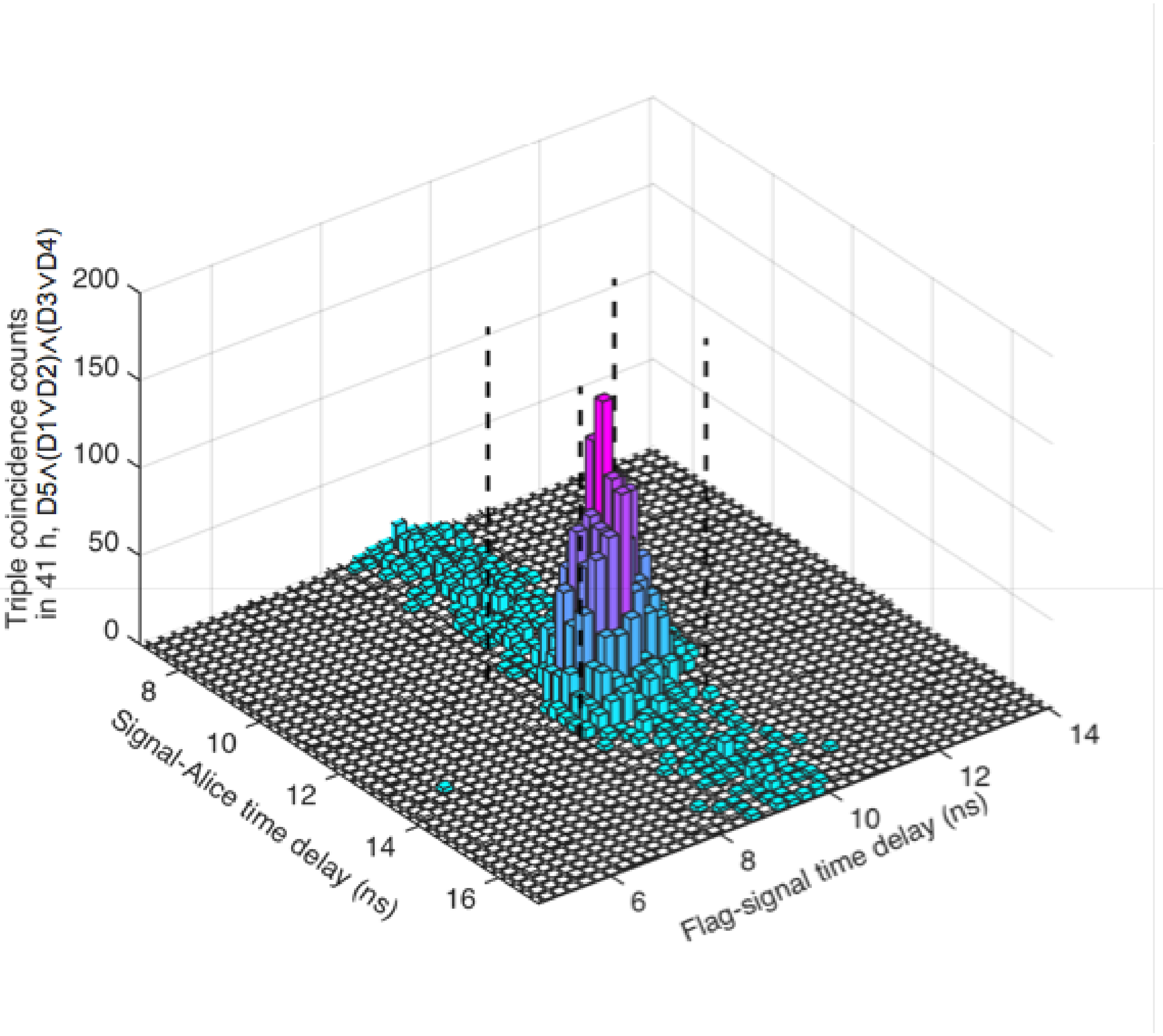

Figure 4.5: Measured triple coincidence histogram $D5\wedge(D1\vee D2)\wedge(D3\vee D4)$ with the same timing resolution (234 ps) as fig. 4.4, but for a different experimental run. The blue stripe is due to accidental coincidences consisting of a real photon pair from the precertification stage in coincidence with an uncorrelated detection in Alice's $D5$. The dashed lines indicate the approximate corners of the 2.3 ns timing window used in the experiment.

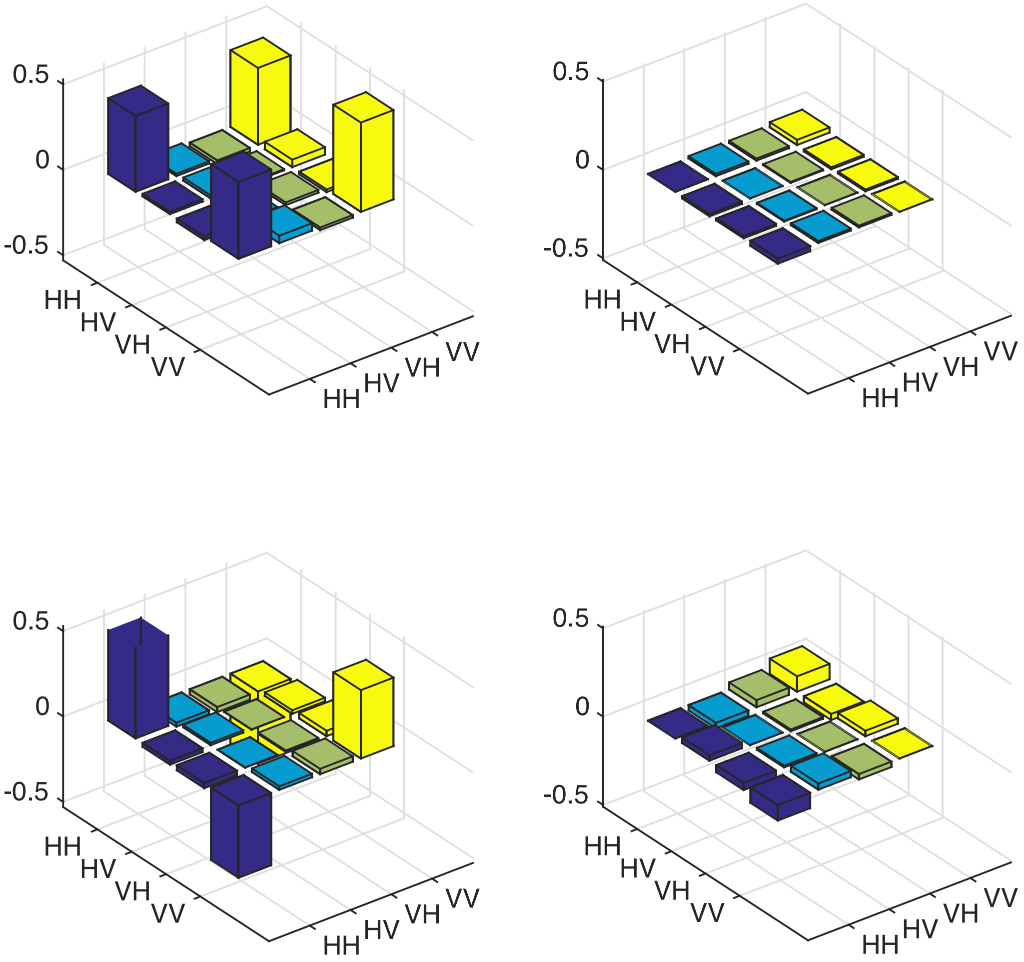

Figure 4.6: Density matrices for entangled photon pairs pumped by single photons, reconstructed from measured coincidence counts. The top row is when the precertification stage is pumped by $|D\rangle_i$ and the bottom by $|A\rangle_i$. The left column is real parts of the density matrices and the right imaginary. The top matrix has $(93.5 \pm 0.5)\,\%$ fidelity to $|\Phi^+\rangle$ and the bottom has $(91.2 \pm 0.6)\,\%$ fidelity to $|\Phi^-\rangle$.

4.3 Results: process tomography and heralding efficiency

To characterize the performance of qubit precertification, we performed quantum process tomography [176, 177] in the qubit subspace by inputting 6 polarization states $|H\rangle$, $|V\rangle$, $|D\rangle$, $|A\rangle$, $|R\rangle = \frac{1}{\sqrt{2}}\left(|H\rangle - i\,|V\rangle\right)$, and $|L\rangle = \frac{1}{\sqrt{2}}\left(|H\rangle + i\,|V\rangle\right)$, and performing tomographically-overcomplete measurements on the signal qubit for each input. These data were inverted by a maximum-likelihood method [178] to reconstruct the process matrix [179]. A perfect qubit precertification would perform only the identity, directly mapping any qubit state from input to heralded output. As seen in fig. 4.7(a), our qubit precertification indeed performs the identity, or a phase flip for heralding on $|A\rangle_f$, with fidelities [180] of $(92.3 \pm 0.6)\,\%$ and $(93.2 \pm 1.0)\,\%$ respectively. For this data set, detector $D1$ was turned off. We do not subtract background counts, uncertainties are determined by Monte Carlo simulations assuming Poissonian counting noise. Also, we ignore contributions from multi-photon events. Though those events certainly occur in Alice's source, the likelihood of a single two-photon-pair event after Bob's PDC over an entire 41 h experimental run is approximately 0.003.

We can correct the phase flip using feedforward based on the heralding detection: a detection of $|D\rangle_f$ requires no phase correction, implemented by a QWP at 0° and $-V_{\lambda/4}$ from a Pockels cell, where $V_{\lambda/4}$ is the quarter-wave voltage of the cell. A detection of $|A\rangle_f$ requires a π phase correction by applying $+V_{\lambda/4}$ to the Pockels cell. This correction can be seen in fig. 4.7(b), where now both $|D\rangle_f$ and $|A\rangle_f$ flag detections result in the identity on the qubit state, with $(84.7 \pm 0.6)\,\%$ fidelity. Here both detectors $D1$ and $D2$ are used. The lower fidelity is due to imperfect phase corrections of the Pockels cell.

We subsequently add loss to the channel between Alice and Bob to quantify how the precertified qubit state degrades with loss and to compare with direct transmission. In fig. 4.8 we plot count rate and Bob's measured qubit fidelity for $|H\rangle_i$ and $|D\rangle_i$ input states. Here the total loss is given in terms of the probability of a photon arriving at the final detector p, and includes all losses after the photon is coupled into Alice's fibre. For direct transmission, the count rate (fig. 4.8(a)) is the number of coincidences per second of $D5 \wedge (D1 \vee D2)$, with D1 and D2 replaced by silicon avalanche photodiodes (with the same efficiency and half the dark counts) and the precertification stage removed. With

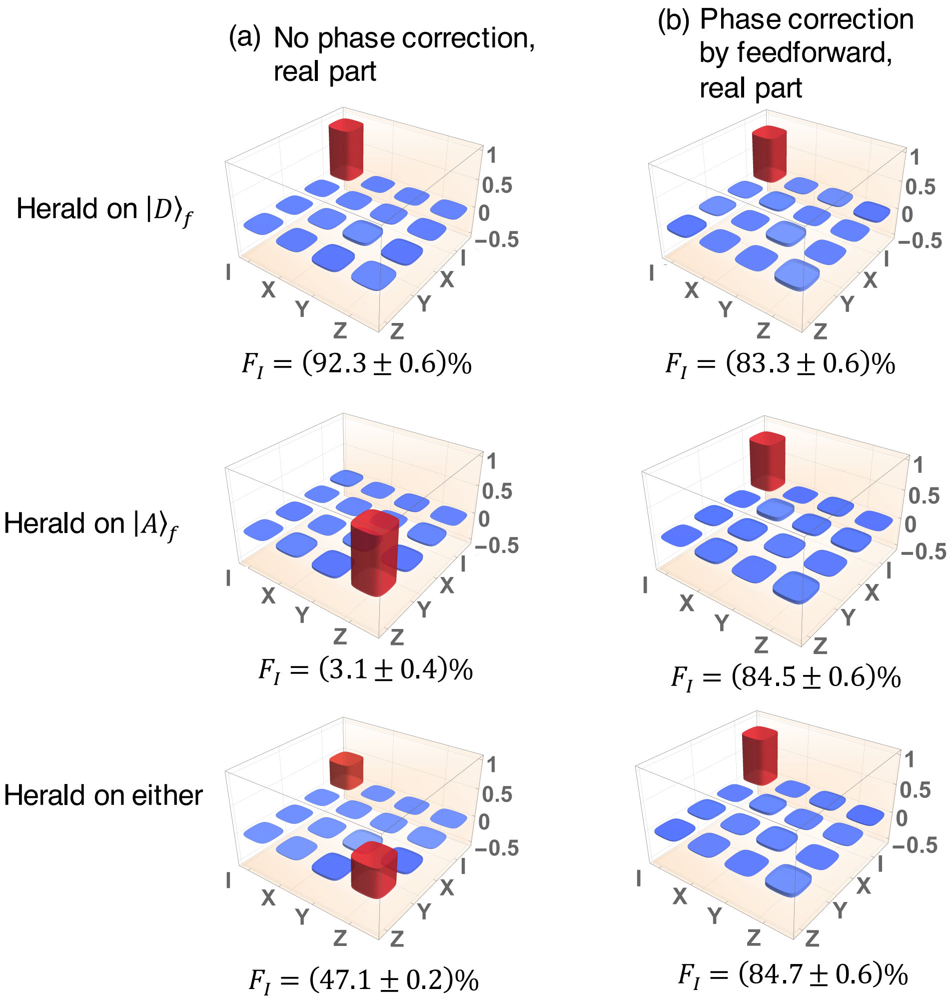

Figure 4.7: Reconstruction of real parts of qubit-subspace process matrices for precertification, without background subtraction. I is the identity, and X, Y, and Z are the Pauli matrices. Process fidelities to the identity F_I are given under each matrix, and imaginary parts are small (absolute values < 0.2) in all cases. (a) Without phase correction, the process fidelity depends on the flag detector. When heralding on state $|A\rangle_f$, the process has $(93.2 \pm 1.0)\,\%$ fidelity to Z but $(3.1 \pm 0.4)\,\%$ fidelity to I. Heralding on either $|D\rangle_f$ or $|A\rangle_f$ gives a mixed channel, with $(95.4 \pm 0.3)\,\%$ fidelity to $(I + Z)/2$. (b) With feedforward phase correction, the process is nearly the identity independent of the flag detection pattern.

precertification, the count rate is the triple coincidences per second $D5 \wedge (D1 \vee D2) \wedge (D3 \vee D4)$. As seen in fig. 4.8(b) the qubit fidelity drops rapidly for direct transmission, whereas the precertified qubit retains a fidelity of 88 % at 80 dB total loss or 4 dB added channel loss. As PDC efficiencies improve with novel materials and engineering, the precertification protocol will be able to tolerate higher channel losses while preserving qubit states.

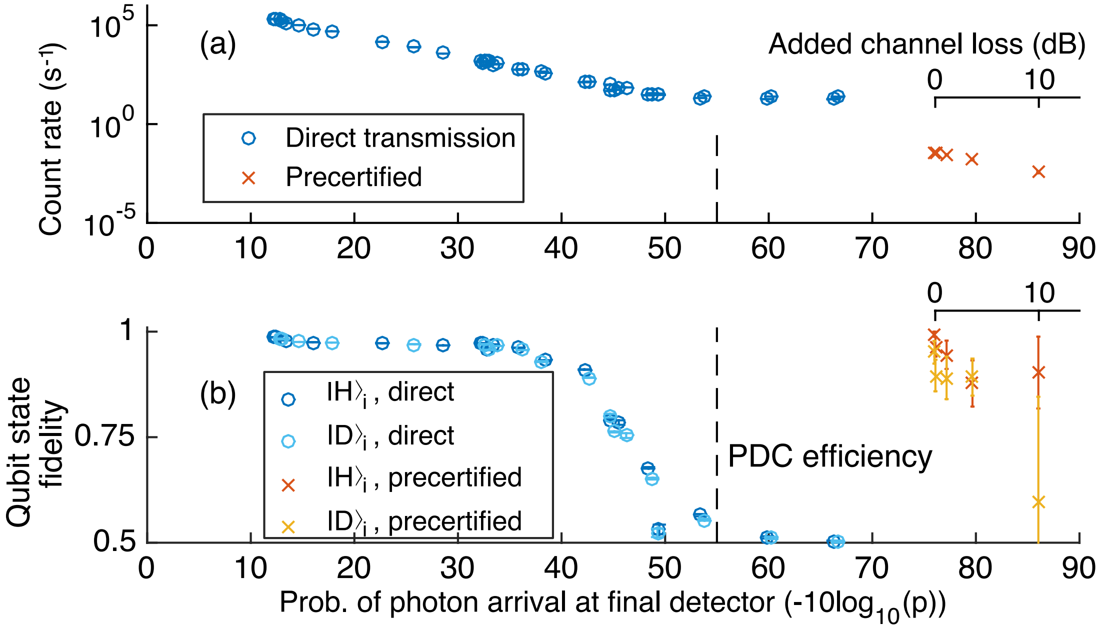

Figure 4.8: (a) Measured count rate versus total loss, given as probability of photon arrival at final detector (p) in decibels, for direct transmission (o) and precertification (x). The latter includes 76 dB loss due to the precertification process, and the PDC efficiency from the PPLN waveguides is marked with a dashed line. The upper scales on each plot show the added channel loss for the precertification data. The direct count rate saturates around 50 dB loss due to dark counts. (b) Qubit fidelities measured from quantum state tomography for input states $|H\rangle_i$ and $|D\rangle_i$. Qubits that are precertified maintain their states at much higher losses compared to those directly transmitted, which are unrecoverable after 50 dB. Error bars on the direct transmission data are smaller than symbol size.

Our measured heralding efficiencies after precertification, defined as the probability of a signal detection by Bob ($D3 \vee D4$) given a detection by Alice ($D5$) and a flag detection

($D1 \vee D2$), are presented in fig. 4.9. The heralding efficiency η_h can be approximated as

$$\eta_h = \frac{\eta_{\text{signal}}}{1 + \frac{p_{\text{dark}}}{p_{\text{flag}}}}, \tag{4.4}$$

where η_{signal} is the total efficiency of the signal photon after Bob's PDC, including coupling and detector efficiencies, and $\frac{p_{\text{dark}}}{p_{\text{flag}}}$ is the ratio of dark counts in the flag detector to detected flag photons, where both are triggered by Alice's $D5$ detection. Equation (4.4) is derived as follows. Considering the precertification stage after triggering by $D5$, the signal heralding efficiency is just the number of detected (flag$\wedge$signal) pairs divided by the number of single flag counts,

$$\eta_h = \frac{N_{\text{pairs}}}{N_{\text{singles, flag}}}. \tag{4.5}$$

Now we switch to pair-emission probabilities per coincidence window p_{pair} and total detection efficiencies, such that $N_{\text{pairs}} = t \times p_{\text{pair}}\eta_{\text{signal}}\eta_{\text{flag}}$, where t is the integration time. We neglect dark counts in the pair rate but not the flag singles rate, which is $N_{\text{singles, flag}} = t \times (p_{\text{pair}}\eta_f + p_{\text{dark}})$. Then the heralding efficiency is

$$\eta_h = \frac{p_{\text{pair}}\eta_{\text{signal}}\eta_{\text{flag}}}{p_{\text{pair}}\eta_{\text{flag}} + p_{\text{dark}}} = \frac{\eta_{\text{signal}}}{1 + \frac{p_{\text{dark}}}{p_{\text{pair}}\eta_{\text{flag}}}}, \tag{4.6}$$

which is eq. (4.4) after defining the flag single detection probability $p_{\text{flag}} = p_{\text{pair}}\eta_{\text{flag}}$.

Our heralding efficiencies are limited mostly by dark counts in the flag detectors (large $\frac{p_{\text{dark}}}{p_{\text{flag}}}$), and partially by optical losses and detection efficiency after precertification (small η_{signal}). The former could be drastically improved with blackbody filters in the flag detector [181], bringing $\eta_h \approx \eta_{\text{signal}} = 19\,\%$ for our system. The coupling efficiency η_{signal} could be improved with low-loss optical components or a chip-based architecture [182]. Therefore in fig. 4.9 we also show simulated heralding efficiencies given flag detectors with 1 dark count/s, 10 % system efficiency, and 100 ps jitter, and also with 10^{-3} dark counts/s and 2.3 % efficiency as recently demonstrated for 1550 nm [183]. For the latter case we assume 80 % coupling efficiency from the precertification to the detectors [184, 185], and 90 % efficient signal detectors [162, 186].

Our precertification rate of $0.3\,\text{s}^{-1}$ compares favourably to state-of-the-art entanglement-swapping and quantum repeater experiments that achieved entanglement detection rates of $1.3 \times 10^{-3}\,\mathrm{s}^{-1}$ with 3 m separation in diamond [45], and $9 \times 10^{-3}\,\mathrm{s}^{-1}$ over 20 m using rubidium atoms [187].

4.4 Simulations toward violating a Bell inequality

For qubit precertification to be a viable alternative to entanglement swapping, the heralding efficiency must be large enough to close the detector loophole, with lower bounds of 50 % for perfect detection efficiency on Alice's qubit [188, 189], or 66 % for symmetric detection efficiency between Alice and Bob [47]. The simulated heralding efficiency after precertification with 10^{-3} darks/s and improved coupling does not drop below 66 % until 35 dB channel loss as seen in fig. 4.9, making such a system practical for long-distance device-independent quantum communication, for example over 144 km in free space [190]. For optical fiber transmission, 35 dB channel loss allows 10 km transmission at 780 nm. This could be improved to 175 km by moving to 1550 nm, which could be possible using four-wave mixing instead of PDC.

Next, we show in simulation how flag detector dark counts and signal coupling efficiencies combine to determine total heralding efficiency and violation of the CH inequality with photon pairs and with spin-photon systems. We see in fig. 4.10 that neither dominates at the moderate values presented here. In fig. 4.11 we see that the CH inequality can be violated with up to 40 dB channel loss between Alice and Bob, assuming Alice's photon and Bob's signal photon are detected with 72 % total efficiency, and Bob detects his flag photon with 50 % efficiency. The CH value is optimized at each point as in section 1.1.1 using the code in appendix A.

A loophole-free violation of Bell's inequality has recently been shown using entanglement swapping between pairs of photons and electron spins [39]. Here we give one example where, for cases where a second cryogenic qubit setup is impractical, precertification can act as a heralded interface between stored and flying qubits, allowing closure of the detection loophole even for low coupling efficiency out of the emitter. We simulate an upgraded qubit precertification with low-noise detectors and low-loss optics and show an asymmetric Bell-test setup with one spin and one precertified photon performs as well as a pair of

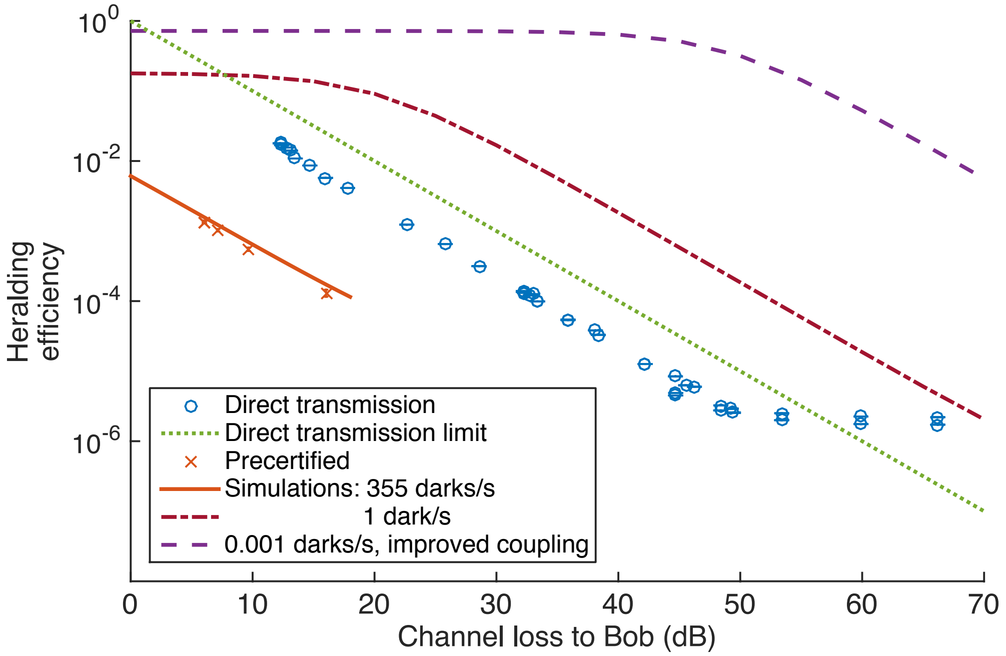

Figure 4.9: Heralding efficiencies versus channel loss between Alice and Bob. The measured heralding efficiency for direct transmission falls linearly on the log-log scale, then saturates at 2×10^{-6} at high loss due to dark counts. The precertified heralding efficiency reaches 1×10^{-3} before also falling due to the decrease in p_{flag} relative to p_{dark} with channel loss. Our simulation in the solid line reproduces this behaviour. The ultimate limit for heralding efficiency for direct transmission is the channel loss itself, plotted as the dotted line. The dot-dashed line shows the simulated precertification heralding efficiency that would be possible with the same coupling efficiency, but 1 dark count/s in the flag detector and 100 ps coincidence window, and the dashed line shows the additional improvement given 10^{-3} darks/s and $\eta_{\text{signal}} = 72\,\%$, greatly outperforming direct transmission.

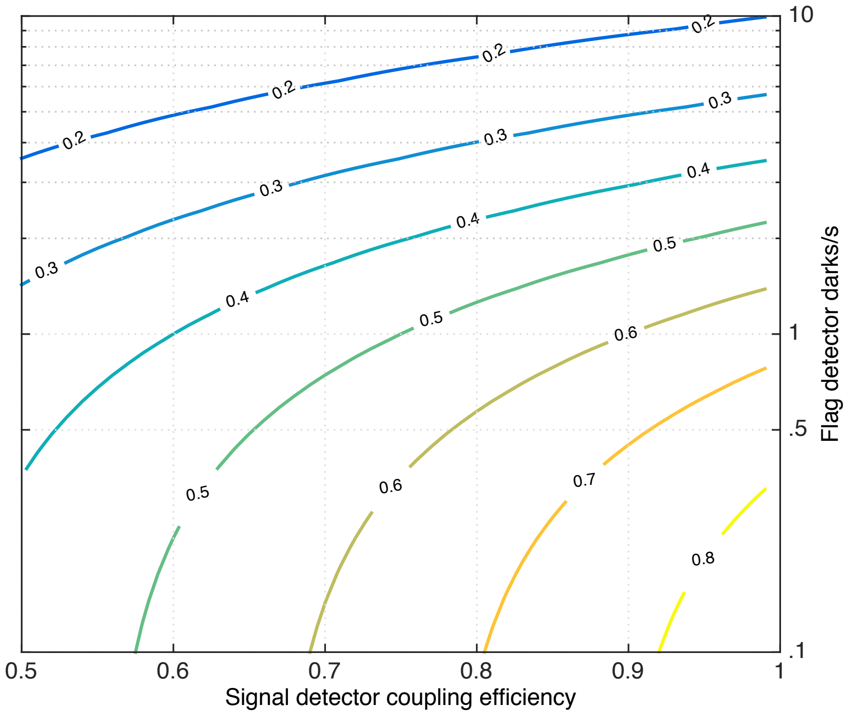

Figure 4.10: Simulated heralding efficiencies (contours) versus flag dark counts and signal coupling efficiency after precertification. Here we assume 90 % efficiency for the flag and signal detectors, 33 % coupling efficiency to the flag detector, and 1000 darks/s on the signal detector. To reach 70 % heralding efficiency for example, we must be below the orange line.

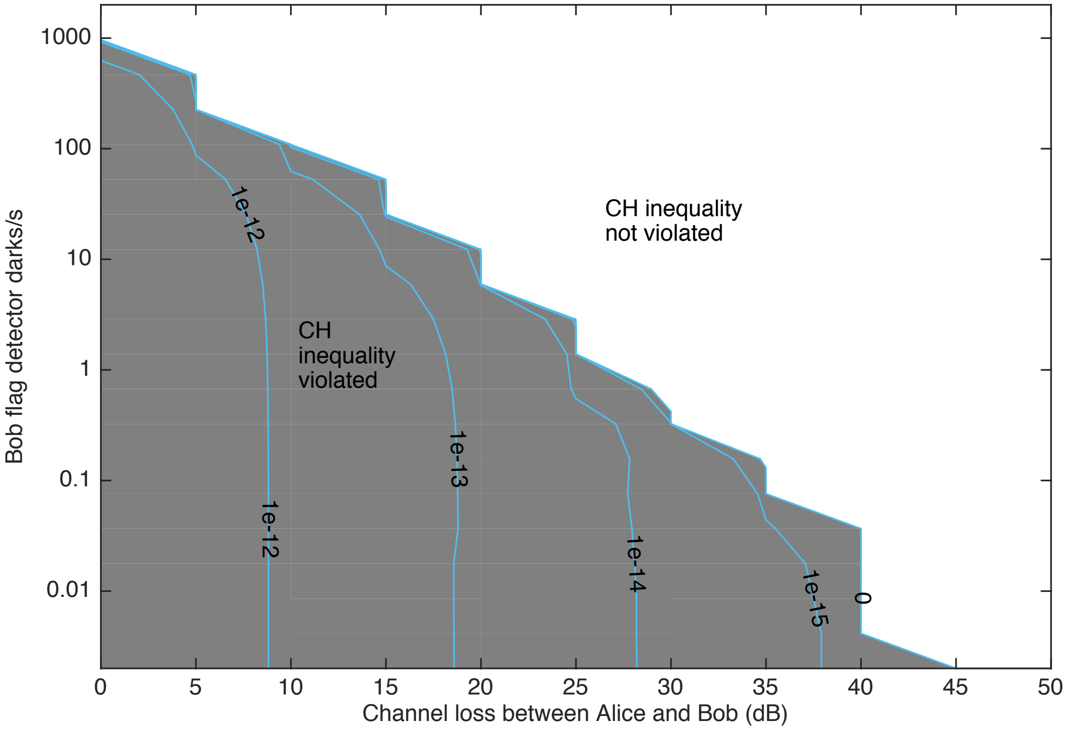

Figure 4.11: Simulated violation of CH inequality for entangled photon pairs after precertification, versus channel loss between Alice and Bob and the dark counts in Bob's flag detector. Values >0 indicate a violation of the CH inequality (grey shading), given here as violation per trial. Here we assume Alice and Bob detect their signal photons with 72 % total efficiency and 10 darks/s each, and Bob detects his flag photon with 50 % efficiency. The source rate and PDC efficiency are the same as in our experiment, and no causes of reduced visibility are included except dark counts. At each point the CH value is optimized over nonmaximally-entangled states and measurement settings, as in section 1.1.1, which causes the jagged contours. With this system a loophole-free Bell inequality violation would be possible over 40 dB channel loss, or 11 km of fibre at 780 nm.

spins with entanglement swapping. We assume coupling efficiency out of the spin system of 4.2 % [191] and a repetition rate of 40 kHz [39], the same signal to noise ratio (70:1) as [45], and 60 %-efficient detectors in the Bell-state measurement. For precertification we assume 80 % coupling into and out of the PPLN waveguides, the same down-conversion probability we observed experimentally (3.4×10^{-6}), and 10^{-5} dark counts per second in the flag detectors which may be difficult to achieve experimentally. Precertification is especially useful if the spin system emits in the visible [192], as precertification and down-conversion to the infrared before transmission allows much lower loss in fibre [193] (e.g. $0.2\,\mathrm{dB\,km^{-1}}$ at 1550 nm versus $8\,\mathrm{dB\,km^{-1}}$ at 640 nm, the zero phonon line of nitrogen-vacancy centres). As shown in fig. 4.12 the spin-spin system can violate the CH inequality [42] with up to 3.3 km optical fibre between spins, while precertification allows violation up to 4.5 km, after optimizing over nonmaximally-entangled states and measurement settings.

4.5 Discussion

We have presented a proof-of-principle demonstration of photonic qubit precertification. Our device maintains the input qubit state with $(92.3 \pm 0.6)\,\%$ process fidelity to the identity, or $(84.7 \pm 0.6)\,\%$ with feedforward phase correction. Our heralding efficiency after precertification, up to 1×10^{-3} , can be immediately improved with recently-demonstrated low-noise detectors [183], and by improvements in optical components.

Though feedforward phase correction is not required to close the detector loophole and serves only to double the rate, it could be possible to engineer phasematching in a single crystal or in a cascaded configuration to eliminate the entanglement between flag and signal photons, preserving the higher rate without feedforward. The effective Hamiltonian would then be

$$H_{\mathrm{PDC}} = \Gamma\left(\left[a_{H_i} a^\dagger_{H_s} + a_{V_i} a^\dagger_{V_s}\right] a^\dagger_{H_f} + H.c.\right). \tag{4.7}$$

One way to do this is to use two crystals in a sandwich configuration [132], but where one crystal is type-0 and the other type-II as in fig. 4.13(a). Thus the first crystal transforms $|H\rangle_i \to |H\rangle_s |H\rangle_f$, and the second $|V\rangle_i \to |V\rangle_s |H\rangle_f$. Matching the conversion probabilities and phasematching bandwidths of the two processes would be difficult, but could be

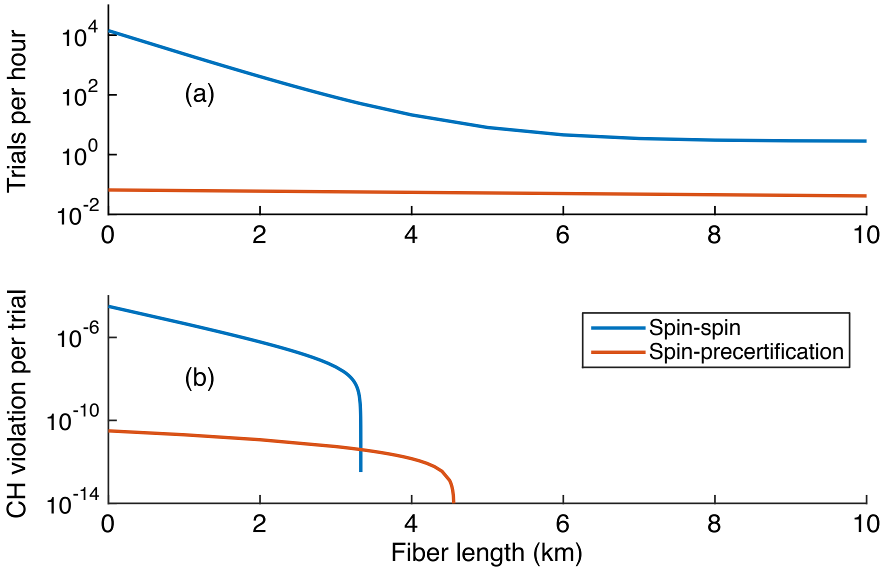

Figure 4.12: (a) Bell test events (heralded/precertified coincident detections) per hour for a loophole-free test, using either spin-spin entanglement via entanglement swapping, or spin-photon entanglement via photon precertification. The spin-spin rate saturates due to dark counts in the Bell state measurement. (b) CH inequality violation per trial. Though the rate is lower, precertification allows loophole-free violation of the CH inequality over longer distance than entanglement swapping between two spins.

accomplished with filtering on the flag photon, leading to the Hamiltonian of eq. (4.7) without requiring an interferometer. A recent integrated entangled-pair source has demonstrated all three types of phasematching in a single chip, which could allow realizing this precertification scheme [194]. A related method is based on induced coherence between two separate type-0 crystals [195], as seen in fig. 4.13(b). The flag mode from the first, $|H\rangle_i \to |H\rangle_s |H\rangle_f$ crystal is passed through the second, $|V\rangle_i \to |V\rangle_s |V\rangle_f$ crystal after a polarization flip, erasing its path information and ensuring its polarization is always $|V\rangle_f$. This requires interferometric stability, but avoids the phasematching difficulties of the sandwich arrangement above by using two of the same crystal, and could be implemented in fibre similarly to our work.

Additionally, it should be possible to use other encodings for precertification beyond polarization. For example, mapping horizontal and vertical polarizations to early and late time bins would allow precertification using time-bin qubits. Here the time-bin-preserving down-conversion is straightforward since only one crystal is needed, but a stabilized time-bin qubit analyzer is required to measure the flag photon in the superposition basis. Other encodings may have similar advantages or drawbacks.

We look forward to improvements in splitting efficiency from novel materials [196], especially those based on $\chi^{(3)}$ that allow all operations at telecommunications wavelengths [197], and from waveguide [198] or resonator [199] engineering, which would make precertification even more competitive. These improvements and the applicability of precertification to both entangled photon and spin-photon systems will make it a useful tool in long-distance quantum communication.

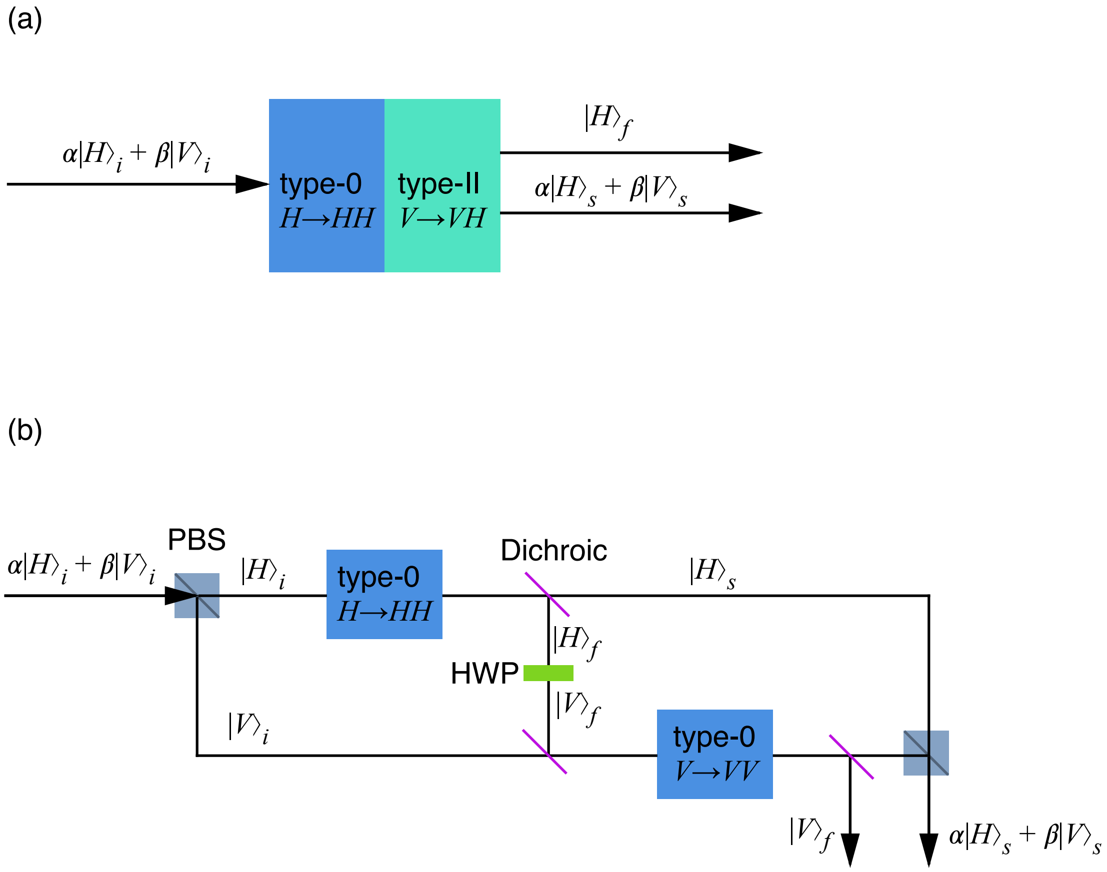

Figure 4.13: Schemes for avoiding feedforward in precertification. (a) A sandwich configuration with two different types of phasematching ensures the flag photon always exits as $|H\rangle_f$. (b) An induced-coherence configuration passes the flag mode through both crystals, ensuring it always exits as $|V\rangle_f$ while erasing information on which crystal it came from.

Chapter 5

Theory of converting one photon into two through four-wave mixing

This chapter is based on a theory paper written in 2014. As seen in chapter 4, one of the main limitations of photonic qubit precertification is the conversion efficiency of the input photon into the flag-signal pair. In this chapter we investigate fibre media to replace the lithium niobate waveguides for single-photon down-conversion, and find that chalcogenide microwires could provide better efficiency.

Statement of contributions: TJ, AD, and I conceived the idea and I co-authored the paper with AD and with input from all authors. AD performed the detailed derivations of four-wave mixing, and I wrote the section on Raman scattering. RA and MR supplied data on chalcogenide microwires. MR and TJ supervised the work. As I did not perform the derivation, I reproduce only the main results here. The content of this chapter was published in Physical Review A in expanded form as [196]:

A. Dot, E. Meyer-Scott, R. Ahmad, M. Rochette, and T. Jennewein. Converting one photon into two via four-wave mixing in optical fibres. *Phys. Rev. A*, **90**:043808, 2014.

I am allowed by the policies of Phys. Rev. A. and by permission from my co-authors to republish this work here.

5.1 Introduction

Pairs of photons created via Spontaneous Parametric Down-Conversion (SPDC) [200] or spontaneous Four-Wave Mixing (FWM) [201] in a nonlinear optical material with a high-intensity pump laser have been used in many experiments in quantum optics, quantum metrology, and optical quantum information processing. As exemplified by the previous chapter, interest is mounting in using SPDC or FWM in later stages of quantum information protocols, rather than just initial sources of photons [202, 172, 203]. This requires efficient operation with very low intensity input states, including converting a single photon into a pair.

Should an efficient one-to-two-photon conversion be realized, one important application is the entangling of three or more photons [169, 171]. These large entangled photon states are useful in quantum communication protocols [204, 205] and fundamental tests of quantum mechanics [171, 206, 207]. Increased efficiency in converting single photons to pairs would allow larger states to be generated with greater speed. Single photon conversion could also be used for heralding photons after long-distance transmission to close the Bell test detection loophole through photonic qubit precertification [120] and for device-independent quantum key distribution [104]; any improvement in conversion efficiency directly increases the communication rates, and also increases the tolerable level of noise. Finally, if efficient enough, single photon conversion could also be used directly in quantum computing as a two-qubit gate [119].

The key challenge in converting a single photon into a pair is the low efficiency of nonlinear optical processes at ultralow power. In principle, standard SPDC or FWM sources could be used, but the low efficiency (less than 10^{-5}) limits the conversion to rates too low to be useful [208]. Therefore we consider here specialty fibre media, which we show can result in large conversion efficiencies thanks to long length, small core size, and high nonlinearity.

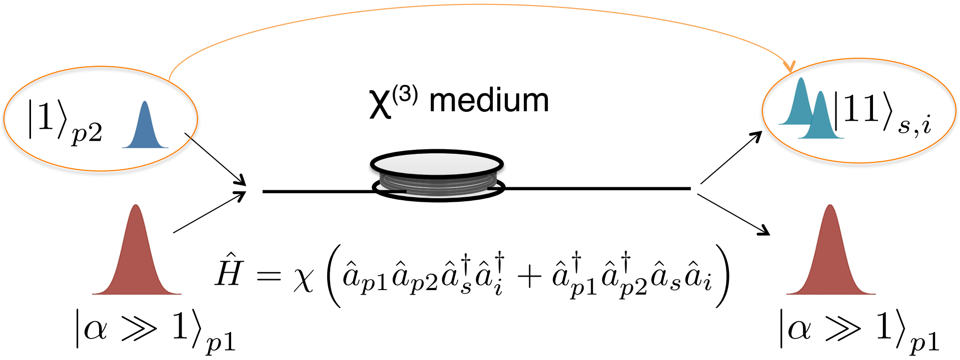

Figure 5.1: Four-wave mixing (FWM) with single photon and strong pump inputs. The model Hamiltonian with interaction parameter χ illustrates the processes, but the full development is given in the text.

5.2 Quantum theory of FWM pumped by a single photon and strong laser

We determine the operator evolution of a system consisting of a strong pump beam and a single photon entering a nonlinear, dispersive, single-mode fibre, and undergoing four-wave mixing and phase modulation as in fig. 5.1. We proceed in the Heisenberg representation by solving the equation of motion for the field-amplitude operators [209]. The two pumping fields are considered monochromatic or quasi-monochromatic, and we include self- and cross-phase modulation, but not parasitic effects such as Raman scattering and multi-photon absorption due to the low power of the inputs. We stay in the low gain regime, which means that only spontaneous FWM (also called four-photon scattering) is studied. This low-gain approximation stands if the total probability of generating a photon pair during the interaction is much lower than 1, and certainly holds since one of our pumps is a single photon.

5.2.1 Operator evolution

The field is quantized in one dimension in a length large enough for the electric field to be written in the continuous limit [210]. We then choose for convenience to write this field in the frequency space, as a sum of its space-dependent spatial mode operators, an approach introduced in ref. [209]. The quantization time T, equal to the quantization length divided by the speed of light, is then the time periodicity of the field, and the density of the frequency space is $\delta\omega = 2\pi/T$. T has to be long enough to allow the writing of the frequency modes in the continuous limit. The electric field operator is then

$$\begin{aligned} \hat{E}(z,t) &= \sqrt{\frac{\hbar}{4\pi\varepsilon_0 c A_{\text{eff}}}} \int d\omega \sqrt{\frac{\omega}{n(\omega)}} \hat{a}(\omega, z) e^{-i\omega t} + h.c. \\ &= \hat{E}^{(+)}(z,t) + \hat{E}^{(-)}(z,t), \end{aligned} \tag{5.1}$$

where ε_0 is the permittivity of free space, c is the speed of light, A_{eff} is the effective area of the fibre modes, taken as the same for all frequency components, ω is the angular frequency and z the propagation distance of the mode corresponding to the annihilation operator $\hat{a}(\omega, z)$, and $n(\omega)$ is the refractive index.

In ref. [196] we take the strong pump (ω_{p1}) as classical then solve to first order for the evolution of the annihilation operators for the weak pump (ω_{p2}) and generated photons (ω), giving

$$\begin{aligned} \hat{a}_0(\omega, L) e^{-i2\gamma P_1 L} = \hat{a}_0(\omega, 0) + 2i\gamma \times \sqrt{P_1}\sqrt{\zeta_2} L e^{-\frac{iKL}{2}} \operatorname{sinc}\left(\frac{KL}{2}\right) \\ \times \hat{a}_0^\dagger(\omega_{p1} + \omega_{p2} - \omega, 0) \hat{a}_0(\omega_{p2}, 0), \end{aligned} \tag{5.2}$$

where L is the length of the medium, $\gamma(\omega) = \frac{3\chi^{(3)}\omega}{2\varepsilon_0 c^2 n(\omega)^2 A_{\text{eff}}}$ is the waveguide nonlinear parameter, P_1 is the strong pump peak power, $\zeta_2 = \frac{P_2}{\left\langle \hat{a}^\dagger(\omega_{p2},0)\hat{a}(\omega_{p2},0)\right\rangle}$ is the peak power of the weak pump normalized to one photon at the input, and $K = \Delta k + \gamma P_1$ is the total phase mismatch, sum of the linear and nonlinear parts (see eq. (5.11)).

By considering only the first order gain, we assume that the conversion efficiency η is low enough that the conversion is described by a single process, described by

$$\hat{a}_0(\omega_{p1}, L)\hat{a}_0(\omega_{p2}, L)\hat{a}_0^\dagger(\omega, L)\hat{a}_0^\dagger(\omega_{p1} + \omega_{p2} - \omega, L). \tag{5.3}$$

Going to the second order in η allows the possibility of having a pair converted back into a single photon, which occurs with probability η^2, but the forward single photon conversion efficiency is unchanged. Going to the third order in η then lowers the single photon conversion efficiency to $\eta - 2\eta^2 + \eta^3$. This allows us to define the error due to taking the gain to first order as $2\eta^2$. Thus we find that the first-order approximation causes deviation less than 2×10^{-6} for conversion efficiency $\eta = 0.1\,\%$, and less than 0.02 for a single photon conversion efficiency up to $\eta = 10\,\%$.

When the efficiency approaches 1, higher-order development is necessary to describe the interaction correctly. In principle, η could have an arbitrarily large value by increasing the strong pump power. When η goes beyond 1, it can no longer be interpreted as a probability of conversion, and we must solve the exact operator evolution. As noted in [119], Rabi-like oscillations will occur between the pump photon state and the signal/idler pair state, and the higher the η, the more oscillations will occur in the fibre.

5.2.2 Conversion efficiency for a single-photon input

The conversion efficiency of a single photon into a pair can now be derived from eq. (5.2). The spectral density of the photons created is given by

$$n_{\mathrm{d}}(\omega, L) = \left\langle \psi \left| \hat{a}_0^{\dagger}(\omega, L) \hat{a}_0(\omega, L) \right| \psi \right\rangle . \tag{5.4}$$

The quantum state $|\psi\rangle$ is the input state of the weak pump and generated photon pairs. For a single-photon pump 2, $|\psi\rangle = |1\rangle_{p2} |0\rangle_s |0\rangle_i$, where we label the lower frequency half of the output pair spectrum *idler*, and the higher half *signal*. The total number of photons generated is then given by the integral of the spectral density over the output spectrum. Putting eq. (5.2) into eq. (5.4) gives the photon-number spectral density

$$n_{\mathrm{d}}(\omega, L) \quad = \quad 4\gamma^2 P_1 \frac{\hbar \omega_{p2}}{2\pi} L^2 \mathrm{sinc}^2 \left(\frac{KL}{2} \right) \tag{5.5}$$

where the generation of a photon at frequency ω implies the generation of its pair photon at frequency $\omega_{p1} + \omega_{p2} - \omega$.

Let us now find the total number of photon pairs generated out of a single photon. If both pumps are pulsed simultaneously with a spectral width $\delta\omega_p$ and transform-limited pulse length $T = \frac{2\pi}{\delta\omega_p}$ (the only regime with significant conversion probability), the total number of photon pairs generated per pulse is

$$\begin{aligned} N_{\text{pairs/pulse}} &= \frac{1}{2}\int d\omega n_{\text{d}}(\omega, L) \\ &= 4\gamma^2 P_1 P_2 L^2 \frac{\Delta\omega_s}{\delta\omega_p} \\ &= 4\gamma^2 P_1 \frac{\hbar\omega_{p2}}{2\pi} L^2 \Delta\omega_s, \end{aligned} \tag{5.6}$$

with

$$\Delta\omega_s = \frac{1}{2}\int d\omega \text{sinc}^2\left(\frac{K(\omega_{p1}, \omega_{p2}, \omega)L}{2}\right) \tag{5.7}$$

and $P_2 = \frac{\hbar\omega_{p2}}{T}$, where the factor 1/2 in the first line is due to the spectrum covering both signal and idler frequencies, leading to double counting. The integral is over the whole spectral range except the two pump frequencies $\omega_{p1,p2}$.

The number of generated photon pairs per second is thus

$$\begin{aligned} N_{\text{pairs/sec}} &= f_{\text{rep}} \times 4\gamma^2 P_1 P_2 L^2 \frac{\Delta\omega_s}{\delta\omega_p} \\ &= 4\gamma^2 P_{1\text{avg}} P_2 L^2 \frac{\Delta\omega_s}{2\pi}, \end{aligned} \tag{5.8}$$

where $P_1 = \frac{P_{1\text{avg}}}{f_{\text{rep}}} \times \frac{\delta\omega_p}{2\pi}$ and f_{rep} is the repetition rate of the source.

Finally, the single photon conversion efficiency can be defined for a weak pump of N_{p2} photons as $\eta = \frac{N_{\text{pairs}}}{N_{\text{p2}}}$. When $N_{\text{p2}} = 1$, the conversion efficiency as given by eq. (5.6) is

$$\eta = \frac{N_{\text{pairs}}}{N_{\text{p2}}} = 4\gamma^2 P_1 \frac{\hbar\omega_{p2}}{2\pi} L^2 \Delta\omega_s. \tag{5.9}$$

5.3 Noise from Raman scattering

Raman scattering is a non-parametric nonlinear optical process involving optical photons and molecular-vibration phonons (see chapter 8 of [211]). Spontaneous Raman scattering converts pump light to frequencies 1 THz to 50 THz away from the pump, producing unwanted noise photons in the signal and idler modes [212] as shown in fig. 5.2. A pump photon with frequency ν_p interacts with a molecular vibration mode, adding or subtracting the frequency of the molecular transition ν_m from the photon and destroying or creating a phonon respectively. Scattering to longer wavelengths is called Stokes scattering, with output photon frequency $\nu_p - \nu_m$, and to shorter wavelengths anti-Stokes, with output photon frequency $\nu_p + \nu_m$. The spectrum of Raman scattering is commonly called a gain spectrum due to the use of Raman scattering in amplifiers, and is determined by the spectrum of material phonon transitions (see sec. 14.3D of [74]). Though Raman scattering in the amorphous materials that make up optical fibres is broadband, it often exhibits regions with little gain within a few THz from the pump, and certainly has little gain beyond 50 THz. Because Stokes scattering transfers energy from photons to the material, it is much more likely to occur than anti-Stokes scattering, which relies on thermal excitations in the material to add energy to the photons.

Thus strategies emerge to reduce the impact of Raman scattering on photon pair generation. Because thermal excitations in the material are governed by the Boltzmann distribution which decays exponentially with increasing energy, anti-Stokes scattering is exponentially suppressed far from the pump [213]. By contrast, Stokes scattering decays slowly far from the pump. Thus it is important for the single-photon four-wave mixing scheme to choose the wavelength of the strong pump to be longer than the signal and idler's as in fig. 5.3, meaning the main Stokes portion of the Raman gain spectrum does not overlap the photons' spectrum and can be removed by filtering. Engineering phasematching that occurs far from the pump is also important to make spectral filtering possible [214]. Cooling the fibre additionally exponentially suppresses anti-Stokes scattering, important for this pumping scheme, and partially suppresses Stokes scattering near the pump [145, 215, 216].

In fig. 5.2 I show the result of calculations of Raman scattering in a silica fibre, as a function of wavelength and temperature. The Raman spectrum is based on a model of vibrational modes from [217], which is then scaled in wavelength [218], pump power [148], temperature [219], and fibre parameters to obtain the final spectrum. The code for calculating Raman scattering is reproduced in appendix C. In my experience this code reproduces

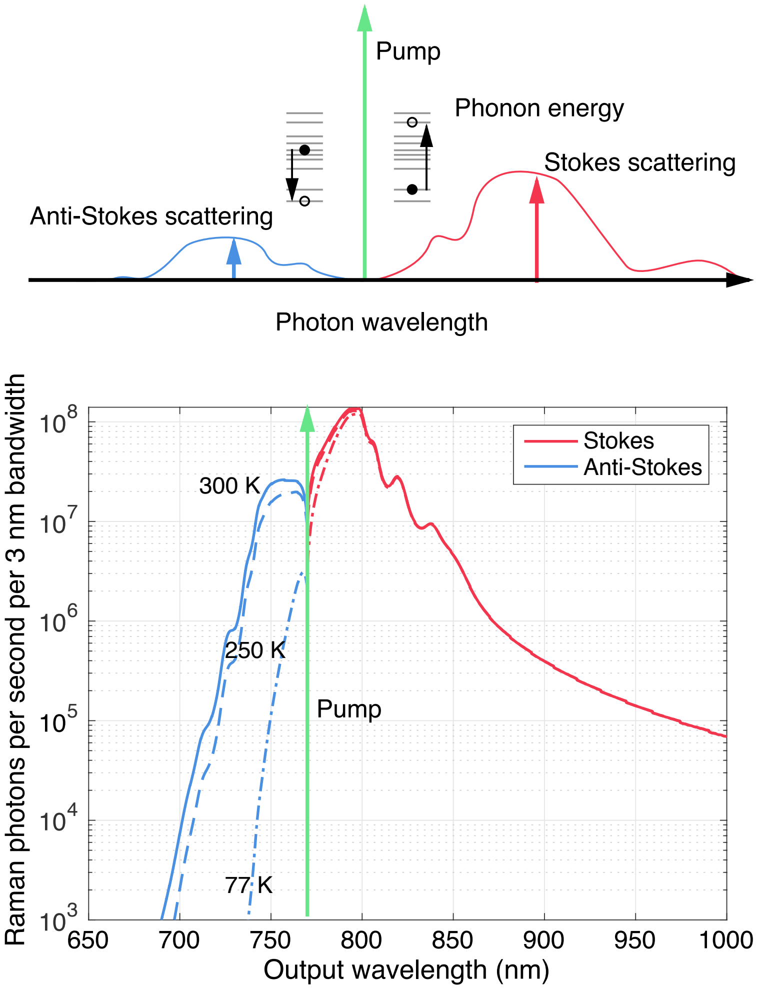

Figure 5.2: Schematic of Raman scattering and calculated Raman scattering in silica fibre. The diagram on top shows an overview of Raman scattering, wherein a photon is scattered to longer or shorter wavelength from a material vibration mode. Inset is the corresponding phonon transition in the material. The calculated Raman spectrum on the bottom is for a 26 cm long single-mode silica fibre of 6 µm core diameter with pump wavelength 770 nm and average power 30 mW. It shows the suppression of the anti-Stokes gain with temperature of the fibre (300 K, 250 K, and 77 K are the solid, dashed, and dot-dashed lines respectively) and distance from the pump, while the Stokes wave is suppressed with cooling only very close to the pump, and has a long tail to long wavelengths.

the correct dependence of Raman scattering on the relevant parameters, but does not exactly reproduce directly measured spectra, due to the difficulty in matching vibrational models to real amorphous materials and noise contributions from other sources in experiments. However, it does correctly calculate the number of background photons in the idler mode in chapter 6.

In experiments, Raman scattering can have a large or small effect depending on the wavelength arrangement, phasematching, material, and temperature [220]. For silica, collecting photons >100 nm from the pump leads to a high signal-to-noise ratio, as I show in chapter 6. In section 7.2 I show a measured Raman scattering spectrum in a chalcogenide microwire, and discuss how to achieve a high signal-to-noise ratio in that system.

5.4 Candidate fibres for maximizing conversion efficiency

In this section we compare three fibre types with unique methods of phasematching to find the best for single-photon conversion. The parameters that can be tuned to maximize conversion efficiency

$$\eta = 4\gamma^2 P_1 \frac{\hbar\omega_{p2}}{2\pi} L^2 \Delta\omega_s \tag{5.10}$$

are nonlinearity $\chi^{(3)}$ and mode area A_{eff} through γ, length L, phasematching bandwidth $\Delta\omega_s$, and peak power P_1 of the strong pump. Since γ is squared, decreasing A_{eff} and increasing $\chi^{(3)}$ will have the greatest effect. By contrast, conversion efficiency appears quadratic in the length of fibre L, but the signal and idler bandwidths given by eq. (5.7) will vary approximately with $1/L$, giving an overall linear dependence on fibre length. The spectral width $\Delta\omega_s$ can also vary independent of L from tiny ($\delta\omega$) to hundreds of nanometres, depending on the pump configuration, and most importantly on the type of phasematching chosen.

We examine three methods of phasematching in optical fibres: birefringence, operation near a zero-dispersion wavelength (ZDW), and nonlinear phasematching using self-phase modulation. The phasematched frequencies generated by the use of birefringence are spectrally narrow and highly tunable. The frequencies phasematched around the ZDW or due to nonlinear phase modulation can have a broader spectrum, and are centered around or near the ZDW. We compare the potential for single photon conversion in three different fibre types corresponding to those three types of phasematching, and find the optimal parameters to maximize pair generation.

The phase mismatch, with $\beta(\omega)$ the propagation constant in the fibre, is

$$K = \beta(\omega) + \beta(\omega_{p1} + \omega_{p2} - \omega) - \beta(\omega_{p1}) - \beta(\omega_{p2}) + \gamma P_1. \tag{5.11}$$

It can be expressed using a Taylor expansion of the propagation constants (see eqs. 2.3.23 and 10.3.6 of ref. [211]) around the central frequency $\omega_0 = \frac{\omega_{p2}+\omega_{p1}}{2}$ of

$$\beta(\omega) = \beta_0 + (\omega - \omega_0)\beta_1 + \tfrac{1}{2}(\omega - \omega_0)^2\beta_2 + \tfrac{1}{6}(\omega - \omega_0)^3\beta_3 + \tfrac{1}{24}(\omega - \omega_0^4)\beta_4, \tag{5.12}$$

with the dispersion coefficients given by

$$\beta_i(\omega_0) = \left(\frac{\partial^i \beta(\omega)}{\partial \omega^i}\right)_{\omega_0}. \tag{5.13}$$

Thus, since $\omega_{p1} + \omega_{p2} - \omega - \omega_0 = \omega_0 - \omega$ and $\omega_{p2} - \omega_0 = \omega_0 - \omega_{p1} = \frac{\omega_{p2}-\omega_{p1}}{2}$, and dropping the argument of the β_i until the last line,

$$\begin{aligned}
K(\omega) &= \beta_0 + (\omega - \omega_0)\beta_1 + \tfrac{1}{2}(\omega - \omega_0)^2\beta_2 + \tfrac{1}{6}(\omega - \omega_0)^3\beta_3 + \tfrac{1}{24}(\omega - \omega_0)^4\beta_4 \\
&\quad + \beta_0 + (\omega_0 - \omega)\beta_1 + \tfrac{1}{2}(\omega_0 - \omega)^2\beta_2 + \tfrac{1}{6}(\omega_0 - \omega)^3\beta_3 + \tfrac{1}{24}(\omega_0 - \omega)^4\beta_4 \\
&\quad - \big(\beta_0 + (\omega_{p1} - \omega_0)\beta_1 + \tfrac{1}{2}(\omega_{p1} - \omega_0)^2\beta_2 + \tfrac{1}{6}(\omega_{p1} - \omega_0)^3\beta_3 + \tfrac{1}{24}(\omega_{p1} - \omega_0)^4\beta_4\big) \\
&\quad - \big(\beta_0 + (\omega_{p2} - \omega_0)\beta_1 + \tfrac{1}{2}(\omega_{p2} - \omega_0)^2\beta_2 + \tfrac{1}{6}(\omega_{p2} - \omega_0)^3\beta_3 + \tfrac{1}{24}(\omega_{p2} - \omega_0)^4\beta_4\big) \\
&= (\omega - \omega_0)^2\beta_2 + \tfrac{1}{12}(\omega_0 - \omega)^4\beta_4 - \left(\tfrac{\omega_{p2}-\omega_{p1}}{2}\right)^2\beta_2 - \tfrac{1}{12}\left(\tfrac{\omega_{p2}-\omega_{p1}}{2}\right)^4\beta_4 + \gamma P_1 \\
&= (\Omega^2 - \Delta\omega_p^2)\beta_2(\omega_0) + \tfrac{1}{12}(\Omega^4 - \Delta\omega_p^4)\beta_4(\omega_0) + \gamma P_1,
\end{aligned} \tag{5.14}$$

with the offset frequency $\Omega = \omega - \omega_0$ and the pump offset $\Delta\omega_p = \frac{\omega_{p2}-\omega_{p1}}{2}$.

Two schemes can be considered when the pump wavelengths are nondegenerate as required for single-photon FWM: external pumping, with generation of new wavelengths in between the pump wavelengths and $|\Omega| < |\Delta\omega_p|$, or internal pumping, with generation of new wavelengths to the exterior and $|\Omega| > |\Delta\omega_p|$. We focus on external pumping as illustrated in fig. 5.3 because, assuming the strong pump has the highest wavelength, it allows filtering the main Raman noise from the strong pump as this will be at higher wavelengths still. However, the large separation in pump wavelengths can lead to temporal walk-off between the pump pulses in the fibre, reducing efficiency. This effect is mitigated by situating the pumps symmetrically about the ZDW.

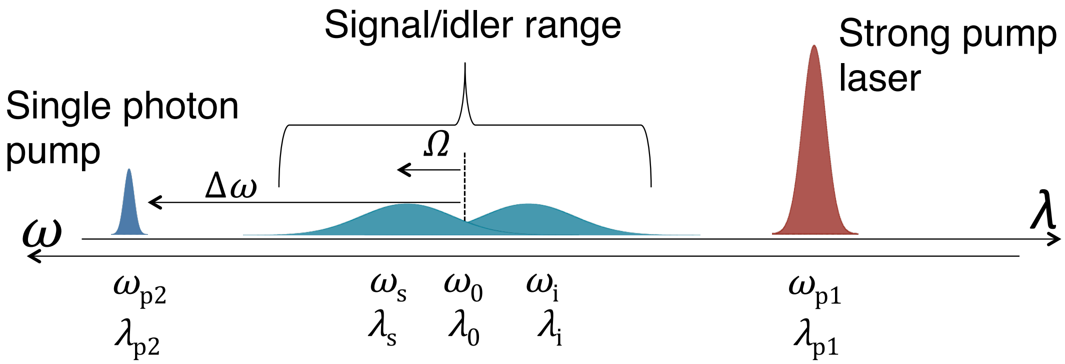

Figure 5.3: Arrangement of pump and signal/idler wavelengths (amplitudes and widths not to scale). The main source of noise, spontaneous Raman scattering from the strong pump, will occur to the far right of this figure, allowing its removal by spectral filtering.

5.4.1 Polarization-maintaining fibre: birefringent phasematching

Standard polarization maintaining (PM) fibre exhibits a birefringence large enough to achieve phasematching some dozens to hundreds of terahertz from the pumps (~100 nm) [214]. These fibres are commercially available, with lengths up to kilometres, and spatially uniform. The phasematching is easy to obtain and widely tunable by tuning the pump wavelengths. Further, the birefringent phasematching means that the photon pairs can come out with opposite polarizations from the pumps, enabling polarization filtering of the pumps and associated Raman noise. However, the relatively large core size leads to a modest waveguide nonlinear parameter of $\gamma = 4.6 \times 10^{-3}\,\mathrm{W}^{-1}\,\mathrm{m}^{-1}$ in our example below.

We consider the two pumps co-polarized along the fast axis and the generated signal and idler polarized along the slow axis, which gives total phase mismatch

$$\begin{aligned} K(\Omega) &= \beta_2(\omega_0)\left(\Omega^2 - \Delta\omega_p^2\right) + \frac{\beta_4(\omega_0)}{12}\left(\Omega^4 - \Delta\omega_p^4\right) \\ &\quad + \gamma P_1 + 2\omega_0 \frac{\delta n}{c}, \end{aligned} \tag{5.15}$$

where the birefringence $\delta n = n^{slow} - n^{fast}$ is written separately from the dispersion coefficients. Far from the ZDW ($\beta_2 \gg \beta_4, \gamma P_1$), the phasematched frequencies are

$$\Omega^2 = -\frac{2\omega_0}{\beta_2(\omega_0)}\frac{\delta n}{c} + \Delta\omega_p^2. \tag{5.16}$$

We consider a silica PM fibre with birefringence $\delta n = 3 \times 10^{-4}$ (e.g. Panda PM630), and take both pumps pulsed with 80 MHz repetition rate and 5 ps duration. We take a 5 W average power for the strong pump, and a single photon for the weak pump. The walk-off length between the two pump pulses in this configuration being 18 cm, we consider an 11 cm fibre which gives an effective interaction length of $L = 10\,\mathrm{cm}$.

With the strong pump at 890 nm and the weak pump at 660 nm, we obtain a signal and idler phasematched at 728 nm and 790 nm with spectral width $\Delta\omega_s = 7\,\mathrm{rad\,THz}$ (2 nm), as shown in fig. 5.4. The conversion efficiency given by eq. (5.10) is $\eta = 2 \times 10^{-8}$, well below that achievable in $\chi^{(2)}$ media. We plot the signal and idler spectral density (photons per (rad Hz) per pulse) in fig. 5.4, accurate to the precision of our frequency space mapping, $\delta\omega_p = 1.3\,\mathrm{rad\,THz}$ (0.5 nm, given by the width of the grey lines on the graph).

5.4.2 Microstructured fibre: phasematching near the zero-dispersion wavelength

Phasematching occurs in a fibre near the ZDW when the material and waveguide contributions to dispersion cancel. We will take the example of silica microstructured fibres, which

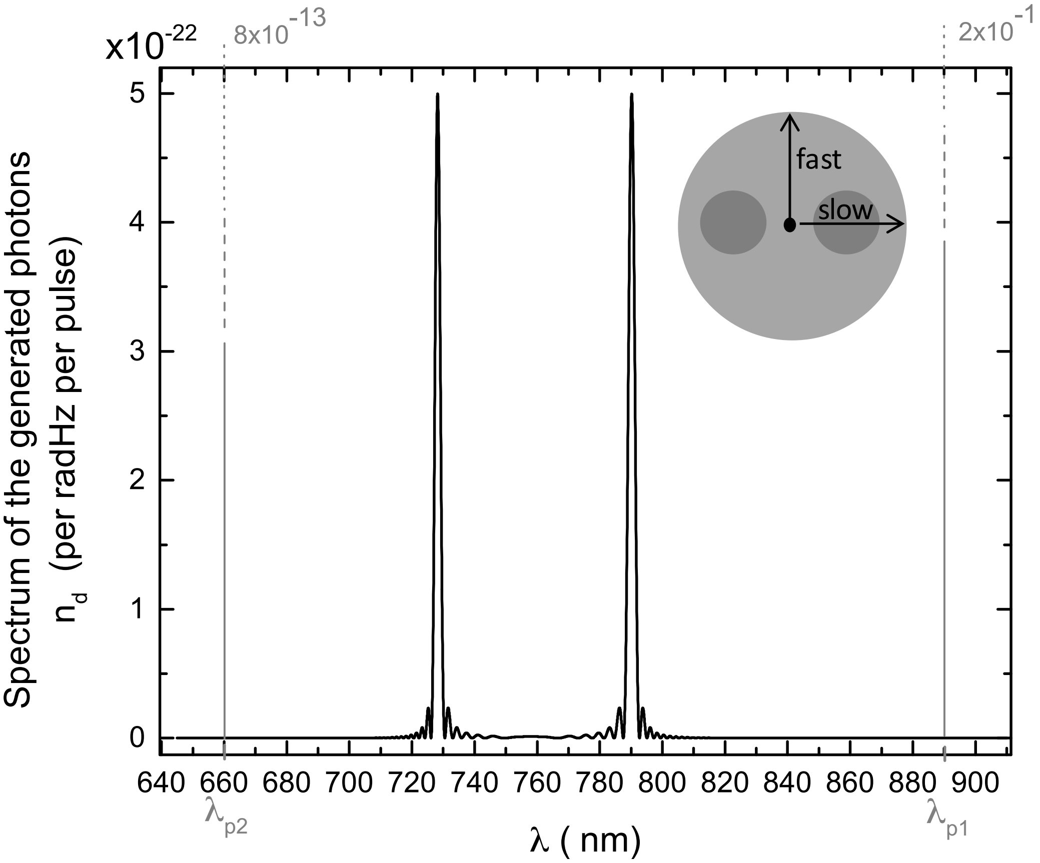

Figure 5.4: Calculated phasematching for four-wave mixing in polarization-maintaining fibre. Converting a single photon to a pair via FWM is possible in principle using a PM fibre, but the very narrow phasematching limits the efficiency to $\eta = 2 \times 10^{-8}$ in this example. The quasi-monochromatic pump wavelengths are represented by grey lines of width 1.3 rad THz with values labeled above the graph (well above the y-axis shown), while the generated signal and idler spectra are the black lines in the centre. A cross-section of a "Panda" PM fibre is shown in the inset, with stress rods providing the birefringence around the core and its fast and slow axes labeled.

are commercially available and can be fabricated to exhibit a ZDW in the visible and telecom ranges. The microstructured fibres (also called photonic crystal fibres) we consider have a solid silica core surrounded by a lattice of air holes [221]. They are made by stacking glass capillary tubes and melting them together, then drawing a fibre out of the melt [222]. The interest in such a fibre is that the high index contrast between the silica core and air-hole cladding allow the core to be much smaller than regular single-mode fibres. This increases the waveguide nonlinear parameter, e.g. up to $\gamma = 2.7 \times 10^{-2}\,\mathrm{W}^{-1}\,\mathrm{m}^{-1}$ in our example, with lengths up to a few metres [223]. The spectral broadness of the phasematching depends on the length considered, and is only tuneable in a small range once the ZDW is chosen.

We model a microstructured fibre with core diameter of 1.8 µm and air fraction 0.72 in the cladding, which give the ZDW at 716 nm. The wavelengths and the pump powers are altered slightly from the previous example to achieve phasematching. We take a 1 W average power for the strong pump in a 2 m long fibre, with 2 ps long pump and single photon pulses at 80 MHz repetition rate. As a consequence of working near the ZDW, we must keep the strong pump power lower than in PM fibre to avoid noise from self-phase modulation. Additionally, the walk-off length is now over 100 m, since the pumps have approximately the same propagation constant β on either side of the ZDW. The single photon frequency is at wavelength 676.75 nm and the strong pump is now at 760 nm. Simulations give a much broader spectrum for the signal and idler (around 160 rad THz, fig. 5.5), and consequently the efficiency, still given by eq. (5.10), is now up to $\eta = 4 \times 10^{-4}$. Even including filtration of the generated photons between 686 nm and 750 nm to allow pump removal, this efficiency is four orders of magnitude better than the PM fibre.

However, this method of phasematching is very sensitive to core diameter and pump wavelengths. For example, a 0.5 nm deviation of pump wavelength changes the output spectral shape completely and, even if still phasematched, may give no pairs at the centre of the spectrum. Additionally, obtaining a 2 m microstructured fibre with good uniformity for the whole length is not straightforward; some variations in the core diameter will occur, deteriorating the perfect phasematching.

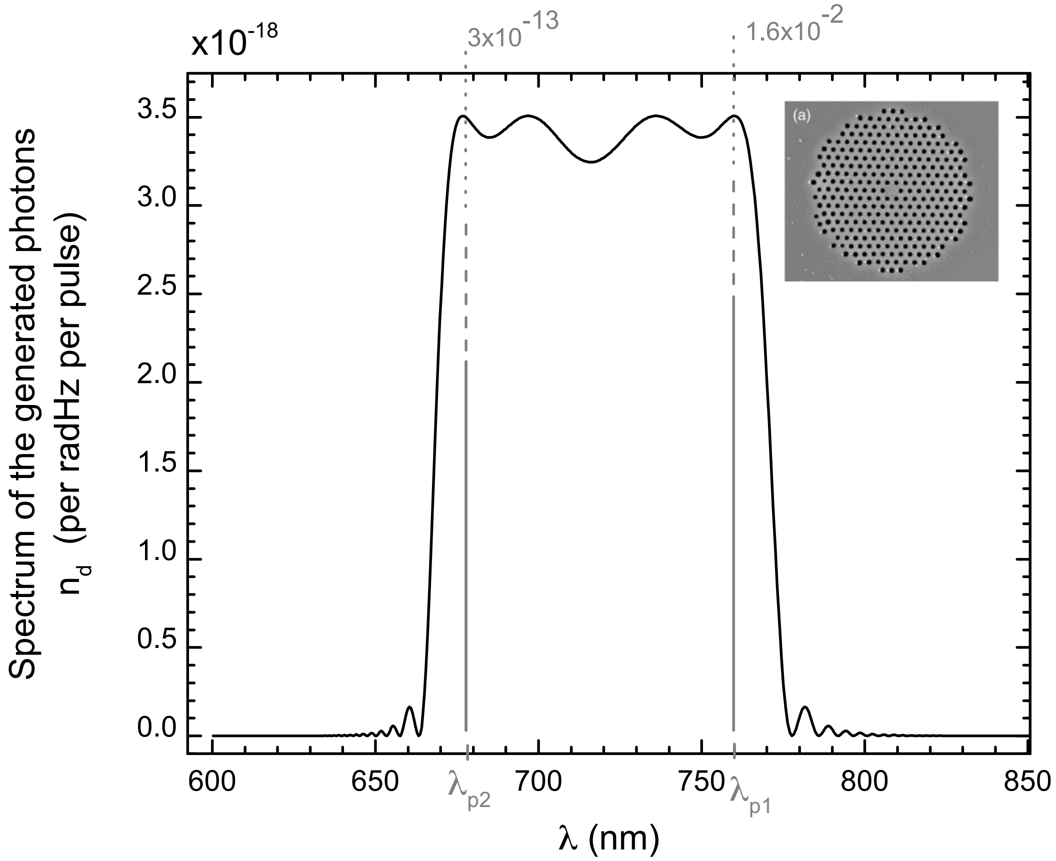

Figure 5.5: Calculated phasematching for four-wave mixing in microstructured fibre. A much broader signal and idler spectrum is obtained near the ZDW using a microstructured fibre. Even after filtering between 675 nm and 760 nm to remove noise photons near the pumps, the efficiency $\eta = 4 \times 10^{-4}$ over the remaining signal/idler range is four orders of magnitude larger than for the PM fibre. The grey lines represent the pumps' wavelengths, widths (now 3.1 rad THz), and intensity as in fig. 5.4. Inset is a cross-section of an example microstructured fibre, which is reprinted with permission from [224]. © 2011 by the American Physical Society.

5.4.3 Chalcogenide microwire fibre: phasematching due to self-phase modulation

Achieving the best conversion efficiency requires ultrahigh nonlinearity and small cross-sectional area. These can be achieved by tapering fibres made of chalcogenide glass as in refs. [225, 226]. The chalcogenide glass As_2Se_3 has a $\chi^{(3)}$ nonlinearity three orders of magnitude larger than that of silica glass and core diameters in the tapered microwire region can be as small as 500 nm thanks to its large refractive index, while still maintaining good coupling to standard single-mode fibre and lengths beyond 10 cm. These microwires exhibit ultrahigh waveguide nonlinear parameters up to $\gamma = 180\,\mathrm{W^{-1}\,m^{-1}}$, and allow tuning the ZDW by controlling the microwire diameter.

This large γ directly leads to high conversion efficiency, but also allows nonlinear phasematching. As seen in eq. (5.14) it is possible to compensate for positive or negative linear phase mismatch by the nonlinear contribution γP_1 due to the strong pump self-phase modulation. The higher the dispersive mismatch, the higher the pump powers must be to compensate, so moderate pump powers still require working near the ZDW. In the external pumping configuration of fig. 5.3, the dispersion β_2 or β_4 has to be positive to compensate for self-phase modulation because the pump offset is greater than the frequency offset, i.e. $\Delta\omega_p^2 > \Omega^2$. The pump power necessary to reach perfect phasematching for degenerate photon pairs ($\Omega = 0$) is

$$P_1 = \frac{1}{\gamma}\left(\beta_2(\omega_0)\Delta\omega_p^2 + \frac{\beta_4(\omega_0)}{12}\Delta\omega_p^4\right). \tag{5.17}$$

For convenient operation with all wavelengths in the telecommunication band and to avoid the two-photon absorption at short wavelengths in As_2Se_3 [227], we take the example of the FWM scheme pumped at 1480 nm by the single photon and at 1620 nm by the strong pump. The two fields are pulsed at 80 MHz with 2 ps pulse duration. The fibre considered is similar to the samples described in [226]. A fibre diameter of 0.555 µm for the microwire gives a dispersion coefficient at 1550 nm of $\beta_2(\omega_0) = 0.05\,\mathrm{ps^2\,m^{-1}}$, and β_4 is negligible. Phasematching is achieved for 0.8 W peak power, which corresponds to an average power of only 0.13 mW. Simulation of the spectral density is given in fig. 5.6 in a

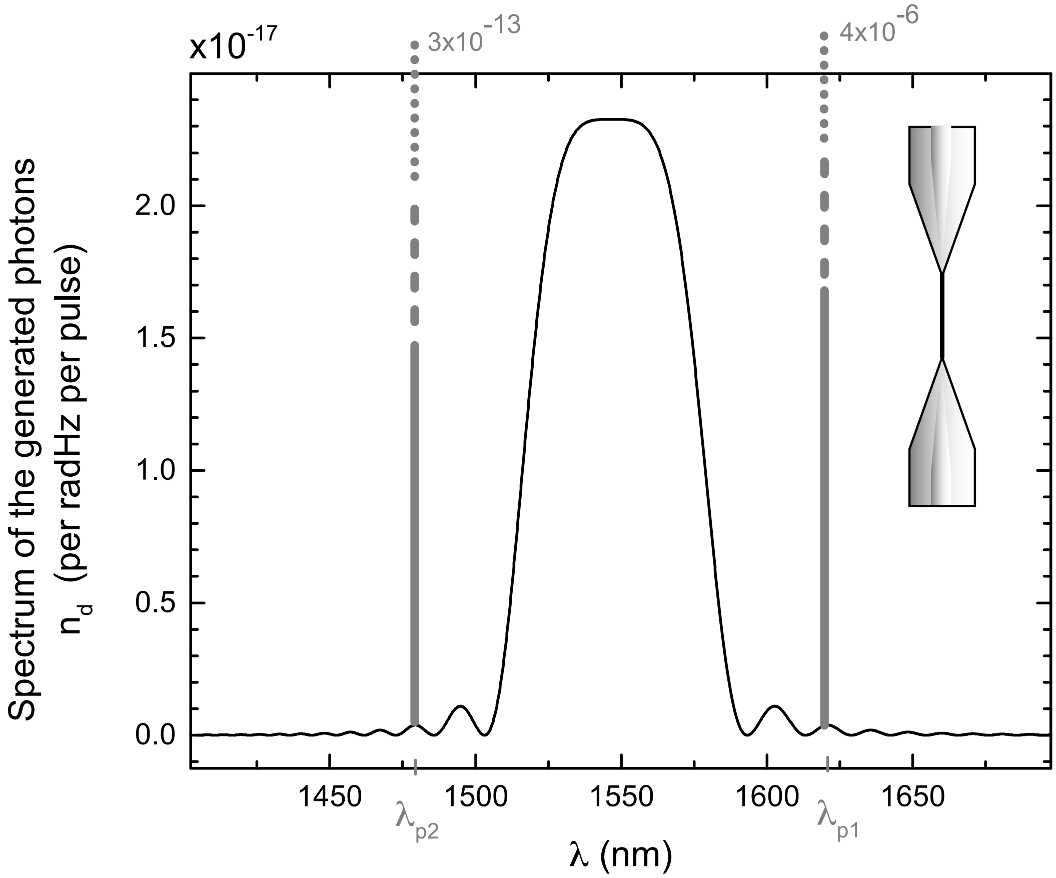

Figure 5.6: Calculated phasematching for four-wave mixing in chalcogenide microwire. Due to high intrinsic $\chi^{(3)}$ and strong confinement, the chalcogenide microwire gives the highest conversion rate, with an efficiency of $\eta = 1.1 \times 10^{-3}$. The grey lines represent the pumps' wavelengths, widths (3.1 rad THz), and intensity as in fig. 5.4. An illustration of the tapered microwire is inset.

Fibre type	Strong pump avg. power (mW)	Conversion efficiency η	Photon pairs per second
Birefringent (silica)	5000	2×10^{-8}	1.6
Microstructured (silica)	1000	4×10^{-4}	32,000
Microwire (As_2Se_3)	0.13	1×10^{-3}	80,000

Table 5.1: Summary of expected single-photon-to-pair conversion efficiency and strong pump power required for the three fibre types considered: birefringent silica fibres, microstructured silica fibres, and chalcogenide As_2Se_3 microwires. Considering the 80 MHz repetition rate and inputting one photon per pulse, we also calculate the expected number of pairs produced per second.

10 cm long microwire section, where the walk-off length between the two pump pulses is now so large as to be effectively infinite. The high intrinsic $\chi^{(3)}$ of the chalcogenide and the strong confinement allows a conversion efficiency of $\eta = 1.1 \times 10^{-3}$. However, as in the silica microstructured fibres, caution must be taken in filtering the desired photons, since high nonlinearity means high Raman noise, large phase modulation broadening, and other undesired interactions such as degenerate FWM from the strong pump.

5.5 Conclusion

We have predicted a promising result in the conversion of single photons into pairs via four-wave mixing. As shown from our simulations based on evolution of the quantum field operators, conversion efficiencies up to 0.1 % should be achievable in chalcogenide microwires. The results in the three types of fibres we modelled are summarized in table 5.1.

In this work, the low gain approximation is sufficient for applications in generating large entangled states and photon heralding, though a non-perturbative approach keeping all orders of gain would make for an interesting study and allow exploring the deterministic pair generation $|1\rangle_{p2} \to |11\rangle_{si}$ and oscillatory $|1\rangle_{p2} \to |11\rangle_{si} \to |1\rangle_{p2} \to \ldots$ regimes. However, finding a material enabling photon conversion with an efficiency high enough to justify this non-perturbative approach remains a challenge.

Interestingly, neither the derivation nor value of the conversion efficiency we found depend on the single photon being quantized: the same conversion efficiency can be obtained by assuming a classical pulse with the same input peak power as the single photon. This implies there is no new quantumness in this process, beyond the well-established spontaneous generation of pairs in standard spontaneous FWM or SPDC.

In implementations, caution must be paid to the various sources of noise possible: degenerate FWM and spontaneous Raman scattering [216] from the strong pump, and even second orders or combinations of these effects.

Chapter 6

Experiments toward single-photon four-wave mixing: entangled photons from PM fibre

This chapter is based on an experiment begun at Institut National d'Optique and completed in Waterloo in 2012. Due to the relationship between photonic qubit precertification and entangled photon pair generation (section 1.3.3), it is important to demonstrate an architecture capable of both. Though birefringent fibres do not offer a large conversion probability as seen in section 5.4, they are convenient for generating entangled pairs, as we show in this chapter.

Statement of contributions: BL, LKS, and TJ conceived the experiment. VR, JPB, and I began the experiment at INO; I finished it in Waterloo. VR provided code to simulate phasematching in fibres and performed the cross-splice. I collected and analyzed the data, and wrote the paper with input form all authors. The content of this chapter was published in Optics Express in condensed form as [142]:

E. Meyer-Scott, V. Roy, J.-P. Bourgoin, B. L. Higgins, L. K. Shalm, and T. Jennewein. Generating polarization-entangled photon pairs using cross-spliced birefringent fibers. *Opt. Express*, **21**:6205–6212, 2013. © 2013 Optical Society of America

I am allowed by the policies of Opt. Express and by permission from my co-authors to republish this work here.

6.1 Introduction

Many tasks in quantum information, such as loophole-free tests of Bell's inequality [14], long-distance quantum cryptography [25], quantum metrology [228], and integrated quantum information processing [229], require the generation and detection of entangled photon pairs with high efficiency. While recent advances using superconductors have led to detectors with efficiencies over 90 %, these detectors require the photons to be fibre-coupled or integrated with a waveguide [162, 230]. Simple low-loss and integrable sources of entangled photons remain a challenge. Sources based on spontaneous parametric down-conversion in bulk crystals, where a pump photon splits into two daughter photons, are challenging to couple into single-mode fibre. Much work has recently focused on using the process of four-wave mixing to create entangled photon pairs directly in fibre [144]. Current sources either require interferometric stability, have excess noise, or suffer from losses in bulk optical components. Here we present a fibre source of entangled photons that is simple, stable, integrable with all-fibre components, and is well-suited for carrying out a wide variety of quantum information processing tasks.

To generate entanglement (or to precertify photonic qubits), two processes distinct in some degree of freedom must interfere. One of the most successful sources of entangled photon pairs uses two nonlinear crystals back-to-back with their optic axes rotated 90° with respect to one another (fig. 1.7(c)) [132]. The interference between the possibility of down-conversion in the first or second crystal, upon which the polarization of the photon pairs depends, leads to the creation of an entangled polarization state between the two photons. Inspired by this "sandwiched" cross-crystal source, we have devised a cross-spliced source[1] using four-wave mixing in birefringent polarization-maintaining (PM) fibre. In the fibre, two pump photons can spontaneously interact to produce a pair of photons

---

[1] Following the trend of culinary nomenclature, we informally refer to our cross-spliced source as a "sausage" source.

labeled signal and idler. The signal and idler photons possess the same polarization, perpendicular to that of the pump photons. To create entanglement, we take two PM fibres, rotate them 90° with respect to one another, and splice them together. Pump photons polarized at 45° with respect to the fibre axes will be equally likely to generate photon pairs in either fibre section, leading to the creation of the polarization entangled state $|\phi\rangle = (|HH\rangle + e^{i\phi}|VV\rangle)/\sqrt{2}$, where H and V are horizontal and vertical polarizations respectively. This single-path geometry permits direct fibre splicing to the output, is interferometrically stable, and allows the source to be compact. In comparison, other schemes for generating entangled photon pairs in fibre require polarization stabilization [150, 231], suffer from losses and imperfections in the optical components needed to interfere the polarizations of the photons [151, 232], or produce photons very close to the pump leading to unwanted Raman noise [233]. Approaches based on a fibre Sagnac loop are promising [234] but prone to imperfect interference on the beam-splitter and temporal walk-off due to beam splitter birefringence [146].

To create the signal and idler photons through four-wave mixing, energy and momentum must be conserved. Energy conservation is satisfied when the sum of the frequencies of the two pump photons equals the sum of the signal and idler frequencies. In our scheme, momentum conservation, or phasematching, is engineered using the birefringence in our PM fibres [235]. PM fibres can support vector phasematching wherein the pump is polarized on the slow axis of the fibre and the outgoing signal and idler photons on the fast axis [149, 214, 236, 237]. This form of phasematching is intrinsically narrowband and has the signal and idler photons located spectrally far from the pump (~100 nm or ~50 THz) [235]. This reduces the noise from Raman scattering, which extends about 15 THz on either side of the pump but has a long tail on the low-frequency side [212] that can dramatically degrade the heralding efficiency (probability of detecting signal (idler) photon given an idler (signal) detection) and entanglement fidelity. An additional benefit is that two-photon states free of frequency correlations can be created in PM fibres by controlling only the fibre length and pump bandwidth [214], or by pumping with two different wavelengths [238]. These spectrally pure photon states are critical for multi-photon interference experiments and for quantum computing protocols, as otherwise tight inefficient spectral filtering of the photon pairs is needed. Using a similar phasematching scheme, heralded (unentangled) photons with a purity of up to 84 % [239] have been demonstrated.

6.2 Phase compensation

In our cross-spliced source, photons produced in the first fibre will be partially distinguishable from those produced in second. This distinguishability is due to the poor temporal overlap caused by additional dispersion that photons generated in the first fibre experience in the second. Please see also appendix D for temporal calculations and further analysis, including different compensation arrangements and measurements of birefringence. It is convenient to reframe this temporal problem as a spectral one: the phase ϕ in the maximally entangled state $|\phi\rangle = (|HH\rangle + e^{i\phi}|VV\rangle)/\sqrt{2}$ becomes wavelength-dependent due to the different effective fibre lengths seen by different spectral components [240, 241]. This leads to a mixture over the pump and output signal bandwidths [2] of the form

$$\rho = \int\int |\phi\rangle\langle\phi| p_{\mathrm{s}}(\lambda_{\mathrm{s}}) p_{\mathrm{p}}(\lambda_{\mathrm{p}})\, \mathrm{d}\lambda_{\mathrm{s}} \mathrm{d}\lambda_{\mathrm{p}}, \tag{6.1}$$

where $p_{\mathrm{p}}(\lambda_{\mathrm{p}})$ and $p_{\mathrm{s}}(\lambda_{\mathrm{s}})$ describe the spectra of the pump and signal respectively, and $\lambda_{\mathrm{p/s/i}}$ is the wavelength of the pump/signal/idler. Equation (6.1) is not describing the spectral components of the output photon state but, rather the effective two-qubit state given the spectral dependence of the phase ϕ. To produce high-quality entanglement we must find and compensate for this spectral dependence.

We assume the two fibre segments have the same length L and that the first fibre has its slow axis vertical such that $|HH\rangle$ photon pairs are produced first. These photons acquire an extra phase

$$\phi_1(\lambda_{\mathrm{s}}, \lambda_{\mathrm{p}}) = \frac{2\pi L}{\lambda_{\mathrm{s}}}\left[n(\lambda_{\mathrm{s}}) + B\right] + \frac{2\pi L}{\lambda_{\mathrm{i}}}\left[n(\lambda_{\mathrm{i}}) + B\right] \tag{6.2}$$

in the second length of fibre, where (from energy conservation) $\lambda_{\mathrm{i}} = \lambda_{\mathrm{s}}\lambda_{\mathrm{p}}/(2\lambda_{\mathrm{s}} - \lambda_{\mathrm{p}})$, $n(\lambda)$ is the propagation constant on the fast axis in the fibre, and B is the birefringence between

---

[2] Due to energy conservation, the phase dependence on the idler wavelength is fully determined by the signal and pump wavelengths.

the fibre's fast and slow axes. Additionally, the $|VV\rangle$ term acquires a phase

$$\phi_2(\lambda_{\mathrm{p}}) = 2\frac{2\pi L}{\lambda_{\mathrm{p}}}\left[n(\lambda_{\mathrm{p}})\right] \tag{6.3}$$

in the first stretch of fibre via the pump. This phase is double that of its counterpart for $\chi^{(2)}$ sources [240] because here two pump photons combine to make the $|VV\rangle$ photon pairs. There are no additional B terms in eq. (6.3) because the pump that will produce $|VV\rangle$ photons in the second stretch of fibre is polarized on the fast axis in the first stretch.

Finally, there is a nonlinear contribution to the $|VV\rangle$ phase term from self- and cross-phase modulation of the pump,

$$\phi_{2,\mathrm{NL}}(\lambda_p) = \left[1 + (2/3)\right]\gamma P L, \tag{6.4}$$

where γ is the fibre's nonlinear parameter and P is the pulse peak power. This contributes only a small offset in our pumping regime, but could become important at very short pulse length, high intensity, or for frequency-chirped pulses.

The total phase is then

$$\phi(\lambda_{\mathrm{s}}, \lambda_{\mathrm{p}}) = \phi_2 + \phi_{2,\mathrm{NL}} - \phi_1. \tag{6.5}$$

This phase is plotted in fig. 6.1 and displays a variation of 800° over the pump and signal bandwidths. To compensate this variation, birefringent crystals of appropriate length are introduced into the signal and idler output arms, adding two controllable phases to eq. (6.5). After optimizing, the compensators flatten the phase profile in fig. 6.1 (the edges of the phase profile are about 5° above zero). While we use quartz wedges with variable thicknesses, a production source could use precisely cut lengths of most any birefringent material. With $L = 13\,\mathrm{cm}$, the optimal total length of quartz is calculated to be 67.3 mm with slow axis vertical on the signal arm, implemented by rotating the polarization of the signal photons by 90°, and 47.6 mm with slow axis horizontal on the idler arm. This flattens the phase map sufficiently that no drop in entanglement fidelity is expected due to phase/temporal distinguishability.

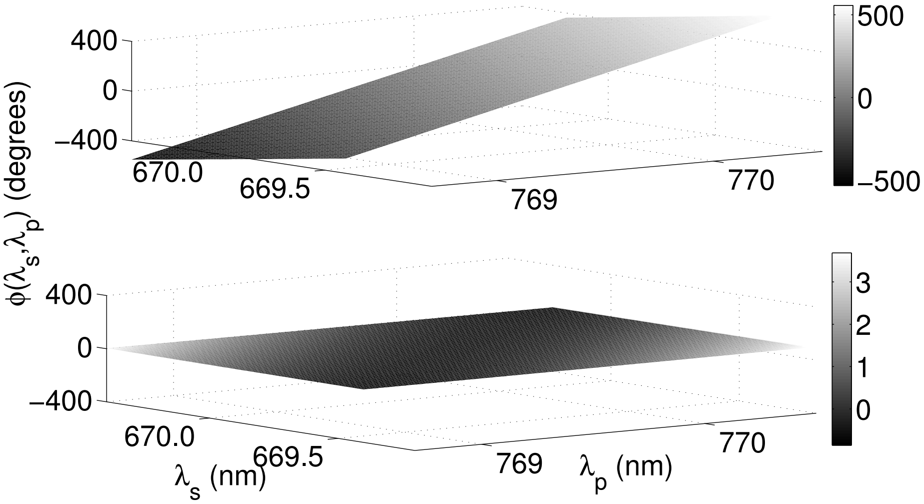

Figure 6.1: Calculated phase deviation around the mean phase, before (top) and after (bottom) compensation, versus signal and pump wavelengths. The shading also indicates the phase deviation, with drastically different scales before and after compensation. The strong phase change over pump and signal bandwidths in the uncompensated case leads to a highly mixed state, while the nearly flat map after compensation leads to a nearly pure entangled state. See appendix D for further analysis.

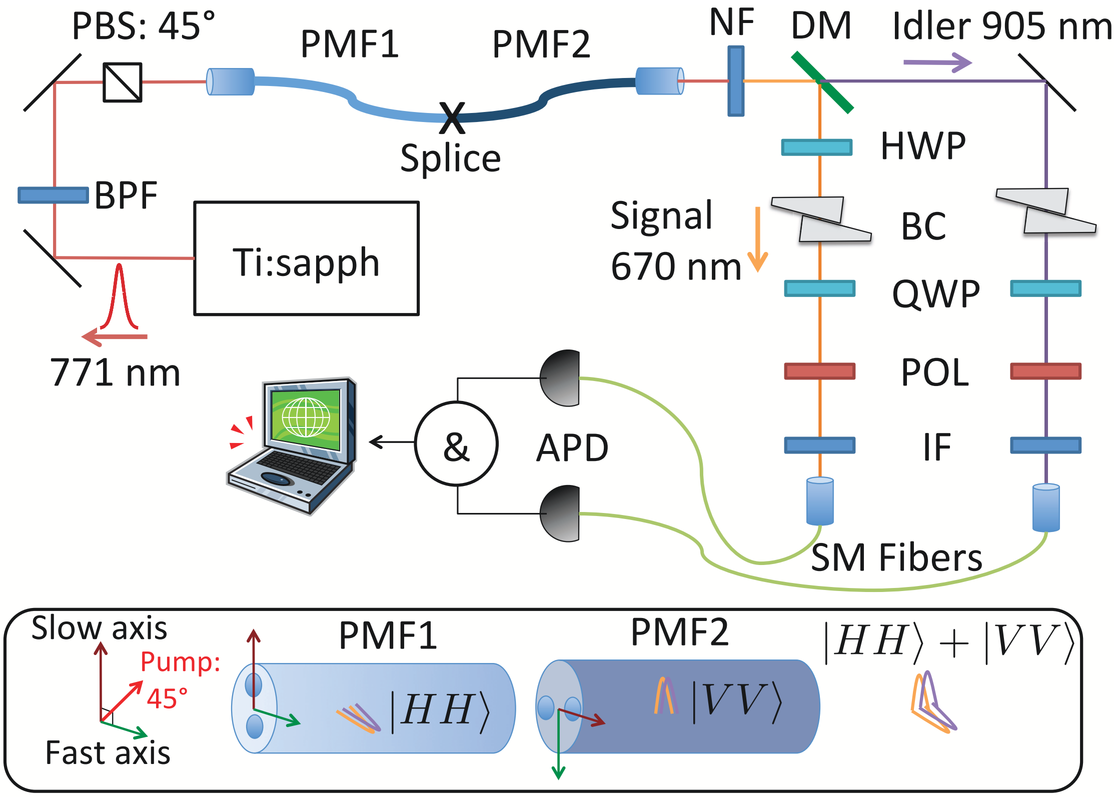

Figure 6.2: Experimental apparatus for the cross-spliced entanglement source. Pulses generated by the mode-locked Ti:sapphire laser pass though a bandpass filter (BPF) centred at 771 nm wavelength, then through a polarizing beam-splitter (PBS) oriented at 45°. This light is coupled into the cross-spliced fibres (PMF1 and PMF2) where entangled photon pair generation occurs via four-wave mixing. The pump is removed with a notch filter (NF) and the signal and idler photons are separated with a dichroic mirror (DM). The signal photon passes through a half-wave plate (HWP) and both photons are phase/time compensated with tuneable birefringent compensators (BC). The polarization correlations of the photons are analyzed with quarter-wave plates (QWP) and polarizers (POL) before photons pass through interference filters (IF) and are coupled into single-mode (SM) fibres. The photons are detected by silicon avalanche photodiodes (APD) and their detection and coincidence counts are registered by a timetagging module (&), then recorded by a computer. Inset: illustration of the polarization axes of crossed-fibres and photon generation.

6.3 Experimental demonstration

The experimental apparatus is shown in fig. 6.2. The cross-splice process was carried out using an arc fusion splicer which provides automated alignment of the polarization axes of PM fibres (FSM-45PM, Fujikura Ltd.). The source is pumped with a mode-locked Ti:sapphire laser at 76 MHz repetition rate, 3 ps pulse length, and full width at half maximum bandwidth of 0.3 nm, with polarization set to 45°. It is crucial to include a bandpass filter on the pump beam before it enters the fibre to remove spontaneous emission from the Ti:sapphire crystal, which would pollute the photon pair signal. After photon generation in the two cross-spliced 13 cm sections of PM630-HP fibre, the pump light is removed with a notch filter providing 60 dB isolation. The half-wave plate in the signal arm flips the polarization of the signal photons by 90°, so that they are correctly compensated by the birefringent quartz crystals.

To characterize the output from the source, we collected signal and idler photons and sent them to an optical spectrometer and cooled CCD camera (SpectraPro 2750 and Spec-10-LN model 7508, Princeton Instruments). A sample spectrum is shown in fig. 6.3(a) where the signal and idler peaks are clearly identifiable, and far enough from the pump to avoid the bulk of the Raman noise. The phasematching curve in fig. 6.3(b) demonstrates the wide tunability of our source, with the idler photon ranging from the visible to telecom bands as the pump wavelength is changed. In this work, the 771 nm pump generates signal photons at 670 nm and idler photons at 905 nm, with full width at half maximum bandwidths of 0.23 nm and 0.61 nm respectively.

To count photon pairs, signal and idler photons exiting the source are split on a dichroic mirror, analyzed by a quarter-wave plate and polarizer, and filtered with an interference filter centered on 670 nm for the signal and 905 nm for the idler, each providing an additional 60 dB isolation from the pump. Photons are then coupled into SM780 single-mode fibre and sent to SPCM-AQ4C single photon detectors (Perkin-Elmer). By retuning the Ti:sapphire pump laser to the signal and idler wavelengths, we saw a total coupling efficiency from the PM fibre to the output of the single-mode fibre of 60 % and 69 %, respectively, including the notch filter, dichroic mirror, and birefringent compensators.

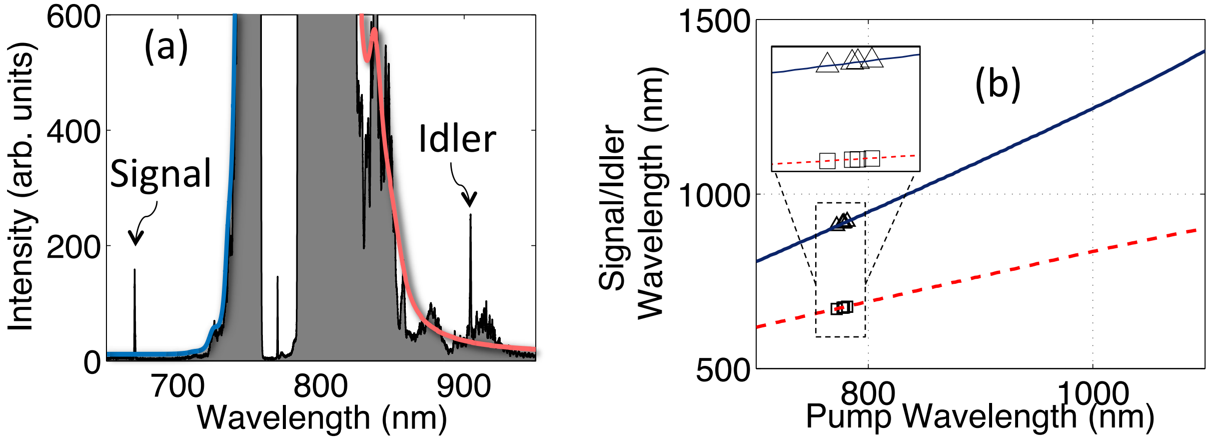

Figure 6.3: (a) Measured spectrum from our cross-spliced fibre source, showing narrowband signal and idler modes well away from the main Raman contamination, which extends beyond the vertical range shown. The calculated Raman spectrum using the code in appendix C is overlaid on the measured spectrum. Some residual pump in the centre of the notch filter is also visible. (b) Theoretical phasematching curves for signal (dashed red) and idler (solid blue) with measured points indicated by squares and triangles, respectively. A wide range of signal and idler wavelengths are available in PM fibre by tuning the pump wavelength. Other vector and scalar phasematching conditions exist (see e.g. [235, 236, 149]) but are not relevant here.

6.4 Performance of the cross-spliced source

As the number of double-pair emissions is negligible for our pump powers, we can determine the total heralding efficiency of the signal and idler photons. In 30 s with 30 mW pump power, we collected 488 350 total and 146 901 background signal counts; 1 657 630 total and 1 435 459 background idler counts; and 53 256 total and 55 background coincidence counts. Here there is a large contribution from Raman scattering to the idler background counts, calculated to be 1 694 400 from fig. 5.2. This slightly overestimates the Raman contribution, likely because it assumes a flat-top filter of bandwidth 3 nm, while the real filter in the idler mode has a more complex profile. This noise could be reduced experimentally with narrower filtering (see fig. 6.3, which shows that the narrowband idler photon is four times higher than the background), and by pushing the signal and idler farther from the pump by using fibres with more birefringence.

After subtracting background counts (due to Raman scattering, dark counts, and stray light) these results give heralding efficiencies of 24 % for the signal and 16 % for the idler, including detectors. This efficiency is limited mainly by our avalanche photodiodes, which have moderate detection efficiency especially at the idler wavelength. Additional losses are not intrinsic to the source, but are rather due transmission through bulk optics necessary in this first demonstration.

By measuring the heralding efficiency of $|HH\rangle$ and $|VV\rangle$ photon pairs separately, we can infer the transmission of the splice to be at least 93 % at the signal wavelength and at least 96 % at the idler wavelength.

To show that the source produces a viable entangled state, we measured both the timing and polarization correlations between photons. The timing histograms in fig. 6.4(a) quantify the arrival time of the idler conditioned on a signal photon detection, and clearly show a strong peak of coincident detections. At the highest power level it is possible to see accidental coincidences 13 ns (the laser repetition period) on either side of the main peak, but their relative strength is so low as to affect the entangled state negligibly. The coincidences-to-accidentals ratio for 50 mW average pump power is 110, based on a 1 ns coincidence timing window, and increases to 260 at 10 mW.

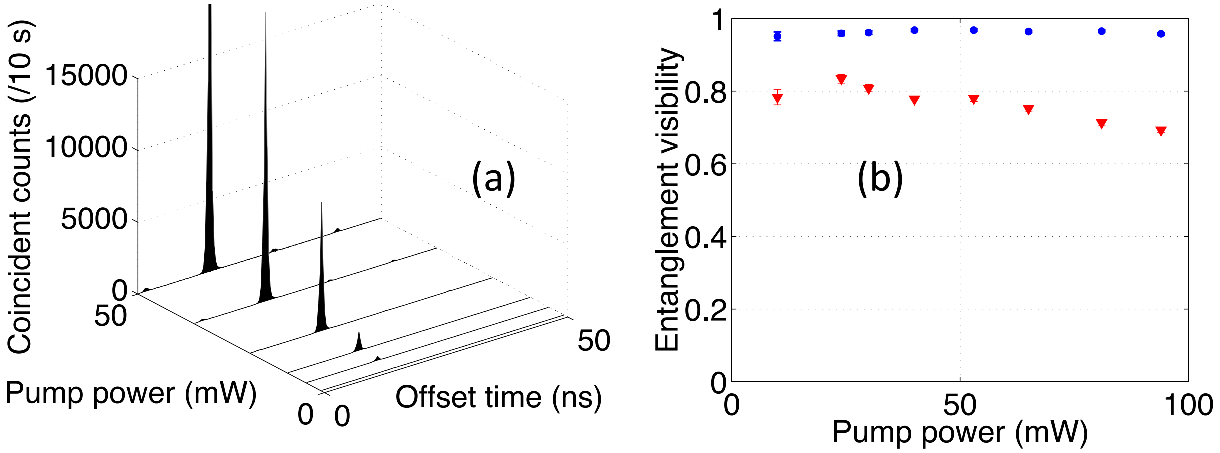

Figure 6.4: (a) Measured coincidence timing histograms, showing excellent timing correlation of signal and idler photons and negligible background. The 50 mW peak extends beyond the top of the graph, which has a shortened vertical scale in order to see accidental coincidences that occur regularly at the pump repetition period. (b) Dependence of entanglement visibility on average pump power, for rectilinear basis (blue circles) and diagonal basis (red triangles). Total visibility reaches a maximum around 30 mW pump power. Error bars are comparable to symbol size.

The entanglement visibility in fig. 6.4(b) is high for all power settings in the rectilinear basis (i.e. double-pair emissions remain negligible), but shows a degradation at high pump power in the diagonal basis. At high pump powers, we saw a noticeable broadening of the pump and therefore signal and idler spectra, due to self-phase modulation of the pump. This has the effect of distinguishing photons created in the first fibre segment from those created in second, since the pump is broader by the time it reaches second fibre, decreasing visibility in the diagonal basis. At low pump powers, the visibility also degrades due to noise from spontaneous Raman scattering, which is linear in pump power, compared to the quadratic response of four-wave mixing. Therefore, a pumping strength optimal for entanglement visibility emerges, which in our case is around 30 mW.

Pumping at 33 mW with a pair production rate in the fibre inferred to be 45 000 pairs/s, we took tomographic data to reconstruct the two-qubit density matrix of our entangled state, shown in fig. 6.5. Without any background subtraction or correction, the fidelity with the maximally entangled singlet Bell state $|\Psi\rangle = (|HV\rangle - |VH\rangle)/\sqrt{2}$ is 0.922 ± 0.002 and the tangle is 0.721 ± 0.008.

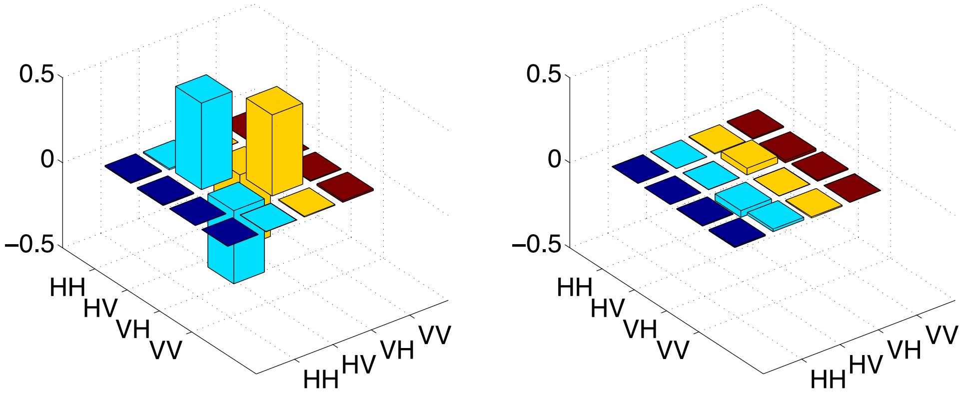

Figure 6.5: Real (left) and imaginary (right) parts of the two-qubit tomographically reconstructed density matrix of the photon pair produced by the source, showing fidelity with the maximally entangled state singlet state $|\Psi^-\rangle$ of 0.922 ± 0.002. The source produces this state instead of $|\Phi^-\rangle$ due to the polarization flip of the signal photon.

As an important point for integrability and coupling efficiency, the bulk pump laser, filters, dichroic mirror, and birefringent compensating optics could be replaced respectively by a fibre laser [242], fibre Bragg gratings [243], wavelength-division multiplexing, and birefringent fibre. These technologies have been heavily developed for the telecom band around 1500 nm and, as seen in fig. 6.3(b), the idler photon can be tuned to this regime, while development is ongoing for these fibre technologies in the visible spectrum. Replacing our bulk optics with in-fibre equivalents would greatly decrease reflection and coupling losses.

6.5 Conclusion

We have demonstrated a simple source of entangled photon pairs based on a single path of standard optical fibre. Splicing two stretches of PM fibre with rotated polarization axes allows high quality entanglement without problems of spatial mode overlap or stability. The source demonstrates narrowband photons (<1 nm), the possibility of wide tunability of output wavelengths, >60 % optical coupling efficiency to optical fibre networks, and fidelity with a maximally entangled state of 0.922. We experimentally verified that the quality of a regular fibre splice is sufficient for connecting independent four-wave mixing processes without degrading the entangled state. Thus we envisage future experiments with multiple fibre links to compensate dispersive broadening or walk-off, or a fibre version of a superlattice for spectral engineering [244]. With the goal of improving heralding efficiencies, future work could study the reduction of Raman noise through optimization of spectral filtering, fibre cooling, and novel pumping schemes [245]. The simplicity of our new photon source architecture is expected to drive use in upcoming experiments requiring integrable sources and narrowband, tuneable photons, as well as spur thought into the possibilities afforded by direct splicing of fibres for photon sources.

Chapter 7

Experiments toward single-photon four-wave mixing: efficient production of photon pairs

This chapter focuses on high-efficiency production of photon pairs in fibre media, as a path to increasing the conversion probability for photonic qubit precertification using four-wave mixing. In section 7.1 I show pair generation in microstructured fibres, which was soon surpassed by chalcogenide microwires in section 7.2, from an experiment performed in 2014.

Statement of contributions: AD, TJ, and I conceived the experiments, and AD and I performed them. RA, LL, and MR provided the chalcogenide microwires and related data. I collected and analyzed the data, and wrote the paper with input from all authors. The content of section 7.2 was previously published in Applied Physics Letters in condensed form as [197]:

E. Meyer-Scott, A. Dot, R. Ahmad, L. Li, M. Rochette, and T. Jennewein. Power-efficient production of photon pairs in a tapered chalcogenide microwire. *Appl. Phys. Lett.*, **106**:081111, 2015. © 2015 American Institute of Physics.

I am allowed by the policies of Appl. Phys. Lett. and by permission from my co-authors to republish this work here.

7.1 Photon pairs from microstructured fibres

As seen in section 5.4 microstructured fibres, compared to PM fibres, significantly increase the probability of converting one photon into two due to their small core size. The two-pump source of [119] in birefringent microstructured fibres allowed an inferred conversion efficiency of single photons to pairs of 3×10^{-9}, with the weak pump at 4.8 µW average power, well above the single-photon level. This was achieved for strong-pump average powers under 100 mW and employed narrowband birefringent phasematching, which limits conversion efficiency but demonstrates the principle of single photon conversion.

We investigated photon pair generation in microstructured fibres provided by INO. Figure 7.1 shows the phasematching obtained, measured by pumping with a tuneable, pulsed Ti:sapphire laser and sending the signal photon to a spectrometer. Fitting our calculated phasematching to the measured data returns the following fit parameters: core diameter $d = 1.353\,\mu\text{m}$ (made of solid silica), air filling fraction outside the core of 46.8 % [246], and birefringence 2.21×10^{-5} (difference between refractive indices of fast and slow axes). Unfortunately this fibre was not designed to be birefringent and had a quoted diameter of 2 µm, exemplifying the difficulty of controlling the parameters of microstructured fibres during fabrication. In other samples, we saw multiple phasematching peaks due to non-uniformities in the fibre, even in lengths as short as 1 m. Thus we look beyond microstructured fibres to materials and architectures with more nonlinearity and uniformity.

7.2 Highly efficient production of photon pairs in chalcogenide microwires

7.2.1 Introduction

Photon pair sources are the simplest and most abundant devices used to produce quantum entanglement [247], and are normally based on nonlinear optical effects that require large input light intensities for useful production rates. With highly efficient photon sources, it becomes possible to use spontaneous parametric down-conversion (SPDC) or four-wave

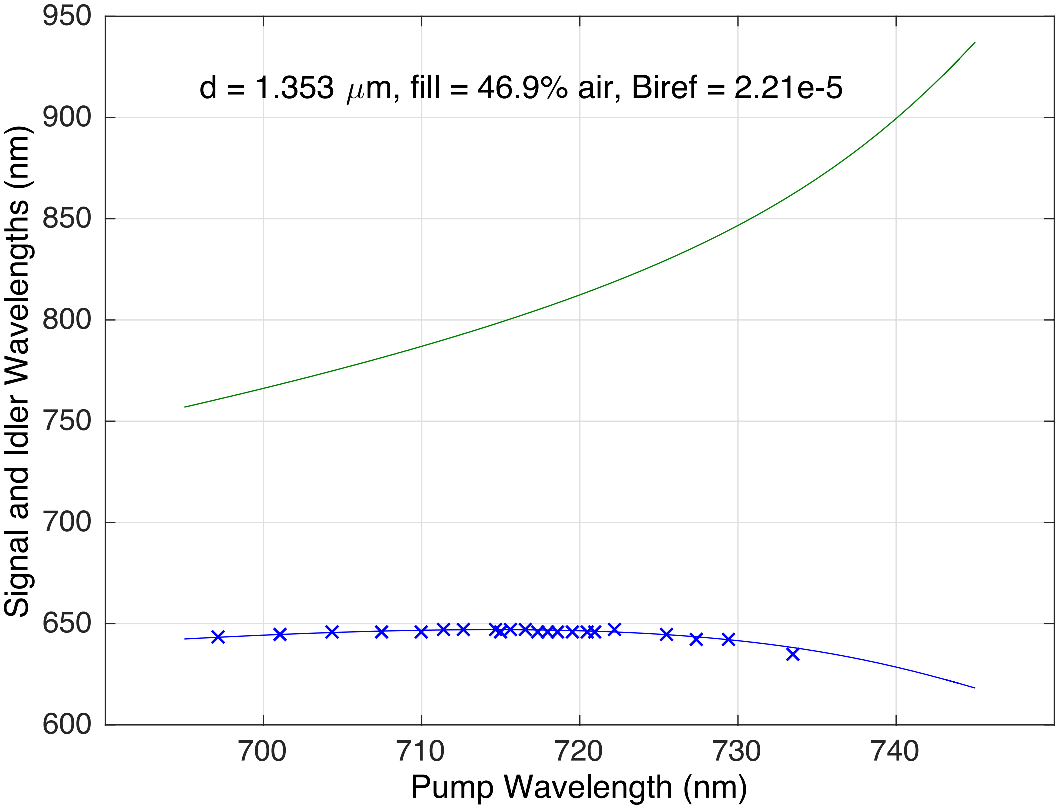

Figure 7.1: Measured signal wavelength (x markers), and fit (blue line) for a microstructured fibre with a nominal core diameter $d = 2\,\mu\text{m}$. The parameters returned from the fit are above the plot. The green line plots the corresponding idler wavelengths via energy conservation with the pump and signal wavelengths.

mixing (FWM) acting on *single* photons as pumps in later stages of quantum information experiments [248, 172], enabling advanced protocols like loophole-free Bell tests via photon precertification [120] and photonic quantum computing [119].

However, the conversion efficiency of one pump photon into a pair through SPDC in $\chi^{(2)}$ media has not substantially increased [208, 249] beyond 10^{-6}. Focus has shifted to developing efficient FWM in $\chi^{(3)}$ fibres and waveguides, using materials with large nonlinearities such as silicon [250] and chalcogenide glasses [251, 252], and also using resonator-enhanced processes [253, 254], atomic vapors [255], and microstructured silica fibres [119]. These would allow non-degenerate pumping using a single photon alongside a strong pump to produce pairs.

Unfortunately, none of these sources is ideally suited for converting single photons to pairs, and it remains a challenge to design the device that offers the highest efficiency with convenient operation and low noise. Silica devices cannot reach sufficiently high efficiency due to low nonlinearity [256], and though silicon exhibits much lower noise [257], it suffers from two-photon and free-carrier absorption [258], limiting the maximum useable pump power. Enhancing the nonlinearity through resonators or using atomic vapors requires the input photon to be narrowband, limiting the suitable types of initial sources for this photon.

Here we demonstrate production of photon pairs in tapered As_2Se_3 microwires, capable in principle of converting a broadband single photon into a pair with 10^{-3} probability [196], as shown in chapter 5. First we characterize the four-wave mixing properties of the microwires, then we produce photon pairs from degenerate pumping, and finally produce pairs from low-power non-degenerate pumps, as would be required for a single-photon-pumping experiment.

7.2.2 Chalcogenide microwire characterization

Our microwires, shown in fig. 7.2, combine a small cross-sectional area ($0.24\,\mu\mathrm{m}^2$) with large nonlinear coefficient ($n_2 = 1.1 \times 10^{-17}\,\mathrm{m}^2\,\mathrm{W}^{-1}$) [259] to produce a large waveguide nonlinear parameter ($\gamma = 188\,\mathrm{W}^{-1}\,\mathrm{m}^{-1}$), $\sim$100 000 times larger than standard silica fibres, and ten times larger than As_2S_3 chalcogenide waveguides [252]. Furthermore, in contrast to on-chip waveguides, microwires are drop-in compatible with existing single-mode silica fibre, are made with lengths up to tens of centimeters, and demonstrate low loss. Coupling to the microwire is accomplished by gluing standard single-mode fibre (SMF) to the chalcogenide step-index fibres on either side of the tapered region. A coating of poly(methyl methacrylate) (PMMA) increases the mechanical robustness and influences the phasematching properties of the microwires. Broadband phasematching of up to 190 nm bandwidth at telecommunication wavelengths has been shown using classical four-wave mixing [226].

The tapered fibre used in this work has a 12 cm long microwire with a diameter of 550 nm, with total insertion loss including pigtails of 10 dB. We estimate the breakdown of the losses as follows: inside the microwire, 5 dB due to sidewall roughness, absorption of the evanescent field by the polymer coating, and mode conversion in the tapering sections; at the SMF-chalcogenide interfaces, 0.5 dB per interface due to Fresnel reflection, and 2 dB per interface due to mode mismatch because the glued pigtails have been disrupted by transport. Losses per SMF-chalcogenide interface as low as 0.66 dB have been reported [225].

Figure 7.3 shows the phasematching profile of our microwire at ∼1550 nm, far from any zero-dispersion wavelength, for a degenerate pump (a) and for two non-degenerate pumps 13 nm apart (b). These data were obtained by pumping with continuous-wave lasers with 190 µW coupled power (inferred power inside the microwire after accounting for coupling losses) each. A seed laser is used to stimulate the four-wave mixing process, allowing characterization at powers well above the single-photon level. Thus three of the four waves are present at the input, and we measure the (macroscopic) power in the fourth wave at the output. For the degenerate case, the seed laser was scanned to the shorter wavelength side of the pump, and for the non-degenerate case, the seed was scanned between the two pump wavelengths, leaving a gap in the middle where the seed and signal cross over. In both cases the output signal was filtered through a dense-wavelength-division multiplexer (DWDM) and measured on a power meter. The values reported here have the DWDM losses factored out. Please see appendix B for plots of the transmission of the chalcogenide microwires and DWDMs.

We calculated the expected phasematching and power outputs from a standard four-

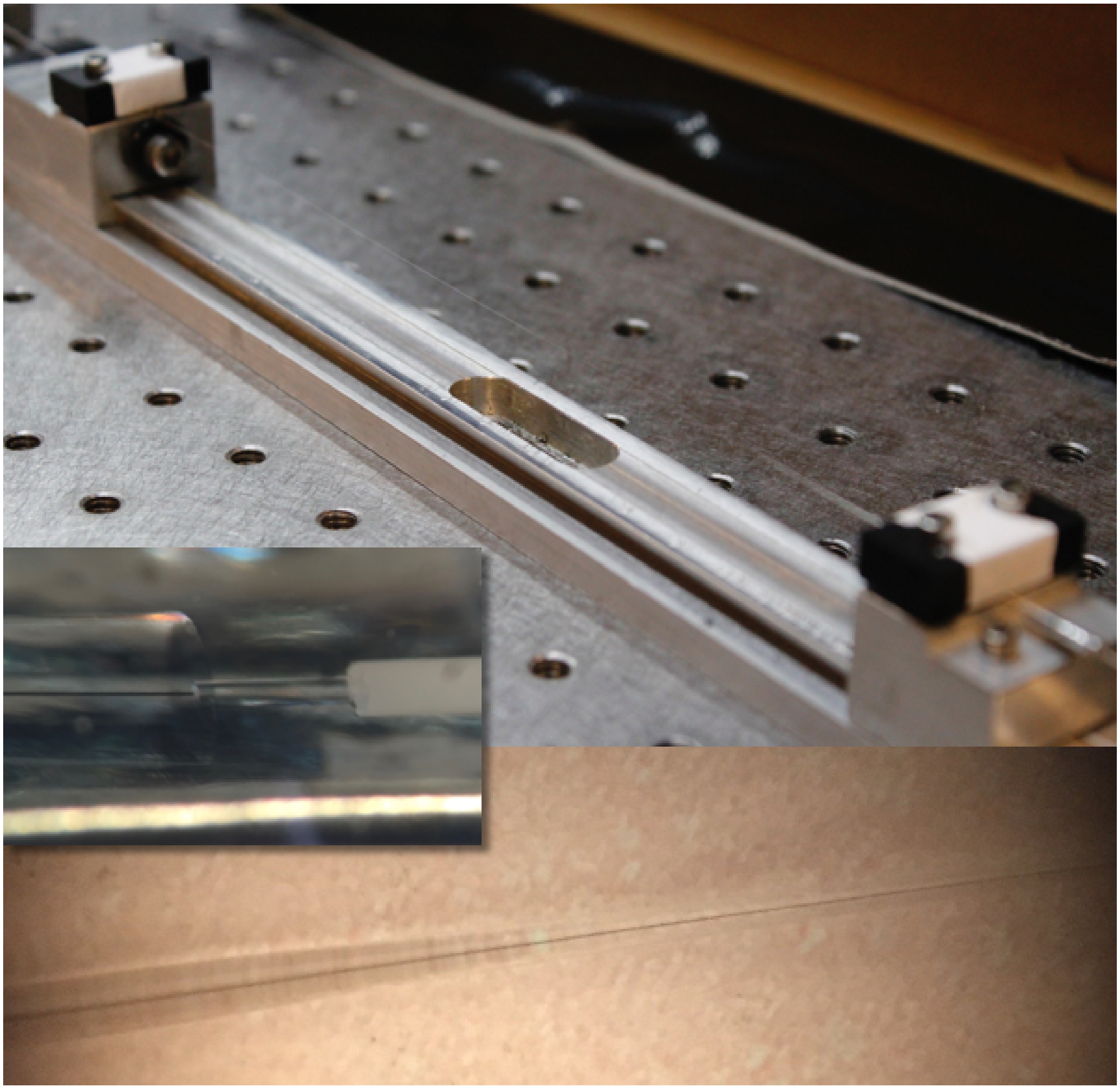

Figure 7.2: (top) Chalcogenide microwire suspended in its holder. (inset) Butt-coupling chalcogenide-PMMA fibre on the left to standard silica fibre on the right. (bottom) Tapering region of microwire, with dark chalcogenide core.

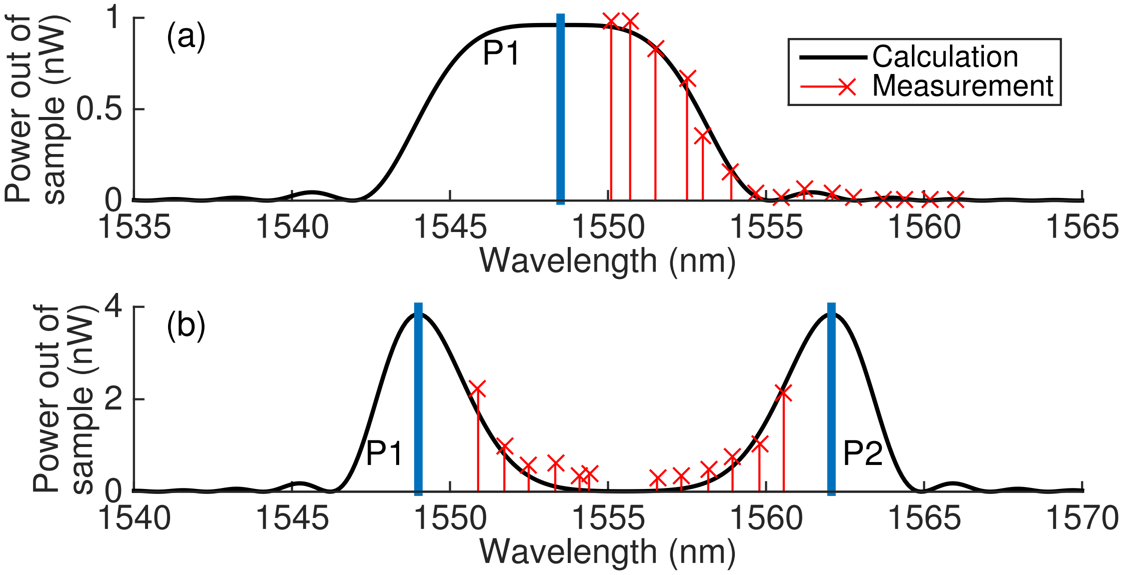

Figure 7.3: Measured phasematching in the chalcogenide microwire (red markers) for (a) degenerate pumping at 1548.5 nm and (b) non-degenerate pumping at 1549.0 nm and 1562.1 nm. The pumps P1 and P2 are marked with thick blue bars, and the phasematching calculated directly from sample parameters is given by the black lines.

wave mixing treatment [211], with the length, diameter, insertion loss, and nonlinear parameter as mentioned above, and calculated loss in the microwire [260] of 5.1 dB/m excluding tapering loss. In order to find the propagation constant and effective refractive index inside the microwire, we solved the characteristic equation for a step-index fibre with As_2Se_3 core [259] and PMMA cladding [261]. Even without fitting parameters, the phasematching calculations in fig. 7.3 agree with the measured data.

7.2.3 Production of photon pairs

Next we produced photon pairs using a degenerate pump, with the setup shown in fig. 7.4. The output of an optical parametric oscillator at 1553.33 nm with ∼4 ps pulse length and 76 MHz repetition rate was filtered through a DWDM and sent through the tapered chalcogenide microwire. The FWM output signal and idler photons were split into the 1550.12 nm and 1556.56 nm channels of a DWDM, and subsequently filtered in an arrayed waveguide grating (AWG) and DWDM respectively, giving total pump isolation of 118 dB and 122 dB (see appendix B). The signal photon was detected with a free-running InGaAs negative-feedback avalanche photodiode (NFAD) with 10 % detection efficiency and 100 dark counts per second [262], which gated an id201 InGaAs single-photon detector from IDQ SA for the idler photon, with 50 ns gate width and 20 % efficiency. The gate-out and detector channels from the id201 were recorded in a timetagger to either produce timing histograms between signal and idler, or to filter with a 2 ns timing window to record coincident counts.

The timing histograms in fig. 7.5 show the presence of photon pairs, as evidenced by a higher peak at the time delay of 22 ns than the background peaks at other time delays. At the lowest power, detector dark counts at random times become prominent, while at the highest power, accidental coincidences from multiple photon pairs make a large contribution to the noise. When the idler channel is moved to 1558.17 nm (black lines in fig. 7.5) such that photon pairs detected would not conserve energy and could not be from four-wave mixing, the peak at 22 ns falls to the same height as the others.

As seen in fig. 7.6(a), the number of pairs per pulse increases quadratically with pump power, with dropoff seen at high count rates due to the dead time of the NFAD detector. To compare with previous photon pair sources, we calculate the number of pairs produced

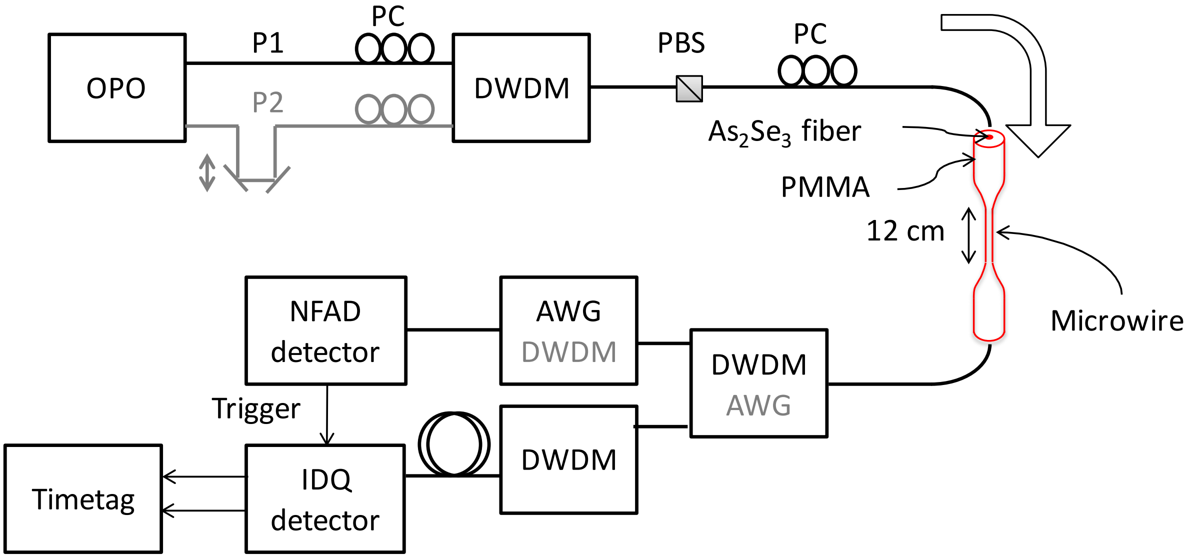

Figure 7.4: Experimental setup for the generation of photon pairs with a chalcogenide microwire pumped by one (P1, black) or two (P1 and P2, grey) beams from an optical parametric oscillator (OPO). For non-degenerate pumping, the two pumps were made to be copolarized with polarization controllers (PC) and a fibre polarization beam splitter (PBS). In both degenerate and non-degenerate cases a final PC sets the polarization entering the microwire. The pump and signal/idler beams were filtered by dense-wavelength-division multiplexers (DWDM) and an arrayed waveguide grating (AWG). The signal photon was detected by a free-running negative-feedback avalanche photodiode (NFAD) which gated the idler's single-photon detector (IDQ). Both signal and idler detection signals were recorded and timestamped by the timetag unit from Universal Quantum Devices, Inc.

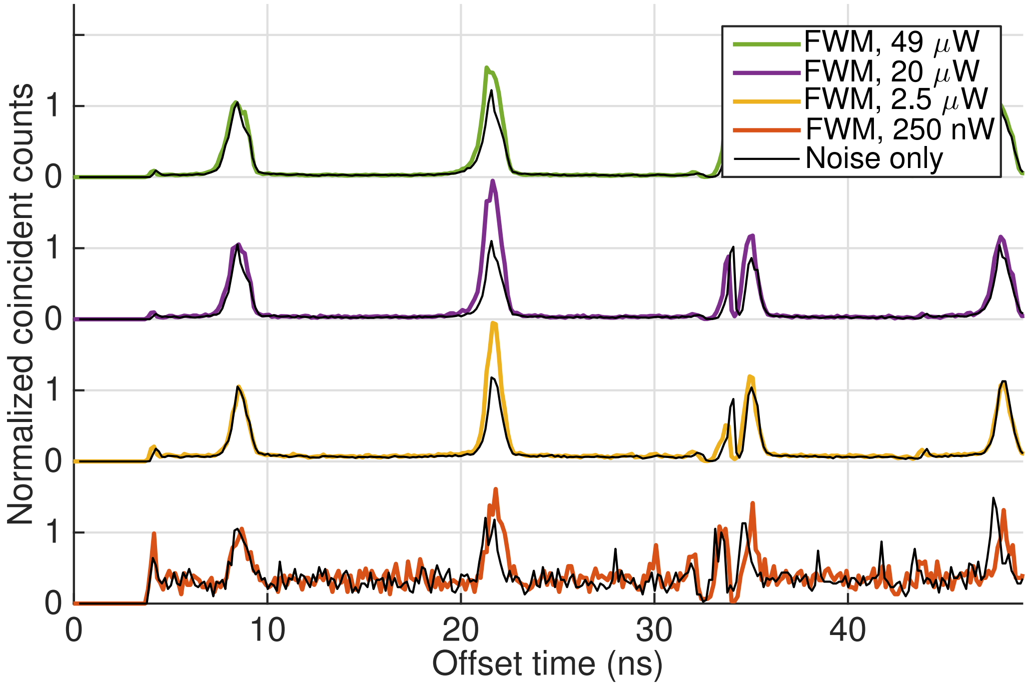

Figure 7.5: Measured timing histograms for photon pair production for coupled average pump powers of 49 µW, 20 µW, 2.5 µW, and 250 nW. The photon pairs appear in the peak at the time offset between signal and idler detection of 22 ns, which is higher than the accidental coincidence peaks from subsequent pump pulses at other delays. In all cases the accidentals peak height is normalized to 1. For the "noise only" measurement (black lines), the filter channels connected to the detectors did not conserve energy with the pump, leading to the disappearance of the legitimate photon pairs. The double peak at 35 ns could be due to the timing electronics in the IDQ detector or timetagger, but no events are lost.

per second, per nanometre of signal bandwidth, per milliwatt of average pump power as 2.5×10^8 pairs/s/nm/mW for the data point with 30 µW pump power. This is significantly above what is possible in $\chi^{(2)}$ crystals [263], and rivals the highest values reported in silicon [264]. Note that our filters had 0.5 nm bandwidth, and milliwatt pump powers are too large to avoid damage to the microwire.

In fig. 7.6(b), the coincidences-to-accidentals ratio reaches its maximum value of 2.13 ± 0.07 at a coupled pump power of 3.2 µW. This ratio is defined as $\mathrm{CAR} = C/A$, where C is the total number of coincident counts in the main coincidence peak and A is the number of accidental coincidences, and has a lower bound of $\mathrm{CAR} = 1$ for no timing correlation. At a coupled pump power of 490 nW, the CAR is 1.5 ± 0.2, and statistical significance increases with increasing pump power. Here the coincidences are collected at the 22 ns offset time of fig. 7.5, while the accidentals, which are due to detector dark counts, double-pair emissions from FWM, and Raman and other optical noise, are collected at 9 ns, which allows an estimation of the contribution of accidentals to the main coincidence peak. At low power, the CAR decreases due to the small number of real photon pairs compared to noise photons, and at high power, the CAR slowly decreases due to double-pair emissions from four-wave mixing. The fits to pair probability and CAR come from the FWM calculation described above, which feeds into a quantum-optical simulation including FWM, loss, detector models, and background counts measured with a continuous-wave pump. Here the pump pulse length inside the microwire is used as a fitting parameter and found to be 25 ps.

7.2.4 Nondegenerate pumping

In order to approach the regime of converting a single photon into a pair, the two pump photons absorbed in the FWM process must be non-degenerate in wavelength. Since FWM probability goes as the product of the pump peak powers, it is important that both pumps be synchronously pulsed, rather than continuous-wave. To demonstrate non-degenerate pumping, we took two outputs from an optical parametric oscillator, passing one through a trombone delay line to synchronize the pulses in the microwire as in the grey lines and text in fig. 7.4.

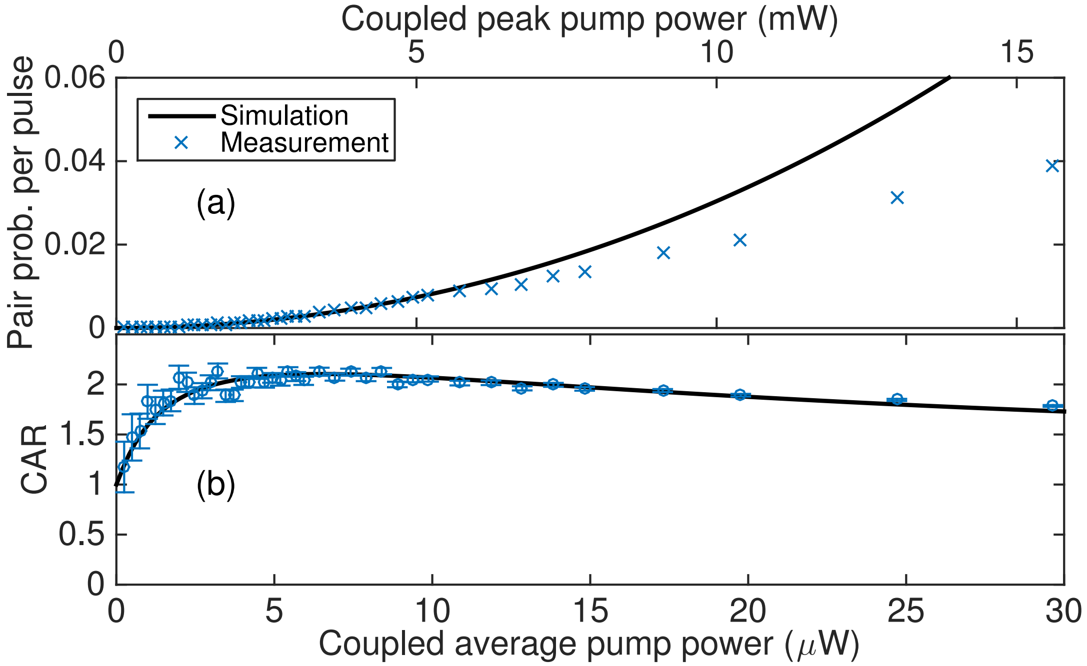

Figure 7.6: Pair probability per laser pulse with accidentals subtracted (a) and coincidences-to-accidentals ratio (b) as measured for degenerate-pumping FWM in our chalcogenide microwire. The curves are from a FWM simulation including measured background counts, with the pump pulse length inside the microwire as a fitting parameter. CAR > 1 indicates photon pairs are detected above the noise. Error bars are based on Poissonian uncertainty in photon counts (1σ), and are smaller than symbol size for (a). The x-axes on figures (a) and (b) coincide, with the top scale showing peak power and the bottom average power.

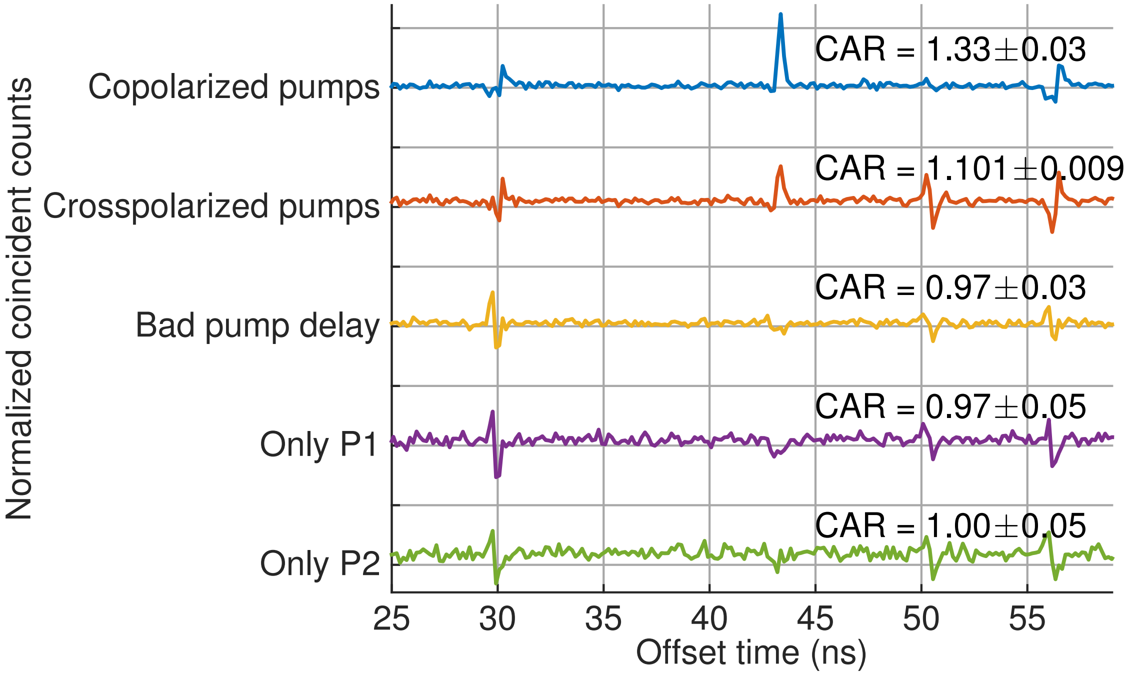

Figure 7.7: Measured timing histograms for photon pair production for non-degenerate pumping. The photon pairs appear in the peak at timing delay 43 ns only for the top two cases, with copolarized and crosspolarized pumps respectively, giving CAR > 1. In the other cases, where FWM is not expected, the peak at 43 ns vanishes and CAR $= 1$ within error. Here each dataset has had the background "noise only" counts subtracted.

To find evidence of photon pairs with non-degenerate pumping, we took timing histograms as shown in fig. 7.7. We present a number of different scenarios: co- and crosspolarized pumps, changing the delay between the two pumps so they do not overlap in the microwire, and removing either of the pumps. Only the first two cases, with the crosspolarized pumps producing 4/9 the number of pairs of the copolarized pumps [211], provide a peak at the proper delay after background subtraction, indicating these photons are due to non-degenerate FWM as desired. The maximum CAR for non-degenerate pumping was 1.33 ± 0.03 with 1.0 µW and 1.5 µW coupled powers of the two pumps, while the CAR for the lowest asymmetric pump power was 1.17 ± 0.06 with coupled pump powers of 480 nW and 1.5 µW.

Unfortunately due to bad phasematching (see fig. 7.3) these data are not as clear as the degenerate case. A more convincing measurement is one of coincidences and accidentals versus time delay between the two pumps, where photon pairs are produced only when the two pumps overlap, on top a constant background caused by spontaneous Raman scattering. In fig. 7.8, we show these data for P1 = 1551.72 nm, P2 = 1561.42 nm, and the signal and idler wavelengths 1554.13 nm and 1558.98 nm. The coincidence curve is a Gaussian fit to the data, and is fed into a quantum-optical FWM simulation that includes higher-order emission but no other nonlinearities (like cross-phase modulation or stimulated Raman scattering) to find the expected number of accidentals. The simulated accidentals agree with the data, indicating that the increased accidentals when the pumps overlap are due only to photon emission statistics of the FWM process.

To achieve in future the splitting of a single photon into two will require operating with a single-photon pump of 10 pW average power. Due to the narrow phasematching shown in fig. 7.3, we are currently forced to collect photon pairs in a wavelength region close to the pumps that is contaminated with noise (fig. 7.9). The lowest pump power for non-degenerate pumping with which we found CAR > 1 was 480 nW. Additionally, reaching 10^{-3} conversion efficiency [196] would require an average power for the other pump of 130 µW, whereas we found CAR > 1 for non-degenerate pump power only up to 3 µW. This does not mean that the high conversion efficiency cannot be achieved, but it requires moving the signal and idler much farther in wavelength from the strong pump to avoid noise and broadening their phasematching bandwidths to increase efficiency. By

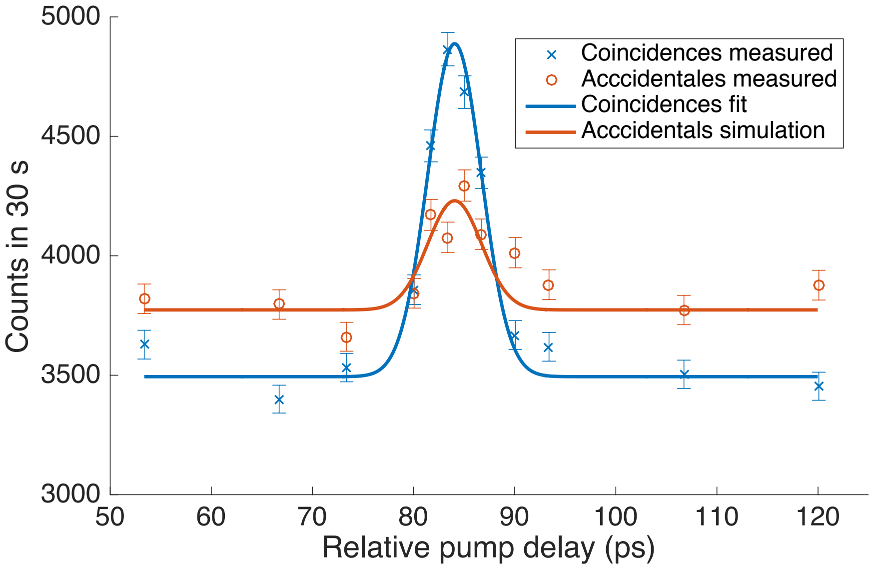

Figure 7.8: Measured coincident and accidental counts versus time delay between pump pulses for non-degenerate pumping. Photon pairs are only produced when the pumps overlap in the microwire; accidentals measured 13 ns (one pump period) later also increase as the pumps overlap due to multi-pair emissions. Here the accidentals are higher than the coincidences outside the peak because the accidentals were collected from a more efficient part of the IDQ detector's gate. The line on the coincidence data is a Gaussian fit which is fed into a FWM simulation to generate the accidentals curve.

carefully controlling core size and cladding material, it will be possible in future to fabricate microwires with engineered dispersion to reproduce broadband phasematching previously obtained [226]. If the current 0.5 nm photon bandwidth can be expanded to 40 nm, centered 100 nm from the pump, 80 times more efficient conversion is expected. These photon pairs would be produced in the Raman gain dips or even beyond the gain peaks, which would improve CAR drastically as shown in chalcogenide waveguides [265, 266].

7.2.5 Raman scattering

As seen in figs. 7.6 and 7.7, the ratio of coincidences to accidentals in our experiment is rather low. This is largely due to Raman scattering in the region where we collect photons, very close to the pumps. Figure 7.9 shows the measured Raman scattering spectrum for our chalcogenide micowire, pumped by a continuous-wave laser at 1550 nm and 1 mW coupled power. Since Raman scattering depends on average power rather than peak power, using a continuous-wave pump with low peak power allows us to isolate the Raman scattering from the self-phase modulation and four-wave mixing processes, which depend on peak power. The Raman gain is large near the pump, then shows two minima ±40 nm from the pump [259], two gain peaks ±60 nm from the pump, and low gain beyond ±80 nm from the pump.

Using the data in fig. 7.9, we can find the contribution of Raman scattering at other pump powers and phasematching conditions. Since our spectrometer is limited in sensitivity to -80 dBm, we can only upper bound the Raman contribution, with the expectation that it could be much lower especially on the anti-Stokes side. Using the same 0.5 nm filters as in this experiment, but engineering phase matching to occur in the gain dip, we expect the CAR to increase to at least 30 for degenerate pumping and 20 for non-degenerate pumping. This was estimated by multiplying the measured CAR by the ratio of Raman power where we collect photons near the pump and in the gain dip. The improvement is similar to that achieved in chalcogenide As_2S_3 waveguides after phasematching was obtained in the Raman gain dip [252, 266]. This lower-bound signal-to-noise ratio is just a factor 10 below that in the precertification experiment in chapter 4, meaning single-photon four-wave mixing could be possible in these chalcogenide microwires after appropriate phasematching

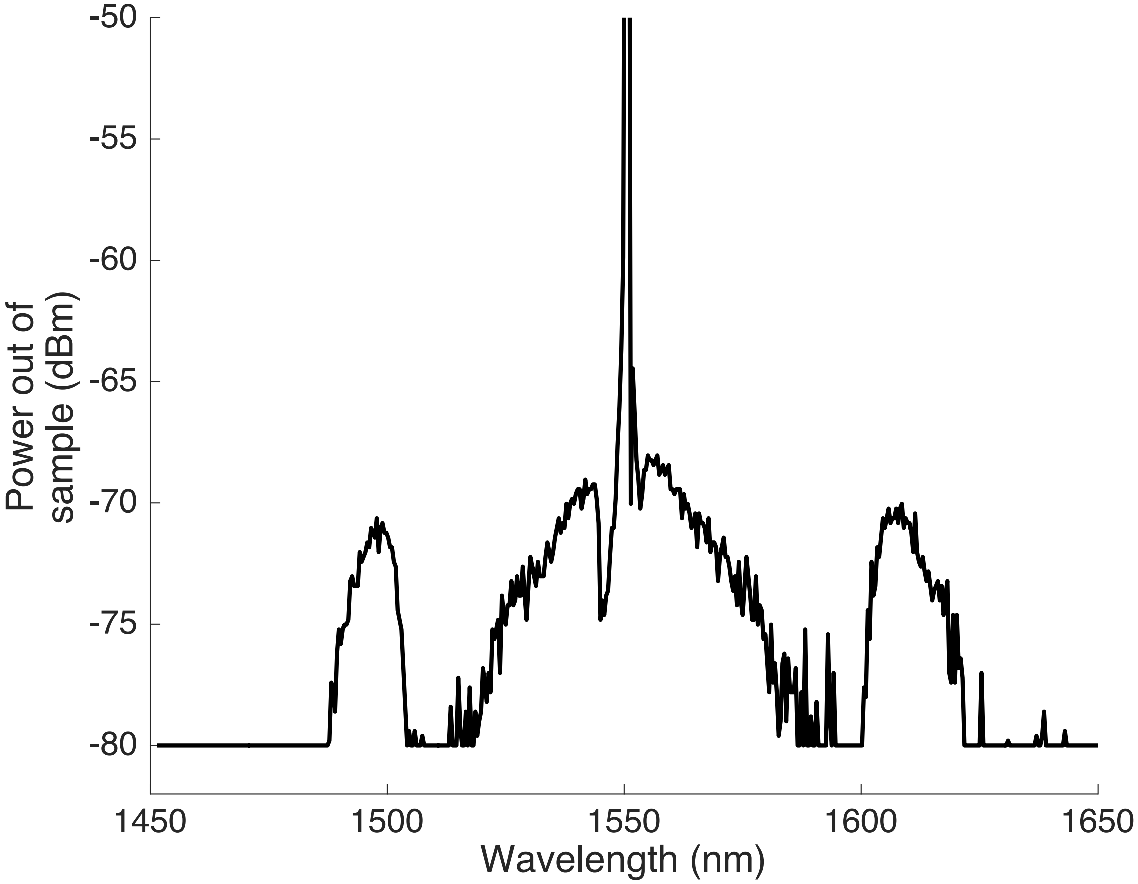

Figure 7.9: Measured Raman scattering noise spectrum of the microwire pumped at a wavelength of 1550 nm with 1 mW coupled power. Two minima occur at ±40 nm from the pump. This spectrum includes a 10 nm-wide notch filter with 30 dB blocking centered at 1550 nm. The pump at 1550 nm extends off the top of the graph to −34 dBm, and our spectrometer's sensitivity is limited to −80 dBm. Engineering phasematching to occur in the Raman minima or beyond the peaks would help our signal-to-noise ratio by a factor of 15.

engineering. With a 40 nm filter bandwidth and pair production beyond the gain peaks, CAR could decrease to 0.5 due to the extra noise admitted by the filter, but this lower bound will be offset by the decay of Raman scattering far from the pumps. Cooling the microwire to 77 K and assuming the strong pump has the longest wavelength would reduce the anti-Stokes Raman scattering by an additional factor of 328, as calculated from the Boltzmann distribution at 77 K versus 300 K, returning the CAR to 164. This large coincidental-to-accidentals ratio means this scheme could be useful for precertification. However, these are only estimates, and it remains to be seen if in practice the absolute number of noise photons in the signal or idler channel can be brought low enough to allow high heralding efficiency with a single-photon pump.

7.2.6 Conclusion

We have presented evidence of photon pairs produced in an As_2Se_3 chalcogenide microwire for both degenerate and non-degenerate pumping. Because this device is a tapered fibre, the coupling of optical signals in and out is straightforward and stable with room for improvement in efficiency, making the system very interesting for future applications. Through timing analysis of photon pairs, we found that the coincidences-to-accidentals ratio maintains a value of CAR > 1 over a wide range of pump powers, and inferred a maximum pair production rate inside the microwire (limited by detector dead time) of 2.9×10^6 pairs/s. We look forward to reducing the background noise by engineering the phasematching conditions and pushing closer to the predicted 10^{-3} efficiency for converting a single photon into a pair in these microwires. Our scheme of generating photon pairs between the pumps with the strong pump the longest wavelength will be critical in reducing the noise from Raman scattering.

Chapter 8

Conclusion

Working towards the loophole-free Bell test, it became clear how difficult it is to remove transmission loss: this strategy certainly fails for long-distance communication. Photonic-qubit precertification has the potential to allow device-independent quantum protocols over lossy channels longer than a few kilometres by circumventing the problem of loss. I showed in this first implementation how it preserves qubit states, and identified a straightforward path to improving heralding efficiency over direct transmission, with the immediate next step of decreasing the dark counts in the flag detector. As ultra-low-noise superconducting nanowire detectors have already been demonstrated, it is a matter of building, borrowing, or buying some. This, accompanied by improvements in coupling efficiency from the precertification to the detectors could already allow closing the detector loophole in a Bell test with direct transmission efficiency $<67\,\%$.

In the longer term, higher efficiency is needed in converting one photon to two. I showed some first steps toward this goal using four-wave mixing in optical fibres, confirming the extreme nonlinearity present in chalcogenide microwires. These devices need further engineering to produce the desired phasematching and limit noise as much as possible. The outside pumping strategy I used together with wide-band phasematching should allow use of these $\chi^{(3)}$ materials without issues of Raman noise. There may also still be room for improvements in waveguiding $\chi^{(2)}$ materials.

Nicolas Gisin recently said “I bet that *photon amplifiers* will [be] used in the first demonstrations of DIQIP [device-independent quantum information processing] over tens of km” [267]. Though I agree with the spirit of the assertion, in this thesis I have made the case for substituting photon amplifiers with photonic precertification. Each may find its application in future quantum networks, but I bet that the requirement of remotely-prepared ancilla photons in photon amplification allows precertification to win the 10 km race.

References

[1] Bennett, C. H. & Wiesner, S. J. Communication via one- and two-particle operators on Einstein-Podolsky-Rosen states. *Phys. Rev. Lett.* **69**, 2881–2884 (1992). URL `http://dx.doi.org/10.1103/PhysRevLett.69.2881`. 1

[2] Mattle, K., Weinfurter, H., Kwiat, P. G. & Zeilinger, A. Dense coding in experimental quantum communication. *Phys. Rev. Lett.* **76**, 4656–4659 (1996). URL `http://dx.doi.org/10.1103/PhysRevLett.76.4656`. 1

[3] Bennett, C. H. & Brassard, G. Quantum cryptography: Public key distribution and coin tossing. *International Conference on Computers, Systems & Signal Processing* (1984). 1

[4] Bennett, C., Bessette, F., Brassard, G., Salvail, L. & Smolin, J. Experimental quantum cryptography. In Damgard, I. (ed.) *Advances in Cryptology — EUROCRYPT '90*, vol. 473 of *Lecture Notes in Computer Science*, 253–265 (Springer Berlin / Heidelberg, 1991). 1

[5] Ekert, A. K. Quantum cryptography based on Bell's theorem. *Phys. Rev. Lett.* **67**, 661–663 (1991). URL `http://dx.doi.org/10.1103/PhysRevLett.67.661`. 1, 7

[6] Gisin, N., Ribordy, G., Tittel, W. & Zbinden, H. Quantum cryptography. *Rev. Mod. Phys.* **74**, 145 (2002). URL `http://journals.aps.org/rmp/abstract/10.1103/RevModPhys.74.145`. 1

[7] Bennett, C. H. *et al.* Teleporting an unknown quantum state via dual classical and Einstein-Podolsky-Rosen channels. *Phys. Rev. Lett.* **70**, 1895–1899 (1993). URL `http://dx.doi.org/10.1103/PhysRevLett.70.1895`. 1

[8] Bouwmeester, D. *et al.* Experimental quantum teleportation. *Nature* **390**, 575–579 (1997). URL `http://dx.doi.org/10.1038/37539`. 1

[9] Furusawa, A. *et al.* Unconditional quantum teleportation. *Science* **282**, 706–709 (1998). URL `http://dx.doi.org/10.1126/science.282.5389.706`. 1

[10] Pan, J.-W., Gasparoni, S., Aspelmeyer, M., Jennewein, T. & Zeilinger, A. Experimental realization of freely propagating teleported qubits. *Nature* **421**, 721–725 (2003). URL `http://dx.doi.org/10.1038/nature01412`. 1, 12

[11] Ursin, R. *et al.* Communications: Quantum teleportation across the Danube. *Nature* **430**, 849–849 (2004). URL `http://dx.doi.org/10.1038/430849a`. 1

[12] Bell, J. S. On the Einstein-Podolsky-Rosen paradox. *Physics* **1**, 195–200 (1964). URL `http://cds.cern.ch/record/111654/files/vol1p195-200_001.pdf`. 1, 3, 52

[13] Aspect, A., Dalibard, J. & Roger, G. Experimental test of Bell's inequalities using time-varying analyzers. *Phys. Rev. Lett.* **49**, 1804–1807 (1982). URL `http://dx.doi.org/10.1103/PhysRevLett.49.1804`. 1, 4

[14] Weihs, G., Jennewein, T., Simon, C., Weinfurter, H. & Zeilinger, A. Violation of Bell's inequality under strict Einstein locality conditions. *Phys. Rev. Lett.* **81**, 5039–5043 (1998). URL `http://dx.doi.org/10.1103/PhysRevLett.81.5039`. 1, 11, 94

[15] Jennewein, T., Achleitner, U., Weihs, G., Weinfurter, H. & Zeilinger, A. A fast and compact quantum random number generator. *Review of Scientific Instruments* **71**, 1675–1680 (2000). URL `http://link.aip.org/link/?RSI/71/1675/1`. 1

[16] Pironio, S. *et al.* Random numbers certified by Bell's theorem. *Nature* **464**, 1021–1024 (2010). URL `http://dx.doi.org/10.1038/nature09008`. 1, 25

[17] Pirandola, S., Eisert, J., Weedbrook, C., Furusawa, A. & Braunstein, S. L. Advances in quantum teleportation. *Nat. Photon.* **9**, 641–652 (2015). URL `http://dx.doi.org/10.1038/nphoton.2015.154`. 1

[18] Yin, J. *et al.* Quantum teleportation and entanglement distribution over 100-kilometre free-space channels. *Nature* **488**, 185–188 (2012). URL `http://dx.doi.org/10.1038/nature11332`. 1

[19] Ma, X.-S. *et al.* Quantum teleportation over 143 kilometres using active feed-forward. *Nature* **489**, 269–273 (2012). URL `http://dx.doi.org/10.1038/nature11472`. 1

[20] Takesue, H. *et al.* Quantum teleportation over 100 km of fiber using highly efficient superconducting nanowire single-photon detectors. *Optica* **2**, 832–835 (2015). URL `http://www.osapublishing.org/optica/abstract.cfm?URI=optica-2-10-832`. 1

[21] Stucki, D. *et al.* High rate long distance quantum key distribution over 250 km of ultra low loss fibres. *New Journal of Physics* **11**, 075003 (2009). URL `http://dx.doi.org/10.1088/1367-2630/11/7/075003`. 1, 11

[22] Liu, Y. *et al.* Decoy-state quantum key distribution with polarized photons over 200 km. *Opt. Express* **18**, 8587–8594 (2010). URL `http://www.opticsexpress.org/abstract.cfm?URI=oe-18-8-8587`. 1

[23] Wang, S. *et al.* 2 GHz clock quantum key distribution over 260 km of standard telecom fiber. *Opt. Lett.* **37**, 1008–1010 (2012). URL `http://ol.osa.org/abstract.cfm?URI=ol-37-6-1008`. 1, 40

[24] Korzh, B. *et al.* Provably secure and practical quantum key distribution over 307 km of optical fibre. *Nat. Photon.* **9**, 163–168 (2015). URL `http://dx.doi.org/10.1038/nphoton.2014.327`. 1

[25] Scheidl, T. *et al.* Feasibility of 300 km quantum key distribution with entangled states. *New Journal of Physics* **11**, 085002 (13pp) (2009). URL `http://stacks.iop.org/1367-2630/11/085002`. 1, 94

[26] Gordon, K. J. *et al.* Quantum key distribution system clocked at 2 GHz. *Opt. Express* **13**, 3015 (2005). URL `http://dx.doi.org/10.1364/OPEX.13.003015`. 1

[27] Dixon, A. R., Yuan, Z. L., Dynes, J. F., Sharpe, A. W. & Shields, A. J. Gigahertz decoy quantum key distribution with 1 Mbit/s secure key rate. *Opt. Express* **16**, 18790–18979 (2008). URL `http://www.opticsexpress.org/abstract.cfm?URI=oe-16-23-18790`. 1

[28] Patel, K. A. *et al.* Quantum key distribution for 10 Gb/s dense wavelength division multiplexing networks. *Applied Physics Letters* **104**, 051123 (2014). URL `http://scitation.aip.org/content/aip/journal/apl/104/5/10.1063/1.4864398`. 1

[29] Fry, E. S. & Thompson, R. C. Experimental test of local hidden-variable theories. *Phys. Rev. Lett.* **37**, 465–468 (1976). URL `http://link.aps.org/doi/10.1103/PhysRevLett.37.465`. 1

[30] Tittel, W., Brendel, J., Zbinden, H. & Gisin, N. Violation of Bell inequalities by photons more than 10 km apart. *Phys. Rev. Lett.* **81**, 3563–3566 (1998). URL `http://dx.doi.org/10.1103/PhysRevLett.81.3563`. 1

[31] Rowe, M. A. *et al.* Experimental violation of a Bell's inequality with efficient detection. *Nature* **409**, 791–794 (2001). URL `http://dx.doi.org/10.1038/35057215`. 1, 3, 11, 12, 47

[32] Inagaki, T., Matsuda, N., Tadanaga, O., Asobe, M. & Takesue, H. Entanglement distribution over 300 km of fiber. *Opt. Express* **21**, 23241–23249 (2013). URL `http://www.opticsexpress.org/abstract.cfm?URI=oe-21-20-23241`. 1

[33] Brunner, N., Cavalcanti, D., Pironio, S., Scarani, V. & Wehner, S. Bell nonlocality. *Rev. Mod. Phys.* **86**, 419–478 (2014). URL `http://link.aps.org/doi/10.1103/RevModPhys.86.419`. 1

[34] Carvacho, G. *et al.* Postselection-loophole-free Bell test over an installed optical fiber network. *Phys. Rev. Lett.* **115**, 030503 (2015). URL `http://link.aps.org/doi/10.1103/PhysRevLett.115.030503`. 1

[35] Acín, A. *et al.* Device-independent security of quantum cryptography against collective attacks. *Phys. Rev. Lett.* **98**, 230501 (2007). URL `http://journals.aps.org/prl/abstract/10.1103/PhysRevLett.98.230501`. 3, 7, 47

[36] Pironio, S. *et al.* Device-independent quantum key distribution secure against collective attacks. *New Journal of Physics* **11**, 045021 (2009). URL `http://stacks.iop.org/1367-2630/11/i=4/a=045021`. 3, 7, 40

[37] Shalm, L. K., Meyer-Scott, E. *et al.* Strong loophole-free test of local realism. *Phys. Rev. Lett.* **115**, 250402 (2015). URL `http://link.aps.org/doi/10.1103/PhysRevLett.115.250402`. 3, 7, 11, 21, 24, 34, 38, 40

[38] Giustina, M. *et al.* Significant-loophole-free test of Bell's theorem with entangled photons. *Phys. Rev. Lett.* **115**, 250401 (2015). URL `http://link.aps.org/doi/10.1103/PhysRevLett.115.250401`. 3, 7, 11, 40

[39] Hensen, B. *et al.* Loophole-free Bell inequality violation using electron spins separated by 1.3 kilometres. *Nature* **526**, 682–686 (2015). URL `http://dx.doi.org/10.1038/nature15759`. 3, 11, 12, 40, 52, 66, 70

[40] Christian, J. Disproof of Bell's Theorem. *ArXiv e-prints* (2011). `http://arxiv.org/abs/1103.1879`. 3

[41] Clauser, J. F., Horne, M. A., Shimony, A. & Holt, R. A. Proposed experiment to test local hidden-variable theories. *Phys. Rev. Lett.* **23**, 880–884 (1969). URL `http://dx.doi.org/10.1103/PhysRevLett.23.880`. 3, 32

[42] Clauser, J. F. & Horne, M. A. Experimental consequences of objective local theories. *Phys. Rev. D* **10**, 526–535 (1974). URL `http://link.aps.org/doi/10.1103/PhysRevD.10.526`. 3, 25, 70

[43] Matsukevich, D. N., Maunz, P., Moehring, D. L., Olmschenk, S. & Monroe, C. Bell inequality violation with two remote atomic qubits. *Phys. Rev. Lett.* **100**, 150404 (2008). URL `http://link.aps.org/doi/10.1103/PhysRevLett.100.150404`. 3, 11, 12, 47

[44] Rosenfeld, W. *et al.* Towards a loophole-free test of Bell's inequality with entangled pairs of neutral atoms. *Advanced Science Letters* **2**, 469–474 (2009). URL `http://dx.doi.org/10.1166/asl.2009.1059`. 3, 52

[45] Bernien, H. *et al.* Heralded entanglement between solid-state qubits separated by three metres. *Nature* **497**, 86–90 (2013). URL `http://dx.doi.org/10.1038/nature12016`. 3, 66, 70

[46] Güney, V. U. & Hillery, M. Maximum quantum violations of a class of Bell inequalities. *Phys. Rev. A* **87**, 052126 (2013). URL `http://link.aps.org/doi/10.1103/PhysRevA.87.052126`. 4

[47] Eberhard, P. H. Background level and counter efficiencies required for a loophole-free Einstein-Podolsky-Rosen experiment. *Phys. Rev. A* **47**, R747–R750 (1993). URL `http://link.aps.org/doi/10.1103/PhysRevA.47.R747`. 5, 34, 38, 66

[48] Christensen, B. G. *et al.* Detection-loophole-free test of quantum nonlocality, and applications. *Phys. Rev. Lett.* **111**, 130406 (2013). URL `http://link.aps.org/doi/10.1103/PhysRevLett.111.130406`. 5, 7, 11

[49] Dehlinger, D. & Mitchell, M. W. Entangled photons, nonlocality, and Bell inequalities in the undergraduate laboratory. *American Journal of Physics* **70**, 903–910 (2002). URL `http://scitation.aip.org/content/aapt/journal/ajp/70/9/10.1119/1.1498860`. 5

[50] Giustina, M. *et al.* Bell violation using entangled photons without the fair-sampling assumption. *Nature* **497**, 227–230 (2013). URL `http://dx.doi.org/10.1038/nature12012`. 7, 11, 47

[51] Acín, A., Massar, S. & Pironio, S. Efficient quantum key distribution secure against no-signalling eavesdroppers. *New Journal of Physics* **8**, 126 (2006). URL `http://stacks.iop.org/1367-2630/8/i=8/a=126`. 7

[52] Acín, A., Gisin, N. & Masanes, L. From Bell's theorem to secure quantum key distribution. *Phys. Rev. Lett.* **97**, 120405 (2006). URL `http://link.aps.org/doi/10.1103/PhysRevLett.97.120405`. 7

[53] Larsson, J.-Å. Loopholes in Bell inequality tests of local realism. *Journal of Physics A: Mathematical and Theoretical* **47**, 424003 (2014). URL `http://stacks.iop.org/1751-8121/47/i=42/a=424003`. 7, 9, 10

[54] Masanes, L., Renner, R., Christandl, M., Winter, A. & Barrett, J. Full security of quantum key distribution from no-signaling constraints. *Information Theory, IEEE Transactions on* **60**, 4973–4986 (2014). URL `http://dx.doi.org/10.1109/TIT.2014.2329417`. 7

[55] Makarov, V., Anisimov, A. & Skaar, J. Effects of detector efficiency mismatch on security of quantum cryptosystems. *Phys. Rev. A* **74**, 022313 (2006). URL `http://link.aps.org/doi/10.1103/PhysRevA.74.022313`. 9

[56] Fei, Y., Gao, M., Wang, W., Li, C. & Ma, Z. Practical attacks on decoy-state quantum-key-distribution systems with detector efficiency mismatch. *Phys. Rev. A* **91**, 052305 (2015). URL `http://link.aps.org/doi/10.1103/PhysRevA.91.052305`. 9

[57] Zhao, Y., Fung, C.-H. F., Qi, B., Chen, C. & Lo, H.-K. Quantum hacking: Experimental demonstration of time-shift attack against practical quantum-key-distribution systems. *Phys. Rev. A* **78**, 042333 (2008). URL `http://dx.doi.org/10.1103/PhysRevA.78.042333`. 9

[58] Makarov, V. Controlling passively quenched single photon detectors by bright light. *New Journal of Physics* **11**, 065003 (2009). URL `http://stacks.iop.org/1367-2630/11/i=6/a=065003`. 9

[59] Lydersen, L. *et al.* Hacking commercial quantum cryptography systems by tailored bright illumination. *Nat. Photon.* **4**, 686–689 (2010). URL `http://dx.doi.org/10.1038/nphoton.2010.214`. 9, 40

[60] Wiechers, C. *et al.* After-gate attack on a quantum cryptosystem. *New Journal of Physics* **13**, 013043 (2011). URL `http://stacks.iop.org/1367-2630/13/i=1/a=013043`. 9

[61] Bugge, A. N. *et al.* Laser damage helps the eavesdropper in quantum cryptography. *Phys. Rev. Lett.* **112**, 070503 (2014). URL `http://link.aps.org/doi/10.1103/PhysRevLett.112.070503`. 9

[62] Tanner, M. G., Makarov, V. & Hadfield, R. H. Optimised quantum hacking of superconducting nanowire single-photon detectors. *Opt. Express* **22**, 6734–6748 (2014). URL `http://www.opticsexpress.org/abstract.cfm?URI=oe-22-6-6734`. 9

[63] Vakhitov, A., Makarov, V. & Hjelme, D. R. Large pulse attack as a method of conventional optical eavesdropping in quantum cryptography. *Journal of Modern Optics* **48**, 2023–2038 (2001). URL `http://www.informaworld.com/10.1080/09500340108240904`. 9

[64] Gisin, N., Fasel, S., Kraus, B., Zbinden, H. & Ribordy, G. Trojan-horse attacks on quantum-key-distribution systems. *Phys. Rev. A* **73**, 022320 (2006). URL `http://link.aps.org/doi/10.1103/PhysRevA.73.022320`. 9

[65] Jain, N. *et al.* Trojan-horse attacks threaten the security of practical quantum cryptography. *New Journal of Physics* **16**, 123030 (2014). URL `http://stacks.iop.org/1367-2630/16/i=12/a=123030`. 9

[66] Nauerth, S., Fürst, M., Schmitt-Manderbach, T., Weier, H. & Weinfurter, H. Information leakage via side channels in freespace BB84 quantum cryptography. *New Journal of Physics* **11**, 065001 (2009). URL `http://stacks.iop.org/1367-2630/11/i=6/a=065001`. 9

[67] Fung, C.-H. F., Qi, B., Tamaki, K. & Lo, H.-K. Phase-remapping attack in practical quantum-key-distribution systems. *Phys. Rev. A* **75**, 032314 (2007). URL `http://link.aps.org/doi/10.1103/PhysRevA.75.032314`. 9

[68] Xu, F., Qi, B. & Lo, H.-K. Experimental demonstration of phase-remapping attack in a practical quantum key distribution system. *New Journal of Physics* **12**, 113026 (2010). URL `http://stacks.iop.org/1367-2630/12/i=11/a=113026`. 9

[69] Sun, S.-H., Jiang, M.-S., Ma, X.-C., Li, C.-Y. & Liang, L.-M. Hacking on decoy-state quantum key distribution system with partial phase randomization. *Sci. Rep.* **4** (2014). URL `http://dx.doi.org/10.1038/srep04759`. 9

[70] Gerhardt, I. *et al.* Experimentally faking the violation of Bell's inequalities. *Phys. Rev. Lett.* **107**, 170404 (2011). URL `http://link.aps.org/doi/10.1103/PhysRevLett.107.170404`. 9

[71] Kofler, J. & Giustina, M. Requirements for a loophole-free Bell test using imperfect setting generators. *ArXiv e-prints* (2014). `http://arxiv.org/abs/1411.4787`. 9

[72] Pearle, P. M. Hidden-variable example based upon data rejection. *Phys. Rev. D* **2**, 1418–1425 (1970). URL `http://link.aps.org/doi/10.1103/PhysRevD.2.1418`. 9, 47

[73] Bell, J. S., Clauser, J. F., Horne, M. A. & Shimony, A. An exchange on local beables. *Dialectica* **39**, 85–96 (1985). URL `http://dx.doi.org/10.1111/j.1746-8361.1985.tb01249.x`. 10

[74] Saleh, B. E. A. & Teich, M. C. *Fundamentals of Photonics* (Wiley, 2007), 2nd edn. 10, 34, 80

[75] Lo, H.-K., Curty, M. & Qi, B. Measurement-device-independent quantum key distribution. *Phys. Rev. Lett.* **108**, 130503 (2012). URL `http://link.aps.org/doi/10.1103/PhysRevLett.108.130503`. 10, 40

[76] Braunstein, S. L. & Pirandola, S. Side-channel-free quantum key distribution. *Phys. Rev. Lett.* **108**, 130502 (2012). URL `http://link.aps.org/doi/10.1103/PhysRevLett.108.130502`. 10, 40

[77] Sun, S.-H. *et al.* Effect of source tampering in the security of quantum cryptography. *Phys. Rev. A* **92**, 022304 (2015). URL `http://link.aps.org/doi/10.1103/PhysRevA.92.022304`. 10

[78] Rubenok, A., Slater, J. A., Chan, P., Lucio-Martinez, I. & Tittel, W. Real-world two-photon interference and proof-of-principle quantum key distribution immune to

detector attacks. *Phys. Rev. Lett.* **111**, 130501 (2013). URL `http://link.aps.org/doi/10.1103/PhysRevLett.111.130501`. 11

[79] Liu, Y. *et al.* Experimental measurement-device-independent quantum key distribution. *Phys. Rev. Lett.* **111**, 130502 (2013). URL `http://link.aps.org/doi/10.1103/PhysRevLett.111.130502`. 11

[80] Ferreira da Silva, T. *et al.* Proof-of-principle demonstration of measurement-device-independent quantum key distribution using polarization qubits. *Phys. Rev. A* **88**, 052303 (2013). URL `http://link.aps.org/doi/10.1103/PhysRevA.88.052303`. 11

[81] Tang, Z. *et al.* Experimental demonstration of polarization encoding measurement-device-independent quantum key distribution. *Phys. Rev. Lett.* **112**, 190503 (2014). URL `http://link.aps.org/doi/10.1103/PhysRevLett.112.190503`. 11

[82] Yin, H.-L. *et al.* Long-distance measurement-device-independent quantum key distribution with coherent-state superpositions. *Opt. Lett.* **39**, 5451–5454 (2014). URL `http://ol.osa.org/abstract.cfm?URI=ol-39-18-5451`. 11

[83] Tang, Y.-L. *et al.* Measurement-device-independent quantum key distribution over 200 km. *Phys. Rev. Lett.* **113**, 190501 (2014). URL `http://link.aps.org/doi/10.1103/PhysRevLett.113.190501`. 11

[84] Lim, C. C. W. *et al.* Detector-device-independent quantum key distribution. *Applied Physics Letters* **105**, 221112 (2014). URL `http://scitation.aip.org/content/aip/journal/apl/105/22/10.1063/1.4903350`. 11

[85] Cao, W.-F. *et al.* Highly efficient quantum key distribution immune to all detector attacks. *ArXiv e-prints* (2014). `http://arxiv.org/abs/1410.2928`. 11

[86] González, P. *et al.* Quantum key distribution with untrusted detectors. *Phys. Rev. A* **92**, 022337 (2015). URL `http://link.aps.org/doi/10.1103/PhysRevA.92.022337`. 11

[87] Qi, B. Trustworthiness of detectors in quantum key distribution with untrusted detectors. *Phys. Rev. A* **91**, 020303 (2015). URL `http://link.aps.org/doi/10.1103/PhysRevA.91.020303`. 11

[88] Ansmann, M. *et al.* Violation of Bell's inequality in Josephson phase qubits. *Nature* **461**, 504–506 (2009). URL `http://dx.doi.org/10.1038/nature08363`. 11

[89] Scheidl, T. *et al.* Violation of local realism with freedom of choice. *Proceedings of the National Academy of Sciences* **107**, 19708–19713 (2010). URL `http://www.pnas.org/content/107/46/19708.abstract`. 11

[90] Erven, C., Meyer-Scott, E. *et al.* Experimental three-photon quantum nonlocality under strict locality conditions. *Nat. Photon.* **8**, 292–296 (2014). URL `http://dx.doi.org/10.1038/nphoton.2014.50`. 11

[91] Bell, J. S. *Speakable and unspeakable in quantum mechanics* (Cambridge University Press, 1987). 12

[92] Żukowski, M., Zeilinger, A., Horne, M. A. & Ekert, A. K. "Event-ready-detectors" Bell experiment via entanglement swapping. *Phys. Rev. Lett.* **71**, 4287–4290 (1993). URL `http://dx.doi.org/10.1103/PhysRevLett.71.4287`. 12, 52

[93] Simon, C. & Irvine, W. T. M. Robust long-distance entanglement and a loophole-free Bell test with ions and photons. *Phys. Rev. Lett.* **91**, 110405 (2003). URL `http://link.aps.org/doi/10.1103/PhysRevLett.91.110405`. 13

[94] Braginsky, V. B. & Khalili, F. Y. Quantum nondemolition measurements: the route from toys to tools. *Rev. Mod. Phys.* **68**, 1–11 (1996). URL `http://link.aps.org/doi/10.1103/RevModPhys.68.1`. 13

[95] Kok, P., Lee, H. & Dowling, J. P. Single-photon quantum-nondemolition detectors constructed with linear optics and projective measurements. *Phys. Rev. A* **66**, 063814 (2002). URL `http://link.aps.org/doi/10.1103/PhysRevA.66.063814`. 13

[96] Imoto, N., Haus, H. A. & Yamamoto, Y. Quantum nondemolition measurement of the photon number via the optical Kerr effect. *Phys. Rev. A* **32**, 2287–2292 (1985). URL `http://link.aps.org/doi/10.1103/PhysRevA.32.2287`. 13

[97] Grangier, P., Levenson, J. A. & Poizat, J.-P. Quantum non-demolition measurements in optics. *Nature* **396**, 537–542 (1998). URL `http://dx.doi.org/10.1038/25059`. 13, 52

[98] Kapale, K. T. Polarization preserving quantum nondemolition photodetector. *Journal of Modern Optics* **54**, 327–335 (2007). URL `http://dx.doi.org/10.1080/09500340600753822`. 13

[99] Feizpour, A., Hallaji, M., Dmochowski, G. & Steinberg, A. M. Observation of the nonlinear phase shift due to single post-selected photons. *Nat. Phys.* **11**, 905–909 (2015). URL `http://dx.doi.org/10.1038/nphys3433`. 13, 52

[100] Pryde, G. J., O'Brien, J. L., White, A. G., Bartlett, S. D. & Ralph, T. C. Measuring a photonic qubit without destroying it. *Phys. Rev. Lett.* **92**, 190402 (2004). URL `http://link.aps.org/doi/10.1103/PhysRevLett.92.190402`. 13

[101] Witthaut, D., Lukin, M. D. & Sørensen, A. S. Photon sorters and qnd detectors using single photon emitters. *EPL (Europhysics Letters)* **97**, 50007 (2012). URL `http://stacks.iop.org/0295-5075/97/i=5/a=50007`. 13

[102] Reiserer, A., Ritter, S. & Rempe, G. Nondestructive detection of an optical photon. *Science* **342**, 1349–1351 (2013). URL `http://www.sciencemag.org/content/342/6164/1349`. 13, 52

[103] Sinclair, N. *et al.* Cross-phase modulation of a probe stored in a waveguide for non-destructive detection of photonic qubits. *ArXiv e-prints* (2015). `http://arxiv.org/abs/1510.01164`. 13, 52

[104] Gisin, N., Pironio, S. & Sangouard, N. Proposal for implementing device-independent quantum key distribution based on a heralded qubit amplifier. *Phys. Rev. Lett.* **105**, 070501 (2010). URL `http://journals.aps.org/prl/abstract/10.1103/PhysRevLett.105.070501`. 13, 15, 40, 45, 46, 47, 48, 52, 75

[105] Caves, C. M. Quantum-mechanical noise in an interferometer. *Phys. Rev. D* **23**, 1693–1708 (1981). URL `http://link.aps.org/doi/10.1103/PhysRevD.23.1693`. 13

[106] Wootters, W. K. & Zurek, W. H. A single quantum cannot be cloned. *Nature* **299**, 802–803 (1982). URL `http://dx.doi.org/10.1038/299802a0`. 13, 40, 55

[107] Mandel, L. Is a photon amplifier always polarization dependent? *Nature* **304**, 188– (1983). URL `http://dx.doi.org/10.1038/304188a0`. 13

[108] Ralph, T. C. & Lund, A. P. Nondeterministic Noiseless Linear Amplification of Quantum Systems. In Lvovsky, A. (ed.) *American Institute of Physics Conference Series*, vol. 1110 of *American Institute of Physics Conference Series*, 155–160 (2009). `0809.0326`. 13

[109] Pegg, D. T., Phillips, L. S. & Barnett, S. M. Optical state truncation by projection synthesis. *Phys. Rev. Lett.* **81**, 1604–1606 (1998). URL `http://link.aps.org/doi/10.1103/PhysRevLett.81.1604`. 13

[110] Osorio, C. I. *et al.* Heralded photon amplification for quantum communication. *Phys. Rev. A* **86**, 023815 (2012). URL `http://link.aps.org/doi/10.1103/PhysRevA.86.023815`. 13, 40

[111] Bruno, N., Pini, V., Martin, A. & Thew, R. T. A complete characterization of the heralded noiseless amplification of photons. *New Journal of Physics* **15**, 093002 (2013). URL `http://stacks.iop.org/1367-2630/15/i=9/a=093002`. 13, 40, 52

[112] Xiang, G. Y., Ralph, T. C., Lund, A. P., Walk, N. & Pryde, G. J. Heralded noiseless linear amplification and distillation of entanglement. *Nat. Photon.* **4**, 316–319 (2010). URL `http://dx.doi.org/10.1038/nphoton.2010.35`. 13, 40

[113] Ulanov, A. E. *et al.* Undoing the effect of loss on quantum entanglement. *Nat. Photon.* **9**, 764–768 (2015). URL `http://dx.doi.org/10.1038/nphoton.2015.195`. 13

[114] Kocsis, S., Xiang, G. Y., Ralph, T. C. & Pryde, G. J. Heralded noiseless amplification of a photon polarization qubit. *Nat. Phys.* **9**, 23–28 (2013). URL `http://dx.doi.org/10.1038/nphys2469`. 13, 14, 40, 46, 52

[115] Bruno, N. *et al.* Heralded amplification of photonic qubits. *Opt. Express* **24**, 125–133 (2016). URL `http://www.opticsexpress.org/abstract.cfm?URI=oe-24-1-125`. 13, 15, 16, 52

[116] Curty, M. & Moroder, T. Heralded-qubit amplifiers for practical device-independent quantum key distribution. *Phys. Rev. A* **84**, 010304 (2011). URL `http://link.aps.org/doi/10.1103/PhysRevA.84.010304`. 13, 41, 46, 47, 48, 52

[117] Pitkanen, D., Ma, X., Wickert, R., van Loock, P. & Lütkenhaus, N. Efficient heralding of photonic qubits with applications to device-independent quantum key distribution. *Phys. Rev. A* **84**, 022325 (2011). URL `http://link.aps.org/doi/10.1103/PhysRevA.84.022325`. 13, 40, 41, 47, 48, 52

[118] Meyer-Scott, E. *et al.* Entanglement-based linear-optical qubit amplifier. *Phys. Rev. A* **88**, 012327 (2013). URL `http://link.aps.org/doi/10.1103/PhysRevA.88.012327`. 13, 39, 52

[119] Langford, N. K. *et al.* Efficient quantum computing using coherent photon conversion. *Nature* **478**, 360 (2011). URL `http://dx.doi.org/10.1038/nature10463`. 15, 75, 78, 107, 109

[120] Cabello, A. & Sciarrino, F. Loophole-free Bell test based on local precertification of photon's presence. *Phys. Rev. X* **2**, 021010 (2012). URL `http://link.aps.org/doi/10.1103/PhysRevX.2.021010`. 15, 53, 54, 55, 75, 109

[121] Kok, P. & Lovett, B. *Introduction to Optical Quantum Information Processing* (Cambridge University Press, 2010). URL `http://books.google.ca/books?id=G2zKNooOeKcC`. 17, 18, 20

[122] Boyd, R. *Nonlinear Optics* (Academic Press, 2008), third edn. 18

[123] Yamada, M., Nada, N., Saitoh, M. & Watanabe, K. First-order quasi-phase matched $\mathrm{LiNbO_3}$ waveguide periodically poled by applying an external field for efficient blue second-harmonic generation. *Applied Physics Letters* **62**, 435–436 (1993). URL `http://scitation.aip.org/content/aip/journal/apl/62/5/10.1063/1.108925`. 18

[124] Armstrong, J. A., Bloembergen, N., Ducuing, J. & Pershan, P. S. Interactions between light waves in a nonlinear dielectric. *Phys. Rev.* **127**, 1918–1939 (1962). URL `http://link.aps.org/doi/10.1103/PhysRev.127.1918`. 18

[125] Klyshko, D. N. Use of two-photon light for absolute calibration of photoelectric detectors. *Soviet Journal of Quantum Electronics* **10**, 1112 (1980). URL `http://stacks.iop.org/0049-1748/10/i=9/a=A09`. 19, 59

[126] Edamatsu, K. Entangled photons: Generation, observation, and characterization. *Japanese Journal of Applied Physics* **46**, 7175–7187 (2007). URL `http://jjap.ipap.jp/link?JJAP/46/7175/`. 20

[127] Ou, Z. Y. & Mandel, L. Violation of Bell's inequality and classical probability in a two-photon correlation experiment. *Phys. Rev. Lett.* **61**, 50–53 (1988). URL `http://dx.doi.org/10.1103/PhysRevLett.61.50`. 20

[128] Shih, Y. H. & Alley, C. O. New type of Einstein-Podolsky-Rosen-Bohm experiment using pairs of light quanta produced by optical parametric down conversion. *Phys. Rev. Lett.* **61**, 2921–2924 (1988). URL `http://link.aps.org/doi/10.1103/PhysRevLett.61.2921`. 20

[129] Kwiat, P. G. *et al.* New high-intensity source of polarization-entangled photon pairs. *Phys. Rev. Lett.* **75**, 4337–4341 (1995). URL `http://dx.doi.org/10.1103/PhysRevLett.75.4337`. 20

[130] Bruno, N., Zambrini Cruzeiro, E., Martin, A. & Thew, R. T. Simple, pulsed, polarization entangled photon pair source. *Optics Communications* **327**, 3–6 (2014). URL `http://www.sciencedirect.com/science/article/pii/S0030401814001564`. 20

[131] Herrmann, H. *et al.* Post-selection free, integrated optical source of non-degenerate, polarization entangled photon pairs. *Opt. Express* **21**, 27981–27991 (2013). URL `http://www.opticsexpress.org/abstract.cfm?URI=oe-21-23-27981`. 20

[132] Kwiat, P. G., Waks, E., White, A. G., Appelbaum, I. & Eberhard, P. H. Ultrabright source of polarization-entangled photons. *Phys. Rev. A* **60**, R773–R776 (1999). URL `http://dx.doi.org/10.1103/PhysRevA.60.R773`. 21, 70, 94

[133] Kim, T., Fiorentino, M. & Wong, F. N. C. Phase-stable source of polarization-entangled photons using a polarization sagnac interferometer. *Phys. Rev. A* **73**, 012316 (2006). URL `http://dx.doi.org/10.1103/PhysRevA.73.012316`. 21

[134] Arahira, S., Namekata, N., Kishimoto, T., Yaegashi, H. & Inoue, S. Generation of polarization entangled photon pairs at telecommunication wavelength using cascaded $\chi^{(2)}$ processes in a periodically poled LiNbO3 ridge waveguide. *Opt. Express* **19**, 16032–16043 (2011). URL `http://www.opticsexpress.org/abstract.cfm?URI=oe-19-17-16032`. 21

[135] Fiorentino, M., Messin, G., Kuklewicz, C. E., Wong, F. N. C. & Shapiro, J. H. Generation of ultrabright tunable polarization entanglement without spatial, spectral, or temporal constraints. *Phys. Rev. A* **69**, 041801 (2004). URL `http://link.aps.org/doi/10.1103/PhysRevA.69.041801`. 21

[136] Herbauts, I., Blauensteiner, B., Poppe, A., Jennewein, T. & Hübel, H. Demonstration of active routing of entanglement in a multi-user network. *Opt. Express* **21**, 29013–29024 (2013). URL `http://www.opticsexpress.org/abstract.cfm?URI=oe-21-23-29013`. 21

[137] Evans, P. G., Bennink, R. S., Grice, W. P., Humble, T. S. & Schaake, J. Bright source of spectrally uncorrelated polarization-entangled photons with nearly single-mode emission. *Phys. Rev. Lett.* **105**, 253601 (2010). URL `http://link.aps.org/doi/10.1103/PhysRevLett.105.253601`. 21, 27

[138] Muller, M., Bounouar, S., Jons, K. D., Glassl, M. & Michler, P. On-demand generation of indistinguishable polarization-entangled photon pairs. *Nat. Photon.* **8**, 224–228 (2014). URL `http://dx.doi.org/10.1038/nphoton.2013.377`. 21

[139] Versteegh, M. A. M. *et al.* Observation of strongly entangled photon pairs from a nanowire quantum dot. *Nat. Commun.* **5**, 5298 (2014). URL `http://dx.doi.org/10.1038/ncomms6298`. 21

[140] Xiong, C. *et al.* Compact and reconfigurable silicon nitride time-bin entanglement circuit. *Optica* **2**, 724–727 (2015). URL `http://www.osapublishing.org/optica/abstract.cfm?URI=optica-2-8-724`. 21

[141] Jayakumar, H. *et al.* Time-bin entangled photons from a quantum dot. *Nat. Commun.* **5** (2014). URL `http://dx.doi.org/10.1038/ncomms5251`. 21

[142] Meyer-Scott, E. *et al.* Generating polarization-entangled photon pairs using cross-spliced birefringent fibers. *Opt. Express* **21**, 6205–6212 (2013). URL `http://www.opticsexpress.org/abstract.cfm?URI=oe-21-5-6205`. 21, 93

[143] Takesue, H. & Inoue, K. Generation of polarization-entangled photon pairs and violation of Bell's inequality using spontaneous four-wave mixing in a fiber loop. *Phys. Rev. A* **70**, 031802 (2004). URL `http://link.aps.org/doi/10.1103/PhysRevA.70.031802`. 21

[144] Li, X. *et al.* Integrable optical-fiber source of polarization-entangled photon pairs in the telecom band. *Phys. Rev. A* **73**, 052301 (2006). URL `http://dx.doi.org/10.1103/PhysRevA.73.052301`. 21, 94

[145] Lee, K. F. *et al.* Generation of high-purity telecom-band entangled photon pairs in dispersion-shifted fiber. *Opt. Lett.* **31**, 1905–1907 (2006). URL `http://ol.osa.org/abstract.cfm?URI=ol-31-12-1905`. 21, 80

[146] Fang, B., Cohen, O. & Lorenz, V. O. Polarization-entangled photon-pair generation in commercial-grade polarization-maintaining fiber. *J. Opt. Soc. Am. B* **31**, 277–281 (2014). URL `http://josab.osa.org/abstract.cfm?URI=josab-31-2-277`. 21, 95

[147] Fulconis, J., Alibart, O., O'Brien, J. L., Wadsworth, W. J. & Rarity, J. G. Nonclassical interference and entanglement generation using a photonic crystal fiber pair photon source. *Phys. Rev. Lett.* **99**, 120501 (2007). URL `http://link.aps.org/doi/10.1103/PhysRevLett.99.120501`. 21

[148] Fan, J., Migdall, A., Chen, J. & Goldschmidt, E. A. Microstructure-fiber-based source of photonic entanglement. *Selected Topics in Quantum Electronics, IEEE Journal of* **15**, 1724–1732 (2009). URL `http://dx.doi.org/10.1109/JSTQE.2009.2025389`. 21, 80

[149] Clark, A. *et al.* Intrinsically narrowband pair photon generation in microstructured fibres. *New Journal of Physics* **13**, 065009 (2011). URL `http://stacks.iop.org/1367-2630/13/i=6/a=065009`. 21, 95, 101

[150] Medic, M., Altepeter, J. B., Hall, M. A., Patel, M. & Kumar, P. Fiber-based telecommunication-band source of degenerate entangled photons. *Opt. Lett.* **35**, 802–804 (2010). URL `http://ol.osa.org/abstract.cfm?URI=ol-35-6-802`. 21, 95

[151] Liang, C., Lee, K. F., Levin, T., Chen, J. & Kumar, P. Ultra stable all-fiber telecom-band entangled photon-pair source for turnkey quantum communication applications. *Opt. Express* **14**, 6936–6941 (2006). URL `http://www.opticsexpress.org/abstract.cfm?URI=oe-14-15-6936`. 21, 95

[152] Zhou, Z.-Y. *et al.* Classical to quantum optical network link for orbital angular momentum-carrying light. *Opt. Express* **23**, 18435–18444 (2015). URL `http://www.opticsexpress.org/abstract.cfm?URI=oe-23-14-18435`. 23

[153] Avenhaus, M., Eckstein, A., Mosley, P. J. & Silberhorn, C. Fiber-assisted single-photon spectrograph. *Opt. Lett.* **34**, 2873–2875 (2009). URL `http://ol.osa.org/abstract.cfm?URI=ol-34-18-2873`. 25

[154] Gerrits, T. *et al.* Generation of degenerate, factorizable, pulsed squeezed light at telecom wavelengths. *Opt. Express* **19**, 24434–24447 (2011). URL `http://www.opticsexpress.org/abstract.cfm?URI=oe-19-24-24434`. 25

[155] Lutus, P. OpticalRayTracer (2015). URL `http://arachnoid.com/OpticalRayTracer/`. 28

[156] Shalm, L. K. *et al.* Spontaneous parametric downcoversion calculator. URL `http://www.spdcalc.org`. 27

[157] Cirel'son, B. S. Quantum generalizations of Bell's inequality. *Letters in Mathematical Physics* **4**, 93–100 (1980). URL `http://dx.doi.org/10.1007/BF00417500`. 32

[158] Tan, S. M. A computational toolbox for quantum and atomic optics. *Journal of Optics B: Quantum and Semiclassical Optics* **1**, 424 (1999). URL `http://stacks.iop.org/1464-4266/1/i=4/a=312`. 38

[159] Jennewein, T., Barbieri, M. & White, A. G. Single-photon device requirements for operating linear optics quantum computing outside the post-selection basis. *Journal of Modern Optics* **58**, 276–287 (2011). URL `http://www.informaworld.com/10.1080/09500340.2010.546894`. 38

[160] Bartkiewicz, K., Lemr, K., Černoch, A., Soubusta, J. & Miranowicz, A. Experimental eavesdropping based on optimal quantum cloning. *Phys. Rev. Lett.* **110**, 173601 (2013). URL `http://link.aps.org/doi/10.1103/PhysRevLett.110.173601`. 40

[161] Schmitt-Manderbach, T. *et al.* Experimental demonstration of free-space decoy-state quantum key distribution over 144 km. *Phys. Rev. Lett.* **98**, 010504 (2007). URL `http://journals.aps.org/prl/abstract/10.1103/PhysRevLett.98.010504`. 40

[162] Marsili, F. *et al.* Detecting single infrared photons with 93% system efficiency. *Nat. Photon.* **7**, 210–214 (2013). URL `http://dx.doi.org/10.1038/nphoton.2013.13`. 47, 65, 94

[163] Lita, A. E., Miller, A. J. & Nam, S. W. Counting near-infrared single-photons with 95% efficiency. *Opt. Express* **16**, 3032–3040 (2008). URL `http://www.opticsexpress.org/abstract.cfm?URI=oe-16-5-3032`. 47

[164] Meyer-Scott, E. *et al.* Certifying the presence of a photonic qubit by splitting it in two. *ArXiv e-prints* (2015). `http://arxiv.org/abs/1510.04531`. 51

[165] Barrett, J., Hardy, L. & Kent, A. No signaling and quantum key distribution. *Phys. Rev. Lett.* **95**, 010503 (2005). URL `http://link.aps.org/doi/10.1103/PhysRevLett.95.010503`. 52

[166] Vazirani, U. & Vidick, T. Fully device-independent quantum key distribution. *Phys. Rev. Lett.* **113**, 140501 (2014). URL `http://link.aps.org/doi/10.1103/PhysRevLett.113.140501`. 52

[167] Colbeck, R. *Quantum And Relativistic Protocols For Secure Multi-Party Computation*. Ph.D. thesis, Trinity College, University of Cambridge (2006). URL `http://arxiv.org/abs/0911.3814`. 52

[168] Sathyamoorthy, S. R. *et al.* Quantum nondemolition detection of a propagating microwave photon. *Phys. Rev. Lett.* **112**, 093601 (2014). URL `http://link.aps.org/doi/10.1103/PhysRevLett.112.093601`. 52

[169] Hübel, H. *et al.* Direct generation of photon triplets using cascaded photon-pair sources. *Nature* **466**, 601–603 (2010). URL `http://dx.doi.org/10.1038/nature09175`. 53, 55, 75

[170] Ding, D.-S. *et al.* Hybrid-cascaded generation of tripartite telecom photons using an atomic ensemble and a nonlinear waveguide. *Optica* **2**, 642–645 (2015). URL `http://www.osapublishing.org/optica/abstract.cfm?URI=optica-2-7-642`. 53

[171] Shalm, L. K. *et al.* Three-photon energy-time entanglement. *Nat. Phys.* **9**, 19–22 (2013). URL `http://dx.doi.org/10.1038/nphys2492`. 55, 75

[172] Hamel, D. R. *et al.* Direct generation of three-photon polarization entanglement. *Nat. Photon.* **8**, 801–807 (2014). URL `http://dx.doi.org/10.1038/nphoton.2014.218`. 55, 75, 109

[173] Gayer, O., Sacks, Z., Galun, E. & Arie, A. Temperature and wavelength dependent refractive index equations for MgO-doped congruent and stoichiometric $LiNbO_3$. *Applied Physics B* **91**, 343–348 (2008). URL `http://dx.doi.org/10.1007/s00340-008-2998-2`. 55

[174] Hamel, D. *Direct generation of three-photon entanglement using cascaded downconversion*. Ph.D. thesis, University of Waterloo (2013). URL `http://hdl.handle.net/10012/8059`. 55, 58

[175] Hamel, D. *Realization of novel entangled photon sources using periodically poled materials*. Master's thesis, University of Waterloo (2010). URL `http://hdl.handle.net/10012/5575`. 55

[176] Poyatos, J. F., Cirac, J. I. & Zoller, P. Complete characterization of a quantum process: The two-bit quantum gate. *Phys. Rev. Lett.* **78**, 390–393 (1997). URL `http://link.aps.org/doi/10.1103/PhysRevLett.78.390`. 62

[177] Chuang, I. L. & Nielsen, M. A. Prescription for experimental determination of the dynamics of a quantum black box. *Journal of Modern Optics* **44**, 2455–2467 (1997). URL `http://www.tandfonline.com/doi/abs/10.1080/09500349708231894`. 62

[178] O'Brien, J. L. *et al.* Quantum process tomography of a controlled-NOT gate. *Phys. Rev. Lett.* **93**, 080502 (2004). URL `http://link.aps.org/doi/10.1103/PhysRevLett.93.080502`. 62

[179] James, D. F. V., Kwiat, P. G., Munro, W. J. & White, A. G. Measurement of qubits. *Phys. Rev. A* **64**, 052312 (2001). URL `http://link.aps.org/doi/10.1103/PhysRevA.64.052312`. 62

[180] Jozsa, R. Fidelity for mixed quantum states. *Journal of Modern Optics* **41**, 2315–2323 (1994). URL `http://dx.doi.org/10.1080/09500349414552171`. 62

[181] Yang, X. *et al.* Superconducting nanowire single photon detector with on-chip bandpass filter. *Opt. Express* **22**, 16267–16272 (2014). URL `http://www.opticsexpress.org/abstract.cfm?URI=oe-22-13-16267`. 65

[182] Krapick, S. *et al.* On-chip generation of photon-triplet states in integrated waveguide structures. In *CLEO: 2015*, FM2E.3 (Optical Society of America, 2015). URL `http://www.osapublishing.org/abstract.cfm?URI=CLEO_QELS-2015-FM2E.3`. 65

[183] Shibata, H., Shimizu, K., Takesue, H. & Tokura, Y. Ultimate low system dark-count rate for superconducting nanowire single-photon detector. *Optics Letters* **40**, 3428–3431 (2015). URL `http://ol.osa.org/abstract.cfm?URI=ol-40-14-3428`. 65, 70

[184] U'Ren, A. B., Silberhorn, C., Banaszek, K. & Walmsley, I. A. Efficient conditional preparation of high-fidelity single photon states for fiber-optic quantum networks. *Phys. Rev. Lett.* **93**, 093601 (2004). URL `http://link.aps.org/doi/10.1103/PhysRevLett.93.093601`. 65

[185] Harder, G. *et al.* An optimized photon pair source for quantum circuits. *Opt. Express* **21**, 13975–13985 (2013). URL `http://www.opticsexpress.org/abstract.cfm?URI=oe-21-12-13975`. 65

[186] Calkins, B. *et al.* High quantum-efficiency photon-number-resolving detector for photonic on-chip information processing. *Opt. Express* **21**, 22657–22670 (2013). URL `http://www.opticsexpress.org/abstract.cfm?URI=oe-21-19-22657`. 65

[187] Hofmann, J. *et al.* Heralded entanglement between widely separated atoms. *Science* **337**, 72–75 (2012). URL `http://www.sciencemag.org/content/337/6090/72.abstract`. 66

[188] Brunner, N., Gisin, N., Scarani, V. & Simon, C. Detection loophole in asymmetric Bell experiments. *Phys. Rev. Lett.* **98**, 220403 (2007). URL `http://link.aps.org/doi/10.1103/PhysRevLett.98.220403`. 66

[189] Cabello, A. & Larsson, J.-Å. Minimum detection efficiency for a loophole-free atom-photon Bell experiment. *Phys. Rev. Lett.* **98**, 220402 (2007). URL `http://link.aps.org/doi/10.1103/PhysRevLett.98.220402`. 66

[190] Ursin, R. *et al.* Entanglement-based quantum communication over 144 km. *Nat. Phys.* **3**, 481–486 (2007). URL `http://dx.doi.org/10.1038/nphys629`. 66

[191] Patel, R. N. *et al.* Efficient photon coupling from a diamond nitrogen vacancy centre by integration with silica fibre. *ArXiv e-prints* (2015). `http://arxiv.org/abs/1502.07849`. 70

[192] Auchter, C., Chou, C.-K., Noel, T. W. & Blinov, B. B. Ion-photon entanglement and bell inequality violation with $^{138}\mathrm{Ba}^{+}$. *J. Opt. Soc. Am. B* **31**, 1568–1572 (2014). URL `http://josab.osa.org/abstract.cfm?URI=josab-31-7-1568`. 70

[193] De Greve, K. *et al.* Quantum-dot spin-photon entanglement via frequency downconversion to telecom wavelength. *Nature* **491**, 421–425 (2012). URL `http://dx.doi.org/10.1038/nature11577`. 70

[194] Kang, D., Kim, M., He, H. & Helmy, A. S. Two polarization-entangled sources from the same semiconductor chip. *Phys. Rev. A* **92**, 013821 (2015). URL `http://link.aps.org/doi/10.1103/PhysRevA.92.013821`. 72

[195] Zou, X. Y., Wang, L. J. & Mandel, L. Induced coherence and indistinguishability in optical interference. *Phys. Rev. Lett.* **67**, 318–321 (1991). URL `http://link.aps.org/doi/10.1103/PhysRevLett.67.318`. 72

[196] Dot, A., Meyer-Scott, E., Ahmad, R., Rochette, M. & Jennewein, T. Converting one photon into two via four-wave mixing in optical fibers. *Phys. Rev. A* **90**, 043808 (2014). URL `http://link.aps.org/doi/10.1103/PhysRevA.90.043808`. 72, 74, 77, 109, 119

[197] Meyer-Scott, E. *et al.* Power-efficient production of photon pairs in a tapered chalcogenide microwire. *Applied Physics Letters* **106**, 081111 (2015). URL `http://scitation.aip.org/content/aip/journal/apl/106/8/10.1063/1.4913743`. 72, 106

[198] Matsuda, N. *et al.* A monolithically integrated polarization entangled photon pair source on a silicon chip. *Scientific Reports* **2**, 817 EP – (2012). URL `http://dx.doi.org/10.1038/srep00817`. 72

[199] Förtsch, M. *et al.* A versatile source of single photons for quantum information processing. *Nat. Commun.* **4**, 1818 (2013). URL `http://dx.doi.org/10.1038/ncomms2838`. 72

[200] Burnham, D. C. & Weinberg, D. L. Observation of simultaneity in parametric production of optical photon pairs. *Phys. Rev. Lett.* **25**, 84–87 (1970). URL `http://link.aps.org/doi/10.1103/PhysRevLett.25.84`. 75

[201] Fiorentino, M., Voss, P., Sharping, J. & Kumar, P. All-fiber photon-pair source for quantum communications. *IEEE Photonics Technology Letters* **14**, 983–985 (2002). URL `http://dx.doi.org/10.1109/LPT.2002.1012406`. 75

[202] Guerreiro, T. *et al.* Interaction of independent single photons based on integrated nonlinear optics. *Nat. Commun.* **4**, 2324 (2013). URL `http://dx.doi.org/10.1038/ncomms3324`. 75

[203] Miwa, Y. *et al.* Exploring a new regime for processing optical qubits: Squeezing and unsqueezing single photons. *Phys. Rev. Lett.* **113**, 013601 (2014). URL `http://link.aps.org/doi/10.1103/PhysRevLett.113.013601`. 75

[204] Browne, D. E. & Rudolph, T. Resource-efficient linear optical quantum computation. *Phys. Rev. Lett.* **95**, 010501 (2005). URL `http://dx.doi.org/10.1103/PhysRevLett.95.010501`. 75

[205] Hillery, M., Buzek, V. & Berthiaume, A. Quantum secret sharing. *Phys. Rev. A* **59**, 1829–1834 (1999). URL `http://dx.doi.org/10.1103/PhysRevA.59.1829`. 75

[206] Banaszek, K. & Knight, P. L. Quantum interference in three-photon down-conversion. *Phys. Rev. A* **55**, 2368–2375 (1997). URL `http://dx.doi.org/10.1103/PhysRevA.55.2368`. 75

[207] Greenberger, D. M., Horne, M. A., Shimony, A. & Zeilinger, A. Bell's theorem without inequalities. *American Journal of Physics* **58**, 1131–1143 (1990). URL `http://scitation.aip.org/content/aapt/journal/ajp/58/12/10.1119/1.16243`. 75

[208] Tanzilli, S. *et al.* Highly efficient photon-pair source using periodically poled lithium niobate waveguide. *Electronics Letters* **37**, 26–28 (2001). URL `http://dx.doi.org/10.1049/el:20010009`. 75, 109

[209] Huttner, B., Serulnik, S. & Ben-Aryeh, Y. Quantum analysis of light propagation in a parametric amplifier. *Phys. Rev. A* **42**, 5594 (1990). URL `http://dx.doi.org/10.1103/PhysRevA.42.5594`. 76, 77

[210] Blow, K. J., Loudon, R., Phoenix, S. J. D. & Shepherd, T. J. Continuum fields in quantum optics. *Phys. Rev. A* **42**, 4102–4114 (1990). URL `http://dx.doi.org/10.1103/PhysRevA.42.4102`. 77

[211] Agrawal, G. P. *Nonlinear Fiber Optics* (Academic Press, Boston, 2007), fourth edn. URL `http://www.sciencedirect.com/science/book/9780123695161`. 79, 83, 113, 119

[212] Lin, Q., Yaman, F. & Agrawal, G. P. Photon-pair generation in optical fibers through four-wave mixing: Role of Raman scattering and pump polarization. *Phys. Rev. A* **75**, 023803 (2007). URL `http://link.aps.org/doi/10.1103/PhysRevA.75.023803`. 80, 95

[213] Shuker, R. & Gammon, R. W. Raman-scattering selection-rule breaking and the density of states in amorphous materials. *Phys. Rev. Lett.* **25**, 222–225 (1970). URL `http://link.aps.org/doi/10.1103/PhysRevLett.25.222`. 80

[214] Smith, B. J., Mahou, P., Cohen, O., Lundeen, J. S. & Walmsley, I. A. Photon pair generation in birefringent optical fibers. *Opt. Express* **17**, 23589–23602 (2009). URL `http://www.opticsexpress.org/abstract.cfm?URI=oe-17-26-23589`. 80, 84, 95

[215] Takesue, H. & Inoue, K. 1.5-μm band quantum-correlated photon pair generation in dispersion-shifted fiber: suppression of noise photons by cooling fiber. *Opt. Express* **13**, 7832–7839 (2005). URL `http://www.opticsexpress.org/abstract.cfm?URI=oe-13-20-7832`. 80

[216] Clark, A. S. *et al.* Raman scattering effects on correlated photon-pair generation in chalcogenide. *Opt. Express* **20**, 16807–16814 (2012). URL `http://www.opticsexpress.org/abstract.cfm?URI=oe-20-15-16807`. 80, 92

[217] Hollenbeck, D. & Cantrell, C. D. Multiple-vibrational-mode model for fiber-optic raman gain spectrum and response function. *J. Opt. Soc. Am. B* **19**, 2886–2892 (2002). URL `http://josab.osa.org/abstract.cfm?URI=josab-19-12-2886`. 80

[218] Newbury, N. R. Pump-wavelength dependence of Raman gain in single-mode optical fibers. *J. Lightwave Technol.* **21**, 3364–3373 (2003). URL `http://dx.doi.org/10.1109/JLT.2003.821716`. 80

[219] Stolen, R. H. & Bösch, M. A. Low-frequency and low-temperature Raman scattering in silica fibers. *Phys. Rev. Lett.* **48**, 805–808 (1982). URL `http://link.aps.org/doi/10.1103/PhysRevLett.48.805`. 80

[220] Zhou, Q., Zhang, W., rong Cheng, J., dong Huang, Y. & de Peng, J. Noise performance comparison of 1.5 μm correlated photon pair generation in different fibers. *Opt. Express* **18**, 17114–17123 (2010). URL `http://www.opticsexpress.org/abstract.cfm?URI=oe-18-16-17114`. 82

[221] Knight, J. C. Photonic crystal fibres. *Nature* **424**, 847–851 (2003). URL `http://dx.doi.org/10.1038/nature01940`. 87

[222] Russell, P. S. Photonic-crystal fibers. *J. Lightwave Technol.* **24**, 4729–4749 (2006). URL `http://jlt.osa.org/abstract.cfm?URI=jlt-24-12-4729`. 87

[223] Rarity, J., Fulconis, J., Duligall, J., Wadsworth, W. & Russell, P. Photonic crystal fiber source of correlated photon pairs. *Opt. Express* **13**, 534–544 (2005). URL `http://www.opticsexpress.org/abstract.cfm?URI=oe-13-2-534`. 87

[224] Kibler, B. *et al.* Emergence of spectral incoherent solitons through supercontinuum generation in a photonic crystal fiber. *Phys. Rev. E* **84**, 066605 (2011). URL `http://link.aps.org/doi/10.1103/PhysRevE.84.066605`. 88

[225] Baker, C. & Rochette, M. High Nonlinearity and Single-Mode Transmission in Tapered Multimode As_2Se_3-PMMA Fibers. *IEEE Photonics Journal* **4**, 960–969 (2012). URL `http://dx.doi.org/10.1109/JPHOT.2012.2202103`. 89, 110

[226] Ahmad, R. & Rochette, M. High efficiency and ultra broadband optical parametric four-wave mixing in chalcogenide-PMMA hybrid microwires. *Opt. Express* **20**, 9572–9580 (2012). URL `http://www.opticsexpress.org/abstract.cfm?URI=oe-20-9-9572`. 89, 110, 121

[227] Lenz, G. *et al.* Large Kerr effect in bulk Se-based chalcogenide glasses. *Opt. Letters* **25**, 254–6 (2000). URL `http://dx.doi.org/10.1364/OL.25.000254`. 89

[228] Giovannetti, V., Lloyd, S. & Maccone, L. Quantum-enhanced measurements: Beating the standard quantum limit. *Science* **306**, 1330–1336 (2004). URL `http://www.sciencemag.org/content/306/5700/1330.abstract`. 94

[229] Martin-Lopez, E. *et al.* Experimental realization of Shor's quantum factoring algorithm using qubit recycling. *Nat. Photon.* **6**, 773–776 (2012). URL `http://dx.doi.org/10.1038/nphoton.2012.259`. 94

[230] Lamas-Linares, A. *et al.* Nanosecond-scale timing jitter for single photon detection in transition edge sensors. *Applied Physics Letters* **102**, 231117 (2013). URL `http://scitation.aip.org/content/aip/journal/apl/102/23/10.1063/1.4809731`. 94

[231] Chen, J., Lee, K. F., Li, X., Voss, P. L. & Kumar, P. Schemes for fibre-based entanglement generation in the telecom band. *New Journal of Physics* **9**, 289 (2007). URL `http://stacks.iop.org/1367-2630/9/i=8/a=289`. 95

[232] Hall, M. A., Altepeter, J. B. & Kumar, P. Drop-in compatible entanglement for optical-fiber networks. *Opt. Express* **17**, 14558–14566 (2009). URL `http://www.opticsexpress.org/abstract.cfm?URI=oe-17-17-14558`. 95

[233] Zhou, Q., Zhang, W., Wang, P., Huang, Y. & Peng, J. Polarization entanglement generation at 1.5μm based on walk-off effect due to fiber birefringence. *Opt. Lett.* **37**, 1679 (2012). URL `http://ol.osa.org/abstract.cfm?URI=ol-37-10-1679`. 95

[234] Fan, J., Eisaman, M. D. & Migdall, A. Bright phase-stable broadband fiber-based source of polarization-entangled photon pairs. *Phys. Rev. A* **76**, 043836 (2007). URL `http://link.aps.org/doi/10.1103/PhysRevA.76.043836`. 95

[235] Brainis, E. Four-photon scattering in birefringent fibers. *Phys. Rev. A* **79**, 023840 (2009). URL `http://link.aps.org/doi/10.1103/PhysRevA.79.023840`. 95, 101

[236] Halder, M. *et al.* Nonclassical 2-photon interference with separate intrinsically narrowband fibre sources. *Opt. Express* **17**, 4670–4676 (2009). URL `http://www.opticsexpress.org/abstract.cfm?URI=oe-17-6-4670`. 95, 101

[237] Cohen, O. *et al.* Tailored photon-pair generation in optical fibers. *Phys. Rev. Lett.* **102**, 123603 (2009). URL `http://link.aps.org/doi/10.1103/PhysRevLett.102.123603`. 95

[238] Fang, B., Cohen, O., Moreno, J. B. & Lorenz, V. O. State engineering of photon pairs produced through dual-pump spontaneous four-wave mixing. *Opt. Express* **21**, 2707–2717 (2013). URL `http://www.opticsexpress.org/abstract.cfm?URI=oe-21-3-2707`. 95

[239] Söller, C., Cohen, O., Smith, B. J., Walmsley, I. A. & Silberhorn, C. High-performance single-photon generation with commercial-grade optical fiber. *Phys. Rev. A* **83**, 031806 (2011). URL `http://link.aps.org/doi/10.1103/PhysRevA.83.031806`. 96

[240] Trojek, P. *Efficient Generation of Photonic Entanglement and Multiparty Quantum Communication*. Ph.D. thesis, Ludwig-Maximilians-Universität München (2007). URL `http://xqp.physik.uni-muenchen.de/publications/files/theses_phd/phd_trojek.pdf`. 96, 97, 181

[241] Trojek, P. & Weinfurter, H. Collinear source of polarization-entangled photon pairs at nondegenerate wavelengths. *Applied Physics Letters* **92**, 211103 (2008). URL `http://link.aip.org/link/?APL/92/211103/1`. 96, 181

[242] Limpert, J., Roser, F., Schreiber, T. & Tunnermann, A. High-power ultrafast fiber laser systems. *Selected Topics in Quantum Electronics, IEEE Journal of* **12**, 233–244 (2006). URL `http://dx.doi.org/10.1109/JSTQE.2006.872729`. 105

[243] Vengsarkar, A. M. *et al.* Long-period fiber gratings as band-rejection filters. *Lightwave Technology, Journal of* **14**, 58–65 (1996). URL `http://dx.doi.org/10.1109/50.476137`. 105

[244] U'Ren, A. B., Erdmann, R. K., de la Cruz-Gutierrez, M. & Walmsley, I. A. Generation of two-photon states with an arbitrary degree of entanglement via nonlinear crystal superlattices. *Phys. Rev. Lett.* **97**, 223602 (2006). URL `http://link.aps.org/doi/10.1103/PhysRevLett.97.223602`. 105

[245] Fan, J., Dogariu, A. & Wang, L. J. Generation of correlated photon pairs in a microstructure fiber. *Opt. Lett.* **30**, 1530–1532 (2005). URL `http://ol.osa.org/abstract.cfm?URI=ol-30-12-1530`. 105

[246] Garay-Palmett, K. *et al.* Photon pair-state preparation with tailored spectral properties by spontaneous four-wave mixing in photonic-crystal fiber. *Opt. Express* **15**, 14870–14886 (2007). URL `http://www.opticsexpress.org/abstract.cfm?URI=oe-15-22-14870`. 107

[247] Horodecki, R., Horodecki, P., Horodecki, M. & Horodecki, K. Quantum entanglement. *Rev. Mod. Phys.* **81**, 865–942 (2009). URL `http://dx.doi.org/10.1103/RevModPhys.81.865`. 107

[248] Guerreiro, T. *et al.* Nonlinear interaction between single photons. *Phys. Rev. Lett.* **113**, 173601 (2014). URL `http://link.aps.org/doi/10.1103/PhysRevLett.113.173601`. 109

[249] Zhang, Q. *et al.* Correlated photon-pair generation in reverse-proton-exchange PPLN waveguides with integrated mode demultiplexer at 10 GHz clock. *Opt. Express* **15**, 10288–10293 (2007). URL `http://www.opticsexpress.org/abstract.cfm?URI=oe-15-16-10288`. 109

[250] Takesue, H. Entangled photon pair generation using silicon wire waveguides. *Selected Topics in Quantum Electronics, IEEE Journal of* **18**, 1722–1732 (2012). URL `http://dx.doi.org/10.1109/JSTQE.2012.2191538`. 109

[251] Xiong, C. *et al.* Quantum-correlated photon pair generation in chalcogenide As_2S_3 waveguides. *Opt. Express* **18**, 16206–16216 (2010). URL `http://www.opticsexpress.org/abstract.cfm?URI=oe-18-15-16206`. 109

[252] Xiong, C. *et al.* Generation of correlated photon pairs in a chalcogenide As_2S_3 waveguide. *Applied Physics Letters* **98**, 051101 (2011). URL `http://scitation.aip.org/content/aip/journal/apl/98/5/10.1063/1.3549744`. 109, 121

[253] Chen, J., Levine, Z. H., Fan, J. & Migdall, A. L. Frequency-bin entangled comb of photon pairs from a silicon-on-insulatormicro-resonator. *Opt. Express* **19**, 1470–1483 (2011). URL `http://www.opticsexpress.org/abstract.cfm?URI=oe-19-2-1470`. 109

[254] Reimer, C. *et al.* Integrated frequency comb source of heralded single photons. *Opt. Express* **22**, 6535–6546 (2014). URL `http://www.opticsexpress.org/abstract.cfm?URI=oe-22-6-6535`. 109

[255] Chiu, C.-K. *et al.* Low-light-level four-wave mixing by quantum interference. *Phys. Rev. A* **89**, 023839 (2014). URL `http://link.aps.org/doi/10.1103/PhysRevA.89.023839`. 109

[256] Foster, M. A., Turner, A. C., Lipson, M. & Gaeta, A. L. Nonlinear optics in photonic nanowires. *Opt. Express* **16**, 1300–1320 (2008). URL `http://www.opticsexpress.org/abstract.cfm?URI=oe-16-2-1300`. 109

[257] Harada, K. *et al.* Frequency and polarization characteristics of correlated photon-pair generation using a silicon wire waveguide. *Selected Topics in Quantum Electronics, IEEE Journal of* **16**, 325–331 (2010). URL `http://dx.doi.org/10.1109/JSTQE.2009.2023338`. 109

[258] Eggleton, B. J., Luther-Davies, B. & Richardson, K. Chalcogenide photonics. *Nat. Photon.* **5**, 141–148 (2011). URL `http://dx.doi.org/10.1038/nphoton.2011.309`. 109

[259] Slusher, R. E. *et al.* Large Raman gain and nonlinear phase shifts in high-purity As_2Se_3 chalcogenide fibers. *J. Opt. Soc. Am. B* **21**, 1146–1155 (2004). URL `http://josab.osa.org/abstract.cfm?URI=josab-21-6-1146`. 109, 113, 121

[260] Baker, C. & Rochette, M. Highly nonlinear hybrid AsSe-PMMA microtapers. *Opt. Express* **18**, 12391–12398 (2010). URL `http://www.opticsexpress.org/abstract.cfm?URI=oe-18-12-12391`. 113

[261] Kasarova, S. N., Sultanova, N. G., Ivanov, C. D. & Nikolov, I. D. Analysis of the dispersion of optical plastic materials. *Optical Materials* **29**, 1481 – 1490 (2007). URL `http://www.sciencedirect.com/science/article/pii/S0925346706002473`. 113

[262] Yan, Z. *et al.* An ultra low noise telecom wavelength free running single photon detector using negative feedback avalanche diode. *Rev. Sci. Instrum.* **83**, 073105 (2012). URL `http://scitation.aip.org/content/aip/journal/rsi/83/7/10.1063/1.4732813`. 113

[263] Steinlechner, F. *et al.* Phase-stable source of polarization-entangled photons in a linear double-pass configuration. *Opt. Express* **21**, 11943–11951 (2013). URL `http://www.opticsexpress.org/abstract.cfm?URI=oe-21-10-11943`. 116

[264] Engin, E. *et al.* Photon pair generation in a silicon micro-ring resonator with reverse bias enhancement. *Opt. Express* **21**, 27826–27834 (2013). URL `http://www.opticsexpress.org/abstract.cfm?URI=oe-21-23-27826`. 116

[265] He, J. *et al.* Effect of low-Raman window position on correlated photon-pair generation in a chalcogenide $Ge_{11.5}As_{24}Se_{64.5}$ nanowire. *Journal of Applied Physics* **112**, 123101 (2012). URL `http://scitation.aip.org/content/aip/journal/jap/112/12/10.1063/1.4769740`. 121

[266] Collins, M. J. *et al.* Low Raman-noise correlated photon-pair generation in a dispersion-engineered chalcogenide As_2S_3 planar waveguide. *Opt. Lett.* **37**, 3393–3395 (2012). URL `http://ol.osa.org/abstract.cfm?URI=ol-37-16-3393`. 121

[267] Gisin, N. How far can one send a photon? *ArXiv e-prints* (2015). `http://arxiv.org/abs/1508.00351`. 125

[268] Natarajan, C. M., Tanner, M. G. & Hadfield, R. H. Superconducting nanowire single-photon detectors: physics and applications. *Superconductor Science and Technology* **25**, 063001 (2012). URL `http://stacks.iop.org/0953-2048/25/i=6/a=063001`. 166

[269] Steinlechner, F. *et al.* A high-brightness source of polarization-entangled photons optimized for applications in free space. *Opt. Express* **20**, 9640–9649 (2012). URL `http://www.opticsexpress.org/abstract.cfm?URI=oe-20-9-9640`. 181

APPENDICES

Appendix A

Code for optimizing entangled state and measurement settings

Here I provide the MATLAB code for optimizing the violation of the CH inequality as in section 2.5. The software is freely available to use and modify; however, the software is provided "as is", without warranty of any kind, express or implied, including but not limited to the warranties of merchantability, fitness for a particular purpose and noninfringement. In no event shall the authors or copyright holders be liable for any claim, damages or other liability, whether in an action of contract, tort or otherwise, arising from, out of or in connection with the software or the use or other dealings in the software.

```
%%%%%%%%%%%%%%%%%%%% Optimize_CH.m
% Use to optimize the entangled state balance and measurement angles for
% the CH B' parameter (eq 3, Christensen et al, PRL 2013 [48])
% The CH inequality is then B' < 1, with (B' − 1) giving the approximate
% efficiency overhead available.
% Set the experiment parameters in CH_B.m, then run this to optimize.
clear
% X0 is the start point for gamma, alpha, beta, alpha_p, beta_p (degrees)
% where:
% cos(gamma)HH + sin(gamma)VV balance angle (so HWP angle is gamma/2)
% alpha/_p = Alice's first/second polarizer angle (so HWP angle is /2)
```

```
% beta/_p = Bob's first/second polarizer angle (so HWP angle is /2)
% Can get away with optimizing only 3 angles, since beta/_p = −alpha/_p

% X0 = [gamma, alpha, alpha_p,];
X0 = [45, 5, −28]; % A good starting point
% Perform optimization, in degrees for polarizer angles. HWPs would use
% half these angles
X = fminsearch(@(X) CH_B(X,1), X0)
% Run this to generate a matrix of expected counts for all measurement ...
    settings combinations
CH_val = 1/CH_B(X, 0) − 1

%%%%%%%%%%%%%%%%%%%% CH_B.m
function B_inv = CH_B(X, opting)
% Simulation for loophole−free Bell test at NIST
% Evan Meyer−Scott 2015

%% Experiment parameters
coinc_window = .2e−9; % Coincdence window (s) − only used to calculate ...
    probablity of darks
rep_rate = 79.3e6; % Rep rate of laser − used to calculate probabily of ...
    down−conversion
darks_ch1 = 2000; % Darks/s for Alice (could change to pdark per trial ...
    if known)
eff_ch1 = .747; % Heralding efficiency for Alice
darks_ch2 = 2000; % Darks/s for Bob (could change to pdark per trial if ...
    known)
eff_ch2 =.732; % Heralding efficiency for Bob
coinc = 33e3; % Measured coincidences for one polarizer setting (e.g. ...
    HH) for balanced pumping
int_time = 5; % Integration time, useful for comparing measured counts ...
    to counts simulated here

% Optimized parameters:
% Optimize over CH value, or normalized B' value? − The latter doesn't
% converge to 45deg pump for highly−efficient detectors. It is probably not
% awesome.
opt_CH = 1;
```

```
% cos(gamma)HH + sin(gamma)VV balance angle (so HWP angle is gamma/2)
gamma = (X(1)) * pi/180;
% Alice/Bob measurement angles
alpha = X(2);
alpha_p = X(3);
beta = -alpha; % Bob's angles are just the negative of Alice's
beta_p = -alpha_p;

% Set up quantum optics
N = 4;
standard_defintions_qo_toolbox;

%% Create two-photon entangled state
% Net source rate (i.e. backcalculated from the coincidences) gives SPDC ...
    strength
net_source_rate = coinc / eff_ch1 / eff_ch2;
epsilon = sqrt(net_source_rate / rep_rate);
% Create entangled state, modes are |Ha,Va,Hb,Vb>
H_spdc = sqrt(2) * (sin(gamma) * (tensor(a',ida,a',ida) + ...
    tensor(a,ida,a,ida)) +...
     exp(1i*0*pi/180)*cos(gamma) * (tensor(ida,a',ida,a') + ...
         tensor(ida,a,ida,a)))*epsilon;
U_spdc = expm(-1i * H_spdc);
spdc_state = U_spdc * tensor(vacc, vacc, vacc, vacc);
% Ideal state for checks:
% spdc_state = 1/sqrt(2) * (tensor(oneph, vacc, oneph, vacc ) + ...
    tensor(vacc, oneph, vacc, oneph));

% Detector setup
[proj_ch1, ~] = BucketDetector_noise(N, eff_ch1, darks_ch1 * coinc_window);
[proj_ch2, ~] = BucketDetector_noise(N, eff_ch2, darks_ch2 * coinc_window);
% Or use number resolving detectors with no darks:
% [proj_ch1, unproj_ch1] = SPDDetector(N, eff_ch1);
% [proj_ch2, unproj_ch2] = SPDDetector(N, eff_ch2);

% Uncomment to check agreement  with measurements in lab
% H_singles = expect(tensor(proj_ch1, ida, ida, ida), spdc_state) * ...
    rep_rate;
```

```
% HH_coinc = expect(tensor(proj_ch1, ida, proj_ch2, ida), spdc_state) * ...
    rep_rate;
% VH_coinc = expect(tensor(ida, proj_ch1, proj_ch2, ida), spdc_state) * ...
    rep_rate;
% vis = (HH_coinc - VH_coinc) / (HH_coinc + VH_coinc);
% darks_windowed = expect(proj_ch1, vacc) * rep_rate;


%% Measurements
% Use a HWP for polarizer angle alpha/beta and alpha_prime/beta_prime ...
    (degrees):
% Means the HWPs are at alpha/2, etc.
H_HWP_alpha = (tensor(a,a')*exp(1i*pi/2) + tensor(a',a) * exp(-1i*pi/2)) ...
    * alpha * pi/180;
U_HWP_alpha = expm(-1i * H_HWP_alpha);
H_HWP_beta = (tensor(a,a')*exp(1i*pi/2) + tensor(a',a) * exp(-1i*pi/2)) ...
    * beta * pi/180;
U_HWP_beta = expm(-1i * H_HWP_beta);
H_HWP_alpha_p = (tensor(a,a')*exp(1i*pi/2) + tensor(a',a) * ...
    exp(-1i*pi/2)) * alpha_p * pi/180;
U_HWP_alpha_p = expm(-1i * H_HWP_alpha_p);
H_HWP_beta_p = (tensor(a,a')*exp(1i*pi/2) + tensor(a',a) * ...
    exp(-1i*pi/2)) * beta_p * pi/180;
U_HWP_beta_p = expm(-1i * H_HWP_beta_p);

% Measurement probabilities for terms in CH inequality
prob_ab = real(expect(tensor(proj_ch1, ida, proj_ch2, ida), ...
    tensor(U_HWP_alpha, U_HWP_beta) * spdc_state));
prob_abp = real(expect(tensor(proj_ch1, ida, proj_ch2, ida), ...
    tensor(U_HWP_alpha, U_HWP_beta_p) * spdc_state));
prob_apb = real(expect(tensor(proj_ch1, ida, proj_ch2, ida), ...
    tensor(U_HWP_alpha_p, U_HWP_beta) * spdc_state));
prob_apbp = real(expect(tensor(proj_ch1, ida, proj_ch2, ida), ...
    tensor(U_HWP_alpha_p, U_HWP_beta_p) * spdc_state));
prob_a = real(expect(tensor(proj_ch1, ida, ida, ida), ...
    tensor(U_HWP_alpha, ida, ida) * spdc_state));
prob_b = real(expect(tensor(ida, ida, proj_ch2, ida), tensor(ida, ida, ...
    U_HWP_beta) * spdc_state));
```

```
prob_ap = real(expect(tensor(proj_ch1, ida, ida, ida), ...
   tensor(U_HWP_alpha_p, ida, ida) * spdc_state));
prob_bp = real(expect(tensor(ida, ida, proj_ch2, ida), tensor(ida, ida, ...
   U_HWP_beta_p) * spdc_state));

% CH value (scales with pump power)
CH = (prob_ab + prob_apb + prob_abp - prob_apbp - prob_a - prob_b);

% B' value (mostly independent of pump power, but convenient to show ...
   overhead)
B = (prob_ab + prob_apb + prob_abp - prob_apbp) / (prob_a + prob_b)
if ~opting % Display a counts matrix for comparison with experiments
    counts = round([prob_a *rep_rate, prob_ab  *rep_rate, prob_b *rep_rate;
              prob_a *rep_rate, prob_abp *rep_rate, prob_bp*rep_rate;
              prob_ap*rep_rate, prob_apb *rep_rate, prob_b *rep_rate;
              prob_ap*rep_rate, prob_apbp*rep_rate, ...
                 prob_bp*rep_rate]*int_time)
end

% For minimization
if opt_CH
    B_inv = 1/(CH+1);
else
    B_inv = 1/(B+1);
end
if B_inv < 0; % Strong penalty for negative values
    B_inv = 1e6;
end

% Can check CH value agrees with Thomas' code, but only for "standard"
% angles, or set last parameter to 1 to assume fair sampling.
% [ch chsh] = ...
   msrmt_ch_chsh_2side_rho(N,spdc_state,proj_ch1,ida,proj_ch2,ida,0)
```

Appendix B

Component and system characterization

Here I show measured transmission efficiencies for various components used in the experiments, and efficiency curves for our superconducting nanowire single-photon detectors.

B.1 WDMs for precertification

After the precertification stage of chapter 4, the 780 nm stabilization light is first split off from the telecom photon pairs using a fused-fibre wavelength-division multiplexer (WDM). Because the fibre is multimode for 780 nm the isolation and efficiency at this wavelength is not very good, but this is thankfully unimportant, as the stabilization works for detection rates as low as 1×10^6 counts/s, and the laser has plenty of power. Most critical is good transmission of the photon pairs, which fig. B.1 shows is >90 % over the range 1500 nm to 1600 nm. To split the signal and flag photons, a second WDM is employed with centre wavelength 1545 nm as shown in fig. B.1. The band lost during the reflect-transmit transition is very small compared to many WDMs. Finally, the two WDMs together provide 30 dB to 40 dB isolation from the 780 nm stabilization light at the flag and signal wavelengths.

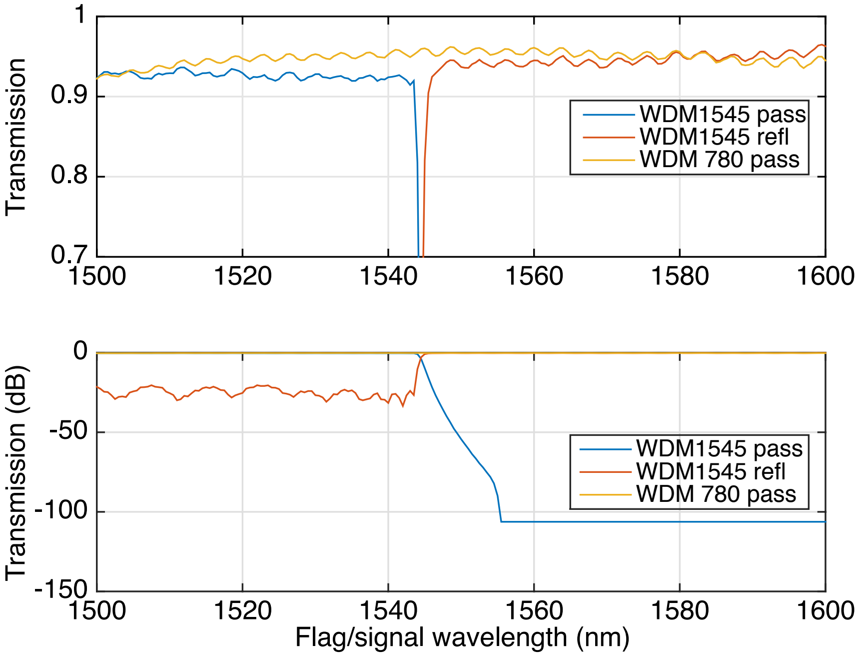

Figure B.1: The WDMs after the precertification PDC split the stabilization light from the photons (WDM780) and subsequently split the flag and signal photons (WDM1545). The measured transmission is plotted both on a linear scale (top) to see the maximum efficiencies, and a log scale (bottom) to see the extinction outside the passbands.

B.2 SNSPDs: efficiency and dark counts

Superconducting nanowire single-photon detectors work by sending a current through a very thin superconducting wire [268]. The current density is so high that absorbing a single photon is enough to trip the wire into the normal-conducting regime. The wire is resistive for a short time before relaxing back to superconductivity, causing a voltage pulse that can be amplified and detected by external circuitry.

The SNSPDs have just one user-controlled parameter, the bias current, set via a bias voltage and resistor. In general, larger currents mean higher detection efficiency, higher dark and background counts, and lower jitter. Thus there is an optimal bias setting that depends on the detector and the application. Here background and dark counts are indistinguishable, though their sources are different: dark counts are intrinsic to the detector and are usually only a few per second, while background counts from blackbody radiation from connecting fibres and other warm objects can be around a thousand per second. In fig. B.2 I show the dependence of efficiency and dark counts (from now on "dark counts" means all dark+background counts) on bias voltage for each of our four detectors, on logarithmic and linear scales. Detector efficiency has a large uncertainty (±10 %) as I measured it with a pulsed laser and attenuators, which are difficult to calibrate well.

Additionally, the timetagger or constant-fraction discriminator used to count the electrical pulses produced by the SNSPDs has a tuneable voltage threshold. In general, lower discriminator thresholds mean lower jitter, with only a little more noise until a lower bound where noise counts become huge. Thus the optimal threshold is usually just above this noise bound. In fig. B.3 I show the count dependence on threshold setting. Most detectors have a nice large plateau where the number of counts is stable versus threshold, with better jitter achieved at lower thresholds. Finally, I show in fig. B.4 the measured jitter of pairs of SNSPD channels. I measured this by pumping the precertification stage with a strong laser to produce photon pairs, plotting a time histogram of coincident detections between two SNSPD channels, and finding the interquartile range, defined as the difference between the 25th and 75th percentiles of the histogram. I took three times the interquartile range as the relevant jitter, as this captures almost all the coincidences. By optimizing the thresholds of all detectors together, I achieved jitter of 2.34 ns between channels 1 and 2,

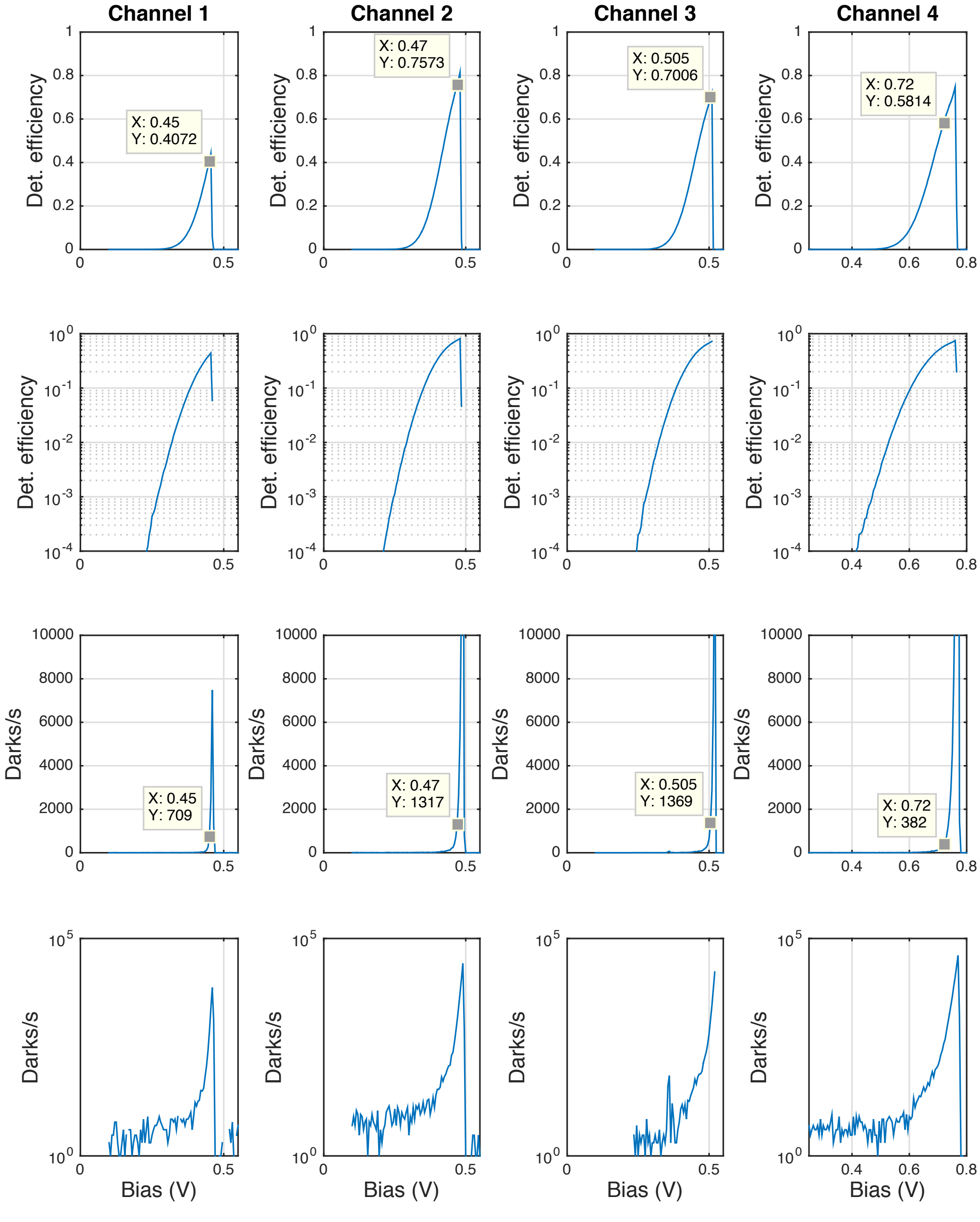

Figure B.2: Measured detection efficiency and dark counts of SNSPDs versus bias voltage. The operation point in chapter 4 is labeled on the linear plots, where channel 1 corresponds to $D1$, channel 4 to $D2$, channel 2 to $D3$, and channel 3 to $D4$.

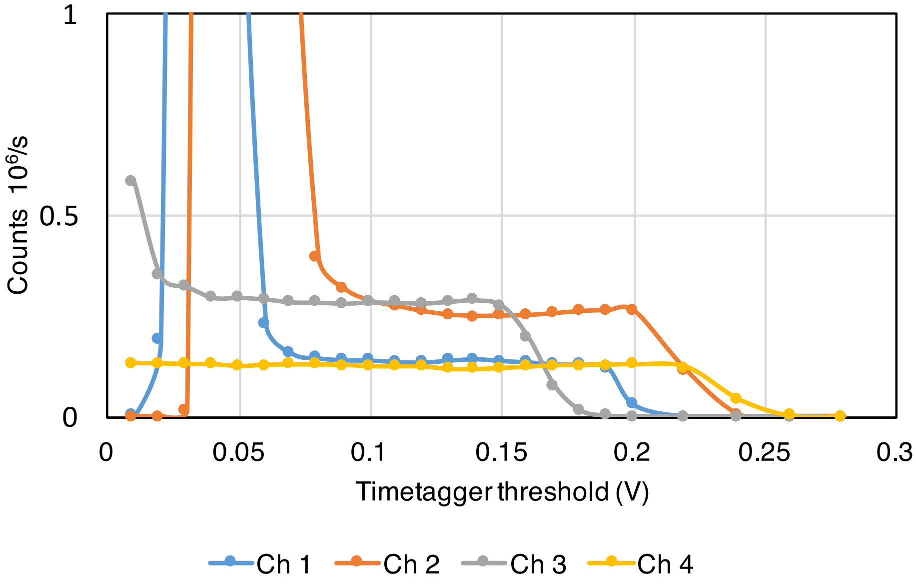

Figure B.3: Number of counts per second versus timetagger voltage threshold for SNSPDs. Each channel has a large range with approximately the same count rate, and a lower threshold above which the count rate increases dramatically due to electronics noise. The different values of this bound are due to DC voltage offsets on each timetagger channel, not the SNSPDs.

2.11 ns between channels 4 and 3, 1.64 ns between channels 4 and 2, and 1.64 ns between channels 1 and 2.

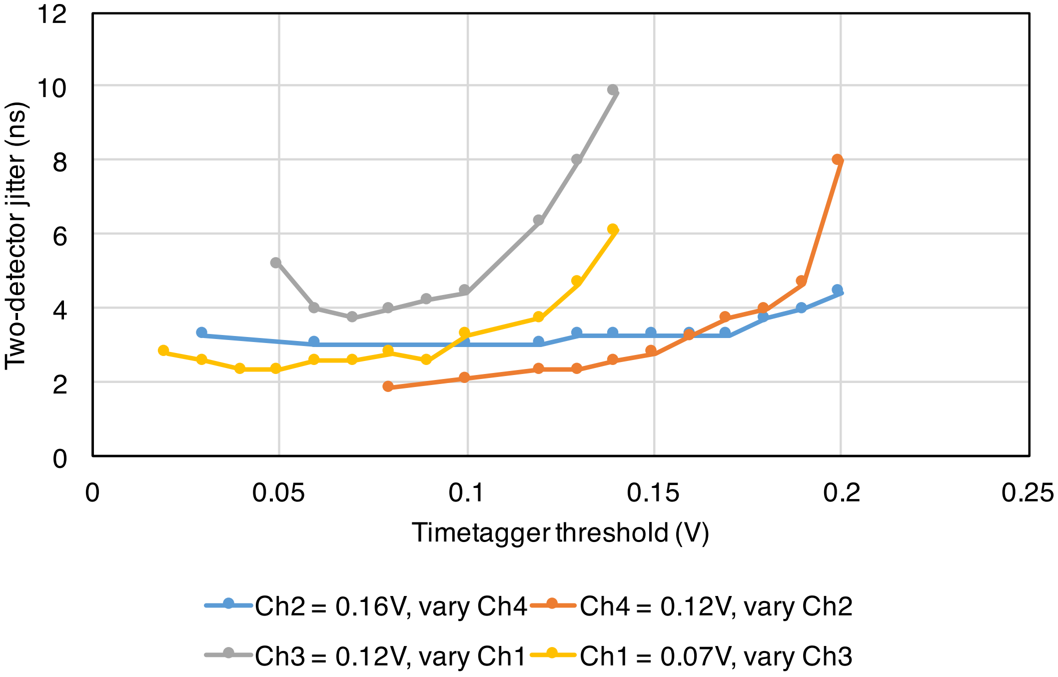

Figure B.4: Detector jitter for pairs of SNSPDs as measured with correlated photon pairs. The jitter is three times the interquartile range of the photon-pair timing histograms. For each line, one detector's threshold is held fixed while the other is varied, as shown in the legend. In all cases the best jitters are for low thresholds, though jitter starts to climb as electronic noise is introduced at the lowest thresholds. The x-axes for each curve are offset due to DC offsets between channels in the timetagger's thresholds.

B.3 Chalcogenide microwires and DWDMs

The transmission of the chalcogenide microwire sample used in section 7.2 is plotted in fig. B.5. At short wavelengths, transmission drops due to two-photon absorption in the As_2Se_3 chalcogenide glass, while at long wavelengths, transmission drops due to absorption in the polymer cladding. For some samples the transmission was strongly polarization dependent, especially if the sample included a bend or touched its container. This sample was suspended in the air and held straight, limiting such effects.

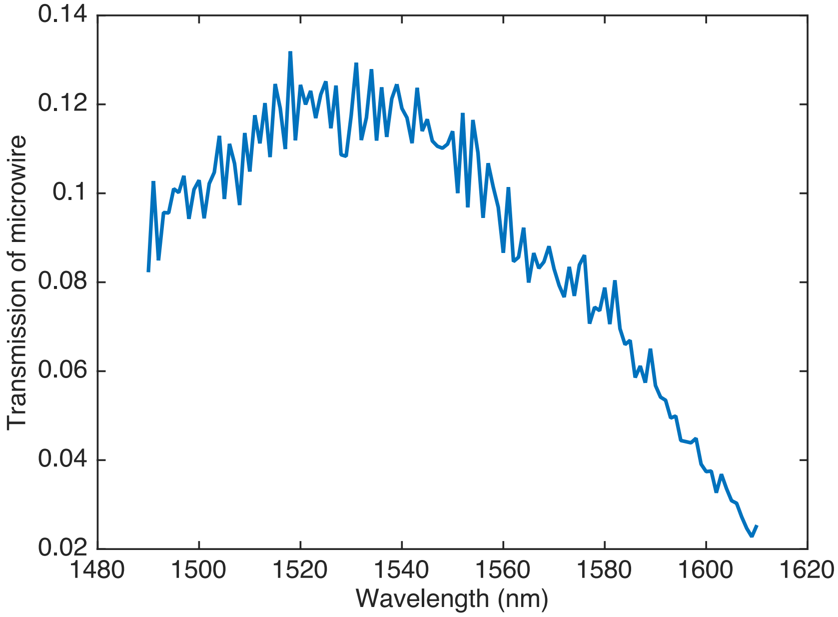

Figure B.5: Measured transmission efficiency of chalcogenide microwire, including single-mode-fibre pigtails.

I also show the transmission data for the wavelength-division-multiplexing filters used to separate signal and idler photons after the chalcogenide microwire. The DWDM filter is shown in fig. B.6(a), and the AWG filter is shown in fig. B.6(b). The DWDM provides flat transmission in the passband and good extinction. The AWG provides more densely spaced channels, but worse transmission and extinction.

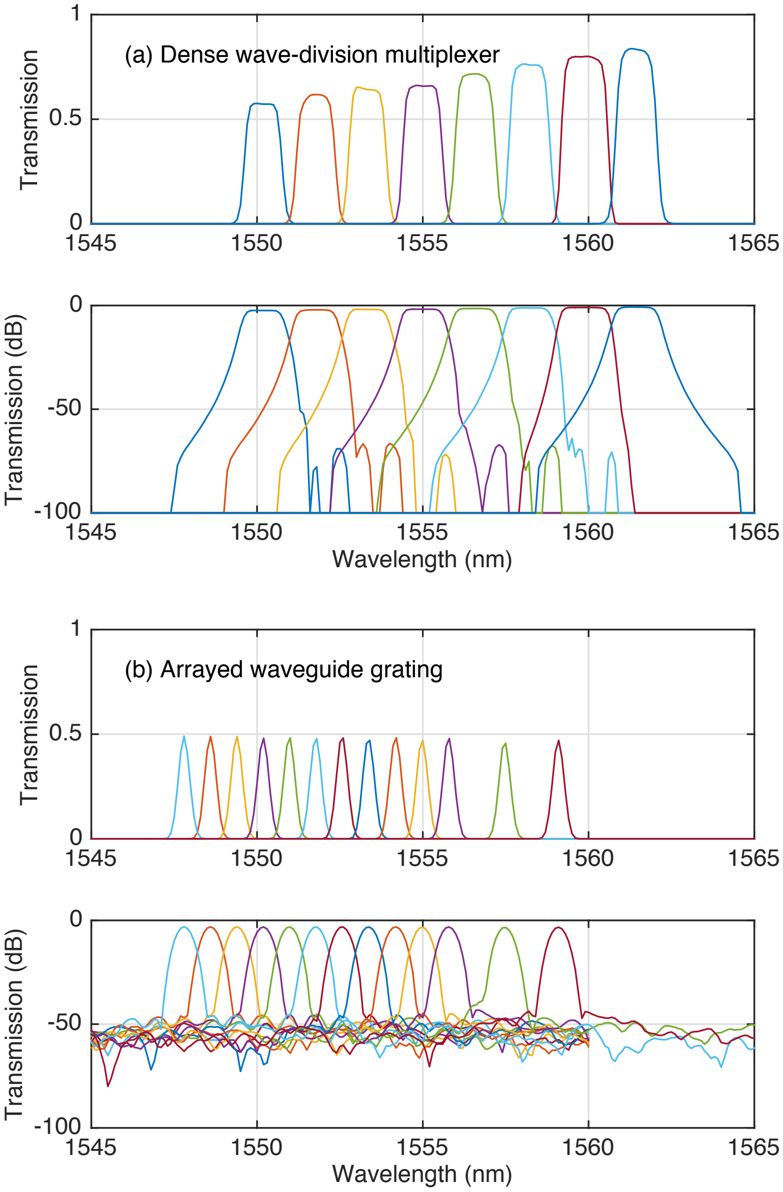

Figure B.6: (a) Measured transmission efficiency and optical density of the dense-wavelength-division multiplexer used to split signal and idler photons produced in chalcogenide microwire. (b) Measured transmission efficiency and optical density of the arrayed-waveguide grating used for additional isolation.

Appendix C

Code calculating Raman scattering spectrum in silica fibres

Here I provide the MATLAB code for calculating the Raman scattering spectrum as in fig. 5.2. The software is freely available to use and modify; however, the software is provided “as is”, without warranty of any kind, express or implied, including but not limited to the warranties of merchantability, fitness for a particular purpose and noninfringement. In no event shall the authors or copyright holders be liable for any claim, damages or other liability, whether in an action of contract, tort or otherwise, arising from, out of or in connection with the software or the use or other dealings in the software.

```
%   This program computes the number of output photons per nm versus
%   wavelength due to spontaneous Raman scattering in fibre
%%
% Parameters to change:
% omega: width of Raman spectrum to calculate, make small enough that
% lambda doesn't go negative
% T: temperature of our fibre
% pump: pump wavelength in nm
% w_actual: radius of fibre mode for effective area
% n_A: pump frequency scaling parameter for effective area
% P: pump peak power, or average power for CW
```

```
% Dc: pump duty cycle, (=1 for CW)
% L: fibre length in m
% loss: fibre loss in dB/km
% bandwidth: bandwidth of output bandpass filter in m
h=6.626e-34;
kb=1.38e-23;
c=2.998e8;
c_cm=c*100; % in cm/s

%% Find Raman spectrum
% Following "Multiple-vibrational-mode model for fiber-optic Raman gain
% spectrum and response function" Hollenbeck and Cantrell,
% J. Opt. Soc. Am. B.  (2002) [216] to find the spectrum.

% This is a very general solution. It provides the output Raman spectrum as
% a function of (f_pump - f) i.e. the red frequency shift from the pump.
% This part must only be run once, then can be reused and rescaled for
% other parameters (temperature, fibre type, pump wavelength)

% Use a 13 oscillator model to approximate the experimental curves
if ~exist('s')  % Only need to run this once
mode_number=1:13;
component_position=[56.25 100 231.25 362.50 463 497 611.5 691.67 793.67 ...
    835.5 930 1080 1215];
peak_intensity=[1 11.4 36.37 67.67 74 4.5 6.8 4.6 4.2 4.5 2.7 3.1 3];
gaussian_FWHM=[52.1 110.42 175 162.5 135.33 24.5 41.5 155 59.5 64.3 150 ...
    91 160];
lorentzian_FWHM=[17.37 38.81 58.33 54.17 45.11 8.17 13.83 51.67 19.83 ...
    21.43 50 30.33 53.33];
% Spectrum in cm^-1: make smaller for speed or larger to see more spectrum
% May have to decrease it so lambda doesn't go negative!
omega=1:6000;
% Relevant timescale: up to 1 ps
t=(0:1000)*1e-15;
s=zeros(1,length(omega));
p = waitbar(0,'Please wait...');
% Perform integration from Hollenbeck
for k=1:length(omega)
```

```
    for m=1:length(mode_number)
        s(k)=s(k)+peak_intensity(m)/2*trapz(t,(cos((2*pi*c_cm...
        *(component_position(m)-omega(k))).*t)...
            -cos((2*pi*c_cm*(component_position(m)+omega(k))).*t))...
            .*exp(-pi*c_cm*lorentzian_FWHM(m)*pi*t)...
            .*exp(-(pi*c_cm*gaussian_FWHM(m))^2*t.^2/4));
    end
    waitbar(k/length(omega))
end
close(p)
s=s/max(s); % normalize Raman gain spectrum to 1
% Convert to delta f (negative since Stokes scatters to lower frequency)
delta_f=-omega*c_cm;
end

%% Add temperature dependence
% "Low-Frequency and Low-Temperature Raman Scattering in Silica Fibers",
% Stolen and Bosch, PRL (1982) [218]

T_meas=300; % Temp at which gain spectrum was measured in above ref
T=300; % Desired temperature

s_Tk=s./(1./(exp(h*-delta_f/(kb*T_meas))-1)+1).*(1./(exp(h*-delta_f/(kb*T))-1)+1);

% plot(delta_f,s,delta_f,s_Tk)

%% Scale for type and size of fibre

% Given pump in nm, convert to frequency
pump=770;
f=c/pump/1e-9;

% Reference fibre parameters:
w_ref=5.06;                                   % Radius of fibre mode
Aeff_ref=pi*w_ref.^2;                         % Simple effective area

% Actual fibre parameters
w_actual=2.02;                                   % Radius of fibre mode
```

```
Aeff_actual=pi*w_actual.^2;                    % Simple effective area

%% Pump frequency dependence
% Pump dependence g=omega_pump^n * s(delta_f) * C from "Pump-wavelength
% dependence of Raman gain in single-mode optical fibers", Newbury, J. ...
   Lightwave
% Technology (2003) [217].
% n = 1.1 + n_A, the effective area scaling parameter: use 1.5 for BSMF and
% 5 for PCF: both approximations for now.
% n~2.3 for SMF-28, highly dependent on effective area

% Find C from reference value, g=5e-4 W^-1 m^-1, where s=1 (max) measured
% for 1460 nm pump
n_A = 1.1;

% Scale also with Aeff(reference)/Aeff(actual) from fibre parameters
C=5e-4/(2*pi*f_ref)^(1.1+n_A);
g=(2*pi*f)^(1.1+n_A)*s_Tk*C*Aeff_ref/Aeff_actual;

%% Finally calculate number of photons per Hz of bandwidth per laser pulse
% Pump average power (watts)
P = .03;
% Energy per pulse
e_pulse=P/76e6;
% Fibre length (m) and loss (dB/km) give effective length
L=.26;
loss=10;
L_eff=(1-exp(-loss/1000*L))/(loss/1000);

% Spectrum: number of output Raman photons per pulse per Hz from
% "Microstructure-fiber-based source of photonic entanglement",
% Fan et al, IEEE Quantum Electronics, (2009) [148].
N=g*L_eff*e_pulse;

% Find also the anti-Stokes version: symmetric around pump and scaled by
% exp(- Delta_E/(kb T)), where Delta_E is the energy difference between
% Stokes and anti-Stokes phonons. (assume degeneracy of phonon modes is
% constant)
```

```
N_a_S=(N.*exp(delta_f*h/kb/T));

% Relevant wavelength ranges in nm
lambda=c./(f+delta_f)*1e9;
lambda_a_S=(c./(f-delta_f)*1e9);
% plot(lambda,N,lambda_a_S,N_a_S)

%% Now make graph of Raman photons output versus wavelength, filtered to ...
    bandwidth
% Bandwith of band pass filter (m)
bandwidth=3e-9;
% Stokes
lambda_out=zeros(1,length(lambda)-100);
N_out=zeros(1,length(lambda)-100);
% Integrate over filter bandwidth, at each wavelength
for m=1:length(lambda)-100
    lambda_out(m)=lambda(m)*1e-9;
    f_low=c/(lambda_out(m)+bandwidth);
    f_high=c/(lambda_out(m));
    stop=find(abs(delta_f+f-f_low)==min(abs(delta_f+f-f_low)));
    start=find(abs(delta_f+f-f_high)==min(abs(delta_f+f-f_high)));
    if start==stop
        N_out(m)=N_out(m-1);
    else
        N_out(m)=trapz(-delta_f(start:stop),N(start:stop));
    end
end

% Anti-stokes
lambda_out_a_S=zeros(1,length(lambda_a_S)-100);
N_out_a_S=zeros(1,length(lambda_a_S)-100);
% Integrate over filter bandwidth, at each wavelength
for m=1:length(lambda_a_S)-100
    lambda_out_a_S(m)=lambda_a_S(m)*1e-9;
    f_low=c/(lambda_out_a_S(m));
    f_high=c/(lambda_out_a_S(m)-bandwidth);
    start=find(abs(-delta_f+f-f_low)==min(abs(-delta_f+f-f_low)));
    stop=find(abs(-delta_f+f-f_high)==min(abs(-delta_f+f-f_high)));
```

```
    if start==stop
        N_out_a_S(m)=N_out_a_S(m-1);
    else
        N_out_a_S(m)=trapz(-delta_f(start:stop),N_a_S(start:stop));
    end
end

%% Plot Raman scattering in photons/nm/s
semilogy(lambda_out/1e-9,N_out*76e6,lambda_out_a_S/1e-9,N_out_a_S*76e6) ...
   %*76e6 for laser rep rate
ylim([1,max(N_out/3*76e6)*10])
grid on
legend('Stokes','Anti-Stokes')
xlabel('Output wavelength (nm)')
ylabel(sprintf('Raman photons per second per %d nm',bandwidth/1e-9))
title(sprintf('Raman noise photons for BSMF %0.2f um fibre \n with %d mW ...
   CW %d nm pump %d m long at %d k',d, P*1000, pump, L, T))
hold on
```

Appendix D

Further details of phase compensation for cross-spliced source

D.1 Temporal calculations: single-twist sausage

I examine the time of arrival of the H and V signal and idler photons at the detectors,

$$t_{s_H},\ t_{i_H},\ t_{s_V},\ t_{i_V}, \tag{D.1}$$

assuming a sausage source with one splice in the middle of two PM fibres each of length L, with the slow axis horizontal for the first section.

I assume no birefringence except for a controlled birefringence before the fibre in the pump beam (with the H portion of the beam arriving T_0 after the V portion) and in the signal arm after the fibre (with H slower than V by T_1). Then the relevant arrival times at the detectors are (neglecting free-space propagation and propagation in collecting fibres, since they are not birefringent)

$$t_{s_H} = \frac{Lg_p}{c} + \frac{Lg_s}{c} + T_0 + T_1, \tag{D.2}$$

$$t_{i_H} = \frac{Lg_p}{c} + \frac{Lg_i}{c} + T_0, \tag{D.3}$$

$$t_{s_V} = \frac{Lg_s}{c} + \frac{L(g_s + B)}{c}, \tag{D.4}$$

$$t_{i_V} = \frac{Lg_i}{c} + \frac{L(g_i + B)}{c}. \tag{D.5}$$

Here g_x is the group refractive index of the x mode (pump, signal, or idler) and B is the wavelength-independent birefringence of the fibre ($B = n_{fast} - n_{slow}$). I assume each photon pair is created at the beginning of its fibre section since each subsequent point in the first section maps equally to a point in the second section.

For maximum entanglement visibility we need $t_{s_H} = t_{s_V}$ and $t_{i_H} = t_{i_V}$. This implies

$$\frac{L}{c}(g_p + g_s) + T_0 + T_1 = \frac{L}{c}(g_s + g_s + B) \tag{D.6}$$

$$\frac{L}{c}(g_p + g_i) + T_0 = \frac{L}{c}(g_i + g_i + B). \tag{D.7}$$

Thus

$$T_0 = \frac{L}{c}(B + g_i - g_p) \tag{D.8}$$

$$T_1 = \frac{L}{c}(B + g_s - g_p) - T_0 = \frac{L}{c}(g_s - g_i). \tag{D.9}$$

This analysis gives identical results for photon pairs created at any point along each fibre section. If the T_0 delay is shifted to the idler arm instead of the input pump, the required delays become

$$T_0 = \frac{L}{c}(B + g_i - g_p) \tag{D.10}$$

$$T_1 = \frac{L}{c}(B + g_s - g_p). \tag{D.11}$$

The parameters from simulation assuming a 4 μm fibre core diameter are

$$\begin{aligned} L &= 0.13\,\mathrm{m} \\ c &= 2.998 \times 10^{3}\,\mathrm{m/s} \\ B &= 3 \times 10^{-4} \\ \lambda_p &= 770\,\mathrm{nm},\ \lambda_s = 670\,\mathrm{nm},\ \lambda_i = 905\,\mathrm{nm} \\ g_p &= 1.46848,\ g_s = 1.47355,\ g_i = 1.46423. \end{aligned} \tag{D.12}$$

This gives $T_0 = -1.7\,\mathrm{ps}$ and $T_1 = 4.0\,\mathrm{ps}$ for the pre-compensation/post-compensation scheme, and $T_0 = -1.7\,\mathrm{ps}$ (idler) and $T_1 = 2.3\,\mathrm{ps}$ (signal) for the double-post-compensation scheme. From Sellmeier equations, this requires total a quartz thickness from 35 mm to 60 mm.

D.2 Temporal calculations: n-twist ($2n$-link) sausage source

It may be beneficial to have many small links interlaced with 90° rotation between each, rather than only two long sections. I find the output times of each signal and idler H/V photon as before, with each link of length L. If the photon pairs are created in the first possible link,

$$t_{s_H} = \frac{Lg_p}{c} + \frac{Lg_s}{c} + T_0 + T_1 + \frac{(n-1)L(g_s+B)}{c} + \frac{(n-1)L(g_s)}{c} \tag{D.13}$$

$$t_{i_H} = \frac{Lg_p}{c} + \frac{Lg_i}{c} + T_0 + \frac{(n-1)L(g_i+B)}{c} + \frac{(n-1)L(g_i)}{c} \tag{D.14}$$

$$t_{s_V} = \frac{Lg_s}{c} + \frac{L(g_s+B)}{c} + \frac{(n-1)L(g_s+B)}{c} + \frac{(n-1)L(g_s)}{c} \tag{D.15}$$

$$t_{i_V} = \frac{Lg_i}{c} + \frac{L(g_i+B)}{c} + \frac{(n-1)L(g_i+B)}{c} + \frac{(n-1)L(g_i)}{c}. \tag{D.16}$$

This leads to the same conditions on T_0 and T_1 as above,

$$T_0 = \frac{L}{c}(B + g_i - g_p) \tag{D.17}$$

$$T_1 = \frac{L}{c}(g_s - g_i), \tag{D.18}$$

only now L is a much smaller length. Given $L = 1\,\text{cm}$, this gives $T_0 = -0.13\,\text{ps}$ and $T_1 = 0.31\,\text{ps}$, or $T_0 = -0.13\,\text{ps}$ and $T_1 = 0.18\,\text{ps}$ for the double post-compensation scheme. This could be accomplished by tilting a multi-order wave plate or with ~1 mm of quartz. The main benefit of many sausage links is that the four-wave mixing probability can be increased with longer fibre length without requiring proportionally more birefringent compensation.

D.3 Phase method

Another method of finding the desired birefringent crystal lengths used in chapter 6 is to plot a map of the phase ϕ in the entangled state $|\phi\rangle = \frac{1}{\sqrt{2}}\left(|HH\rangle + \mathrm{e}^{i\phi}|VV\rangle\right)$. The phase will vary strongly with pump and signal wavelength (the idler's wavelength is determined from the signal and pump wavelengths through energy conservation), due to the different phase accumulations by different spectral components. Making this phase map as flat as possible over the pump and signal bandwidths using birefringent compensators leads to the best (most pure) entangled state and hence gives the optimal length of the compensators. This method comes from similar work on crossed-crystal sandwich sources [240, 241, 269].

I care only about relative phases between the first and second terms of the entangled state. The phase obtained in the length of fibre in which the photons are created is equal for the first and second stretches. Assume that the slow axis is vertical in the first section, such that the $|HH\rangle$ photons are created first. Then these pick up an extra phase in the second length of fibre, given by

$$\phi_1(\lambda_s, \lambda_p) = \frac{2\pi L_2}{\lambda_s}\left(n(\lambda_s) + B\right) + \frac{2\pi L_2}{\lambda_i}\left(n(\lambda_i) + B\right), \tag{D.19}$$

where $\lambda_i = \frac{\lambda_s \lambda_p}{2\lambda_s - \lambda_p}$ and $n(\lambda)$ is the propagation constant in the fibre. Additionally the $|VV\rangle$ term picks up an extra phase in the first stretch of fibre, through the pump. This phase must be multiplied by two as compared to the $\chi^{(2)}$ version, since two pump photons combine to make the $|VV\rangle$ photons, giving

$$\phi_2(\lambda_p) = 2\frac{2\pi L_1}{\lambda_p}\left(n(\lambda_p)\right). \tag{D.20}$$

Here there is no extra B term, since the pump that will produce $|VV\rangle$ photons in the second stretch is polarized on the fast axis in the first stretch. The total phase is then

$$\phi(\lambda_s, \lambda_p) = \phi_2 - \phi_1 \tag{D.21}$$

If, however, the two stretches of fibre have different lengths, $L_1 \neq L_2$, more terms are needed to account for the different phase acquired in the stretch in which photons are created. This additional phase of the $|HH\rangle$ in the first stretch of fibre is

$$\phi_1'(\lambda_s, \lambda_p) = \frac{2\pi L_1}{\lambda_s}\left(n(\lambda_s)\right) + \frac{2\pi L_1}{\lambda_i}\left(n(\lambda_i)\right), \tag{D.22}$$

and the additional phase of the $|VV\rangle$ photons in the second stretch is

$$\phi_2'(\lambda_s, \lambda_p) = \frac{2\pi L_2}{\lambda_s}\left(n(\lambda_s)\right) + \frac{2\pi L_2}{\lambda_i}\left(n(\lambda_i)\right). \tag{D.23}$$

The total phase is then

$$\phi(\lambda_s, \lambda_p) = \phi_2 - \phi_1 + \phi_2' - \phi_1'. \tag{D.24}$$

Taking the parameters as above, this phase varies strongly over the pump and signal bandwidths, as seen in fig. D.1.

The phase variation can be corrected by one of two methods: pre/post compensation with a strongly birefringent crystal like YVO_4, or post/post compensation with much shorter YVO_4 or a weaker birefringent material like quartz. The advantage of the pre/post compensation scheme is that the post-compensation is independent of the

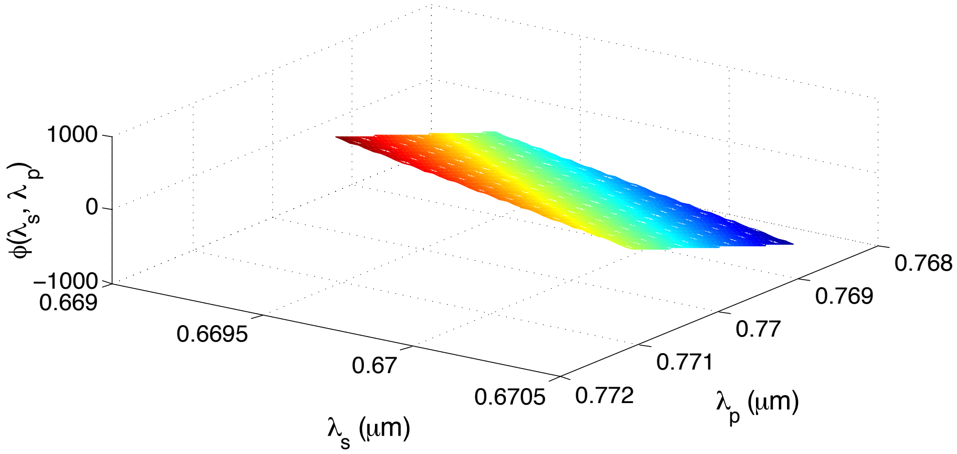

Figure D.1: Calculated phase map (in degrees) versus pump and signal wavelengths. The phase varies by hundreds of degrees over these bandwidths. Here and in all following plots, the irrelevant mean phase has been subtracted, such that the map is centred on 0°.

pre-compensation; one can simply optimize post-compensation and then optimize pre-compensation. (Note that the reverse is not true; pre-compensation does depend on post-compensation.) Additionally, if the pump has a long coherence length (i.e. not pulsed), the variation with pump wavelength can be neglected and only post-compensation is needed. Here the post-compensation is based on birefringence in the dispersion of the compensator crystal. The photons that are created in the second section of fibre need to be spread more in time (idler farther ahead of signal) as they had less time to disperse in fibre compared to photons created in the first section. Thus the post-compensator has more dispersion for V-polarized light (so the slow/extraordinary axis of the YVO_4 is vertical), and is cut to a length such that the final time between signal and idler is the same for the $|HH\rangle$ and $|VV\rangle$ photons. This has the effect of causing additional temporal walk-off *between* $|HH\rangle$ and $|VV\rangle$ photons due to the birefringence of the post-compensator crystal. Hence pre-compensation is then needed to bring the photons back on top of each other. The phase plots after post-compensation and after pre/post compensation (both with YVO_4) are shown in fig. D.2. This gives an optimal length of pre-compensator crystal of 36.19 mm and of post-compensator of 36.36 mm.

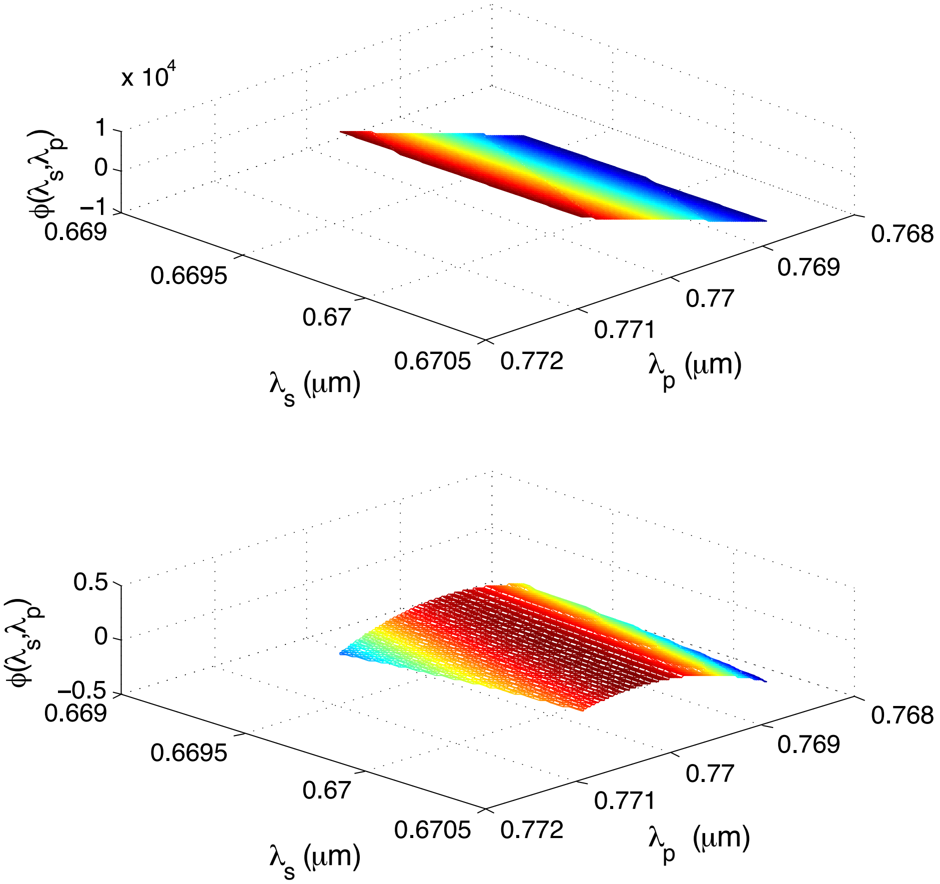

Figure D.2: Calculated phase map in degrees versus pump and signal wavelengths after post-compensation (top) and after pre- and post-compensation (bottom). The post-compensation removes phase dependence on the signal wavelength (note colour contours are now parallel to the λ_s axis), while putting a stronger dependence on the pump wavelength. This dependence is removed by pre-compensation, leading to a nearly flat phase map (note change in scale).

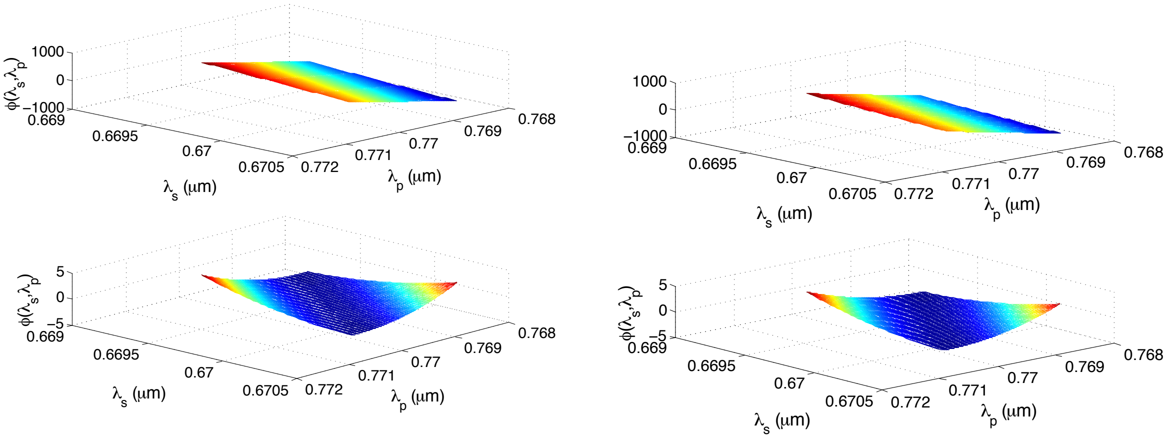

Figure D.3: Calculated phase map in degrees versus pump and signal wavelengths after signal post-compensation (top) and after signal and idler post-compensation (bottom), both using YVO_4 (left) and quartz (right). The map is not as flat as for pre/post compensation, but the main deviations far from the central area are exponentially suppressed by the decaying power spectrum far from the central wavelength.

The advantage of post/post compensation is that much less birefringent material is required, as the compensation relies on birefringence directly and not a birefringence of the material dispersion. For post/post compensation using YVO_4 as seen in fig. D.3, the optimal lengths of material are 1.92 mm and −2.49 mm for the signal and idler arms, respectively. The negative sign indicates the fast (ordinary) axis is oriented vertically, such that the $|VV\rangle$ term picks up less phase than the $|HH\rangle$ term in the compensator. For quartz compensation as in fig. D.3, the optimal lengths are −51.84 mm and 36.56 mm for the signal and idler arms. Here the phase map is not so flat as for pre/post compensation, but the resulting fidelities (below) are nearly unaffected.

After compensation, I can find the expected fidelity of the output state ρ with the maximally entangled state $|\psi\rangle = \frac{1}{\sqrt{2}}(|HH\rangle + e^{i\varphi}|VV\rangle)$, where φ can be any angle. In practice, I would use a small birefringence (e.g. tilted QWP) to tune φ to zero, and find fidelity with $\frac{1}{\sqrt{2}}(|HH\rangle + |VV\rangle)$, but this reverse method is easier computationally. The density matrix describing the mixed state caused by summing the contributions of the different phases is

$$\rho = \int \int |\phi\rangle\langle\phi| p_s(\lambda_s) p_p(\lambda_p) d\lambda_s d\lambda_p, \tag{D.25}$$

where $|\phi\rangle = \frac{1}{\sqrt{2}}\left(|HH\rangle + \mathrm{e}^{i\phi(\lambda_s,\lambda_p)}|VV\rangle\right)$ and $p_s(\lambda_s)$ and $p_p(\lambda_p)$ describe the spectra of the pump and signal respectively. I take them as Gaussian, based on fits to measured spectra,

$$p_k(\lambda_k) = \frac{1}{\sigma_k\sqrt{2\pi}} \exp\left(\frac{-(\lambda_k - \mu_k)^2}{2\sigma_k^2}\right) \tag{D.26}$$

with

$$\begin{aligned} \mu_s &= 669.82\,\mathrm{nm} \\ \sigma_s &= 0.17\,\mathrm{nm} \\ \mu_p &= 769.67\,\mathrm{nm} \\ \sigma_p &= 0.19\,\mathrm{nm}. \end{aligned}$$

The pump bandwidth may not be very precise here, as it includes some broadening in the fibre, which is power dependent.

The fidelity is then given by

$$\begin{aligned} F &= \left[\mathrm{Tr}\left(\sqrt{|\phi\rangle\langle\phi|\rho|\phi\rangle\langle\phi|}\right)\right]^2 \\ F &= |\langle\phi|\rho|\phi\rangle|. \end{aligned}$$

For the uncompensated output state, fidelity is $F = 58\,\%$, almost maximally mixed due to the strong phase change over pump and signal bandwidth. Using pre/post compensation, fidelity can be improved to $F = 99.9994\,\%$. With post/post compensation using YVO_4, the fidelity is $F = 99.9985\,\%$ and using quartz it peaks at $F = 99.98\,\%$.

How strongly is the fidelity affected by small perturbations that are not included in the compensation calculations, for example due to measurement errors? If each length of sausage is increased by 5 cm, fidelity drops to 96.7 %. If each length is increased by 1 cm, fidelity remains at 99.98 %. With 1 cm too little quartz in the signal arm, fidelity stays at 99.98 %, while with 1 cm too little in the idler arm, it stays at 99.91 %. With 1 cm too little quartz in both arms, fidelity stays at 99.8 %. If I use instead the broadened spectra at high power, the fidelities with perturbations are more in the 90 % range. Thus it should suffice to be accurate to within 1 cm when measuring the fibre and quartz lengths.

D.4 Measured parameters of birefringent crystals

Here I summarize the measured birefringences of the various compensator crystals in the source. The experimental setup for generating entanglement and the setup for measuring birefringence are shown in fig. D.4. These are followed by an experimentally-obtained example spectrum from which birefringence is calculated in fig. D.5. Passing diagonally polarized light through a birefringent material followed by a diagonal polarizer leads to fringes in the spectrum due to a wavelength dependent phase ϕ in the polarization state $|H\rangle + \mathrm{e}^{i\phi(\lambda)}|V\rangle$. To find birefringence from a spectrum of fringes I can start from a simple phase difference,

$$\phi(\lambda_1) - \phi(\lambda_2) = 2\pi \tag{D.27}$$

for one fringe. That is, one oscillation of the spectral interference pattern involves a 2π phase difference in the birefringent phase shifts of light of wavelengths λ_1 and λ_2. Here $\phi = \phi_{slow} - \phi_{fast}$ is the phase shift imparted by the fast and slow axes of the birefringent material. Taking the phases gained in the material as

$$\phi_{slow} = \frac{2\pi n_s L}{\lambda} \tag{D.28}$$

$$\phi_{fast} = \frac{2\pi n_f L}{\lambda} \tag{D.29}$$

gives

$$\phi(\lambda) = \frac{2\pi \delta n L}{\lambda} \tag{D.30}$$

with $\delta n = n_{slow} - n_{fast}$. Substituting $\phi(\lambda)$ into eq. (D.27) gives

$$\delta n = \frac{\lambda_1 \lambda_2}{(\lambda_2 - \lambda_1)L} \approx \frac{\lambda_0^2}{(\delta\lambda)L} \tag{D.31}$$

with the assumption that $\lambda_0 \approx \lambda_1 \approx \lambda_2 \gg \delta\lambda = \lambda_2 - \lambda_1$.

I report two values, the birefringence of the sample δn and the effective birefringent length, $\delta n L$, where L is the length of the crystal. Since $\delta n \propto 1/L$ in eq. (D.31), the effective birefringent length does not depend on my measurement of L, and can be used directly in calculations of phase shift from eq. (D.30). Rather than calculate $\delta\lambda$ from successive peaks, I perform a fit to the spectrum with a model function

$$f(\lambda) = a_1 \sin(b_1\lambda + c_1) + a_2 \sin(b_2\lambda + c_2)\,. \tag{D.32}$$

The first term captures the unimportant slowly varying envelope of the spectrum, while the second term and specifically $b_2 = 2\pi/\delta\lambda$ captures the birefringence-induced fringes. The birefringences and effective birefringent lengths are shown in table D.1.

Sample	L	Test λ	δn	Theory δn	$\delta n L$
Signal Quartz 1	40 mm	750 nm	0.0095	0.0089	3.8×10^{-4} m
Signal Quartz 2	27 mm	750 nm	0.0092	0.0089	2.4×10^{-4} m
Signal Quartz $1 + 2$	67 mm	670 nm	0.0096	0.0090	6.4×10^{-4} m
Idler Quartz	46 mm	750 nm	0.0094	0.0089	4.3×10^{-4} m
Idler Quartz	46 mm	905 nm	0.0093	0.0088	4.3×10^{-4} m
YVO_4 Black	4.85 mm	750 nm	0.247	0.215	1.2×10^{-3} m
YVO_4 Silver	4.85 mm	750 nm	0.247	0.215	1.2×10^{-3} m

Table D.1: Calculated birefringence of various crystals from measured spectra.

D.5 Degradation of entanglement visibility if the cross splice is imperfect

The splice in the centre of the sausage source may have its polarization axes misaligned from 90° by a small angle α. Assume $|HH\rangle$ photons are created in the first stretch of fibre then each undergo a unitary transformation $|H\rangle \rightarrow \cos\alpha|H\rangle + \sin\alpha|V\rangle$. The state becomes

$$|HH\rangle \rightarrow \cos^2\alpha|HH\rangle + \sin^2\alpha|VV\rangle + \cos\alpha\sin\alpha\,(|HV\rangle + |VH\rangle)\,. \tag{D.33}$$

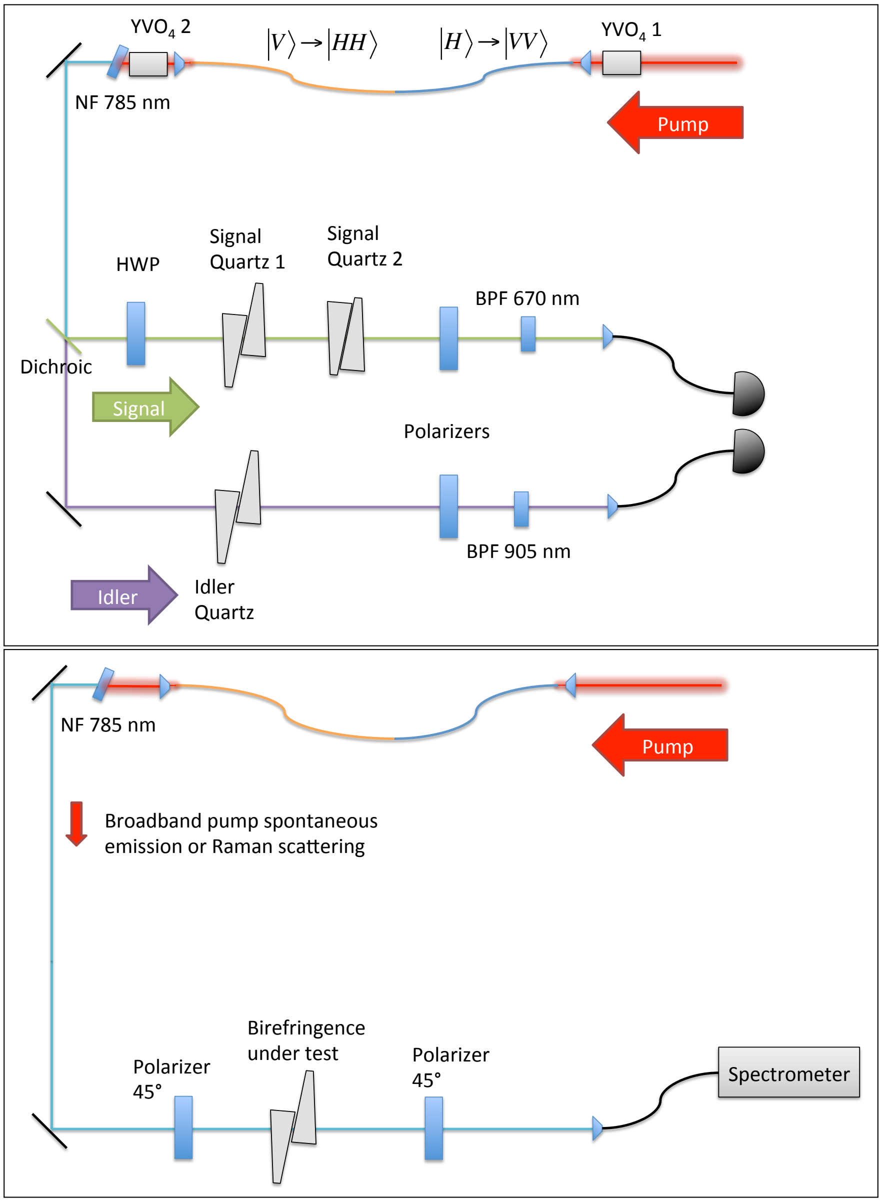

Figure D.4: (top) Experimental setup showing pre-, post- and double-post-compensation. Both YVO_4 crystals have their slow axes aligned vertically, while the quartz have slow axes horizontal (except the signal photons are rotated 90° by the HWP to give an effective vertical slow axis). (bottom) Experimental setup for measuring birefringence, with birefringent element placed between polarizers at 45° and illuminated by broadband light.

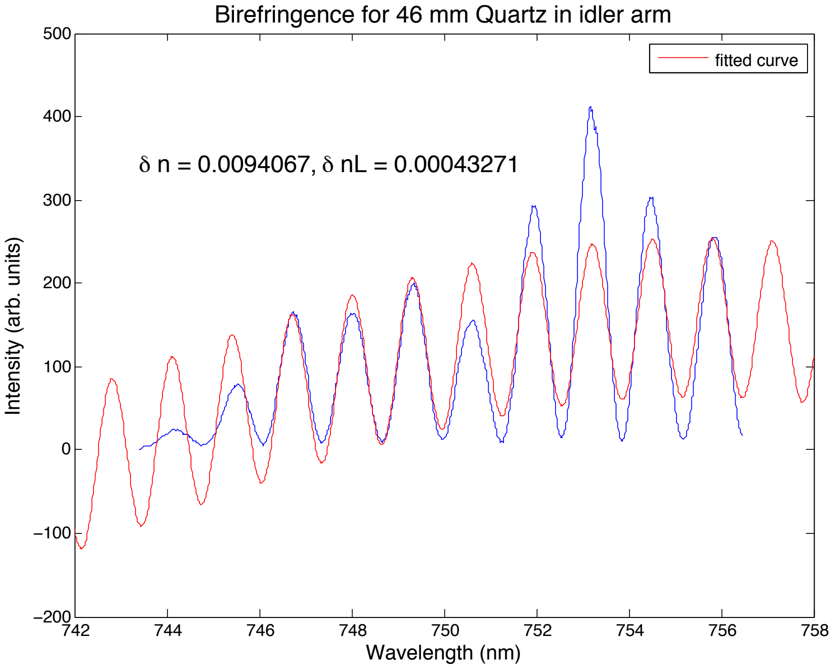

Figure D.5: Sample measured spectrum and fit used to calculate birefringence. The important point is that the experimental data and fitted curve have the same frequency.

It is easiest to find the visibility in the H/V basis, because I can convert everything to incoherent sums and add the $|VV\rangle$ term from the second part of the sausage source. The full state is then

$$\rho = \frac{1}{2}\left(\cos^4\alpha|HH\rangle\langle HH| + \cos^2\alpha\sin^2\alpha\left(|HV\rangle\langle HV| + |VH\rangle\langle VH|\right) + \left(1+\sin^4\alpha\right)|VV\rangle\langle VV|\right). \tag{D.34}$$

Visibility is

$$V = \frac{P_{\text{right}} - P_{\text{wrong}}}{P_{\text{right}} + P_{\text{wrong}}} = \frac{1}{2}\cos^4\alpha + \frac{1}{2} + \frac{1}{2}\sin^4\alpha - \sin^2\alpha\cos^2\alpha, \tag{D.35}$$

where P_{right} applies to $|HH\rangle$ and $|VV\rangle$ and P_{wrong} applies to $|HV\rangle$ and $|VH\rangle$. This simplifies to

$$V = \frac{1}{4}\left(\cos 4\alpha + 3\right). \tag{D.36}$$

Alternatively, an upper bound on the rotation of the splice can be found as a function of V as

$$\alpha = \frac{\arccos\left(4V - 3\right)}{4}. \tag{D.37}$$

Publications during PhD (2012-2016)

1. C. Erven, B. Heim, **E. Meyer-Scott**, J. P. Bourgoin, R. Laflamme, G. Weihs, and T. Jennewein. Studying free-space transmission statistics and improving free-space quantum key distribution in the turbulent atmosphere. New Journal of Physics **14**:123018 (2012).
   Link: arXiv:1208.0609
2. J.-P. Bourgoin, **E. Meyer-Scott**, B. L. Higgins, B. Helou, C. Erven, H. Huebel, B. Kumar, D. Hudson, I. D'Souza, R. Girard, R. Laflamme, and T. Jennewein. A comprehensive design and performance analysis of LEO satellite quantum communication. New Journal of Physics **15**:023006 (2013).
   Link: arXiv:1211.2733
3. Z. Yan, **E. Meyer-Scott**, J.-P. Bourgoin, B. L. Higgins, N. Gigov, A. MacDonald, H. Hübel, and T. Jennewein. Novel high-speed polarization source for decoy-state BB84 quantum key distribution over free space and satellite links. Journal of Lightwave Technology **31**:1399 (2013).
   Link: arXiv:1211.3194
4. **E. Meyer-Scott**, V. Roy, J.-P. Bourgoin, B. L. Higgins, L. K. Shalm, and T. Jennewein. Generating polarization-entangled photon pairs using cross-spliced birefringent fibers. Optics Express **21**:6205 (2013).
   Link: arXiv:1212.4780
5. **E. Meyer-Scott**, M. Bula, K. Bartkiewicz, A. Černoch, J. Soubusta, T. Jennewein, and K. Lemr. Entanglement-based linear-optical qubit amplifier. Physical Review A **88**:012327 (2013).
   Link: arXiv:1306.1342
6. C. Erven, **E. Meyer-Scott**, K. Fisher, J. Lavoie, B. L. Higgins, Z. Yan, C. J. Pugh, J.-P. Bourgoin, R. Prevedel, L. K. Shalm, L. Richards, N. Gigov, R. Laflamme, G. Weihs, T. Jennewein, and K. J. Resch. Experimental three-photon quantum nonlocality under strict locality conditions. Nature Photonics **8**:292 (2014).
   Link: arXiv:1309.1379
7. A. Dot, **E. Meyer-Scott**, R. Ahmad, M. Rochette, and T. Jennewein. Converting one photon into two via four-wave mixing in optical fibers. Physical Review A **90**:043808 (2014).
   Link: arXiv:1407.1250
8. **E. Meyer-Scott**, A. Dot, R. Ahmad, L. Li, M. Rochette, and T. Jennewein. Power-efficient production of photon pairs in a tapered chalcogenide microwire. Applied Physics Letters **106**:081111 (2015).
   Link: arXiv:1501.03532
9. K. Boone, J.-P. Bourgoin, **E. Meyer-Scott**, K. Heshami, T. Jennewein, and C. Simon. Entanglement over global distances via quantum repeaters with satellite links. Physical Review A **91**:052325 (2015).
   Link: arXiv:1410.5384

10. J.-P. Bourgoin, N. Gigov, B. L. Higgins, Z. Yan, **E. Meyer-Scott**, A. K. Khandani, N. Lütkenhaus, and T. Jennewein. Experimental quantum key distribution with simulated ground-to-satellite photon losses and processing limitations. Physical Review A, **92**:052339 (2015).
    Link: arXiv: 1512.05789
11. L. K. Shalm, **E. Meyer-Scott**, B. G. Christensen, P. Bierhorst, M. A. Wayne, M. J. Stevens, T. Gerrits, S. Glancy, D. R. Hamel, M. S. Allman, K. J. Coakley, S. D. Dyer, C. Hodge, A. E. Lita, V. B. Verma, C. Lambrocco, E. Tortorici, A. L. Migdall, Y. Zhang, D. R. Kumor, W. H. Farr, F. Marsili, M. D. Shaw, J. A. Stern, C. Abellán, W. Amaya, V. Pruneri, T. Jennewein, M. W. Mitchell, P. G. Kwiat, J. C. Bienfang, R. P. Mirin, E. Knill, and S. W. Nam. A strong loophole-free test of local realism. Physical Review Letters **115**:250402 (2015).
    Link: arXiv:1511.03189
12. **E. Meyer-Scott**, D. McCloskey, K. Gołos, J. Z. Salvail, K. A. G. Fisher, D. R. Hamel, A. Cabello, K. J. Resch, and T. Jennewein. Certifying the presence of a photonic qubit by splitting it in two. Accepted for publication by Physical Review Letters (2016).
    Link: arXiv:1510.04531